DOCTOR OF PHILOSOPHY

Ophthalmic engineering

the development of novel instrumentation to further research in the field

Thomas Drew

2013

Aston University

OPHTHALMIC ENGINEERING

The development of novel instrumentation to further research in the field

THOMAS EDWARD DREW

Doctor of Philosophy

ASTON UNIVERSITY

AUGUST 2012

ASTON UNIVERSITY

OPHTHALMIC ENGINEERING

The development of novel instrumentation to further research in the field

THOMAS EDWARD DREW

Doctor of Philosophy

August 2012

Thesis Summary

The principle theme of this thesis is the advancement and expansion of ophthalmic research via the collaboration between professional Engineers and professional Optometrists. The aim has been to develop new and novel approaches and solutions to contemporary problems in the field. The work is sub divided into three areas of investigation; 1) High technology systems, 2) Modification of current systems to increase functionality, and 3) Development of smaller more portable and cost effective systems.

High Technology Systems: A novel high speed Optical Coherence Tomography (OCT) system with integrated simultaneous high speed photography was developed achieving better operational speed than is currently available commercially. The mechanical design of the system featured a novel 8 axis alignment system. A full set of capture, analysis, and post processing software was developed providing custom analysis systems for ophthalmic OCT imaging, expanding the current capabilities of the technology. A large clinical trial was undertaken to test the dynamics of contact lens edge interaction with the cornea *in-vivo*. The interaction between lens edge design, lens base curvature, post insertion times and edge positions was investigated. A novel method for correction of optical distortion when assessing lens indentation was also demonstrated.

Modification of Current Systems: A commercial autorefractor, the WAM-5500, was modified with the addition of extra hardware and a custom software and firmware solution to produce a system that was capable of measuring dynamic accommodative response to various stimuli in real time. A novel software package to control the data capture process was developed allowing real time monitoring of data by the practitioner, adding considerable functionality of the instrument further to the standard system. The device was used to assess the accommodative response differences between subjects who had worn UV blocking contact lens for 5 years, verses a control group that had not worn UV blocking lenses. While the standard static measurement of accommodation showed no differences between the two groups, it was determined that the UV blocking group did show better accommodative rise and fall times (faster), thus demonstrating the benefits of the modification of this commercially available instrumentation.

Portable and Cost effective Systems: A new instrument was developed to expand the capability of the now defunct Keeler Tearscope. A device was developed that provided a similar capability in allowing observation of the reflected mires from the tear film surface, but with the added advantage of being able to record the observations. The device was tested comparatively with the tearscope and other tear film break-up techniques, demonstrating its potential.

In Conclusion: This work has successfully demonstrated the advantages of interdisciplinary research between engineering and ophthalmic research has provided new and novel instrumented solutions as well as having added to the sum of scientific understanding in the ophthalmic field

Keywords/Phrases (Ophthalmic Optical Coherence Tomography, Ophthalmic Engineering, Dynamic Accommodation Measurement, Tearfilm Break up Measurement, Grand Seiko WAM-5500)

Acknowledgments

There are many people I would like to thank who have helped me on the long journey to submitting this PhD thesis. Firstly, my supervisor Prof James Wolffsohn who has pushed me to better myself in all of my engineering endeavours. Without his help I wouldn't be where I am today, with all the possibilities the future holds laid before me. It was hard and extremely changing work at times, but absolutely worth it, long may it continue!

I would also like to thank my associated supervisor Dr Mark Prince, who I have spent many an hour discussing Engineering in all its wondrous forms. Dr Leon Davies for been my first year viva examiner. Mr Graham Davies has also provided excellent fabrication support, not only to me personally, but the whole ophthalmic engineering team. His skill and knowledge has being a great asset. The Modelshop team, James and Mike, for their support and advice. Finally from Aston, I would like to thank the LHS support staff, specifically Nicki Lander. Primarily for her help scaling the mountains of administrative paperwork and minifies of purchasing arrangements. We got through it in the end!

On a personal note, I would like to thank my friends for their help and support throughout the previous 4 years. In no particular order they are as follows; Jon, Ene, Joe, Alec, Ben, Becky, Ria, James, Angela and many more too numerous to mention who I have meet at my time at Aston.

And of course not forgetting my wonderful parents Margret and John, and my brother Ben, who have all my life, both loved, and support me, even with my eccentricities. In my youth they fostered my great love for Science and Engineering something that I am, and always will be most grateful for.

I remember as a child visiting Kennedy Space centre in Florida and seeing the mighty Saturn 5 rocket on display. I wondered how men could build such things! I knew then, engineering was something worth devoting one's life to. Therefore I would like to thank all the Engineers and Scientists who came before me, I do indeed stand on the shoulders of giants!

Collaboration Statement

Due to the multi-disciplinary nature of this project the clinical trials were undertaken as part of larger collaborations. The OCT clinical trial (chapter 5) was the core part of a study overseen by Prof James Wolffsohn with help from Dr Amy Sheppard, Dr Olivia Howells and Miss Sandeep Dhallu undertaking the roles of registered optometrists and researchers as legally required.

The trials for the Dyna-WAM system (chapter 6) and TearMaster (chapter 8) are again parts of larger studies overseen by Prof James Wolffsohn. The author's responsibility thought all of these trials were data capture, data analysis, and all engineering related development and design of hardware and software as required. Help with data processing and data entry was also provided by Mrs Ene Nixon working for Prof James Wolffsohn as a research assistant.

“Per aspera ad astra”

Table of Contents

List of Figures

Chapter 5

Chapter 6

Chapter 7

List of Tables

List of Acronyms

Acronym	Full Format	Acronym	Full Format
ABO	Aston Badal Optometers	MSE	Mean Spherical Equivalent
AMF	Aston University Manufacturing Facilities	NITBUT	Non-invasive Tear Break Up Time
API	Application programing interface	NTSC	National Television System Committee
ATD	Aqueous Tear Deficiency	OCT	Optical Coherence Tomography
BCVA	Best corrected visual acuity	OSH	Open Source Hardware
BMI	Body Mass Index	OSS	Open Source Software
CAD	Computer Aided Design	OTS	Off the Shelf Hardware
CAI	Computer Aided Innovation	PCA	Producer Consumer Architecture
CAM	Computer Aided Manufacture/Machining	PCD	Producer and Consumer Design
CAE	Computer Aided Engineering	PCIe	Peripheral Component Interconnect Express
CCD	Charged Couple Device	PCTF	Pre Corneal Tear Film
CCFL	Cold Cathode Fluorescent Lamp	PD	Parametric Design
CE	“Communaute Europeenne”	PE	Polyethylene
CFD	Computational Fluid Dynamics	PNG	Portable Network Graphics
CM	Confocal Microscopy	POLTF	Post Lens Tear Film
CPU	Central Processing Unit	PP	Polypropylene
CRF	Clinical Report Form	PRT	Phenol Red Thread
CSV	Comma Separated Variable	PWM	Pulse Width Modulation
CUDA	Compute Unified Device Architecture	QC	Quality Control
DES	Dry Eye Syndrome	R&D	Research and Development
DL	Diffraction Limit	RAID	Redundant Array of Independent Disks
DOF	Depth of Field	RAM	Random Access Memory
DSP	Digital Signal Processing units	RB	Rose Bengal
EU	European Union	RGB	Red, Green and Blue
FDA	Federal Drug Administration	RP	Rapid Prototyping
FDM	Fused Deposition Modelling	SD-OCT	Spectral Domain OCT
FD-OCT	Fourier Domain OCT	SF	Sodium fluorescein
FEA	Finite Element Analysis	SLP1	Slit Lamp Purkinje 1
FFT	Fast Fourier Transform	SM	State Machine Architecture
FIFO	First in, First out	SME	Small and Medium Enterprises
FL	Sodium fluorescein	SMT	Surface Mount Technology
FOS	Factor of Safety	SOP	Safe Operating Produce
FOV	Field of View	SP	Scheiner Principle
FPGA	Field Programmable Gate Arrays	SPD	Spectral Power Distribution
GMS	Galvanic Mirror System	SS	Sjogrens Syndrome
GUI	Graphical User Interface	SS-OCT	Swept Source OCT
HDD	Hard disk drive	ST	Schirmer Test
IQA	Image Quality Analysis	TD-OCT	Time domain OCT

KTM	Keratometery Mires
LD	Laser Diodes
LG	Lissamine Green
LLA	Local Laser Advisor
LPS	Laser Protection Supervisor
LTD	Lipid Tear Deficiency
MCU	microcontroller
MDC-1	Measurement Data Collection
MDD	Medical Devices Directives
MGD	Meibomian Gland Dysfunction
MHRA	Medical and Healthcare Products Regulatory Agency
MIT	Massachusetts Institute of Technology
MPE	Maximum Permissible Exposure
TM	TearMaster
TS	Tearscope Plus
TTL	Transistor-transistor Logic
UV	Ultra-violet
VDU	Visual Display Units
VI	Virtual Instrument
WCS-1	WAM Commination System

List Equations and Symbols

Symbol	Metric
	Equation 2.1
Δz	Axial Resolution
λ_0	Sweep Range
$\Delta\lambda$	Change in Wavelength
π	Pie
n	Refractive Index
	Equation 2.2/2.3
$\delta\lambda$	Line Width
π	Pie
λ_0	Center Wavelength
cl	Coherence length
Δd	½ Coherence length
	Equation 2.4
N or NA	Numeric Aperture
Θ	Half Angle
f	Focal length
D	Diameter of Optics
π	Pie
	Equation 2.5
d	Lateral Resolution
D	Diameter of Optics
λ f	Center Wavelength
	Equation 2.6
DOF	Degree of Freedom
ω_0	Spot Size
λ	Wavelength
	Equation 2.7
MPE	Mean Permissible Exposure
t	Exposure Time
C_6	Coefficient C6
C_7	Coefficient C7
	Equation 2.8
D	Divergence
Df	Diameter Beam
D_1	Diameter Beam at Far point
l	Separations

Symbol	Metric
	Equation 2.9
MPE	Mean Permissible Exposure
t	Exposure Time
C_6	Coefficient C6
	Equation 4.1
Y	Dependent Variable
a	Coefficient (Amplitude)
b	Decay constant
x	Independent Variable
	Equation 4.2
ϵ	Eccentricity
a	Major Axis
b	Minor Axis
	Equation 4.3
$\bar{x}$	Apparent Size
β	Plane Angle
x	Original Size
	Equation 4.4
β	Plane Angle
ϵ	Eccentricity
	Equation 4.5
B	Plane Angle
ϵ	Eccentricity
	Equation 5.1
N_0	Initial Values
λ	Wavelength
t	Time Constant
	Equation 6.1
y	Final Value
y_0	Initial Value
a	Amplitude coefficient
t	time point
τ	decay (-ve)/rise (+ve) constant

Chapter 1

Chapter 1 Thesis Introduction

1.0 Imaging the Ocular System – The Medical Need

Blindness and vision impediment is a major problem that plagues quality of life as well as economic aspirations of many individuals worldwide. It is estimated that 161 million people have some form of serious visual impairment that costs the world economy between 20-25 billion dollars annually in lost economic output (Ibrahim & Bhandari 2006). Cataracts alone represent 43% of world blindness (Kelly et al. 2005)

Quality vision is essential for many day to day tasks such as driving, cooking and reading. The onset of presbyopia towards later adulthood and the resulting loss of accommodation, leaves the majority of people requiring some form of visual correction for close up work.

Routine eye examinations are essential for health and wellbeing. Time between examinations is often dependent on general ocular health and progression of disease. Most people associate visits to the optometrist with the process of refraction and the fitting of eye glasses. It remains, however, important for a more detailed eye examination to be performed. Indeed there is the legal requirement for the optometrist to evaluate not only your refractive state but your general ocular health (Harvey & Franklin 2005, p.4)

Viewing of the eye through magnification devices can be separated into two areas; anterior segment and posterior segment. Anterior segment imaging generally concentrates on viewing the cornea, tear film, anterior chamber, crystalline lens and the iris. It also includes viewing the eye lids, conjunctiva and other associated external structures. Slit lamps are the most common devices for anterior segment imaging with their use being near universal in both professional practice and education. However, newer more advanced devices such as Optical Coherence Tomography, allow the practitioner a section view at high magnification, not available until recent years.

Posterior imaging is viewing the parts of the eye obscured behind the crystalline lens and iris. Features looked at include the fovea, macula, optic nerve and distribution of retinal veins and arteries. The most common form of investigation is with the direct ophthalmoscope, a handheld device that allows for close up examination of the posterior segment of the eye. Any form of posterior segment viewing will require optics with very short focal lengths to produce clear image of

the retina. Direct ophthalmoscopes are standard pieces of equipment for the optometrist and ophthalmologist. Devices such as the slit lamp can be used for posterior segment imaging with modification (i.e. the use of condensing lenses). Most of the current ophthalmic devices require a large quantity of operator input to achieve desirable results. They are also issues regarding subjectivity of data collection and repeatability with different operators often disagreeing significantly on results (J. J. Nichols et al. 2002).

Machine vision and automated inspection systems allows high speed quality control and inspection in industry. Producing high quality images of the eye can be difficult if taken by a non-specialist or under difficult conditions such as during cataract surgery or on a non-cooperative subject. Automated inspection systems with intelligent algorithms would be able to determine if images are correctly exposed and contain the required features. These could aid practitioners and others who are required to image the eye, but are not actually experienced in ophthalmic imaging.

Reducing the complexity of operation for the end user is also of importance. The modern optometrist is often pressured into performing a large quantity of eye examinations in order to maximise profit. Producing systems that simplify the imaging process and processing of data, while reducing the required input from the operator will be advantageous. The use of non-specialist labour can also reduce the burden placed on the optometrist with assistants performing pre-screening and non-specialist imaging. Reduction in training and certification can also reduce operational costs. Remote data collection and forwarding to specialists can also improve the patient experience by providing more flexible access to enhanced expertise at reduced costs and delay (Fittock 2010, pp.0–12).

Developments in computation technology at the beginning of the 21st century have enabled the rapid advancement in image manipulation and storage capability. Many of the current devices used to image the anterior segment are cumbersome or lack the ability to capture images. It is, therefore, logical to assume that smaller more portable imaging devices that allow images to be captured, digitised and post analysed can provide optometrists with more objective measures. Results can be played back to the patient after examination, aiding understanding and communication with the patient would be helpful to the practising optometrist.

Many current ophthalmic devices have changed little since their inception (such as slit lamps). Although undeniably effective, they still possess design features and manufacturing techniques of a less design conscious age. They utilise antiquated materials and fabrication techniques, often being over engineered for their required use. Using modern materials and design, miniaturisation,

increased functionality and reductions in cost should be readily achievable. Not only would this increase the quality and experience to the end users but also increase the utilisation and uptake of ophthalmic instrumentation.

1.1 Modern Engineering and The Promise it Offers

Engineering is often poorly understood by the general public. Most will never have any interaction with the design process, or a clear understanding of the role of engineering in society. Currently there are approximately 180,000 professional engineers in the United Kingdom; alarmingly their numbers are declining, despite the government efforts to reverse this trend (A. Kumar & Buglass 2009). There is probably no other industry or profession that is as intimately linked and affected by the changing world of technology, relentless progression of science and the ever increasing rate of change. The core ethos of engineering is that we will tomorrow, be able to achieve more, with less, cheaper and quicker than today. Perhaps no one has put it better that Sir Isaac Newton in his 1676 letter to Robert Hooke stating “if I have seen further it is by standing on ye shoulders of Giants” (Shapiro 2006, pp.11–12). Every generation anew adds to the sum of knowledge. Tools become ever more capable, knowledge better accessible, each new generation of engineers can achieve what only the previous generation could dream of.

On the 21st of December 1968 a spacecraft named Apollo 8 blasted off form launch complex 39A at Kennedy Space Center Florida USA with the goal of achieving the first manned orbit of the Moon. It was the first time humans would ever escape the gravitational field of the Earth and see the planet before them with both poles visible in a single vista only 65 years after man’s first flight. Besides being a monumental achievement of modem science, it illustrated the difficulties of working with highly complex systems. Over four hundred thousand people worked directly on the Apollo project. The Saturn 5 rocket consisted of over six million separate parts, in seven hundred thousand sub-assemblies. Costs were never fully accounted, but summed over the entire endeavour to be equivalent least 129 billion dollars (2008 USD). A total of five lives were lost and twelve people walked on the moon (Woods 2008, pp.15–20). The monumental efforts to achieve these goals gave rise to such social concepts and popular phrases as “it’s not rocket science” when referring to a project not been very complex or “we can put a man on the moon, but we can’t …” when faced with poor design (usually some form of inadequate packaging).

On the 3rd of August 2008 at 3:34 GMT an engineering company, Space Exploration Technologies (SpaceX, California, USA) with 500 employees placed the first privately developed spacecraft in orbit.

Four year later, having swelled there ranks to 1800 members, they became the first private company to resupply the international space station (Grantham 2012). Moden engineering principles and techniques have now reduced what was once considered the domain of large government projects, and Mega-Corporations, within the reach and budget of small and medium enterprises (SME). This rapid increase of productivity and capability would have not been possible without modern engineering principles such as Computer Aided Design (CAD), Computer Aided Manufacture/Machining (CAM), Computer Aided Innovation (CAI) and product development strategies such as Product Lifecycle Management (PLM). These tools applied to ophthalmic engineering in the United Kingdom could provide valuable new markets and stimulus for innovation. This thesis aims to investigate the feasibility of applying such tools to developing ophthalmic devices.

1.2 New Tools, New Approaches

1.2.1 Modern CAD and CAE

The most known advanced design tool is probably CAD. The history of CAD systems is complex with many different parallel developments occurring simultaneously. The first basic principles of both CAD and CAM were developed in the 1950's by MIT to manage the complex tasks of producing large aerospace projects (Radhakrishnan et al. 2008, pp.13–35). CAD give an engineer the advantage of producing an object, both single items (components) and complete assemblies in a virtual environment before any physical fabrication takes place. This allows the rapid identification of obvious error (misaligned holes etc…) and the ability to view the device in three dimensions aids understanding of function and utility. One of the major advanced of CAD is information and ideas can be electronically transmitted with ease allowing multiple teams to work, or have input into the design process. This is of specific interested when working with sub-contractors/manufacturers reducing the lead time required for fabrication. An everyday item such as a photocopier may have two thousand separate parts and require over one million engineering decisions to fully develop (Barrios Hernandez 2006). Collaborative CAD systems and concepts have been discussed in detail (Li et al. 2005). CAE bridges the gap between the virtual and real worlds by turning ideas into physical products. CAE is also the general term given to the production of prototypes generated from CAD files using rapid prototyping technologies, something not before seen or used in ophthalmic research at Aston University, but used extensity throughout the research presented in this thesis.

The use of rapid prototyping (RP) is clearly indicated in the prevalent chapters. Advanced design tools such as Finite Element Analysis (FEA) are touched on briefly, but are not used extensively as the types of engineering undertaken are not operating in extreme or highly optimised environments.

1.2.2 The Parametric Design Advantage

Modern CAD packages are based around the parametric design philosophy, of which good examples and practices of such had been reported on (Barrios Hernandez 2006). Parametric design (PD) is using relationships and parameters to define the physical characteristics of a model rather than physical dimensions or sizes. An example of this approach would be defining the number of bolts holding a pressure vessel access plate as a function of the size of the vessel. If you wished to produce a bigger vessel, using traditional approaches, you would have to add more bolts manually. However using PD the computer would be able to plot the new geometry from a set of existing design rules. Parametric modelling is difficult to execute and requires considerable design intent from the outset. Producing fully defined solid models is in this authors experience the hardest part of solid modelling for any engineering students or indeed seasoned professionals. PD was used extensively throughout this project and considerably reduced the time required for modify designs and to develop a quick succession of new versions of components. The extensive use of PD aids the development of modular systems and will eventuality lead to even faster development of prototypes giving closer and better customer interaction.

1.2.3 Why CAI is Important

CAI is a relatively new term but can easily be related to current understating of the use of CAD and CAE systems in industry. The principles of CAI are have been discussed in detail (Leon 2009). CAI takes into account the rapid nature of modern engineering and the extreme pressure for rapid customer focused produce development. In the context of ophthalmic settings, CAI principles allow closer cooperation between customer (optometrist/ophthalmologist/researcher) and engineering professionals to develop novel solutions in very short turnaround times. Traditionally this was something not possible outside of large enterprises before the development of advanced design and analysis tools. This thesis will show an approach that will allow even greater integration of CAI into the field of ophthalmic manufacturing with the hope of expanding current areas of research while minimising cost due to lost man hours and reduced misguided investigations.

1.2.4 Product Lifecycle Management

Product lifecycle management is a strategy for the management of development of products (usually technical, electronic or software in nature). It derives a system for managing the research and engineering involved in product development, streamlining the flow of data between engineers, managers, collaborators and customers more effectively. Part of the work undertaken was to develop management strategies for effective design, construction and design of novel tools for furthering research in vision sciences at Aston University. The ultimate aim was to develop an efficient and effective capability to respond to challenging needs of research and the ever changing capabilities of technology. PLM is have been used effectively to optimise the development of numerous projects; good examples of the process and its capabilities are explained by Farhad Ameri's paper on the subject (Ameri & Dutta 2005).

1.3 The Open Source Alternative

1.3.1 Open Source Software

The Open Source concept involves the user community contributing to a project and building a product (usually software, but increasingly hardware) and distributing it freely and not for profit. The rational is that more people will have access to affordable software than supplied by traditional large venders such as Microsoft, IBM, and Sun Microsystem. The first large scale Open Source Software (OSS) projects was the development of the Linux operating system. It has been estimated that if this project was developed using traditional techniques and costing it would have cost 6.1 billion euros (2005 Euros), currently the entire library consists of over 320 million lines of code (Jos et al. 2009). Open source software was used extensively throughout the project to reduce development cost and times; specifically open-source image manipulation tools such as ImageJ (National Institutes of Health. Maryland, USA), Paint.net (dotPDN LLC, USA)) and C complies such as AVR-GCC were utilised (Atmel Corporation, San Jose, California) The OSS helped reduce the cost of development considerably and can aid SME in achieving competiveness. An equivalent C compiler from Microchip Technology (Chandler, Arizona, USA) the HI-TECH C Compiler costs over $1000 USD (Microchip Technology Inc, Arizona, USA). OSS software has the potential to speed development but is not always applicable; as of July 2012 no viable open source CAD packages exist.

1.3.2 Open Source Hardware

The concept of open source hardware (OSH) is becoming more popular. Much of the electronics prototyping in the projects discussed were undertaken with the Arduino open source hardware platform. Arduino was chosen because it provided a cost effective and scalable system that was proven to be reliable. Both the ATmega 328PU chip with 32KB of flash memory and the ATmega 2560 with 259KB of flash memory were utilised. Software development was undertaken with both the standard integrated development environment (IDE) provided with Arduino and the ATMEL Corporation (San Jose, California, USA) Studio 4/5/ IDE. Experience has indicated the capability to embed up to 15k lines of code onto an ATmega 2560. Without these excellent development tools both hardware and software the time and cost needed to undertake the work detailed in this thesis would have rendered projects as ambitious and out of reach.

1.4 Modern Manufacturing Technology

Aston University possess some of the most advanced rapid manufacturing and rapid prototyping technology currently available. Many of these tools have not been systematically applied to research in the ophthalmic field hitherto. Part of the scope of this thesis will be the investigation into the best method for application of these diverse tools and what possible benefits they could bring and if the use of more modern approached fabrication could reduce the cost of ophthalmic instrumentation.

1.5 Advanced Machine Tools

Aston University possess multiple CNC milling machines, the most capable being the Fanuc ALPHA T21 (Fanuc Corporation, Oshino-mura, Japan) providing high speed 3 axis CNC capabilities. Tear-downs (reverse engineering) of existing ophthalmic equipment has indicated that CNC technology is used widely in the manufacture of many instruments. However slit lamps and more legacy devices tend to rely heavily on casting and Near Net Shape (NNS) fabrication techniques such as casting and forging. Further tooling includes retrofitted and digitally upgraded milling machines and lathes.

Both CNC and manual techniques have been used extensively for devices presented in this research. We have developed library's containing hundreds of designs for custom parts, fabricated from over 10 different base materials, as diverse as from cryogenic aluminium alloys to ultra-low friction, high durability plastics such as Polytetrafluoroethylene (PTFE). Correct material and tool selection play a large role in the final cost of a product development.

CNC tools provide the capability to produce complex but precise geometry directly from CAD provided information, but can also produce considerable quantities of files and data require storage, handling and labelling. The rapid development of subsequent improved designs produces potential confusion and requires a system to handle revisions and updates. This research will also develop data handling and naming strategies.

1.6 Rapid Prototyping and Rapid Manufacturing

The technology behind Rapid Prototyping (RP) and Rapid Manufacturing (RM) and their application had been approached and discussed in detail by numerous authors (Gibson et al. 2010, pp.1–14; Chua et al. 2003). RP and RM are fundamentally different approaches to fabrication than traditional methods called "additive manufacturing". The fundamental difference is that where most process removes material from a larger piece of a raw material, to hone the object closer to its final shape, RP and RM technologies add material. Material is built up layer by layer to produce the final desired geometry. Aston University currently uses two forms of rapid prototyping technology capable of producing structural plastic components. Firstly a Dimension BST (Stratasys Inc, Eden Praireie, Minsaota, USA) based on the process of fused deposition modelling (FDM), a process where material is laid down in tracks producing successive layers. Problems with this process are apparent and the final object is not truly a homogeneous material and this can potentially delaminate at layer intersections under high stress conditions. The second technology used is Stereolithography (SLA) where a laser selectively hardens a layer of fluid by directly illuminating its surface. This hardened area is then dropped below the surface of the fluid and the process repeated . This technology offers very fine surface finished and tolerances but it's extremely expensive with costing over two hundred thousand dollars (2006 USD) and a single replacement tub of fluid costing over five thousand dollars (2012 USD). RP and RM technologies are believed to offer great potential for medical products and are already used extensively in the mass manufacture of hearing aids (Masters & Mathy 2002).

The concept of mass production is familiar to everyone, indeed the industrial revolution started the concept of mass produced identical goods sold in huge quantities. If you look around the room you are in right now, you will certainly notice that nearly everything is a mass produced item. Almost nothing is unique, nearly all of your possessions are also owned by potentially millions of other people. The development of increasingly efficient RM technology could offer a significant paradigm shift in this concept over the coming century. The idea has been discussed that the age of mass production could be coming to an end, and the age of mass customisation is starting (Eyers & Dotchev 2010). Products customised for individual's requirements have the potential to offer much better solution and greater customer satisfaction. This research will investigate the use of RP and RM technologies in the scope of ophthalmic research and identify where there best use is apparent for developing rapid solutions and turnarounds.

1.7 Notes on The technical Development Cycle

When developing systems which integrate multiple engineering technologies and disciplines, it is often difficult to chart the individual steps in the development cycle. Most people are familiar with the concept of a prototype and regard it as the forerunner to a finished device. However when working with complex systems there are often numerous changes throughout the development process; if every minor change resulted in a new version number or prototype designation, it would soon become difficult to track design millstones effectively. The word prototype may be used throughout this report, but unless otherwise stated, it will refer to the final iteration of the systems and can be regards as the pre-production technological demonstrator (i.e. the final device or design put forward for evaluation and/or used for testing).

In line with other engineering disciplines (specifically, Aerospace and Astrospace engineering) the Block design designation system will be used throughout this report. The logical progression is as follows; Block 1 is the initial phase followed by Block 2, Block 3 etc… There may be gaps between phases that are not mentioned i.e. Block 4 may follow Block 2. In this case, Block 3 may have represented a radical departure from the current approach and ultimately failed early into the investigation process. It will be noted in the record of design progression, but may not be listed in detail.

All engineering systems have three common sub areas. These are; 1.) Hardware and electrical systems 2.) Firmware and/or embedded systems 3.) Software systems and user Interface. The Block design system is used to chart the development of the entire system and is not applied to its sub systems. Version numbers will be applied to software and firmware where appropriate.

Each chapter will deal with a different device charting its development, testing and commissioning. Sub areas will be discussed separately within each chapter and related to their overall position within each Block design approach.

1.8 Thesis Aims and Objectives

The aim of this project is to apply modern engineering principles to a selection of ophthalmic devices and develop a strategy for applying modern 21st century engineering tools to a diverse set of problems currently experienced in the ophthalmic industry. This thesis will demonstrate not only a series of novel hardware innovations to aid current research, but also an approach for innovating and generating products, designs and concepts for future work. It is hoped that the work will ultimately lead to a series of novel ophthalmic devices that will be manufactured under the Aston University name.

The first investigations demonstrate how high-end technology can enhance the understanding of *in-vivo* the interaction between medical devices, in this case a contact lens, and ocular tissue in a dynamic in-vivo clinical environment. A dual imaging Optical Coherence Tomography (OCT) / High Speed Camera (HSC) system was developed. This system was designed to study the dynamics of contact lens movement over the corneal surface under varied conditions. The development consisted of hardware, firmware and software solutions. Each of the three area investigates will have an associated study to prove the validity of the instrument.

The second example is how existing commercially available equipment can be enhanced to increase its functionality. In this example a commercially available open-field autorefractor was converted from a basic pupil size and refraction device to one that allowed dynamic monitoring of ocular accommodation and pupil size allowing a project on the effect of ultra-violet light blocking contact lenses on ocular accommodation to be conducted.

Finally, the ability to recreate and expand the functionality of an existing instrument, but in a smaller, portable and lower cost device with objective evaluation capability was investigated. The project focused on the ability to assess the tear film and its dynamics *in-vivo* and allowed a project on dry eye assessment repeatability to be conducted.

Perhaps one of the most difficult parts of the thesis was deciding on what the scope of the projects and what approach would be undertaken. The concept does not easily fit into either a typical, or should it be said classical, optometry or engineering approach. This work is a hybrid of both instrumentation design and clinical application with the aim of producing a knowledge transfer between both systems providing the benefits of a multidisciplinary approach. The thesis concentrates on the more technical areas of the design of the systems but with a deliberate effort to not make the approach overly technical. The three areas each report a brief history and review of

the technology under investigation. Much of the reporting does not fully illustrate every detail of the entire design, fabrication and testing process, but is intended to give the reader a macro scale view of the process. The development of both the hardware described in this thesis and the approach to future design scenarios, encompasses approximately 8,000 man hours of work across multiple engineering disciplines.

Chapter 2

Chapter 2: OCT Technology and Customisation

2.1 Optical Coherence Tomography

Optical Coherence Tomography (OCT) technology can be divided into two distinct sub areas: Time domain OCT (TD-OCT) and Fourier Domain OCT (FD-OCT). FD-OCT can further be split into two different types: Spectral Domain OCT (SD-OCT) and Swept Source OCT (SS-OCT).

The first OCT systems were developed by the Massachusetts Institute of Technology (MIT) in 1991 (Huang et al. 1991). This first system was based on the time domain method and was capable of operating at a scan speed of 2Hz (equivalent A-Scan speed). Further improvements were presented by the same organisation increasing scan speed to 150Hz (E. a Swanson et al. 1993) and to 600Hz in 1997 (Tearney et al. 1997). Modern OCT systems are not usually based on the time domain operation principle. TD-OCT systems have been demonstrated at multi kilohertz operation frequencies, but are not capable of operating at similar speed to FD-OCT (Oldenburg et al. 2003)

2.1.1 Time domain OCT

Time domain OCT relies on the principle of inference of broad spectrum, low coherence (white light) sources. This produces interface data based on backscattered and back reflected light from differing depth penetration points of samples under test. Figure 2.1 shows the optical arrangements of a typical TD-OCT system. All OCT system designs feature an interferometer to produce inference data. Broad spectrum light is split via a beam splitter and directed at a sample under scan via a set of focusing optics and movable galvanic mirrors. The second part of the beam is directed at a moveable reference mirror. A balance detector containing a photodetector, capable of imaging the inference patterns generated by the interaction between the two split beams, is positioned opposite to the reference arm of the system. The entire arrangement is a modified Michelson interferometer with added components and extended optical paths.

In TD-OCT the reference mirror is swept a in a sinusoidal fashion (Z scan) forming interference patterns creating representations of sample depth at differing discreet positions. High speed analog digital converters (ADC) capture the interface patterns. Digital filtering is used to remove unwanted noise and condition the signal ready for mathematical post processing and demodulation.

Demodulated data can be directly related to return reflection intensity at different depths of penetration. Levels of depth penetration are limited by the return intensity of the reflected light. As the light travels further into the medium more is absorbed and scattered, so the signal to noise ratio (SNR) reduces until no definitive data can be distinguished. Depth penetration is usually about 3mm for TD-OCT Systems and is controlled by the spectral spread of the board spectrum source (Tearney et al. 1996).

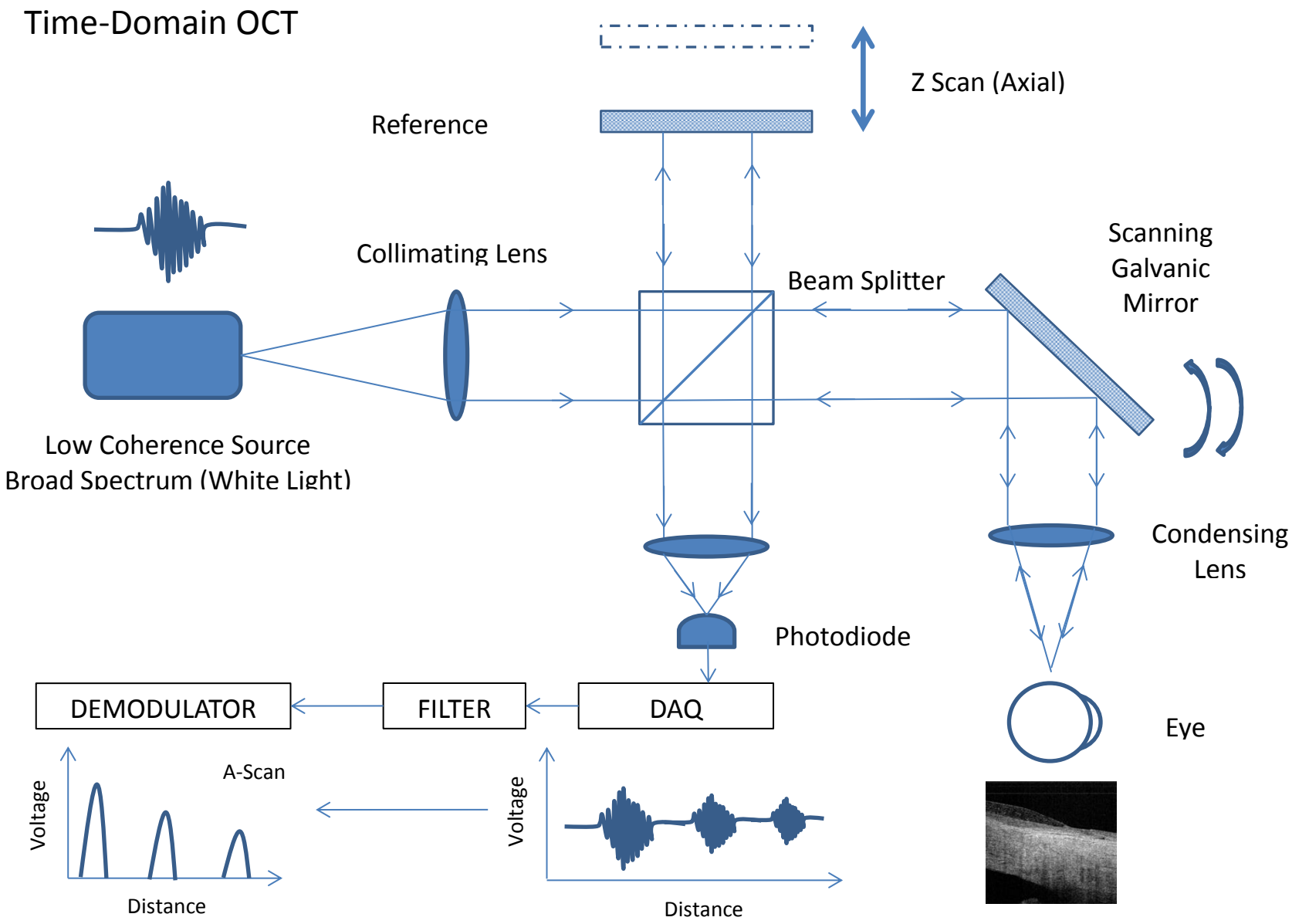

Figure 2.1: General arrangement of a time domain OCT system

2.1.2 Fourier Domain OCT

Fourier domain OCT systems are almost identical mechanically to TD-OCT systems. Figure 2.2 shows the breakdown of a typical SD-OCT system. The first SD-OCT systems was demonstrated in 1995 (Fercher et al. 1995), using a broad-spectrum source similar to TD-OCT systems. The major difference is that the reference arm (reference mirror) does not move when scanning, giving the system a far faster operating capability. SD-OCT systems have a scan range at least 100 times greater than TD-OCT systems (Maciej Wojtkowski 2010). SD-OCT systems became more prominent and reached maturity in the early 2000's, giving the capacity for real time OCT imaging. With initial systems demonstrating operating frequencies of 15kHz (M Wojtkowski & Bajraszewski 2003) and rapidly increasing to scan speed of over 300kHz by 2008 (Potsaid et al. 2008).

The systems optical arrangement is very similar to TD-OCT except the balance detector is replaced by a system of diffraction gratings and a line scan camera. The linescan camera is a CCD device that has a single line of pixels producing a very wide but narrow image. The extremely low pixel density can be indexed at high speed producing extremely fast frame rates. The diffraction grating produces interference patters for a wide range of frequencies. Interferogram patterns captured by the linescan camera are processed with fast Fourier transforms to determine an associated frequency spectrum. This spectral data directly relates to reflection and scattering properties at each discreet depth producing information about the sample under scan.

2.1.3 Swept Source OCT

SS-OCT is a further advancement of the FD-OCT concept. The system shares similar components but swaps the diffraction gratings and linescan camera with a new type of frequency swept light source and a photodiode detection system. The timing between laser pulsed and data capture is controlled via a precision timing line giving interference data for a wide spread of frequencies. Post processing is identical to FD-OCT, using Fourier transforms to construct depth and reflection information.

The SS-OCT concept was developed in 1997 with a scan frequency of 10Hz and a sweep range of 25nm (Chinn et al. 1997). The technology rapidly progressed with systems providing A scan frequencies of 370kHz (Huber & Adler 2006) and light sources with 170nm spread (Chong et al. 2008). Figure 2.3 shows the SS-OCT system diagrammatically. Further advancements are likely to

involve the use of multi-beam OCT systems using parallel light sources to image at differing depths simultaneously (Meixiao Shen et al. 2011)

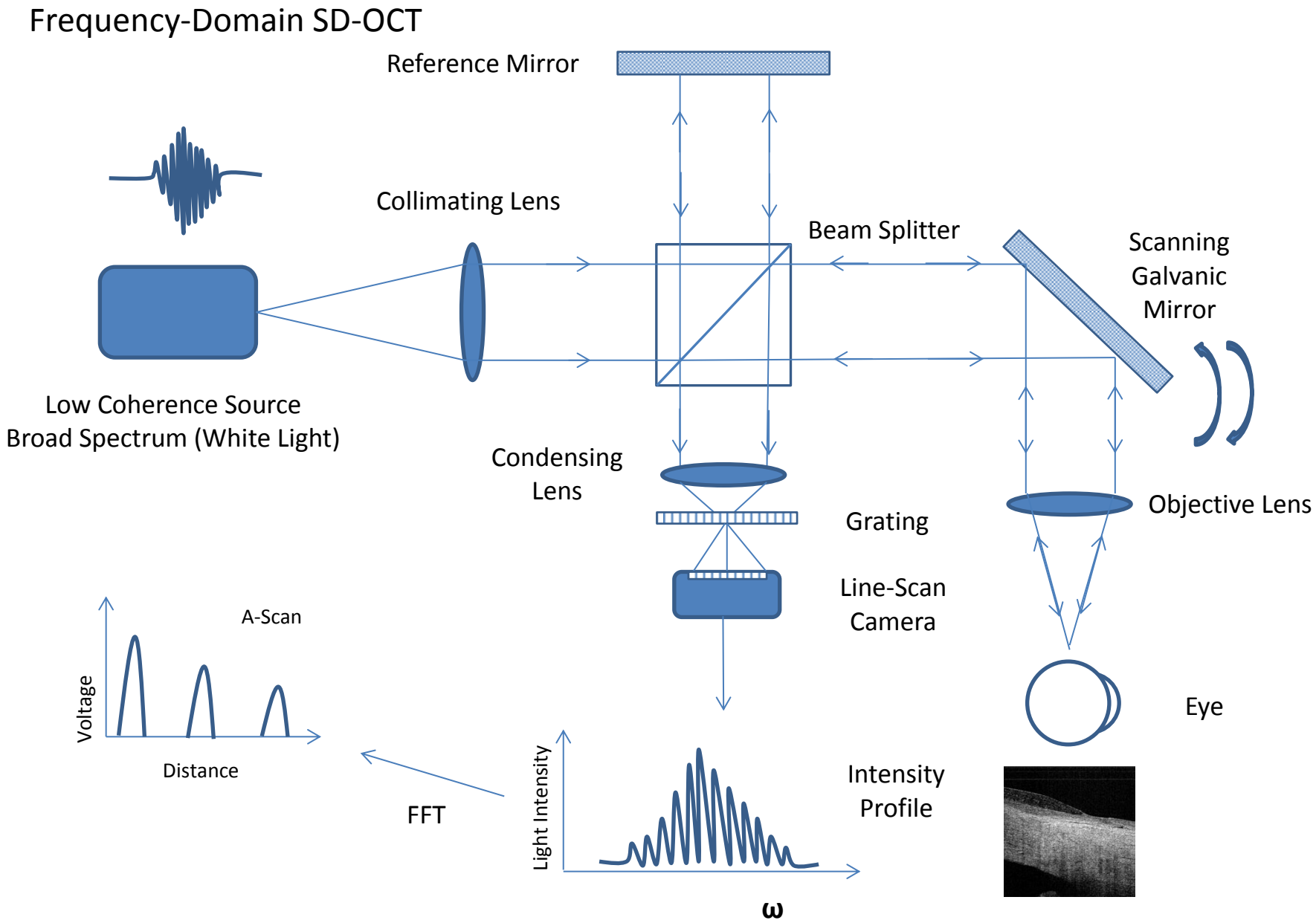

Figure 2.2: General arrangement of a frequency (Fourier) domain OCT system

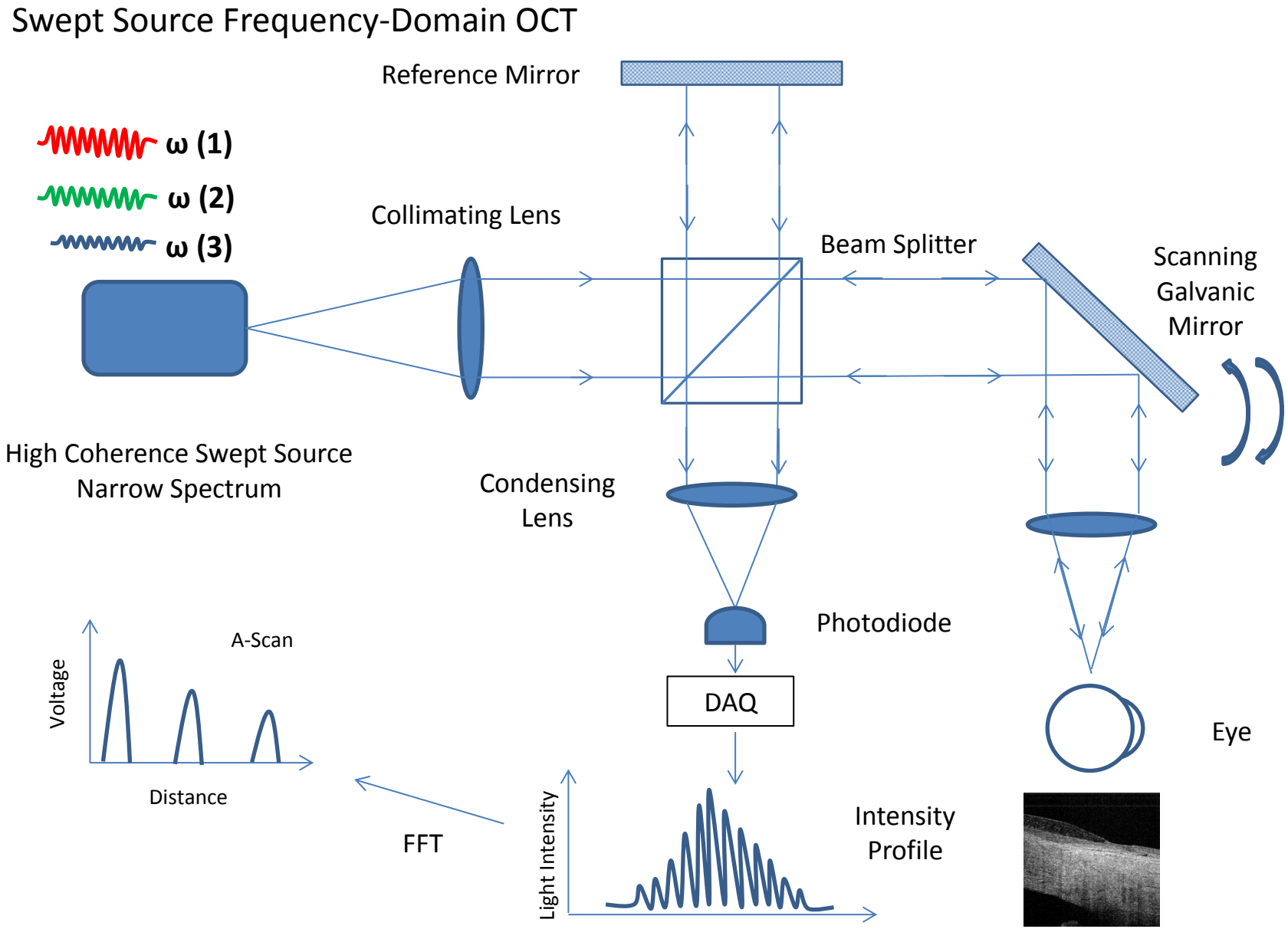

Figure 2.3: General arrangement of a swept source frequency (Fourier) domain OCT system

2.2 Optical Coherence Tomography Resolution Optimisation

When designing any imaging system it's important to quantify the limiting factors that contribute to the final optical performance of the system. A sound understanding of the theory behind OCT and the performance of individual components will aid the optimisation process. OCT, while using many of the principles of normal optical systems, ultimately resolution is not bound by the classical laws of optics. Rather a more complicated set of factors apply relating to the physics behind interference systems. All OCT system consists of roughly the same components. Each will be assessed in turn and quantified in the teams of anterior eye ophthalmic imaging optimisation. System components are as follows:

1. Light Source
2. Interferometer
3. Galvanic Scanning Mirrors (Probe)
4. Digital Capture System
5. Processing System
6. Focusing Optics

2.3 Eye Optical Properties

The wavelength and type of light source is highly influential in the final resolution of the system. For the purposes of this review, only swept light sources will be examined. As with all biological tissue, the human eye optical components constituting of a cornea, polycrystalline lens, aqueous humour and vitreous humour will have different properties of scattering, absorbing and reflecting light at differing wavelengths. There are also optical scattering principles to be considered due to the arrangement of fibrous tissue in the cornea(Tuchin 2007, chap.3). Generally, the lower the frequency, the less absorption is experienced, thus the better the depth penetration achieved.

2.4 Light Sources Swept Source Characteristics

2.4.1 Sweep Range

As discussed previously, swept light sources do not have a single coherent wavelength but are centred on a single point known as the centre wavelength. Swept source lasers are not available in all

wavelengths due to the complexity of producing multi modal resonant cavities. Currently the most encountered centre wavelengths in OCT systems are 800nm, 1060nm and 1310nm. The most important factor in axial resolution is wavelength sweep and coherence length of the light source. Wavelength sweep is defined as the maximum change in wavelength centred on the central wavelength the light source can produce. Equation 2.1 shows the relationship between axial length and wavelength sweep. Figure 2.4 shows the relationship between wavelength sweeps and axial resolution over a broad sweep range. If the best possible axial resolution is deemed a priority, the system should be designed to achieve the maximum wavelength sweep. The smaller the wavelength the better the general resolution achievable, with 800nm showing greater resolution across all sweep ranges than 1060nm and 1310. Structures in the eye such as tear film and the Bowman's layer are known to be in the sub 10 microns range in thickness(King-Smith et al. 2004). Therefore to visualise these structures, an OCT system must be optimised to have a sub 10 micron axial resolution. Figure 2.5 shows a magnified view of the sub 10 micron graph region. To obtain a less that 10 micron resolution, a sweep range of approximately 100nm or greater will be sufficient for all centre wavelengths.

$$\delta z = \frac{2ln2}{\pi}\frac{\lambda_0^2}{n\Delta\lambda} \quad \textbf{(2.1)}$$

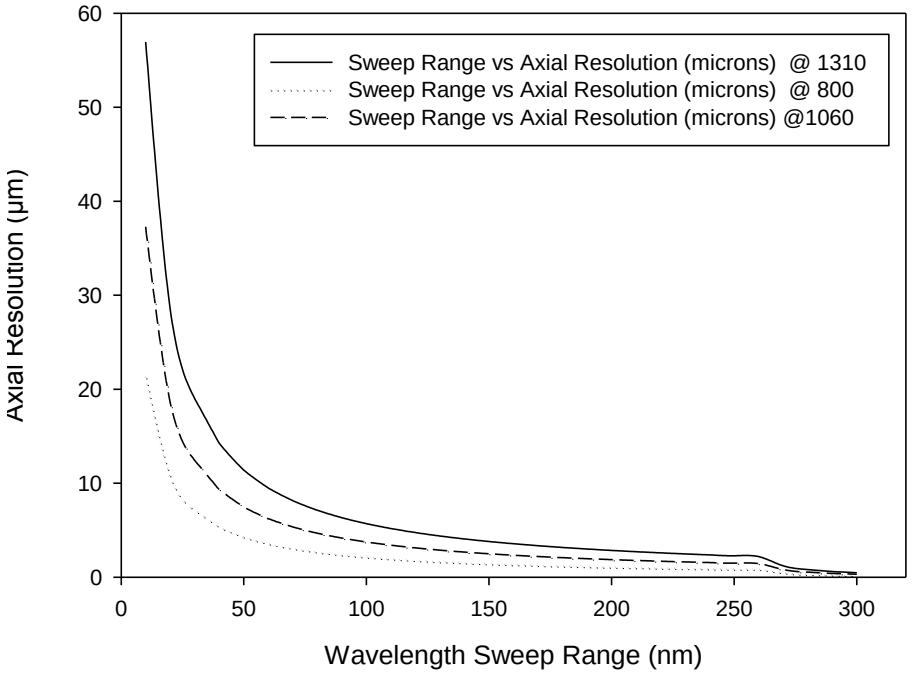

Figure 2.4 Axial resolution achievable with wavelength sweep and centre wavelength variation

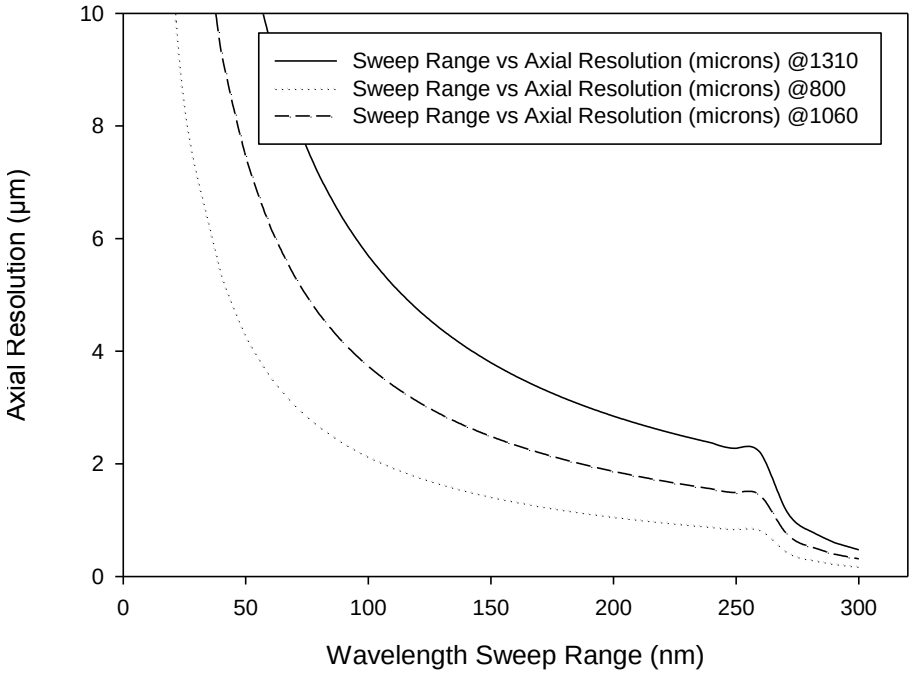

Figure 2.5 Sub 10 micron region of achievable axial resolutions

2.4.2 Coherence length

The depth penetration and axial resolution of an imaging system is also limited by the signal to noise ratio of the sensor system recording the interference patterns. As light passes though the eye median, light is scattered and absorbed. At a certain point the return signal will have degraded to a level where it is not distinguishable from system noise. Coherence length and line widths are measures of a light source's ability to maintain a stable performance over a range of wavelengths. The lasers line width is related to the depth penetration by equation 2.2 and coherence length is related to depth penetration by equation 2.3. Figure 2.6 shows coherence length and depth penetration over a wide range of coherence lengths. For ophthalmic imaging of the anterior chamber, between 3mm-5mm past the corneal apex needs to be visualised. A coherence length of between 6µm and 10µm or greater should be sufficient for a practical testing range.

$$\Delta d = \frac{ln2}{\pi}\frac{\lambda_0^2}{\delta\lambda} \qquad \textbf{(2.2)}$$

$$cl = 2\Delta d \qquad \textbf{(2.3)}$$

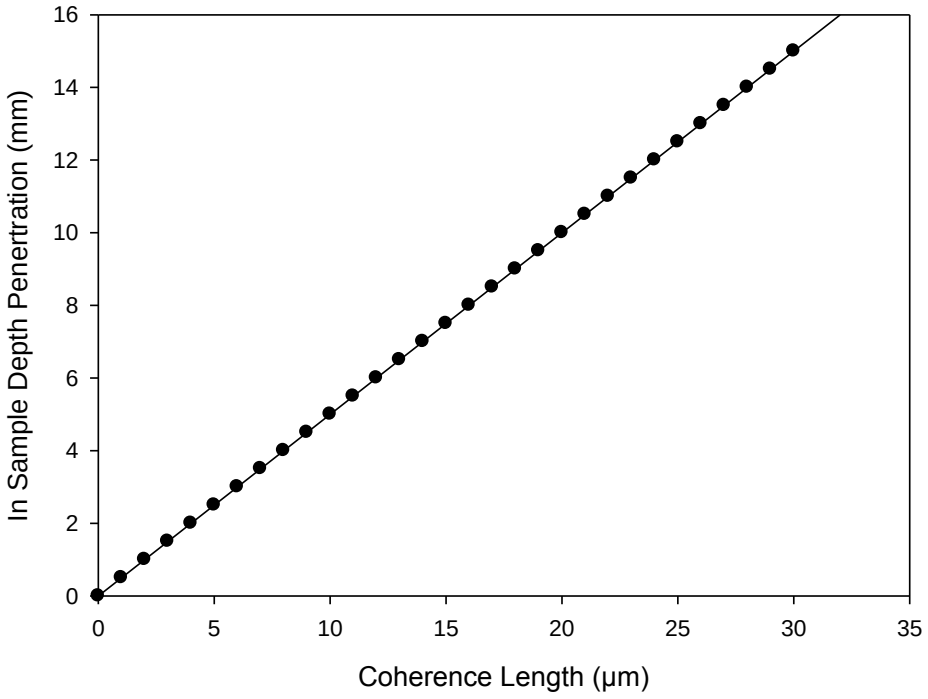

Figure 2.6 Sample penetration depth variations with laser coherence length

2.4.3 Optical System Design

The optical system is designed to focus the light from the source and interferometer onto the sample under test. The system will consist of optical fibre couples, prisms and optical elements. The design of individual elements is often constrained by the choice of operational wavelength of the light source. Many commercial optical fibres are designed to be most efficient at a certain centre wavelengths or can be guaranteed to only maintain polarisation characteristics at these specific wavelengths. Most OCT systems or optical scanning systems have an aiming laser spliced into the optical path, providing a visual indication of the positioning of the lasing beam and its operation. This is extremely useful for the practitioner as most systems operate outside the human visual spectrum.

Types of optical distortion such as chromic aberrations and optical dispersions are usually not important in swept source OCT system design, as they only affect systems that transmit very broadband light. Lenses are chosen that have optimal properties at the desired wavelength and are often custom made. Many systems feature exotic gradient index lens profiles purposely designed to reduce the total part count of optical components in a system. This is of primary importance with new generation designs that are required to be as compact and lightweight as possible.

The final condensing optical element present in the imaging system has the greatest effect on the lateral resolution of the system. Lateral resolution is characterised by the spot size and point spread function formed by this optic. Spot size is a function of the derived numerical aperture which in turn is a function of the focal length divided by the diameter of the lens. Figure 2.7 shows the relation between numeric aperture and spot size or lateral resolution as described by equations 2.4/2.5. As numerical aperture decreases, the focal length of the lens reduces and the diameter of the lens increases. Both of these factors will have an effect on the optical properties such as depth of field (DOF).

Reducing spot size will also increase the power density of the beam on the eye by a cubic relationship. Reduction in spot size has further implications for laser safety and the possibility of optically induced biological damage. A minimum size should be chosen that will give good imaging potential achieving the resolution required for resolving the smallest features required, while minimising power density and maximising depth of field. Axial resolution is generally regarded as more important in corneal/contact lens interface imaging. Therefore a larger value of lateral resolution can be withstood, resulting in an asymmetric imaging resolution. DOF and lateral resolution are related by equation 2.6 as demonstrated in Figure 2.8. As can be clearly determined,

DOF is the limiting factor on spot size. A focal depth of between 3mm-5mm is required for a minimum DOF of ± 1.5mm giving a lateral resolution of approximately 30µm will result.

$$N = \frac{f}{D} \quad \text{Or} \quad NA = n \sin\theta \quad \textbf{(2.4)}$$

$$d = \frac{4\lambda f}{\pi D} \quad \textbf{(2.5)}$$

$$DOF = \frac{2\varpi_0^2}{\lambda} \quad \textbf{(2.6)}$$

2.4.4 Interferometer Design and Connection

All OCT systems utilise interferometers, almost uniquely of the Michelson Interferometer design. Michelson Interferometers are extremely simple devices that display considerable reliability due the absence of moving parts. The OCT interferometer unit will contain most of the hardware required for an OCT besides the laser system and scanning probe. Although named the interferometer unit the device actually contains much of the systems working parts. Hardware includes balance detectors, photo diodes, signal digitisation electronics (analog to digital) and various connections and mechanical switches. The unit is fibre coupled both internally between components and externally to the scanning probe and light source though optimised single mode optical fibre patch cables.

Patch cables are precision devices with lengths that directly relate to the optical path and delay line distances of the system. Fibres are not normally interchangeable and are calibrated for a specific interconnect part of the optical path. Most important is the distance between the fibre and the scanning probe; this length is precisely calibrated and is referred to as the signal arm length. Fibres between the laser and interferometer are not specifically sensitive to changes in length, but can display polarisation sensitivity. If fibres are kinked or coiled in a cable management system, curvature of the optical material can cause changes in the polarization angles and perceived optical intensity. In worst cases, this can severely affect the signal to noise ratio of the system reducing perceived image contrast. Hence, care is needed when laying out an OCT system's physical design and if problems appear to be periodic or insistent, cables and connections should be cleaned and

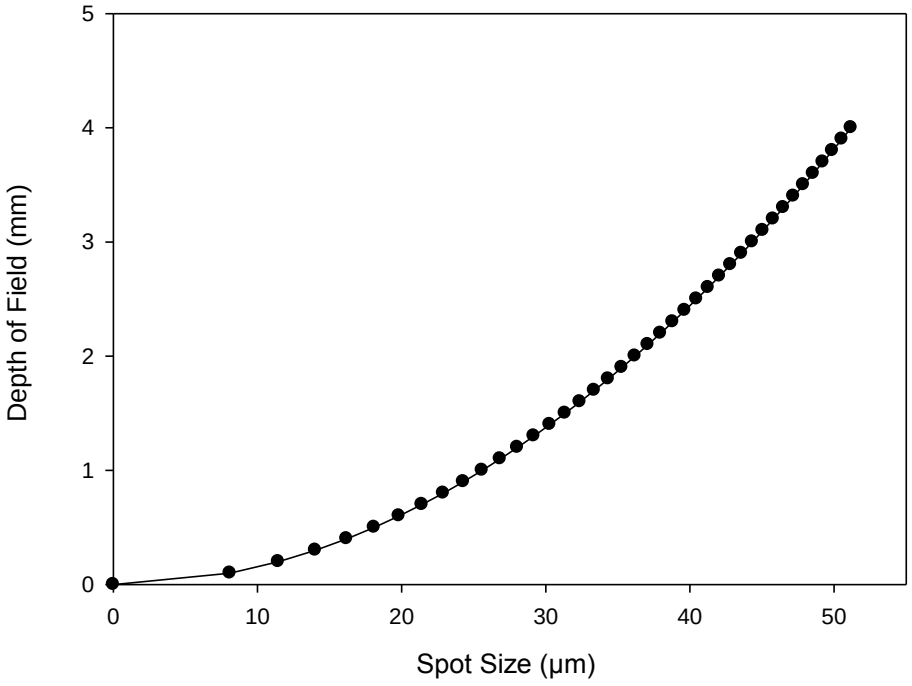

Figure 2.7 Depth of field variation with lateral resolution (spot size) of system

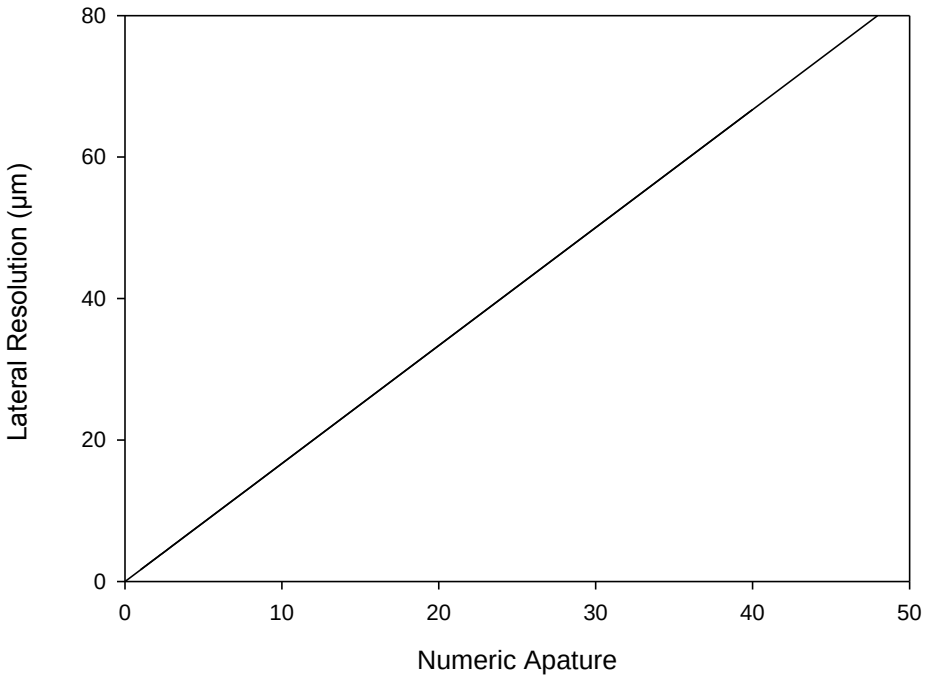

Figure 2.8: Lateral resolution variation with numeric aperture. A highly linear relationship is apparent

checked first. Interferometer units also contain mechanical positioning mechanisms that are designed to allow tuning of the delay line length. Figure 2.9 shows such a device. Altering this length changes the depth penetration of the OCT system and the primary control for the "sweet spot" (point on the Z axis of highest resolution) for optimal imaging. Many systems also house a co-laser with a wavelength in the visible spectrum designed to give an indication where the infrared laser beam is aimed. The aiming laser does not interfere with the imaging systems photodiodes because the associated quantum efficient is extremely poor in the visible range. Potential inference problems can occur with 800nm OCT systems, but such systems are usually deployed in retinal OCT systems where aiming lasers would not be applicable.

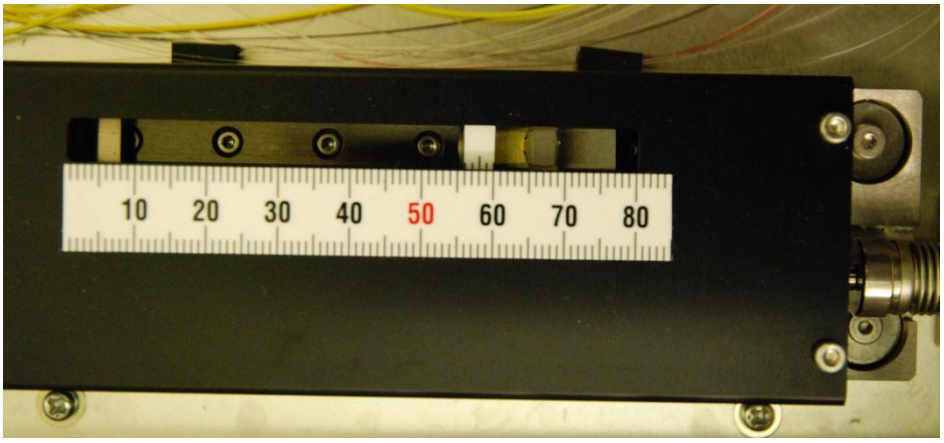

Figure 2.9: Delay line from the Santec OCT system

2.4.5 Galvanic Mirrors and Type of OCT scan

OCT systems do not require a Galvanic Mirror System (GMS) to produce useful data about an object under scan. However without them the data produced will be very limited. GMS are designed to steer the laser beam path over the sample under scan so different areas can be imaged without point where the laser system contacts the sample. Figure 2.10 shows a typical A scan from an OCT system.

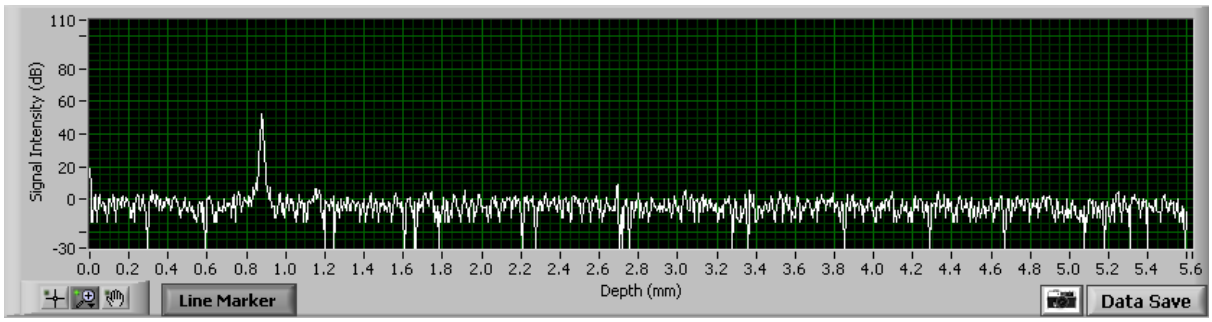

Figure 2.10: Single "A scan" from the OCT system

The peak observed in Figure 2.10 between 0.8mm and 1.0mm indicates that the OCT system observed a strong back scatter from a surface or interface at that depth into the sample under scan. Although useful a single A scan does not provide information about the nature of the surfaces been imaged. Knitting together multiple scans at distances less than the lateral resolution of the system can provide surface information. B-Scans are A scans combined into a two dimensional plot with signal intensity mapped linearly into grayscale intensity plots. Figure 2.11 shows the same surface as in Figure 2.10 but with 519 A scans tiled vertically. The red line shows the single vertical column of pixels representing the A Scan. As can be seen, the surface is curved, which could not have being derived solely from a single A scan. B scans themselves can be stacked to produce 3 dimensional imaging, called a C scan. Each B scan consists of 519 A scans. The processor overhead required in decoding the 14,000 resulting interferometer patterns per second when scanning at a speed of 25fps is considerable. A 'C' scan will consist of several hundred B scans depending on the magnitude of scan size. C scans can take between 0.5 seconds and several seconds. Current decoding speed and galvanic mirror design limitations result in poor C scan imaging of the ocular surface due to small movements of the eye within the capture time causing considerable blur and contrast reduction.

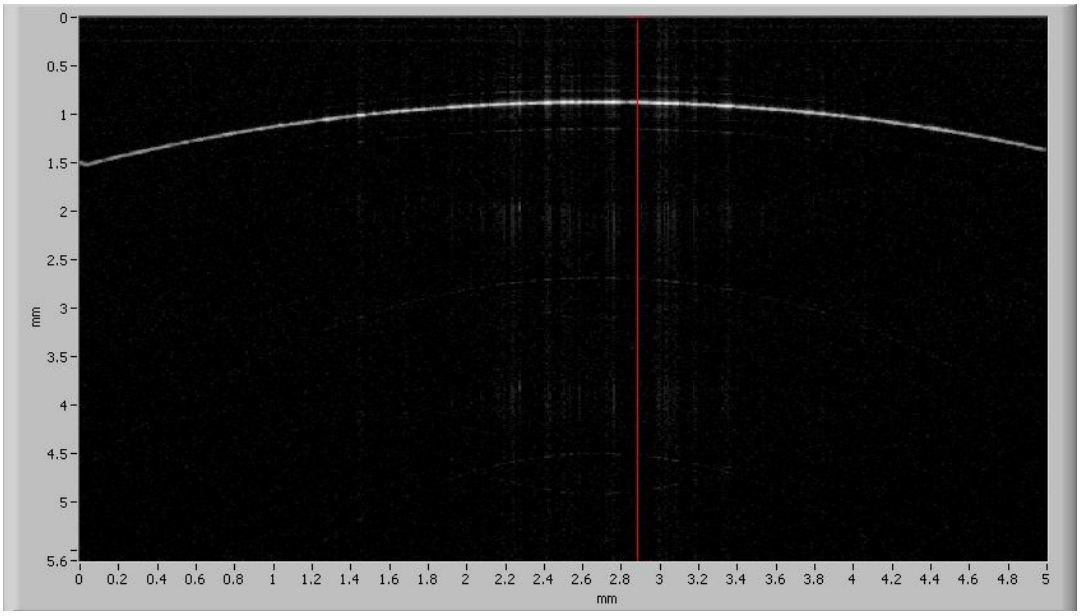

Figure 2.11: Single "B scan" from the OCT system, red line shows "A Scan" location from figure 2.10

Galvanic mirrors are comprised of two reflective surfaces individually attached to high speed low inertial electronic motors. The requirements for a low inertia system are paramount as the mirrors have to change direction extremely quickly and with highly linear acceleration profiles. A single galvanic mirror can produce A or B scans, but a second mirror offset in an orthogonal plane is required to produce a C scan. The mirrors are scanned in a raster pattern to form both B and C scans. An OCT system for optimised ophthalmic imaging must therefore have, at a minimum, a single galvanic mirror system for producing B scans and the processing capability of at least 20fps (>10,000 A scans per second processing capability) for a practical ability to track dynamic features.

2.4.6 Data Capture System and Post Processing

The OCT light source and the analog to digital converters are connected to the photodiodes via a high frequency trigger line producing a beat frequency locking signals together. This timing interlock allows the digital capture cards to produce a calibrated capture system for digitising interference data.

The capture system has to operate at least twice as fast as the A scan rate of the OCT system (due to the Nyquist limit(Nyquist 1928)); for most normal commercial system this is less than 50 kHz. Post processing of inference data requires complicated mathematical analysis to turn the digitised data into useful information. Standard desktop personal computers are not well suited to this task as computing floating point calculations are not highly optimised when compared to bespoke solutions. Tying up main processor time will reduce the capability of the computer to handle further tasks simultaneously. The faster the A scan rate, the more capable the OCT system is for data averaging and advanced post processing.

Many systems used dedicated co-processors such as Field Programmable Gate Arrays (FPGA) or Digital Signal Processing units (DSP). OCT systems with FPGA co-processors have been demonstrated to operate at speed of at least 15,000 A Scans per second (Santec 2011). Aston University has recently demonstrated an in house solution for using 'massively parallel' computation systems based on Nvidia Compute Unified Device Architecture (CUDA) devices. A proven A scan processing rate in excess of 1.8 million calculations per second with standard off the shelf hardware has been achieved. Further calculations have indicated that the latest generations CUDA devices will be capable of producing up to 5 million A scan's per second, delivering two orders of magnitude increases over current commercial systems.

2.6 Development of the Dual Imaging System

The project required cross-sectional OCT imaging of the contact lens edge / corneal epithelial interface as well as simultaneously capturing the en-face dynamic lens movement. This could not be achieved with OCT alone, so a dual imaging system concept was developed and built, coupling the OCT with a time linked high speed image capture system.

2.6.1 The High Speed Image Capture System

The DALSA 4M60 (DALSA, Ontario, Canada) is a high speed, high resolution camera system featuring a native resolution of 2352x1728 pixels and a maximum frame rate of 62fps. The high resolution and frame rate produces a considerable level of data throughput, requiring specialist capture systems and the use of sophisticated high bandwidth dual camera link capture/frame grabber.

The 4M60 has excellent sensitivity in the visible range extending into the near infrared region. Figure 2.12 shows the spectra response of the CMOS sensor on the High Speed Camera (HSC). Due to the large CMOS size, a custom optical solution was required to give a full view of the cornea in section profile, without causing clipping of the image on the CMOS sensor. A custom 45mm Schneider aspheric lens (Hauppauge, New York, USA) was utilised with a series of extension tubes giving a final focal length of 75mm from the front optic. A focus ring was also included aiding quick refocusing.

With the camera tilted 90 degrees to the horizontal, the 2352 pixels were used to image across a corneal section of 16mm, each pixel element imaging 6.8 microns of the image plane. The final lateral resolution of the system has a nyquist limit approaching 14 microns without any post processing or averaging. Figure 2.13 shows a corneal image from an OEMI-7 model eye (Ocular instruments, Bellevue, USA) and real eye with a contact lens partially covering its surface (real eye lens in inserted normally). The images reveal that the system is capable of detecting considerable detail in a still image. However the real benefit is from dynamic imaging. The high frame rate gives smooth capture of slip, tilt and fall of a contact lens

The system uses the National instruments PCIe-1429 full configuration camera link image acquisition card (National Instruments, Austin, Texas, USA) which allows image capture though a standards PCIe x4 Bus. Bandwidth provided is 680MB/s with a pixel clock ranging from 20-85MHz giving considerable flexibility in camera configuration and choice. As standard the capture card has one digital trigger I/O line with the capability to add further channels if required. The HSC camera tied

with the camera link system can deliver a frame rate of up to 500 Hz with required sensor binning. The actual frame rate delivered is a dependent of the image capture size and the bit depth of the analog to digital convertor on the sensor. Bit depth is selectable between 8 and 10 bits via the software. The higher bit depth provides a greater dynamic range at the cost of a reduced frame rate. A 8 bit setting was chosen for imaging because the increased frame rate was considered more important that dynamic range in this application

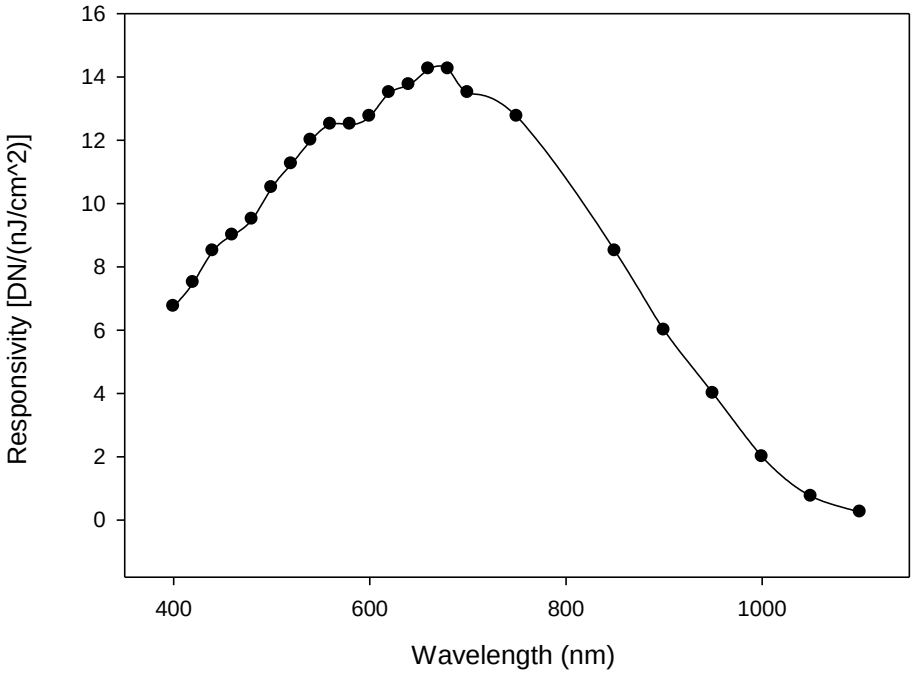

Figure 2.12 Spectral sensitivity of the HSC camera

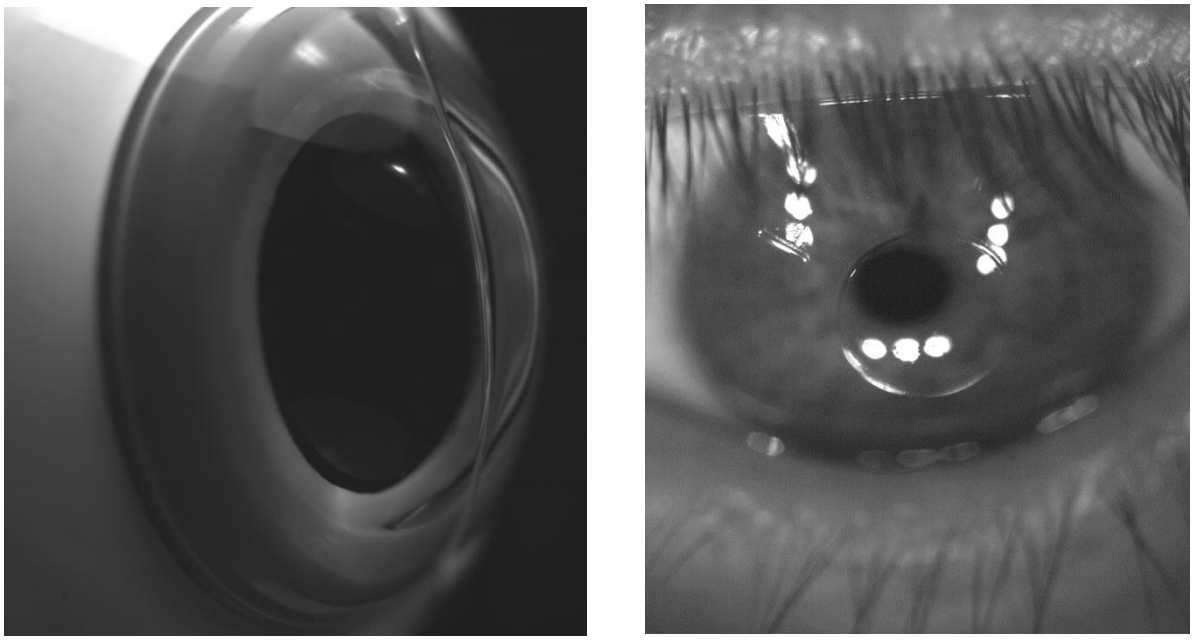

Figure 2.13 Contact lenses covering both real eye and mode eye.
Note marking are clearly visible on real eye

2.7 Santec OCT system

The OCT device consists of a swept source spectral domain laser system that comprises of four principle parts. A light source, interferometer, portable scanning probe and computer acquisition hardware unit. The base system was built by Santec's OCT division (Santec, Japan). The device was customised (more detail provided in following section 2.7-2.9) in consultation with Aston University and optimised for use in ophthalmic imaging. Santec provided limited demonstration software with the device for quick assessment and testing. Application programing interface (API) was provided with root functions to access the OCT hardware giving control as required. Further software was developed in house and customised for use in anterior eye imaging.

2.7.1 Interferometer Unit

The IVS-2000 interferometer unit is based around a core of a Mach Zehnder interferometer with specific modifications for use in an ophthalmic setting. Figure 2.14 shows the electrical connections present in the system. The device also features a separate laser diode operating at 633nm, producing a red marker in the optical path giving visual indication for the path of the beam. Addition of the laser diode also helps show the scan pattern for the galvanic mirrors as well as the scan size and location on the eye. Alignment of the OCT system and the eye is greatly simplified by this addition. Initially there was some concern that a visible scan beam could induce a tear reflex or pupil response however testing indicated that no effect was detected.

2.7.2 Custom Attenuator Unit

The device is very close to a standard off the shelf OCT system, but has had an extra attenuation unit built into the light source. OCT systems naturally have attenuation devices in place before the photo detectors and analogue to digital converters. This allows the incoming signal to be moderated so that saturation of the detection unit does not occur, removing any possible loss of information or sensor clipping. A separate attenuation unit was added between the light source and the probe so that the power of the laser reaching the eye could be reduced to suitable safe levels in accordance with safety requirements. Both attenuation units can be adjusted separately allowing fine balance between the sample and reference resulting in better dynamic range and sample resolution. Both are assessable via a removable panel on the body of the IVS-2000. The reference arm attenuation unit is positioned between the upper optical circulator and the delay line module.

2.7.3 Computer System and Signal Digitation

The computer system designed for use with the OCT system was customised to allow for data throughput over the main board BUS. Three capture and control systems are required; the AlazarTech PCIe ATS-VI AT9462 waveform digitiser with field programmable gate array (Alazar Technologies Inc, Pointe-Claire, OC, Canada) designed specifically for interaction within a LabVIEW environment. Outputs from the systems photodiodes are captured, digitised and analysed with a Fast Fourier Transform (FFT). Onboard FFT processing via the FPGA co-processor reduces processor overhead and stabilises the system performance. The FPGA is designed to operate in a First in, First out (FIFO) configuration operating at capture frequency of 180 MS/S with a 16 bit sample resolution. High levels of hardware and firmware customisation allow for high levels of data throughput giving a maximum data transfer speed via a PCIe X 4 bus of 720Mb/S.

Timing signals are captured via the National instruments NI PCI-6221 M series malfunction digital acquisition device featuring 16 high speed analogue inputs with a sample frequency of 883kS/S and an input resolution of 16 bit depth.

2.7.4 Probe Unit

The scanning probe is a self-contained unit housing the galvanic mirrors and a collimating lens. The device is highly portable and can be used in any orientation as the galvanic mirrors are not sensitive to gravity orientation changes. The condensing lens is of special design and consists of a single positive 60mm focal length lens that corrects aberrations via advanced gradient index materials (Gradum GPX-25-60; Lightpath Technologies Inc, Orlando, FL, USA). The lens can match the perrformance of a much larger multi element optical system without any added design complexity while minimising system mass. The collimating lens between the fibre couple and galvo mirrors is a F260APC-C (Thorlabs Inc, Newton, UK). Figure 2.15 shows a detailed view of the probe layout. The probe is able to image with a horizontal length of up to 15mm and is completely selectable in both scan range and orientation.

2.7.5 System Power and Attenuation Levels

Power loss between input and output of the interferometer unit	= 5dB
Power loss between the input and output of probe	= 1.5dB
Power output at the probe (1310nm laser)	<5mW (3.2mW measured)
Power output at the probe (633nm laser)	= 0.1mW
Beam Size Diameter	= 2.7mm
Focal Length	= 60mm
Numerical Aperture	= 0.0225
Radiation spot size on the cornea at focal point	= 23.1µm

A full system layout diagram is included in Figure 2.16

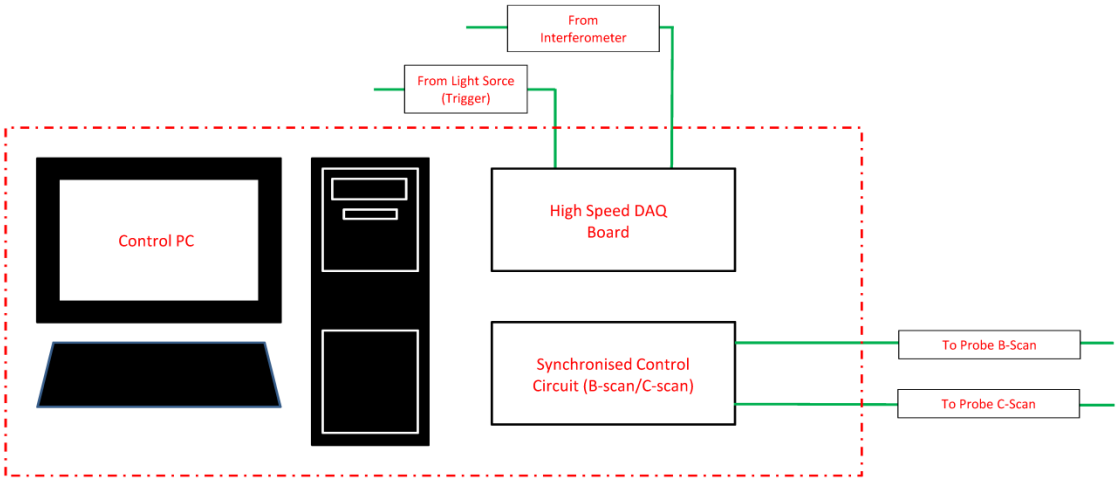

Figure 2.14 OCT system connections

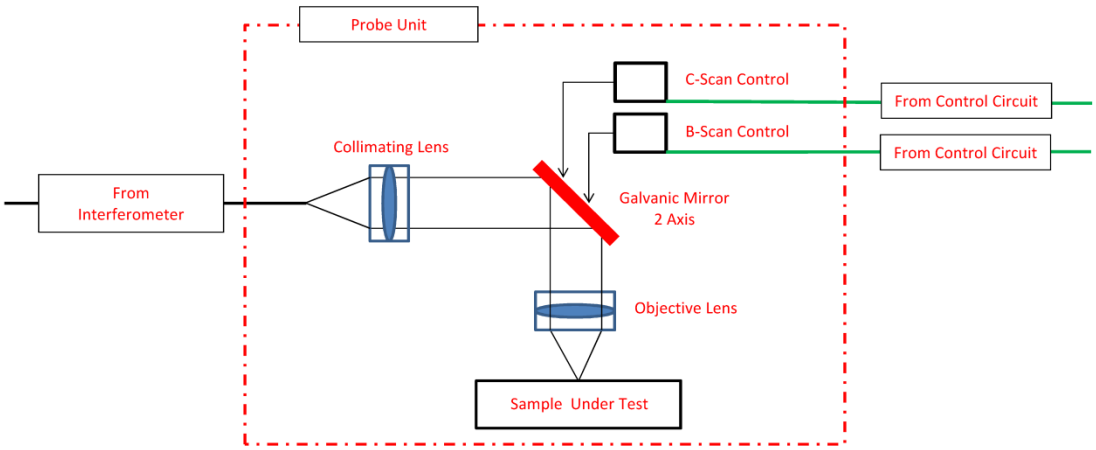

Figure 2.15: Probe unit for the OCT system electrical and optical connections are shown in detail

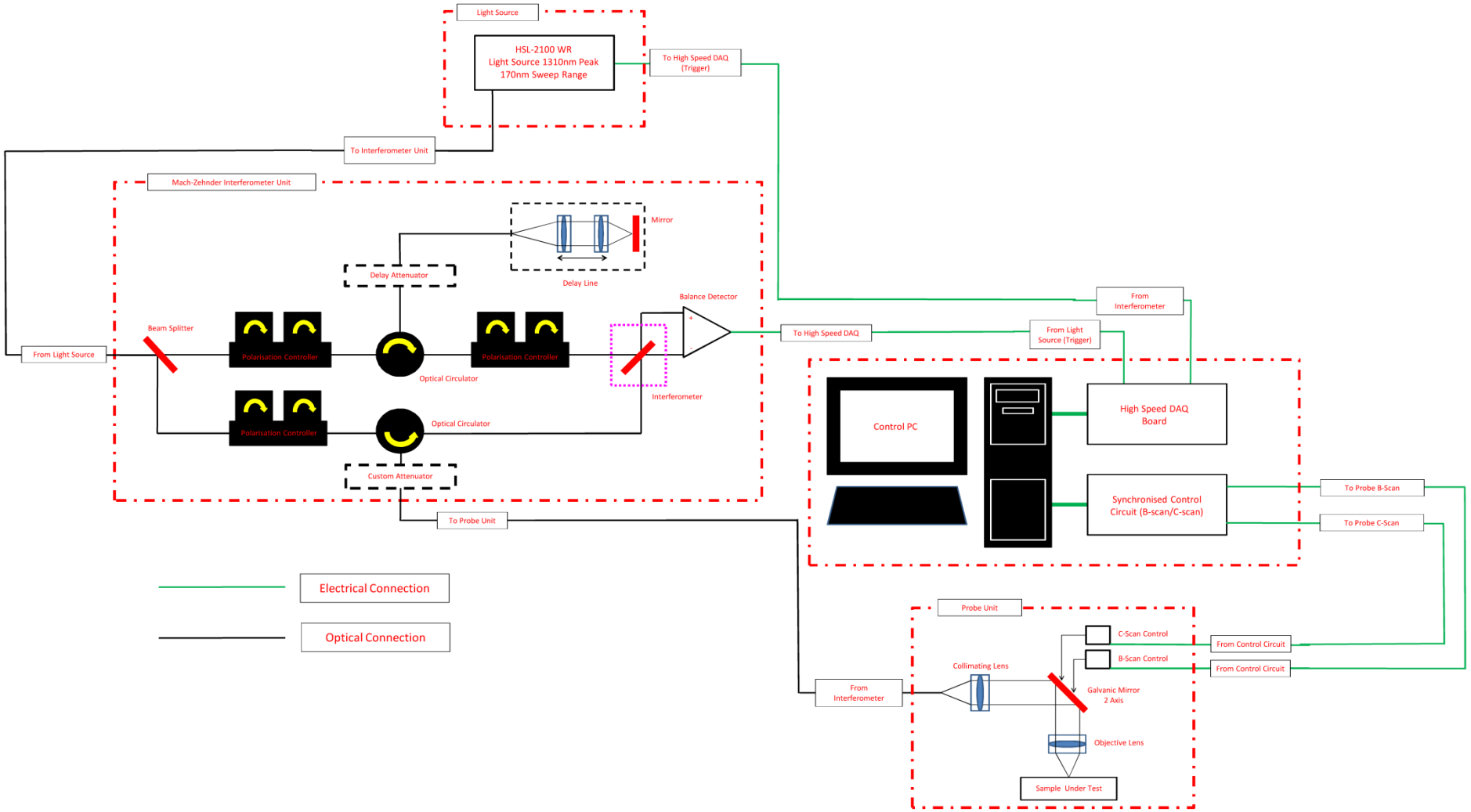

Figure 2.16: Diagram of the full OCT system, electrical, optical and mechanical connections are indicated

2.8 The Multi-axis Alignment Platform

The dual imaging concept required the design of a bespoke alignment platform that could position the HSC and OCT probe with the correct alignment with reference to the corneal surface.

The ideal solution would be for the OCT probe and the HSC camera to image normal to the corneal apex, enface to the surface. Physically, this arrangement would be imposable as both systems would have to occupy the same physical space. Two separate concepts for instrument alignment were developed, Block 1 and Block 2 devices. Both designs are based around a modified slit lamp base giving ease of moment and alignment to either the right or left eye.

2.8.1 Requirements for alignment

The mounting device should allow for both the OCT Probe and HSC camera to be positioned with accuracy while providing independent alignment and focusing of each system. There had to be between 3 or 4 degrees of freedom for both the OCT Probe and HSC camera to allow for correct and highly flexible alignment. The platform should also allow for normal variation between subjects, fitting a wide range of adults in comfort while allowing the operator to swiftly alight the device.

The OCT Probe and HSC Camera should be aligned to instrument mid plane positions. The centre position of each slides movement coincides with the mid plane of the slit lamp base for each axis. This gives maximum possible reach to the probe in the available axis.

2.8.2 Manufacturing requirements

Physical supports were manufactured form high strength, highly machinable aluminium/titanium alloy for rigidity and lightness. All manufacturing was performed in house with CNC machines or manufactured manually by hand where appropriate. Finite element analyse were performed on CAD models to determine the modal frequencies of vibration for the support structure so designs could be optimised.

Resonance frequencies of supports were determined and designed so that there were no crossovers, so that there were no possibilities of causing excessive excitation in the support structure. Therefore none of the cooling systems fans, or galvanic mirrors were likely to set up significant vibrations in the imaging system.

2.9 The Block 1 Device

The initial HSC concept was to track the contact lens edge with a novel backlight technique using an electro-luminescent light source (Lightape, Electro-LuminX Corporation, Virginia, USA). The OCT probe was to be positioned in front of the eyes and normal to the corneal surface. The HSC was at right angles to the OCT Probe matching a similar configuration possible with a conventional slit lamp illumination system. A three axis movement platform, consisting of linear slides, was designed for both the OCT Probe and HSC providing finer control and alignment than is possible with the slit lamp base alone. The differing focal length of both imaging devices also necessitates that each system could be moved independently closer or further away from the eye providing sharp focus. The Block 1 configuration is shown in Figure 2.17 and the slit lamp modification and CAD rendering of the mounting system in in Figure 2.18

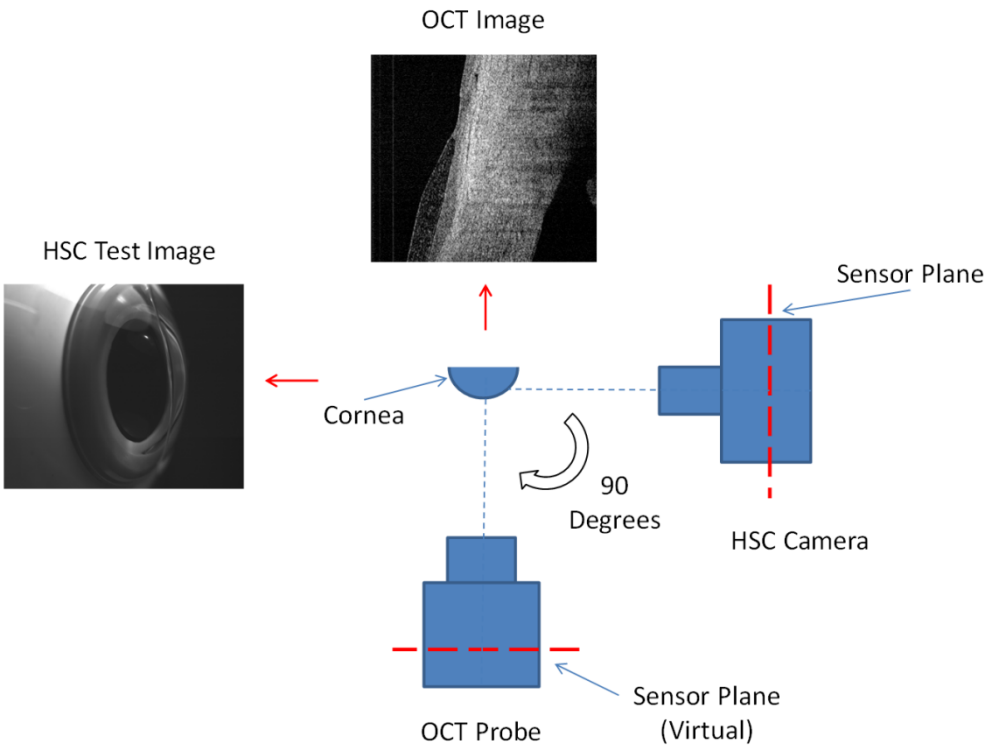

Figure 2.17: Arrangement of the block 1 system with the OCT probe and HSC camera at 90 degrees to each other

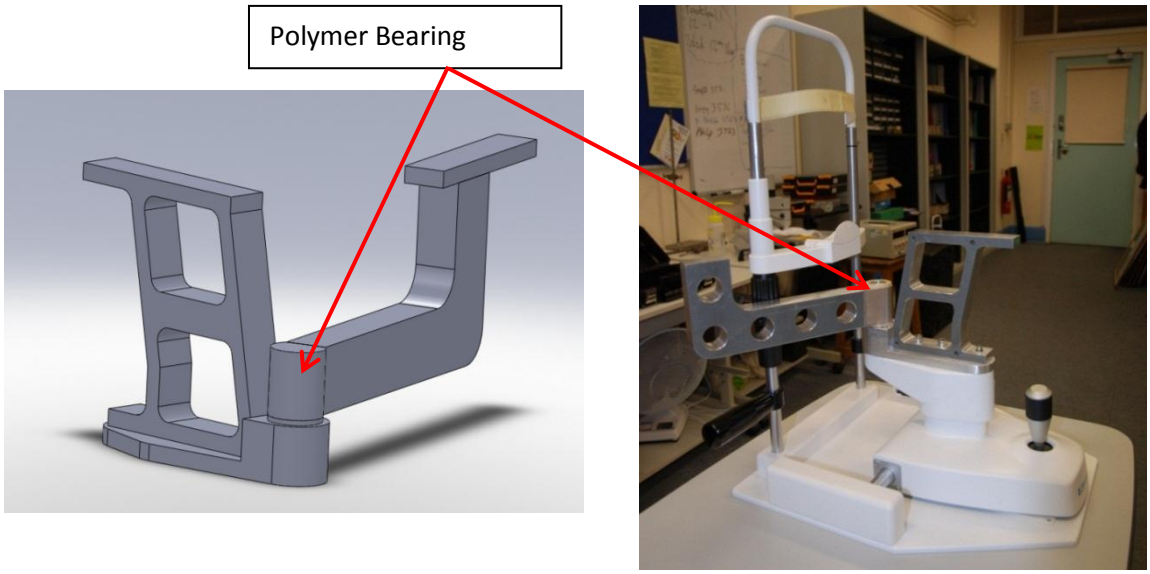

Figure 2.18 Support structure for OCT probe and HSC camera (Multi-axis alignment system not shown). Fully CNC machined with polymer bearings as required

The HSC and OCT Probe positioning system are of identical design and can be seen in Figure 2.19. A 3 axis alignment system was developed allowing both the probe and HSC to share a common focal point (virtual pivot) while still having individual movement flexibility. The pivot point utilises maintenance free polymer bearings (Igus LTD, Northampton, UK) requiring no lubrication under normal conditions. Each linear slide (also provided by IGUS) features the same bearing technology. The requirement for choosing maintenance free bearings was to removed potentially toxic lubrication compounds from contact with people operating or being imaged by the device. The maintenance free aspect of their performance also minimises any down time and servicing complexity. The device also used fused deposition modelling (FDM) rapid prototype technology to produce the linear slide mounting brackets. FDM allows for rapid design changes with minimal cost and lead times. The 3 axis system was tested under weighted load for stability and alignment speed. Figure 2.19 and Figure 2.20 shows the OCT probe mounted on the block 1 three axis alignment system.

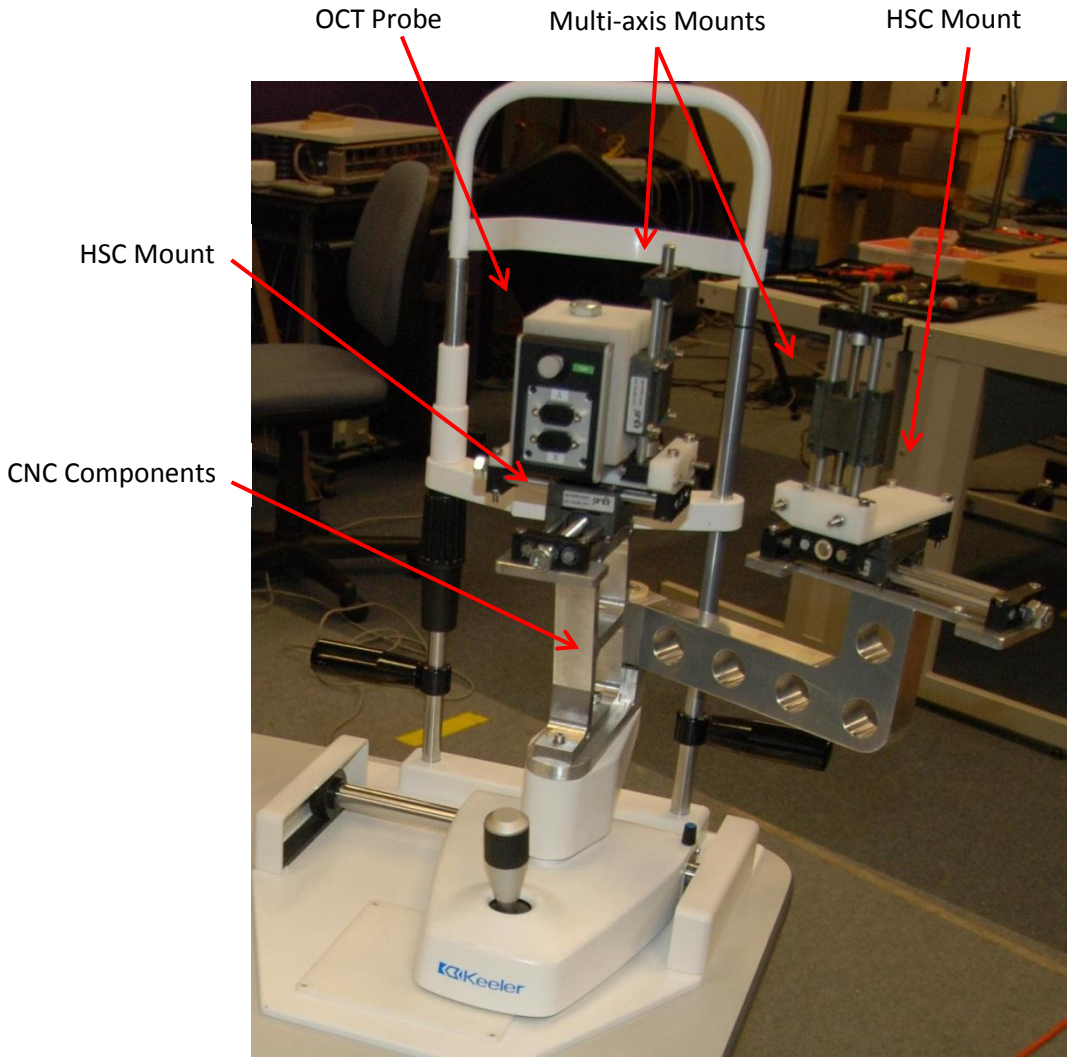

Figure 2.19 OCT probe mounted on multi-axis alignment system and attached to a slit lamp (7 degrees of freedom total)

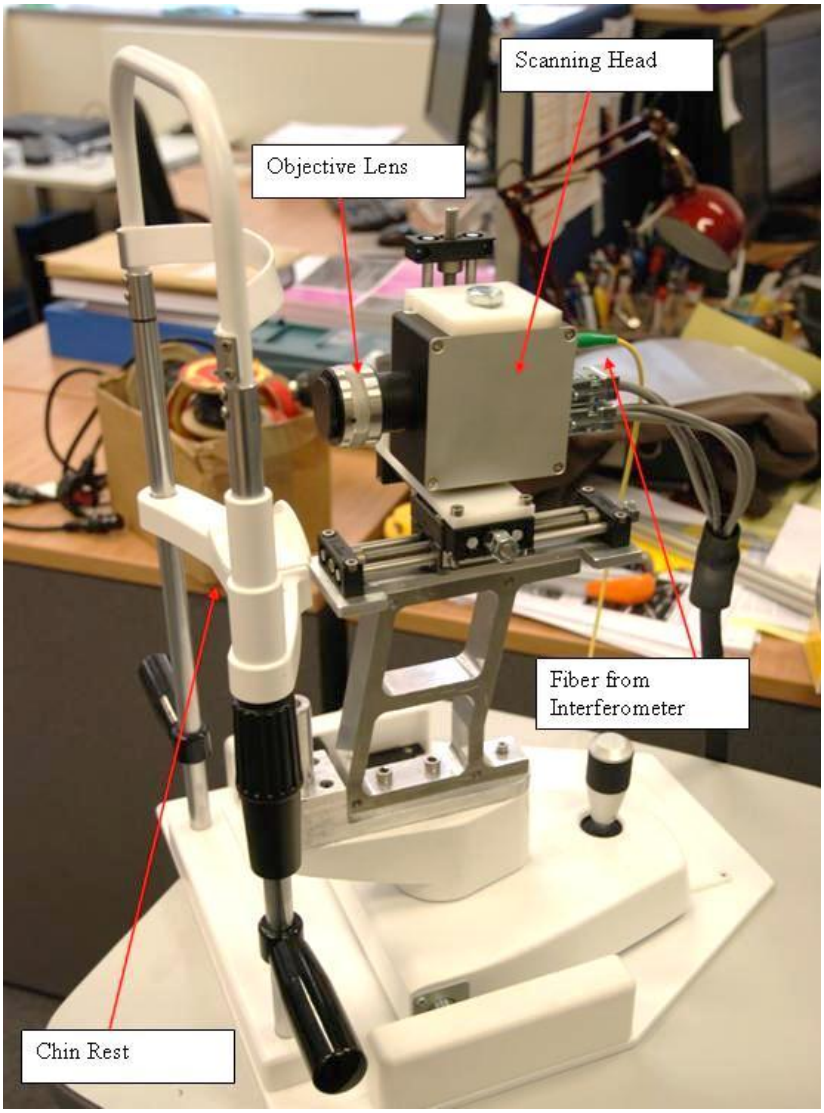

Figure 2.20 OCT probe mounted block 1 system (HSC swing arm not shown)

2.9.1 Discontinuation of the Block 1 Device

Testing indicated that the Depth of Field (DOF) for the HSC camera was not sufficient to allow for high quality imaging of the contact lens on the cornea under real conditions. A maximum of 2mm DOF could be achieved without excessively stopping the camera aperture, reducing illumination beyond reasonable levels.

Electro-luminescent Illumination was also found to be insufficient bright and overly complex to position correctly for rapid imaging. The sponsors new request stating imaging with the OCT probe was to be normal to the corneal surface at each scanning position, necessitated the need for more degrees of freedom on the OCT Probe platform. Finally load testing of the 3 axis slide indicated that there was too much flex in the system and stiffer slides would be required. The cumulated weight of these factors necessitated a new approach.

2.10 The Block 2 Device

A complete redesign was undertaken for the block two device. Photographic imaging of the corneal in cross section was abandoned in favour of imaging enface with both systems. The HSC camera was now mounted directly above the OCT Probe as in Figure 2.21a. Both the HSC and OCT Probe share a common focal point and are independently movable to account for the differing focal length of each unit. The OCT Probe and the HSC have independent degrees of freedom. The OCT Probe required further modification to allow scanning normal to the cornea while imaging at the differing scanning positions. Figure 2.21b shows how the probe can move in a curved path to achieve this requirement

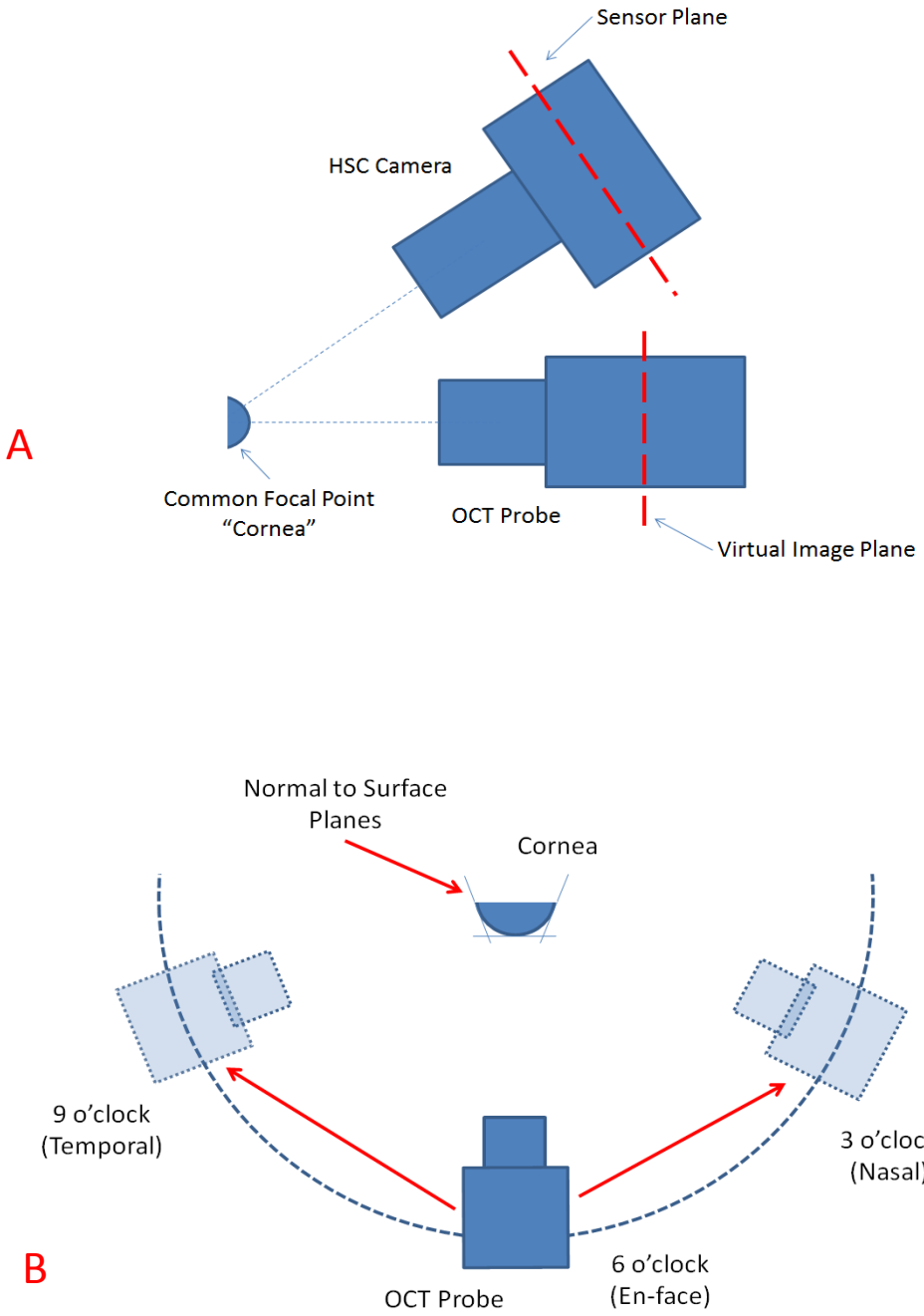

Figure 2.21 (a) HSC system mounted above OCT probe and imaging cornea at angle beta, OCT probe is imaging normal to corneal apex **(b)** Ark of movement for OCT probe allowing the system to be normal to the curves surface of the cornea

2.10.1 Degrees of Freedom

The Block 2 device has 8 independent degrees of freedom, giving considerable flexibility in positioning the scanning devices independently. As with the block 1 device, polymer bearings and linear slides were utilised. Linear slides were upgraded to give better stiffness. The device is based around a 150mm x 300mm double hole density optical breadboard (Thorlabs Inc, Newton, UK) acting as a base unit. A custom mounting bracket attaches the breadboard to the slit Lamp base securely. Figure 2.22a/b and Figure 2.23a shows the degrees of freedom independently. Figure 2.23b shows the finished device.

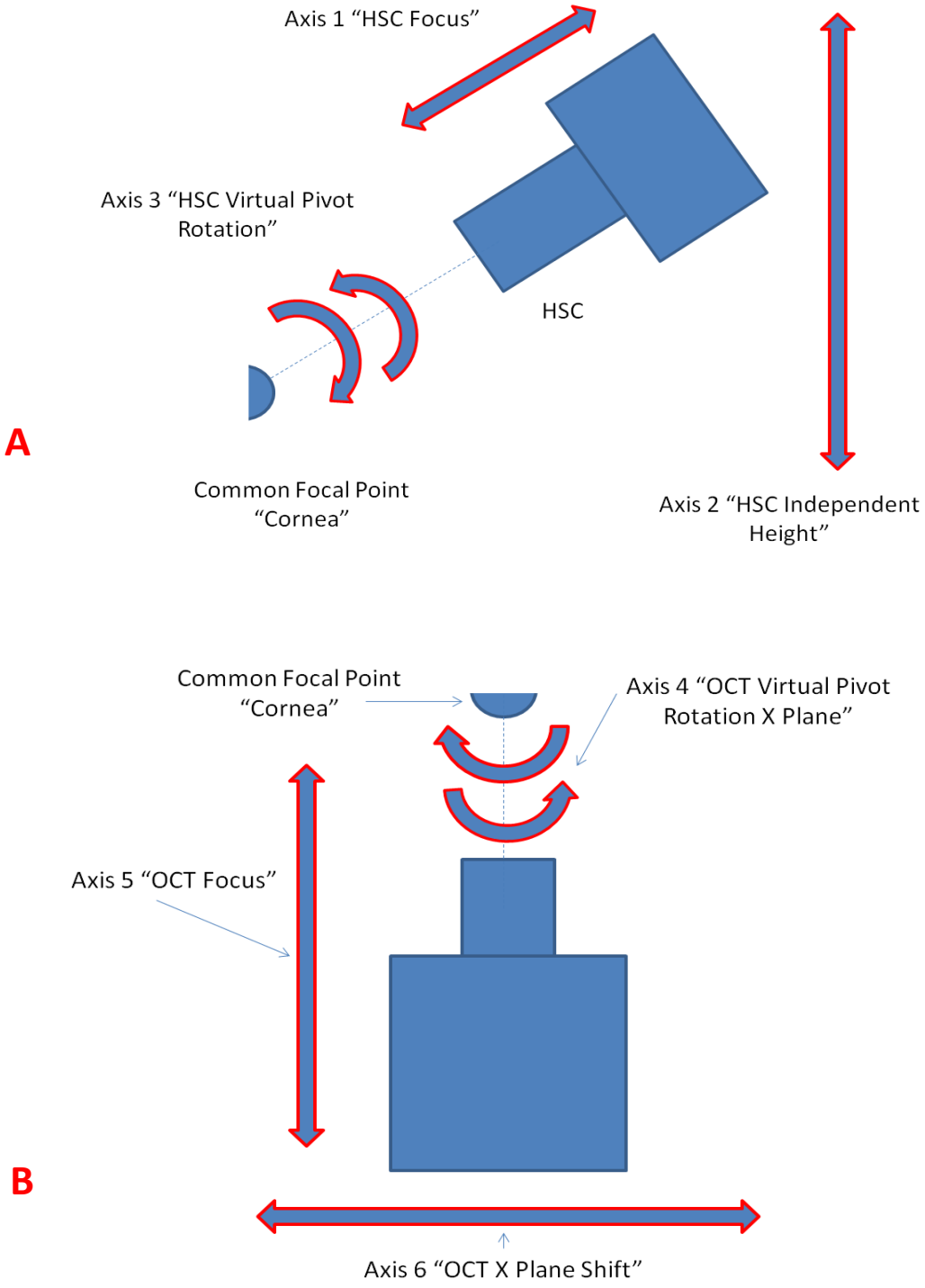

Figure 2.22 (a) Axis breakdown of the HSC system, three independent axis are show **(b)** Axis breakdown for OCT probe, again three independent axis are shown

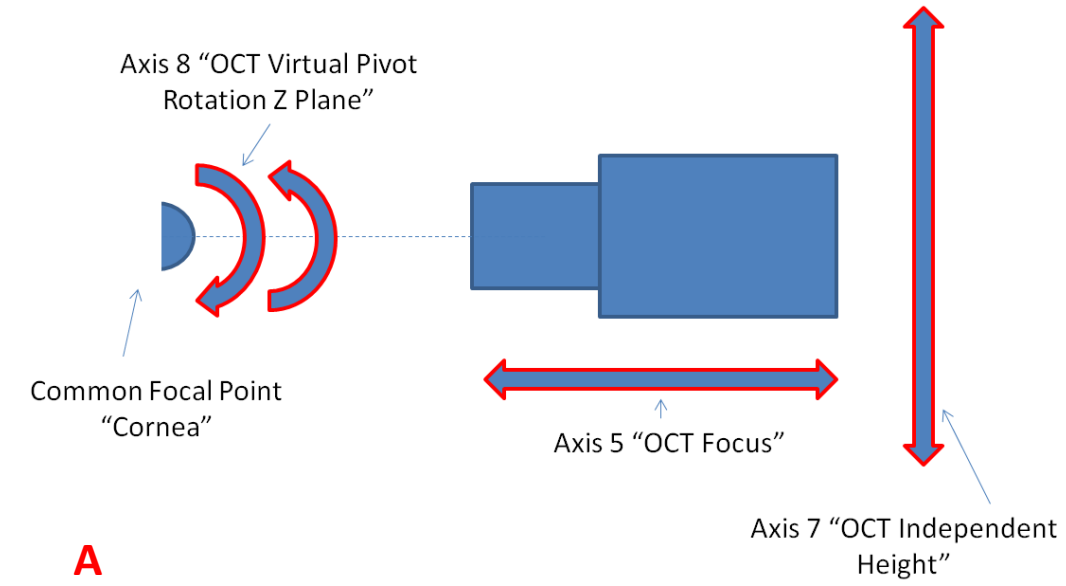

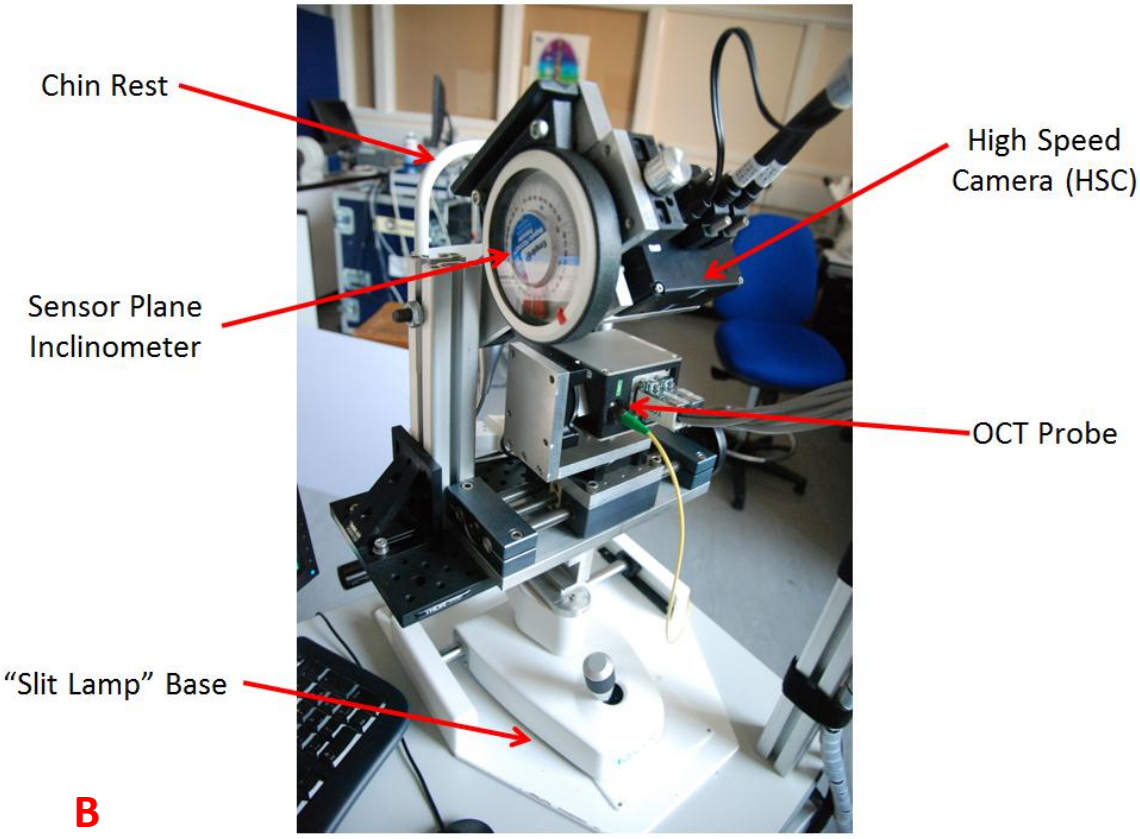

Figure 2.23 (a) Reaming 2 axis of the OCT system, providing full normal imaging to the surface of the cornea **(b)** The final assembled system with inclinometer

2.10.2 HSC Illumination system

The illumination system for the HSC camera was designed to provide constant illumination of the anterior eye and corneal surface without interfering with OCT or HSC operation.

A broad spectrum white LED was chosen with a high colour temperature of 5.4K Kelvin. The LED's spectral spread is shown in Figure 2.24 , with the spectral sensitivity of the HSC camera overlaid. The HSC shows good quantum efficiency in this wavelength range and responds well when imaging under these illumination conditions. The system did not cause any crossover interference or noticeable difference to the signal to noise ratio of the OCT System**.** The wavelength separations between the respective sensor sensitivities are in excess of 500nm.The HSC can visualise the OCT's aiming laser (633nm) when imaging a phantom target. When imaging biological targets the HSC aiming laser is not apparent.

The LED'S are USB's powered and can be positioned in the space between the eye, HSC camera, and OCT Probe without inferring with imaging or contacting the subject's face. A combination between 6 and 9 LED's were used for imaging.

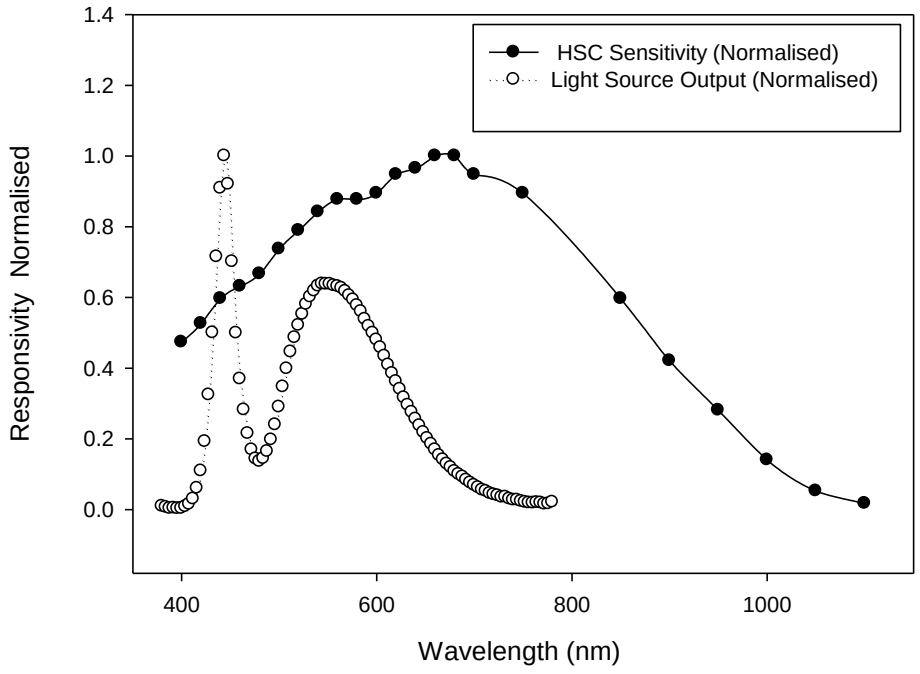

Figure 2.24 Spectral Power Distribution of illumination source and HSC sensor spectral sensitivity. Although not optimum, the camera shows good response to the illumination system

2.10.3 The Portable Support Structure

The OCT system consists of separate modules that are interconnected with various electrical and optical cabling. The entire device is in excess of 30kg with the HSC and control computer system. Because the device is required to accommodate subjects of differing sizes, and be as portable as practicably possible, the system needed to be given a similar level of flexibility as commercial ophthalmic devices.

A support platform providing sturdy mounting for all components and an efficient and compact electrical connection was developed. An equipment table designed for access by a wheelchair bound subjects was heavily modified. A standard equipment table was not recommended to lift more the 25kg without risk of malfunction. An under slung aluminium truss structure was therefore designed to mount the interferometer, laser system and the control PC at a convenient location. The structure was assembled from extruded aluminium sections (Item, Item Industrietechnic GmbH, Solingen, Germany) and laser cut Perspex panels. Figure 2.25 and Figure 2.26a show the device in detail. The structure was bolted and glued to the equipment table base providing a secure mounting platform and vibration damping. A cable and power management system was implemented providing safe arrangement of the 35 electrical connections and fully independent power switching required for each instrument to be powered on or off. Figure 2.26b shows a detailed view of the cable management system. A strain relief system for the HSC camera and OCT Probe is also provided

A separate cantilever monitor support arm was used supporting a widescreen monitor for viewing the OCT output, freeing table space for the slip lamp base, mouse and keyboard

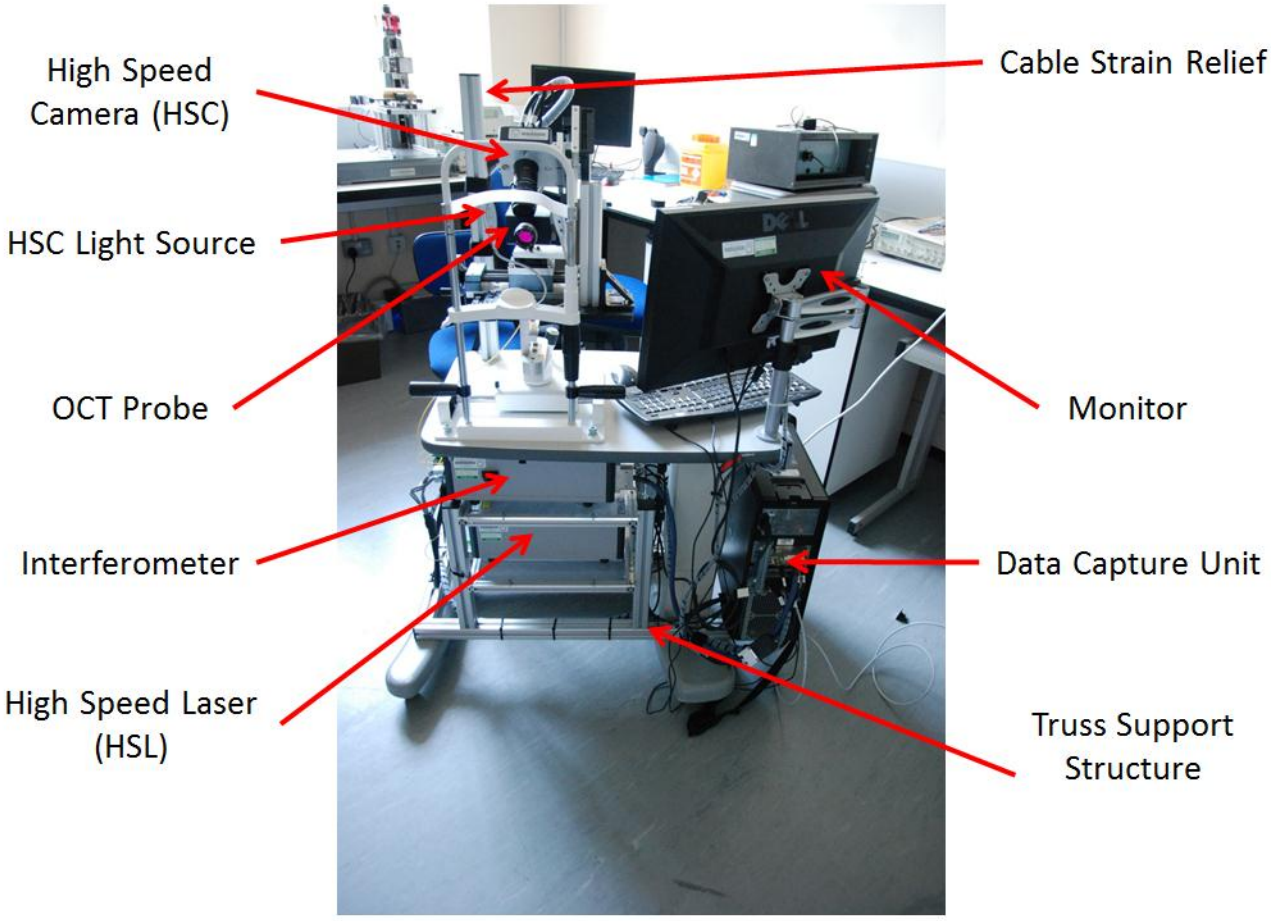

Figure 2.25 The full system assembled and ready for testing subjects.

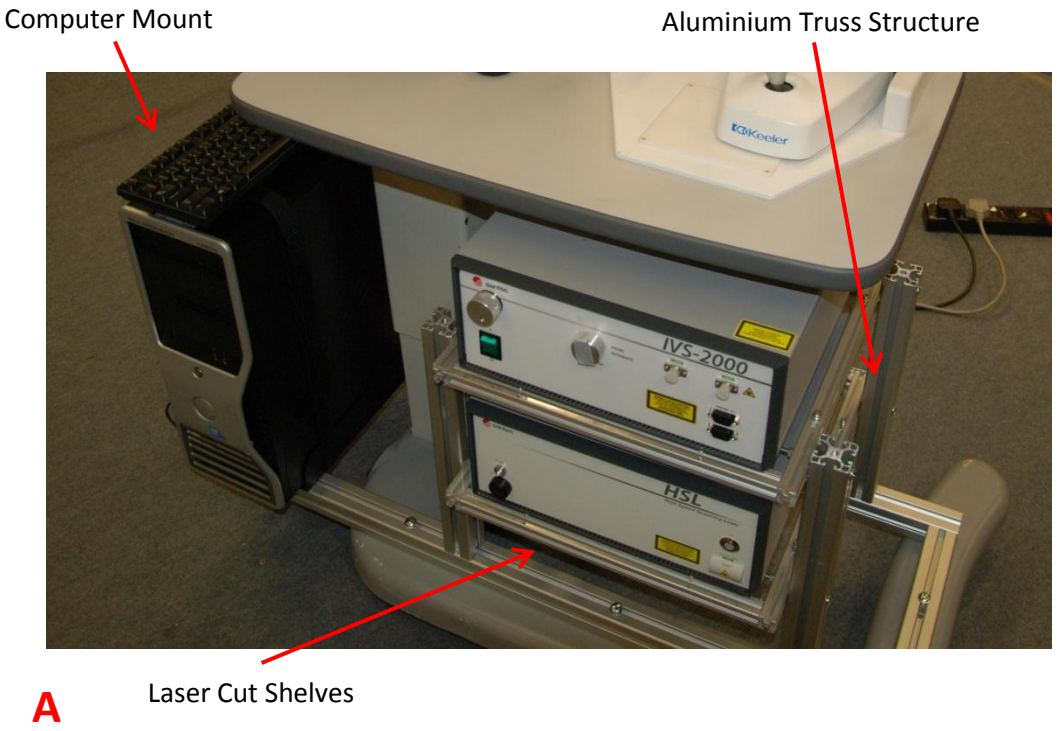

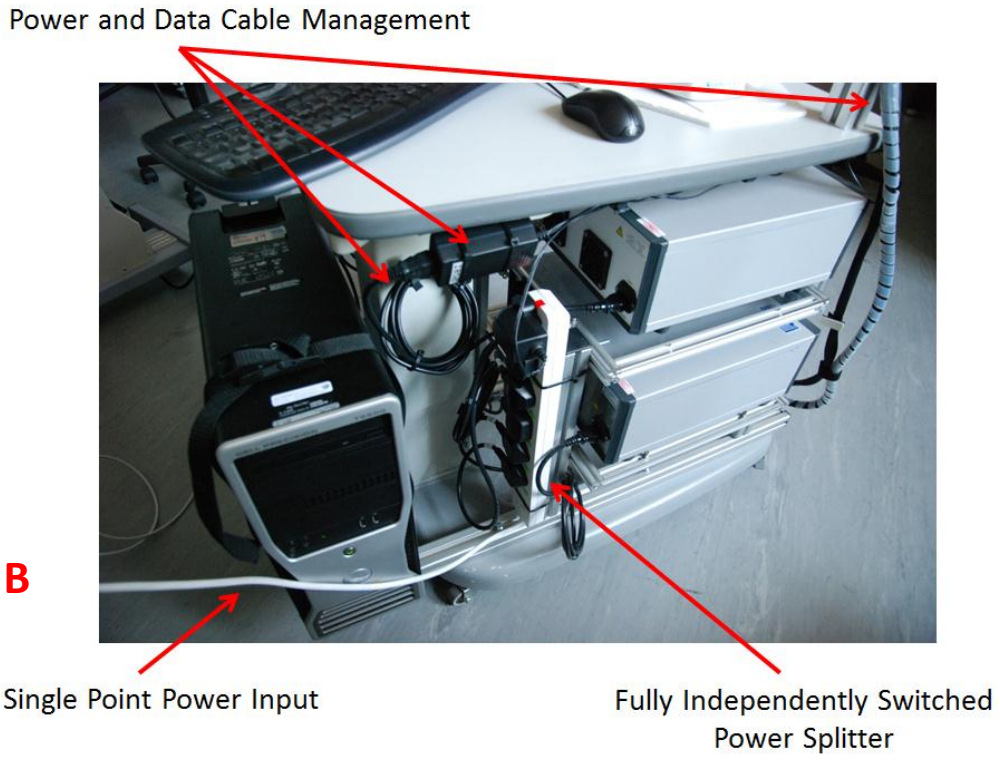

Figure 2.26 (a) The laser and interferometer support structure **(b)** the cable and power management system.

2.11 Laser Safety and Risk Assessment

2.11.1 The Safety Assessment Process Overview

All commercial and research devices are required to meet a set of rigid criteria to certify they are fit for purpose and safe for use. Within the European Union (EU) there are legislative standards that require devices to receive a "Communaute Europeenne" CE mark as according to EN 12100, EN 60204 EN 14121. Although a not quality mark, is it a statement that the device had undergone safety assessment and that if commercialised, the device is safe for use in its intended role. There are no steadfast rules to determine that a particular product is covered under CE marking criteria. Each product is assessed individually and given certification or a waver as required.

Medical devices are covered under CE marking directives and separate rules of the Medical Devices Directives (MDD) (Council Directive 93/42/ECC). Due to the sensitive nature and greater potential risk of a medical device, extra precautions are stipulated by the MDD to ensure the device is "fit for purpose" and will not cause harm in normal use. There is also a requirement to prove claims made about the devices performance.

Research devices are exempt from full CE marking, but must undergo the safety assessment process and receive a CE waver from the UK body responsible for enforcing CE and MDD regulations on medical devices. Enforcement is primarily the responsibility of the Medical and Healthcare Products Regulatory Agency (MHRA). Dual MHRA approval was required for the study as there were two different areas of concern. 1.) Approval for the custom marked contact lenses, classed as an implantable medical device that is not commercially available 2.) Approval for imaging with the OCT system as it is a non-commercial device/prototype and needs to demonstrate it will not cause eye damage. Point 1 was completed by the sponsors and point 2 to was completed by Aston University. The OCT system was also required to pass internal safety assessments within Aston University.

2.11.2 OCT Laser Safety Assessment

Lasers pose a considerable potential threat to the eye. Optical damage of ocular tissue is possible with high powered laser systems. Damage is highly dependent on the emitted wavelength. Visible spectrum (VIS) sources cause damage to retinal tissue specifically the photosensitive cells due to optimisation for the absorbance of radiation in the VIS ranges. Infrared light sources are predominantly likely to cause damage via thermal mechanisms such as flash boiling of aqueous or

vitreous fluids (Fankhauser et al. 1982). Dangers with IR radiation sources are most prevalent at specific wavelengths where water absorbs electromagnetic energy most efficiently. These wavelengths are also highly dependent on the phase of water. Within the Near IR range the most prominent absorption lines are 760nm, 970nm, 1190nm, 1450nm and 1940nm for water in the liquid phase (Joseph & Charles 1951) Any system imaging in these wavelengths will experience a greater degree of absorption and a reduced SNR.

The Santec OCT system light source is classified a class 3R laser in its base configuration and the interferometer a class 1M. Considerable complexity is added to the assessment process because the light source is both pulsed and swept source. The device also has focusing, collimating and diverging optics. The laser beam is treated as a tradition radiation source, experiencing divergence from the point of emission. However, the system can be modelled as a perfect or near perfect Gaussian beam. The addition of the custom attenuation unit as detailed in the OCT system section, alters the final power output of the laser system to the eye. Compliance and testing was performed to British Standard BS EN 60825:2007 as recognised by the MHRA.

2.11.3 Assessment to BS EN 60825:2007

The assessment process required the establishment of several underlining factors such as beam geometry, optical arrangement and required exposure duration. The Maximum permissible exposure (MPE) time was calculated based on a scan time of 10 seconds and 7mm nominal pupil size. The OCT system is not designed to image directly though the pupil but this could accidently occur aligning the system. All calculations were performed as if imaging the retina though the optical structures of the eye. The following calculations were confirmed by Dr Douglas Clarkson from the centre for Clinical Physics and Bioengineering at University Hospital Coventry.

2.11.4 OCT Swept light Source Mean Permissible Exposure

From table A.2 in BS EN 60825:2007, as the central wavelength of the optical system is 1310nm, 400nm-1400nm. Mean Permissible Exposure MPE defined at the allowable level of exposure for laser light at the cornea for the extended sources. Equation 2.7 shows the MPE calculation, coefficients (taken from the standard) of $C_7 = 8$ t = 10 and $C_6 = 1$ (unity) for an ideal system.

$$MPE = 90t^{0.25}c_6c_7 \ (\text{J/m}^2) \ \textbf{(2.7)}$$

MPE for a 10 second expose of 1280 J/m^2 power for the real system was then assessed. Output power was limited to 3.5mW by the custom attenuation unit as measured by a calibrated power measurement probe (Thorlabs PM100D with S132C NIR Probe). Total energy dissipated in the 7mm diameter pupil was 0.035J, equivalent to a radiant exposure of 909J/m^2. Therefore the radiant exposure of the real beam accounted for 72% of the MPE. This is less that the MPE calculated for the system so was regarded as safe. However because this is a divergent beam further calculations were required. A nominal spot size of 2mm at a distance of 60mm from the final optic (focal point) was identified. This relates to a divergence of 0.034mrads (from Equation 2.8) which gives a value of C_6 = 23 from table A.2. This is equivalent to imaging a larger spot size on the retina. Performing the MPE calculation again gives a MPE = 29440 J/m^2. This indicated the NIR beam is inherently safe for imaging the eye at an output power of 3.5mW, giving a factor of safety (FOS) of 23.

$$D = \ 2\tan^{-1}\frac{Df-D1}{2l} \ (\text{mrads}) \ \textbf{(2.8)}$$

2.11.5 Aiming Laser Mean Permissible Exposure

The same procedure was undertaken as for the NIR light source; the ideal MPE for the 633nm aiming laser based on a measured output power of 0.01mW (0.001J over 7mm pupil) and based on a 20db power attenuation of the beam though the interferometer system. The MPE is given by Equation 2.9

$$MPE = 18t^{0.75}c_6 \ (\text{J/m}^2) \ \textbf{(2.9)}$$

For a 10 second exposure C_6 = 1 and the ideal MPE is 32 J/m^2. Radiant exposure was calculated to be 2.60 J/m^2. However, the allowed exposure when the convergent optics were included was MPE = 736 J/m^2 giving a Factor of Safety (FOS) of 23. Again the system is regarded as intently safe for ophthalmic use. As MPE's are cumulative, the 30 second maximum scanning time for the subject in testing is still well within the safety criteria and presents no evident risk.

2.11.6 University Safe Operating Procedure and Risk Assessment

The university requires all laser or ionising radiation items to undergo an internal assessments process. This involve a laser safety assessment with confirmed assessment by an external laser protection advisor and the preparation of a Safe Operating Procedure and Risk Assessment.

The safe operating produce (SOP) is designed to provide a set of rules and procedures for using laser or radiation sources for scientific investigation in a safe manner. It provides a list of qualified instrument operators as well as details and breakdowns of individual's roles and responsibilities. If any radiation source has the potential cause damage with incorrect use, security measures must be put in place and approved by the university.

Specifically with the OCT system, control of laser interlock keys had to be put in place. Keys must never be left with the machine unattended and records of their location must be maintained. The SOP details contingency plans if incident occurs, providing clear indications of the chain of command and emergency medical contacts.

There is also a requirement for the appointment of a Laser Protection Supervisor (LPS) for all system that are a Class 3 or above. The LPS is the University's local expert on laser systems and is usually a senior member of academic staff within the department where the laser system is based. A Local Laser Advisor (LLA) may also be appointed and is usually the person responsible for the day to day operation of the machine. Both the LPS and the LLA have received professional laser safety training. For the OCT system the LPA is Prof James Wolffsohn and the LLA is Mr Thomas Drew.

The most important part of the SOP's function is to detail the limits of the scanning and testing regimes. Maximum exposure times, power settings and configuration settings are detailed. The OCT SOP defines a maximum power setting of 3.5mW at the output probe and a maximum individual scanning time of 30 seconds. One minute rest intervals must be taken between scans. Correct shutdown and start up procedures are also detailed. The light source and interferometer were also sealed with security seals designed to display any attempts to open instrument cases or alter

hardware settings. The university requires a complete reassessment of the laser rules and SOP processes every 24 months.

2.11.7 The Risk Assessment Process

The risk assessment procedure is designed to assess the potential hazards of a piece of equipment. In addition to the eye safety concerns already discussed previously, there were requirements for electrical safety and mechanical safety assessments. The risk assessment was undertaken with the standard university procedure of using a risk assessment matrix. Specific hazards were identified and given a score between 1-5 for severity with 1 being the most severe and 5 the least respectively. Likelihood of event occurrence score is scored with a similar scale of 1-5. The higher the score for the system the more stringent the control measure undertaken. Electrical safety issues included exposure to electric shock and mechanical safety issues were identified as pinch points, fall and back injury related movement hazards. Electrical hazards were reduced with the addition of a residual current device on the main electrical supply circuit designed to cut power to the system in case of a system short. Mechanical hazards were controlled with a combination of SOP rules and mechanical restraints and restrictions.

2.11.8 Finalising of the Approval Process

After the completion of the assessment process, the OCT system at Aston University was granted CE and MDD waver by the MHRA in the first quarter of 2010. University SOP and RA were approved in the second quarter of 2010. The MHRA approvals for the implantable devices (contact lenses) were delayed considerably and granted at the end of 2011.

2.12 Conclusion OCT Hardware Development

The selection of the Santec OCT system and the customisation developments undertaken proved to provide a very efficient and high speed OCT system well suited to ophthalmic imaging. The axial resolution achieved is in the sub 10μm region as required (8μm at the sweet spot, 1mm into the sample) giving clear high contrast images of the epithelial layer and contact lens edge/interface.

The dual imaging system concept has been proved to be reliable and capable with both system optimised to run simultaneously on a single computer without over burdening the system, causing a reduction in speed or memory overflows. Overheating of the PC was noted with long duration testing. Causes were determined to be the large number of PCIe cards in the device reducing airflow through the system, negatively affecting cooling. An internal cable management system and extra venting solved the problem. The final block 2 multi-axis alignment platform proved to be robust in testing providing an excellent platform for performing testing on a wide range of human subjects. The support structure and cable management was effective allowing the machine to be highly mobile and sufficient for use in a high throughput-testing environment.

The laser safety and risk assessment processes proved the system was safe and fit for purpose. The CE waver process also provided a firm platform and approach for future projects and the development of better internal system for risk assessment specifically applied to prototype ophthalmic instruments. Image de-warping, calibration and associated problems inherent with OCT imaging have been effectively quantified and controlled. Algorithms were developed allowing measures to be related to real world values with known degrees of certainty, effectively controlling the source of potential errors. These factors can be applied to the next generation of OCT device proposed for future development.

Chapter 3

Chapter 3: OCT Feasibility Study to Determine Capabilities and a Protocols

3.1.0 Introduction

The factors that govern soft contact lens fit are poorly understood. Poor fitting soft lenses have been shown to have a more negative impact on ocular physiology and comfort than well-fitting lenses. Greater fluorescein staining has been found with both loose and tight fitting lenses and higher levels of bulbar and limbal hyperaemia with loose fitting lenses (G Young & S. Coleman 2001). It is generally believed that, in addition to providing sufficient oxygen levels at the tear-lens interface, it is necessary to have adequate tear interchange beneath the contact lens to remove trapped debris, inflammatory cells, and other tear components that would otherwise accumulate under the lens (McNamara et al. 1999). The tear layer between the contact lens and cornea also reduces the friction between the surfaces by acting as a lubrication barrier and reducing the coefficient of friction between surfaces, avoiding significant mechanical interaction. Smaller diameter soft lenses provide substantially better tear mixing than larger lenses, but only by 0.6% between 12.0mm and 13.5mm diameters (1.8 vs 1.2%; (McNamara et al. 1999)), presumably due to boundary layer effects under the lens introducing a greater level of turbulent flow under larger lenses. However, this is still substantially less than rigid contact lenses (15-16%; (Kok et al. 1992)). Tear mixing with soft lenses showing different amounts of on-eye movement does not seem to have been examined.

Some studies have shown that ease of push up and movement on blink are related to practitioner rating of soft contact lens fit (G Young 1996) while others have shown lens movement to have limited discriminatory value with particular lens mechanics such as materials and lens geometry (JS Wolffsohn et al. 2009; Walker et al. 2003) were the first to objectively analyse all the traditional lens fit parameters, confirming the variability between lens materials/designs and that changing base-curve of a lens design can have little effect on lens movement, as has been found by subjective evaluation previously (G Young 1993; Bruce 1994).

It is well documented that soft contact lens movement on blink varies during the wearing period, with an initial decrease over the first 10 to 15 minutes post-insertion, followed by an increase (G Young & S. Coleman 2001; Brennan et al. 1994; Schwallie & Bauman 1998; Moldonado-Codina & C Efron 2004) Models have been developed to account for the lens and anterior eye parameters that

influence lens movement (Brennan et al. 1994; Bibby & Tomlinson 1983). Several proposed mechanisms, such as dehydration dependent steepening of the base curve or osmotic dependent binding from hypotonic lacrimation, have been disproved (Prichard & Fonn 1995; Golding, Harris, et al. 1995; Brennan et al. 1994). However, there is still a need to determine how the contact lens draping over the corneal-scleral junction (where the lens is required to flex most and mechanical properties of the lens material and geometry will be most dominant) and the lens edge corneal epithelial interaction affects soft contact lens movement and tear mixing over the period of wear.

It has been observed that time independent optical coherence tomography can be used to image the interaction between the lens edge and epithelial layer; with images typically exhibiting an indentation in the epithelial layer near the lens edge (Cui L et al. 2010). Additionally, gaps between the lens and ocular surface have been observed near the corneal-scleral junction. These gaps are thought to reflect the degree to which the lens drapes over the eye (Meixiao Shen et al. 2011).

This feasibility study aimed to test the instrumentation developed in Chapter 4 and to refine a protocol to determine whether high resolution photography and time resolved swept source Fourier domain OCT can be used to image the in-vivo lens in such a manner as to elucidate the relationships between lens draping and edge-epithelial layer interactions, and lens movement and comfort. This information will allow improved modelling of the soft contact lens-eye system, including testing of current theories based on tear film expulsion and negative pressure effects (Martin & Holden 1983; Golding, Harris, et al. 1995) and will inform future lens design and mathematical modeming accuracy of the lens eye system as a whole.

3.1.1 Method and Results

The goals of this study were to:

1. Find the positions (e.g. 2:00, 3:00, 6:00, 9:00, 10:00 with respect to cornea) at which the edge motion, as a function of time between blinks and over 3-5 blinks, can be imaged best. Figure 3.1 shows the scanning positions
2. Attempt to decouple the horizontal and vertical lens motion using the OCT and HSC data.
3. Determine if edge indentation depth and edge coverage can be imaged, as a function of time between blinks and over 3-5 blinks, and that these images can be processed to yield depth and coverage as a function of time

4. Observe whether post lens tear film (POLTF) gaps in the corneal region can be imaged as a function of time between blinks and over 3-5 blinks, and that these images can be processed to yield gap size as a function of time
5. Assess imaging of the tear meniscus along the upper eye lid margin, along the vertical meridian, during a blink and whether these images can be processed to yield meniscus height and area as a function of time.
6. Propose optimised markings on the contact lens for imaging movement with the HSC camera

The study was approved by the institutional ethics committee and conformed to the tenets of Helsinki. Written informed consent was obtained after explanation of the aims and procedures involved in the study.

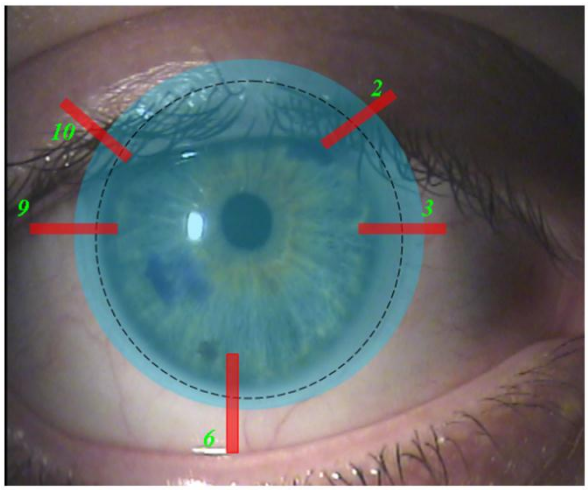

Figure 3.1: OCT scanning positions (clockwise) 2, 3, 6, 9, 10 o'clock, respectively

3.1.2 Imaging Positions and Lens Edge Tracking

Two silicone hydrogel frequent replacement contact lenses with different edge profiles were investigated; Acuvue Oasys (Johnson and Johnson, Jacksonville, Florida, USA) and Biofinity (CooperVision Inc, Fairport, New Your, USA). The order of insertion was randomised and imaging was conducted after 30 minutes of settling time. The lens was imaged in random sequence at the 2 o'clock, 3 o'clock, 6 o'clock, 9 o'clock and 10 o'clock positions with respect to cornea.

The patient was stabilised on a head and chin rest with the OCT head position perpendicular to the ocular surface to optimise the reflection from the contact lens and ocular surfaces. The reference arm of the OCT was tuned so that the 'sweet-spot' with optimal reflection was 1 mm into the 5mm penetration depth. The system is capable of scanning over 15 mm to capture the entire cornea, but the resolution is improved at narrower scan widths. The optimal width to capture the dynamic lens movement with sufficient width of the uncovered conjunctiva and contact lens surface in the field of view for them to be edge detected and curve fitted was found to be between 3 - 5mm. Three subjects aged 25 to 38 years (2 male) were aligned with the OCT beam angled to scan at right angles to the lens edge at that position on the cornea. Once the subject was settled so a steady image could be achieved, they were asked to blink every 5 seconds (indicated by the researcher) and the data for 3 successive blinks were recorded.

The OCT system records 1019x500 pixel images at 27Hz, the storage space required for each 15 seconds of data capture is 0.75Gb when post processed. A pattern matching algorithm was used to track the lens edge and remove unwanted head movement. Figure 3.2 shows the algorithm under test. The tracking algorithm proved robust and predictable.

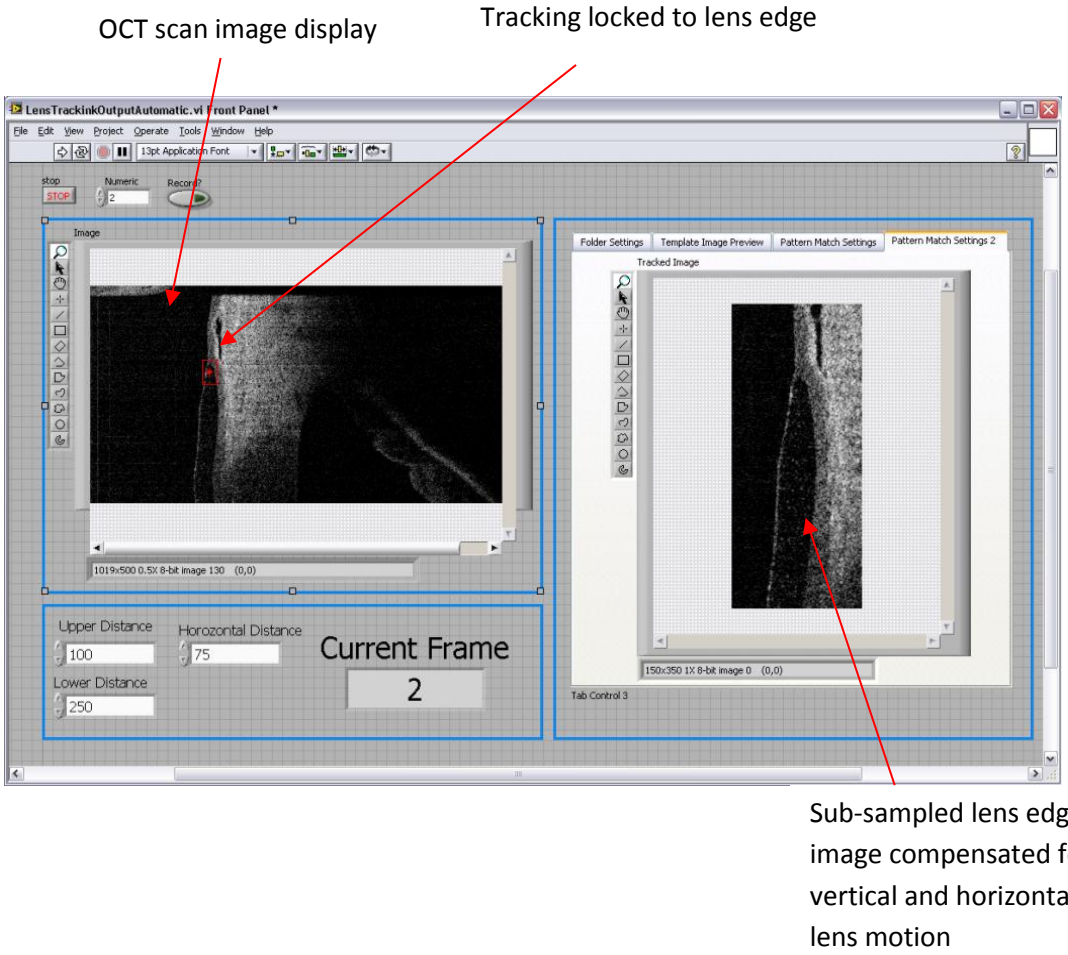

Figure 3.2: Lens edge tracking and segmentation program in LabVIEW.

As the principal lens movement with the blink action is in the vertical meridian, the movement in the 6 o'clock corneal position was greater than the other positions. There were no consistent features on the cornea that allowed reliable reference markers to assess lens movement against as less reflective areas changed with time and the penetration of the laser was not enough to clearly resolve the contact lens and anterior chamber angle simultaneously. Scanning the OCT head horizontally and vertically during the scan to construct a 3D image is possible and would allow horizontal and vertical lens motion to be decoupled, but this would significantly reduce the frequency of the complete scan and / or the resolution and is deemed too damaging to the image to be useful. The corneal appeared less affected by the contact lens at these upper corneal positions and the eyelid and eyelashes interrupted the image unless the lid was artificially restrained, therefore it was felt that that 6 o'clock position is the principal position to image in phase II unless modelling indicates specific regions that might be differentially affected by the contact lens designs under trial. Positions 3 o'clock and 9 o'clock did yield information on lens movements. Positions 10 o'clock and 2 o'clock did not add considerable insight over 3 and 9 and were noticeably harder to image clearly as they are closer to the upper lid, hence are regarded as redundant for future testing. Figure 3.3 shows the typical results for the tracking algorithm operating at 20fps. The edge could be robustly tracked in real time using a pattern detection algorithms (LabVIEW, National Instruments, Austin, Texas, USA). The vertical lens movement movies for the 6 o'clock position for the Acuvue Oasys and Biofinity contact lenses were assessed and there was no clear difference in lens movement between the two lenses for each of the three subjects although the lenses were only imaged 5 minutes after insertion.

Although neither of the lenses showed any apparent standoff proud of the ocular surface at any scan point. Lens indentation, epithelia; and corneal indentation could be considered to be the proportion of the lens thickness at an arbitrary distance past the lens edge. An arbitrary distance of 1mm before and after the lens edge was assigned as soft contact lens diameter typically overlaps the conjunctiva by 1mm. These points could be tracked in real time at 20fps and fitted with edge detection algorithms. Hence these parameters could be calculated and plotted over time post blink. Figure 3.4 shows indentation tracking and edge detection.

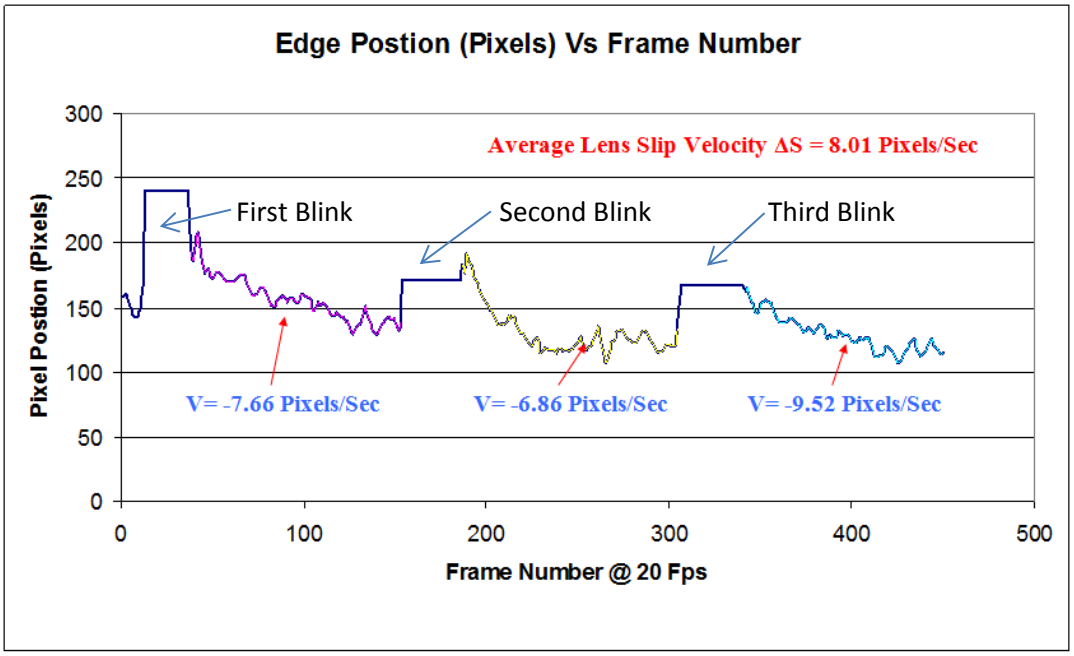

Figure 3.3: Results of the lens edge tracking algorithm, flat tops on peaks represent blinks automatically removed. Fluctuations in decay profile are likely caused by micro eye moments

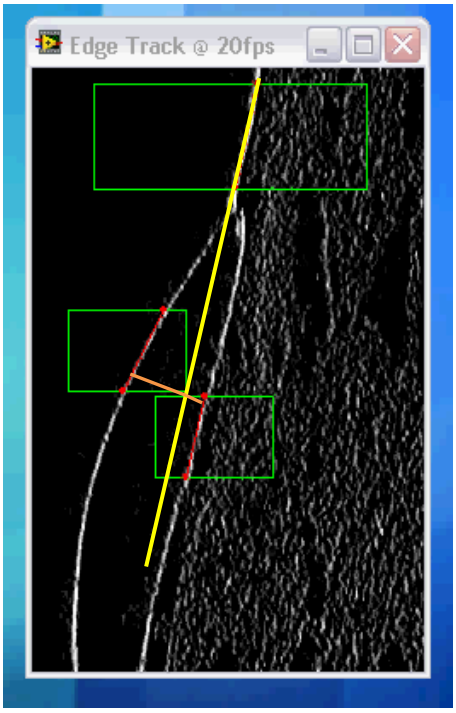

Figure 3.4: Dynamic indentation tracking program developed in LabVIEW, note extensive use of filtration and morphology

3.1.3 Decoupling horizontal and vertical lens motion using the OCT and HSC data

As highlighted in the previous chapter, it was not possible to decouple horizontal and vertical motion using the OCT data alone. The High Speed resolution photography camera could capture the on-face contact lens image at up to 62Hz depending on hardware configuration but was hardware limited to avoid excess loading of the computer BUS. The commercially available lenses used in this feasibility study did not have any markings that could be imaged relative to the pupil or limbus centre. Therefore we were unable to decouple movement with the HSC camera. Figure 3.5 shows a test image of the model eye demonstrating the field of view of the HSC and custom optical software.

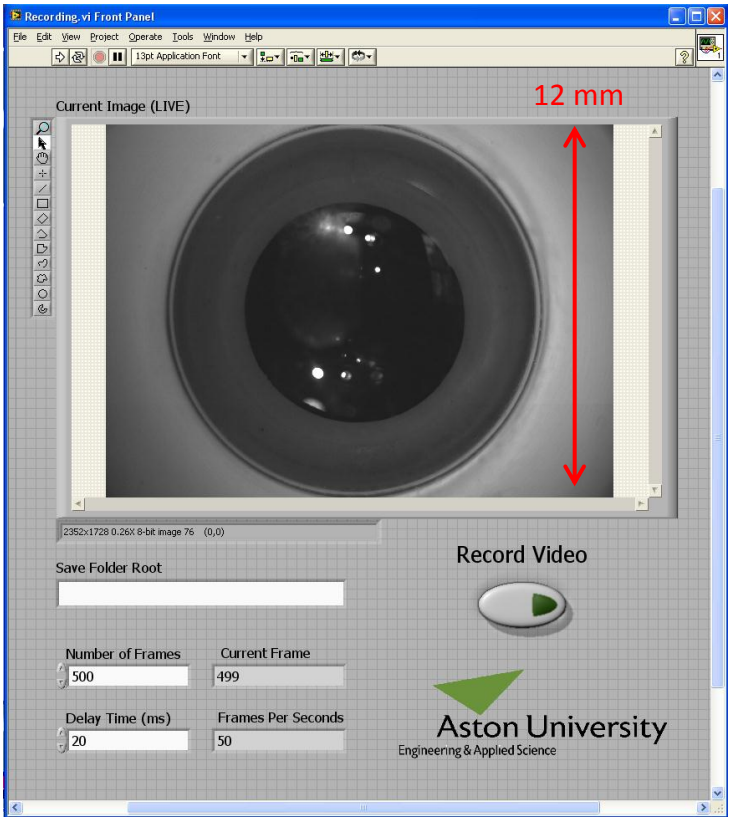

Figure 3.5: HSC capture program prototype

3.1.4 Dynamic Epithelium thickness Measurement

A filtering algorithm for separating the epithelium in the OCT images was being successfully developed. A combination of thresholding, greyscale morphology and Gaussian filtration provided good contrast allowing line profiling to resolve edge detail Figure 3.6. Profiling was then performed at differing horizontal positions allowing a thickness profile for the epithelium to be built up. Real time measurement was possible, with software having been developed to control the measurement process (Figure 3.7).

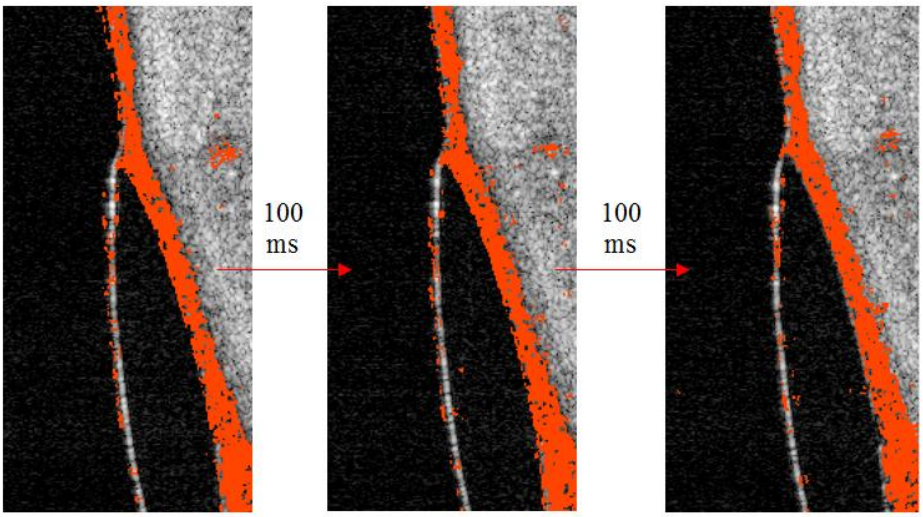

Figure 3.6: Epithelium separation program (epithelium indicated in red) can be run in real time.

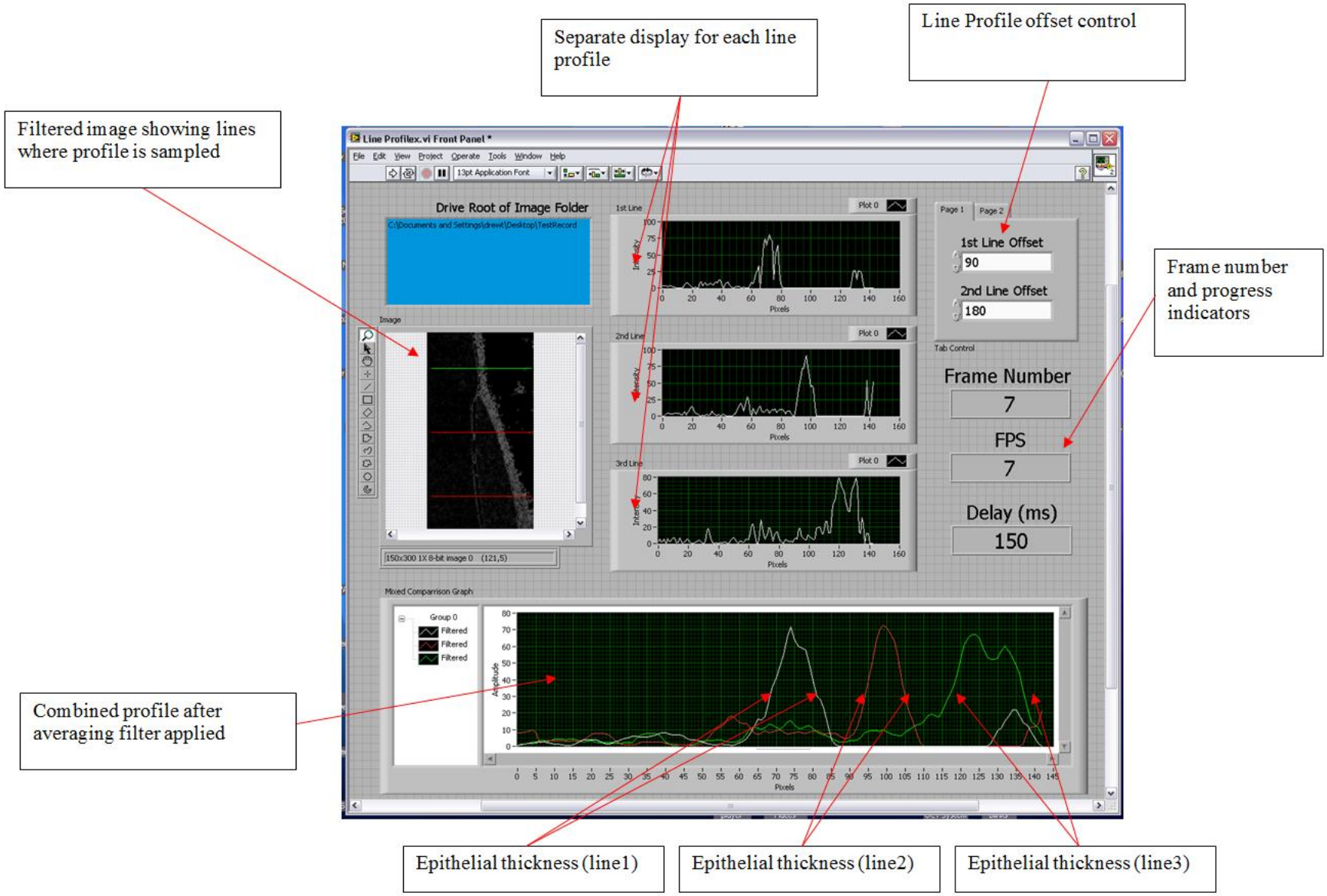

Figure 3.7: Epithelium thickness program showing pre, post and 1mm from lens edge thicknesses values calculated dynamically

3.1.5 Junction Gaps and Post lens Tear Film Gaps

Junction gaps were observed and were both more common and prominent with the Biofinity compared to the Oasys lenses. Figure 3.8 shows the most extreme example seen. The scan was performed in the 6 o'clock position with the tracking algorithm used to segment the position just before the lens edge for closer examination. Gaps were most prominent at the level of Bowman's membrane immediately after the blink and reduced in volume with elapsed time. Splitting and merging of gaps was also apparent, however at this time it is unclear if this is actually some change in geometry of the void or if head movements were producing a change on the plane of the scan. Linking of OCT scans with the high speed camera data should give more insight into this phenomenon.

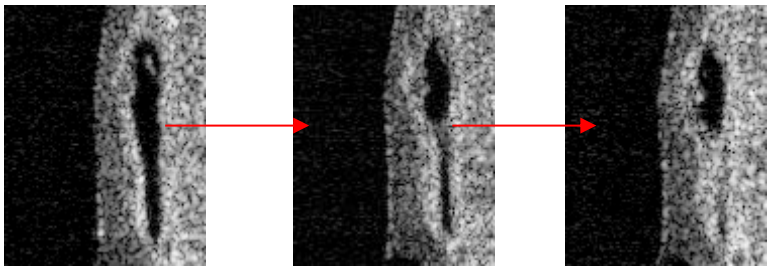

Figure 3.8: Junction gaps imaged with 100ms separation

Gaps were also observed forming beneath the contact lens surface, both at the level of Bowman's membrane and also at the lens edge / epithelium boundary. Figure 3.9a shows a discontinuity forming at the level of Bowman's membrane. Figure 3.9b shows the formation of voids at the lens / epithelium interface. The formation of voids at the epithelium / lens interface appears to be caused by lens "standoff" from the edge. These gaps can be quantified in terms of changes in area and centre location relative to the lens edge with time using particle based analysis.

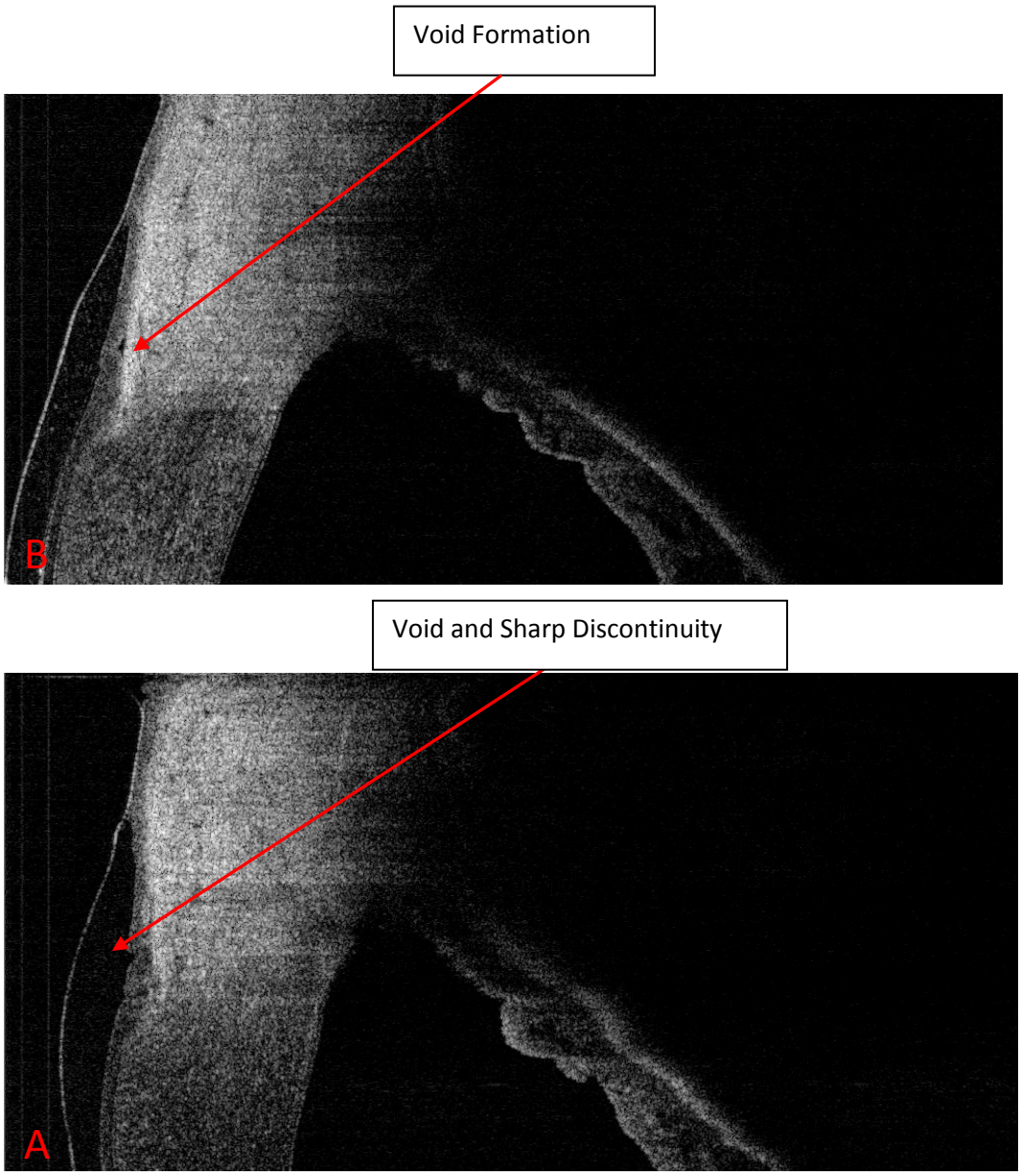

Figure 3.9: (a) Junction gap imaged at lens epithelium boundary.
(b) Gap imaged at epithelium stroma boundary.

3.1.6 Post Lens Tear Film in the Corneal Region

As the Acuvue Oasys and Biofinity lenses did not sit proud of the conjunctival epithelium, the tear meniscus related to the lens edge was minimal and would be difficult to extract due to its similar refractive index to the lens. The flow of the tears on the lens surface could be observed due to the change in reflection from the lens surface immediately after most blinks. However it is currently unclear if there is enough consistency between frames to be able to track and quantify tear movement. Advances in OCT using polarimetry or Doppler shift technology may assist in determining tear flow.

3.1.7 Tear Meniscus at the Eyelid Margin

The tear meniscus at the lower lid margin could be imaged over time. Similar to the sub-sampling performed to separate the junction gaps described previously, a method for extracting the tear meniscus was developed. Figure 3.10 shows the sampled tear film images.

To image the upper lid dynamically would require a 15mm vertical scan and at 20Hz several frames would reveal the upper lid tear margin during the blink. Scanning over a wider field of view (15mm compared to 5mm) to capture lens movement and the tear meniscus simultaneously would reduce the resolution of the scan. It was therefore decided not to image the tear meniscus in the full study.

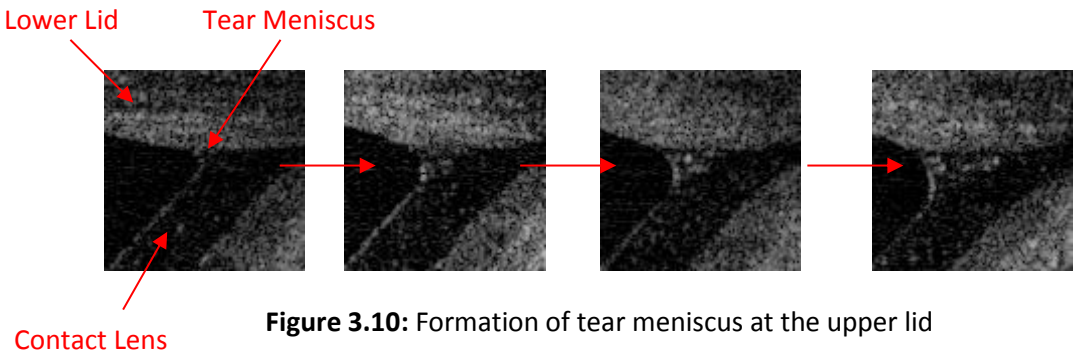

Figure 3.10: Formation of tear meniscus at the upper lid

3.1.8 Conclusions

The contact lens could easily be imaged in the 2 o'clock, 3 o'clock, 6 o'clock, 9 o'clock and 10 o'clock positions with respect to cornea as a as a function of time between blinks and over 3 to 5 blinks. The OCT system was positioned at right angles to the corneal and contact lens surface to optimize the OCT reflection and resulting image contrast. The 6 o'clock position showed the greatest lens movement and hence changes in epithelial thickness, lens coverage and formation of pressure related gaps beneath the contact lens and at the level of Bowman's layer. Positions 3 o'clock, 6 o'clock, 9 o'clock are the most applicable under the current testing requirements, do not require potentially confounding lid manipulation and provide adequate information. Hence in the full study other positions can be removed from testing as they appear to add no further information to characterise the lens-epithelial interaction. Edge indentation depth and edge coverage can be imaged as a function of time between blinks and over 3 to 5 blinks. Image processing algorithms were developed which could separate the epithelium from the rest of the image in real time to allow depth and coverage to be processed. Junction and post lens tear film gaps can be imaged as a function of time between blinks and over 3 to 5 blinks. These gaps seem to occur at both the level of Bowman's layer and also between the contact lens surface and surface of the epithelium. The area and centre of these gaps with respect to the lens edge can be processed as a function of time.

The tear meniscus at the upper eye lid can be imaged along the vertical meridian during a blink, although the scan width needed to be increased, decreasing resolution, if this was sequential to imaging the contact lens movement. These images can be processed to yield meniscus height and area as a function of time. Subject gaze positioning needs to be improved with the addition of separate targets for eye alignment with each scan position. The addition of targets will also aid subject practitioner communication and speed the scanning process. A Metronome system is required to accurately time subject blinks to aid post processing efficiency and subject compliance. Without markings on the contact lenses, the high speed, high resolution photography system and OCT cannot reliably decouple the horizontal and vertical lens motion of the contact lens.

Hence this feasibility study was able to identify the key metrics to be measured in the full study as well as refining the detection and quantification algorithms to produce a robust and reliable measurement system. Producing a batch processing system requiring minimal human input was essential in processing the large quantities of data required for the following full lens-epithelial interaction study with multiple patients, time points and lens designs. Initial estimations place the total of collected data from the OCT system and High speed camera close to 10TB of raw data.

Reducing post processing time was also necessary and achieved. In the full study, the lenses will be marked as proposed above to allow dynamic decoupling of vertical and horizontal movement as the markers will be visible for the HSC to detect. The conjunctival indentation and contact lens edge epithelium coverage will be imaged and analysed dynamically to determine how pressure concentrations induced by contact lenses with different edge profiles and back surface curvatures affect the epithelium which may have consequences on long term ocular health, especially as it is estimated that we blink approximately 17 times per minute (Bentivoglio et al. 1997)

Phase 1 indicated that there was a requirement to improve the image ability of the contact lens surface by the HSC camera. Edge tracking was tested but is deemed to be too inconsistent as lens edges can slip under eye lids or rotate in an undeterminable motion. Guaranteed positions or datum criteria could not be defined.

Engraving the outer surface of a contact is well known in the industry and is used extensively in the alignment of toric contact lenses (Snyder 1989). In consolation with our sponsors and with periodic testing and evaluation a dual marking system was developed. Figure 3.11 shows the positions of the engravings on the lens outer surface. A central circle of 4.40mm and 4 outer lines of 1.25mm positioned at 90 degree offset between each other were finally chosen. Under ideal circumstances the central circle will be positioned concentric with the pupil when correctly fitted. Position differential between pupil and contact can be determined by degree of concentric offset with between pupil centre and or limbus centre. Offset lines are imaged to determine further information about its dynamics. Potentially when the lens falls under the action of gravity after the blink the lens may experience rotation around its central axis.

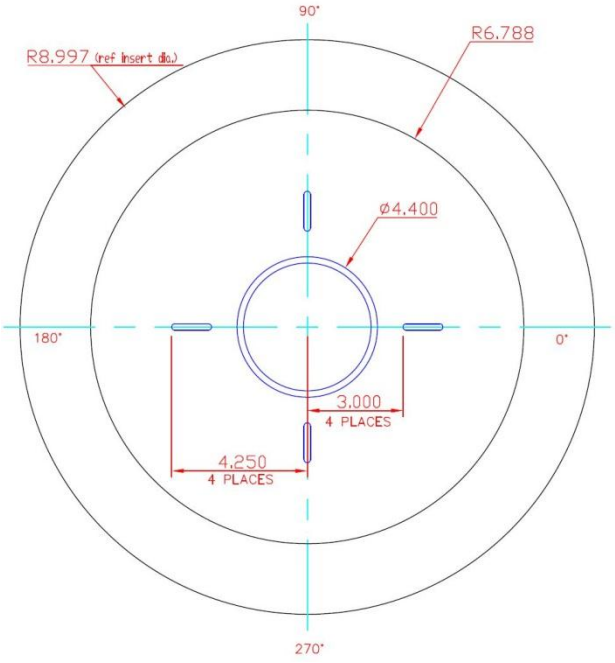

Figure 3.11: Engineering drawing, indicating positions of contact lens markings.

Chapter 4

Chapter 4 : Analysis and De-warping Software Development

This chapter outlines the development of the custom software solutions require to collect, recorded and analyse OCT and HSC data.

Phase 1 shows attempts to automate the analysis of the HSC and OCT data to produce dynamic measures. Although largely successful, considerable variation between human subjects required calibration of the tracking algorithms for each subject in turn. A semi-automated approach was decided to be more time efficient and appropriate. A total of 26 separate software programmes were developed for the OCT project. Figure 4.1 gives an overview of the software developed for each sub category.

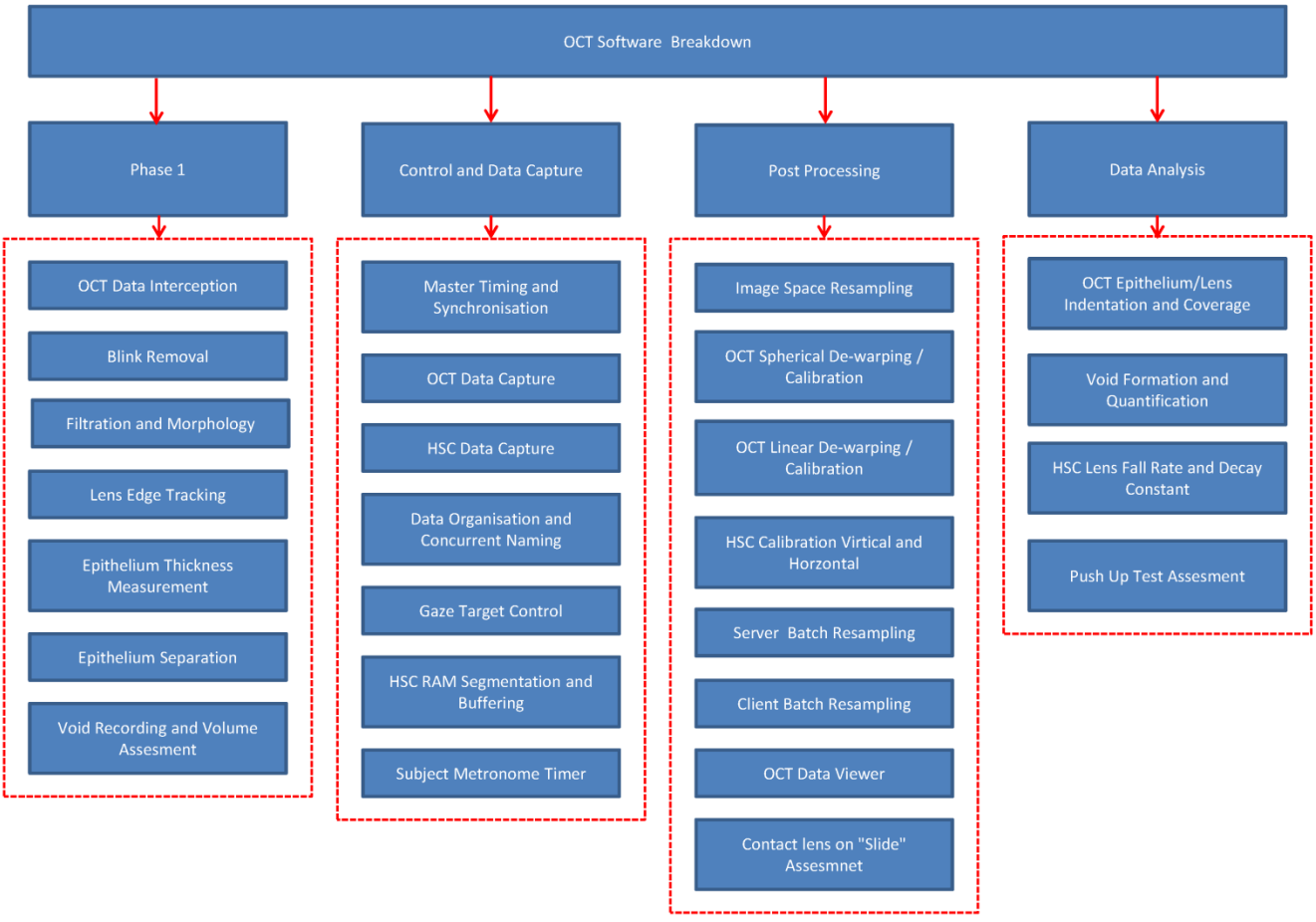

Figure 4.1: Overview of the 26 software programs developed for the OCT project.

4.1 OCT Recording Metrics

Two dimensional images from the OCT system (B scans) were used to measure the following criteria. Epithelium thickness both pre and post lens edge and contact lens thickness and contact lens indention respectively. A constant reference point between images was required the lens edge was utilised. Metrics were assessed at a distance 1mm in front and behind the edge. Figure 4.2a shows a post processed image from the OCT system and Figure 4.2b shows the metrics measured. Measures were taken just before a blink and on the next subsequent clear frame after a blink, with two blinks worth of data taken for each scan.

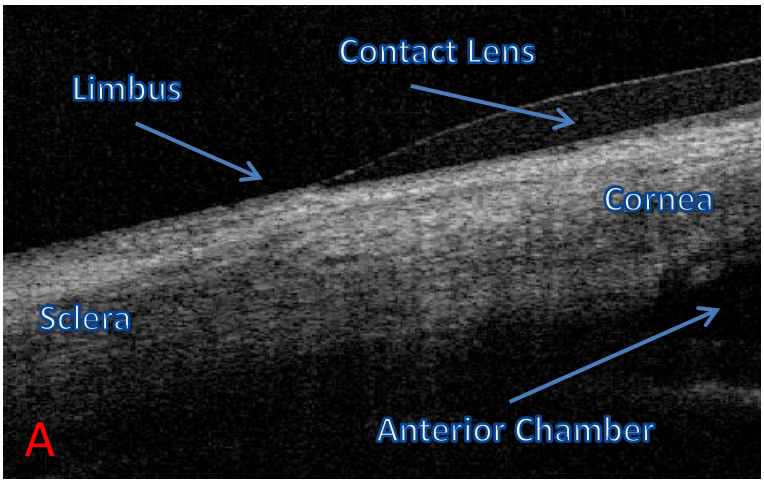

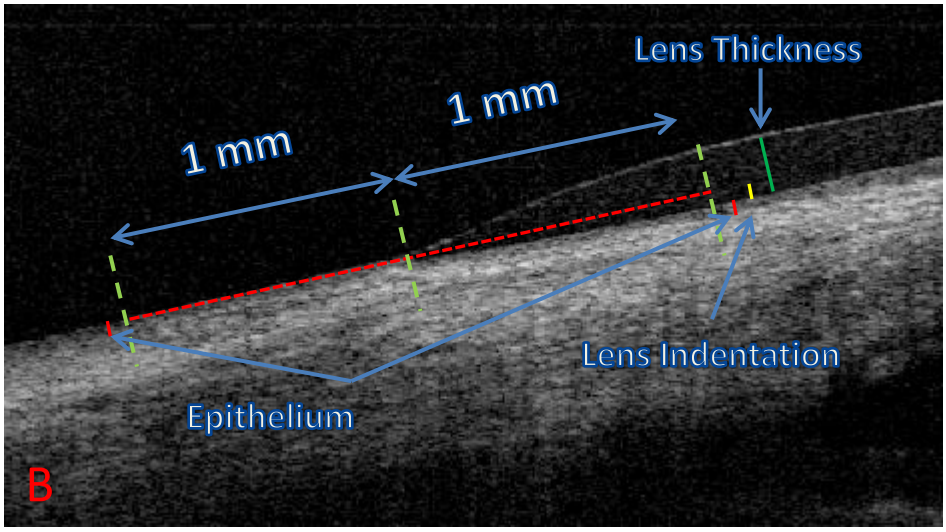

Figure 4.2: (a) *in vivo* OCT image of lens **(b)** Metrics and positioning information used to determine indentation, epithelium thickness and lens thickness.

4.2 OCT Analysis software

A custom standalone LabVIEW program was developed to assess the indentation and thickness measurements. In addition, it allowed de-warping of the images as required before analysis. The software could open and decode the OCT images in real time and provide a novel technique to align the measurement callipers to the corneal surface. The alignment process is detailed in Figure 4.3 and is achieved in the 3 following steps;

Step 1: the lens edge was manually selected with the mouse (Figure 4.3a) and a circle of 1mm diameter was automatically overlaid by the software (red dotted line; Figure 4.3b).

Step 2: an “H Bar” Calliper was drawn with the rotation point centred at the lens edge marker (yellow vertical line and green horizontal line; Figure 4.3c).

Step 3: the leftmost yellow calliper was manually positioned parallel to the corneal surface at the point it was tangential to the red dotted circle. The right yellow calliper was automatically moved by the software to be equi-distant from the lens edge, sharing a common rotational point (Figure 4.3d). The callipers were thus located parallel, but co linear with the corneal surface. The yellow calliper lines were orthogonal with respect to the corneal surface.

Figure 4.4 shows the software and user interface. Points of intersection were marked on the yellow calliper lines in the zoomed area windows giving a more detailed view for artefact selection. Lines may appear aliased on this image, however this is simply an effect of the high magnification and encoding of the image in the saving process. There was no effect on the final outputted data stream. A final image check was displayed with the distance overlaid on the image to check that the correct features had been highlighted. The software corrected for any curvature of the cornea and produced true distances between points by using custom generated coordinate systems for each measurement. The software could select any frame of OCT data or play the entire data file in a separate screen window. This allowed for easy blink identification and frame section. Loading of data files was optimised and was simply a process of dragging and dropping the image into the user interface.

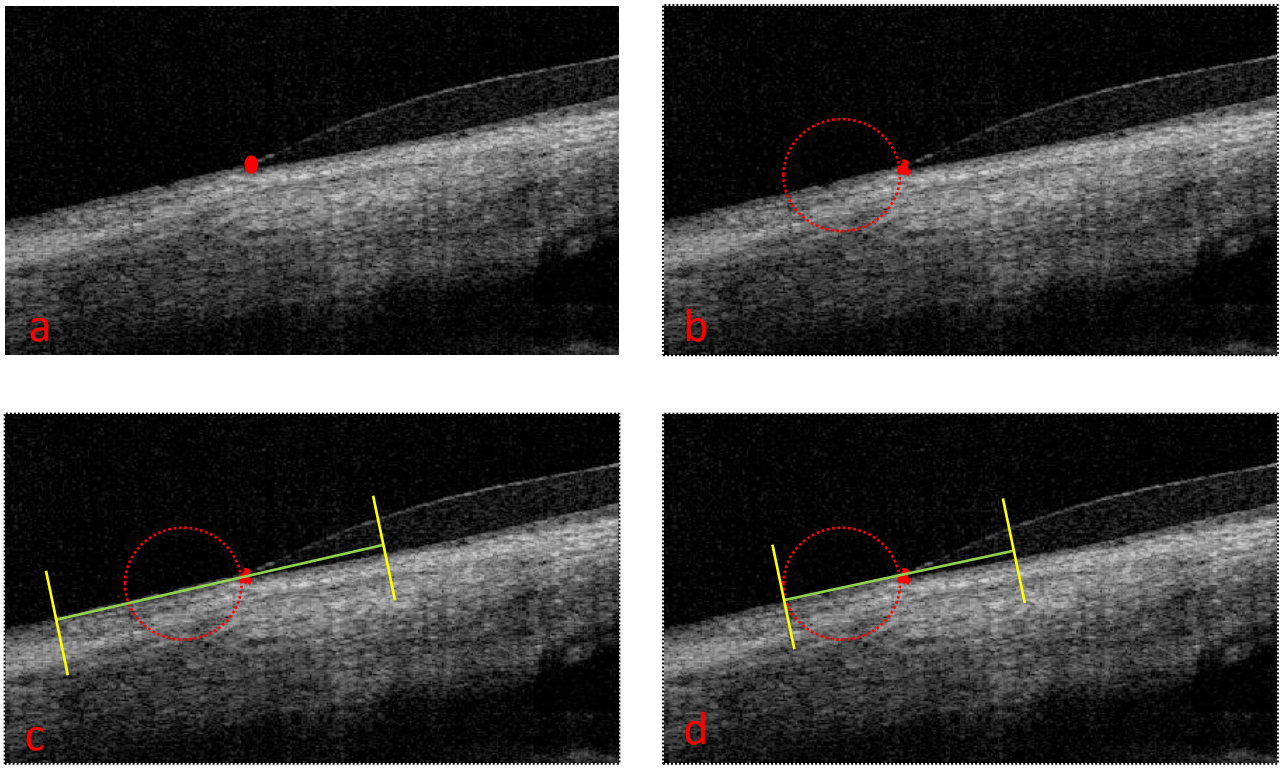

Figure 4.3: (a) Select lens edge **(b)** 1mm diameter circle is rendered over image **(c)** Callipers are displayed and aligned to epithelium **(d)** align clappers to circle, metrics are automatically determined.

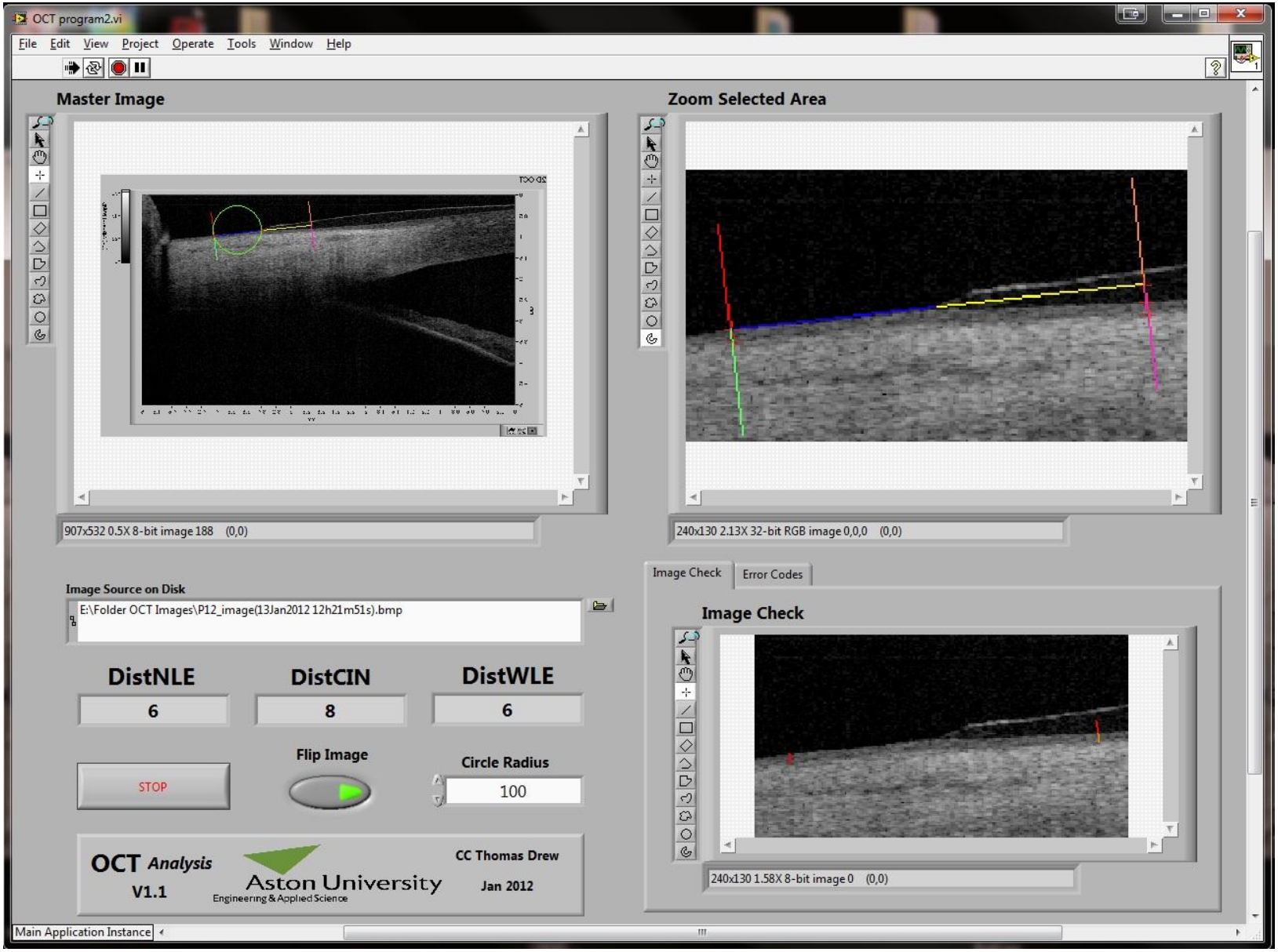

Figure 4.4: GUI of the program developed to compute metrics relating to contact lens fit. Close up sections allow the user to align the callipers with precision and speed.

4.2.1 Calibration through Imaging the Used Contact Lens on a Glass Slide

It is hypothesised that much of the perceived indention observed with contact lens when imaged *in-vivo* in the eye may be produced by optical effects of the curved edge of the lens. Different lens edges and different edge designs are suspected to have a considerable effect on the perceived indentation severity. The situation is further complicated as *in-vivo* imaging, by its nature, images the curved lens on the curved corneal surface, making decoupling of surface interaction physics more complicated. An imaging regime was therefore developed that allowed the contact lens to be placed onto a hard and uncompressible surface (glass microscope slide, backed with plastic tape) where it can form its natural relaxed curved shape due to surface tension and internal elastic tension. The lens must be maintained at as close to possible true level of hydration as was experienced in the eye to maintain dimensionally similar conditions for valid testing. This was achieved by rapidly scanning (<10 seconds) the lens after it was removed from the eye. Figure 4.5a shows an OCT raw B-scan of a lens on a slide and Figure4.5b the image analysis to show the slide distortion artefact. A fast attaching slide holder was developed that allowed rapid scanning without repositioning the OCT system since the subjects previous scan. Figure 4.6 shows the slide holder with the focusing and DOF target positioned. Figure 4.7 shows the device mounted on the OCT ready for scanning. A similar specular reflection alignment technique as used in de-warping was performed before scanning A modified version of the OCT analysis program was used for measurement.

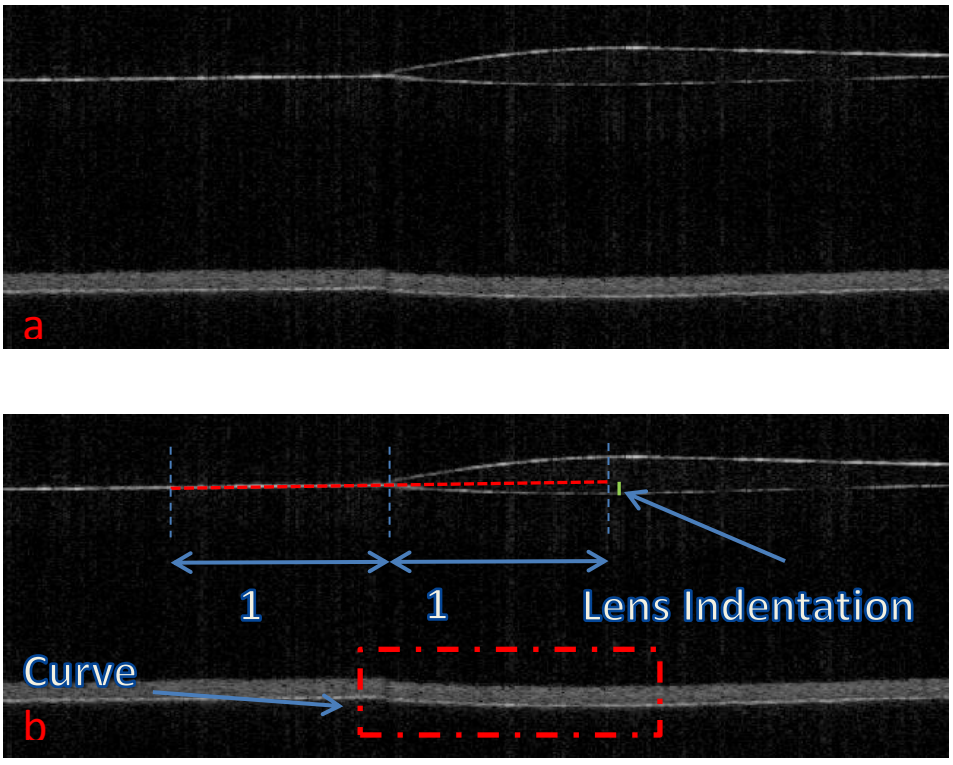

Figure 4.5: (a) Contact lens imaged on glass side for calibration **(b)** metrics to be measures, note the curvature of the sides back surface.

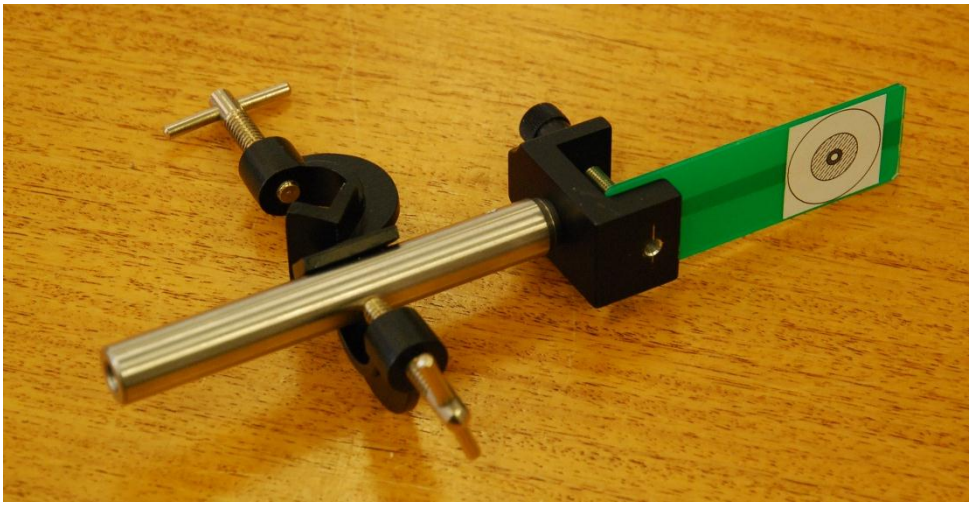

Figure 4.6: Quick “attach and release” system for holding microscope slides. Shown with HSC target slide for correct FOV determination.

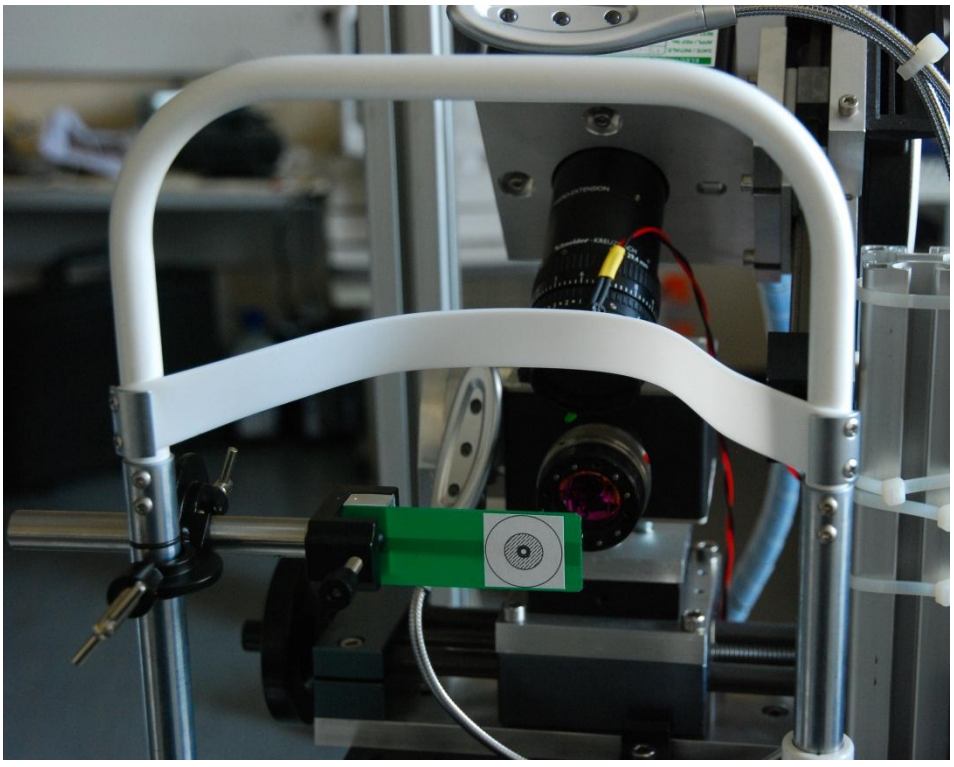

Figure 4.7: Calibration system mounted on headrest.

4.2.3 Data Naming and Storage Conventions

The simultaneous operation of both the HSC and OCT system generated a considerable quantity of information and a requirement for the data to be time locked and correlated. A master data control program was developed that acted as a single point of input for patient data and visit information. The study described in chapter 5 consisted of 28 subjects (P001 – P028) with 4 lens designs (Y,H,S and R) scanned at 3 positions perpendicular to the lens edge (3 o'clock, 6 o'clock and 9 o'clock points). A separate no lens condition was also added scanned, effectively producing data for a 5th 'lens' (NL). Imaging was at 3 time points starting at 15 mins post insertion (H0), 2 hours post insertion (H2) and 4 hours post insertion (H4). Both the OCT system an d HSC had to accomplish 1008 individual scans. Combined with the no lens condition, a total of 2072 individual subject scans were performed. Potential for confusion or lost/misplaced data was deemed high risk and required a sophisticated solution.

The master data control software had to account for the potential need to rescan subjects in case of failure of a scan while maintaining a constant numbering and time stamping system for efficient batch processing of data at later stages. There was also a need for redundancy, test and calibration scanning and a feedback system that warned of potential data overwriting. Figure 4.8 shows the frontend of the master data control system.

The software limited user input to a set of restricted variable names removing the possibility of spelling error or confusion between practitioners. Specific folders and sub folders were automatically created in a file tree structure that closely matched subject information. Each subject was issued with a paper card at the beginning of each visit that contained subject information and breakdown of the scanning required for that test day. This indicated to the practitioner where they were in the scanning process (visit, time, lens etc…). These metrics exactly matched the drop down lists available in the control software options. Variable names and file save locations were passed via a data pipeline to the HSC and OCT capture programs. Neither system could operate without the master data folder passing them information. Data could not be recorded in the incorrect location or overwritten independently. If the master data control program detected previous use of a file name, this was flagged to the user by the system informs, prompting them to check the subject's information card. The researcher could also see at a glance the file that was currently or last recorded

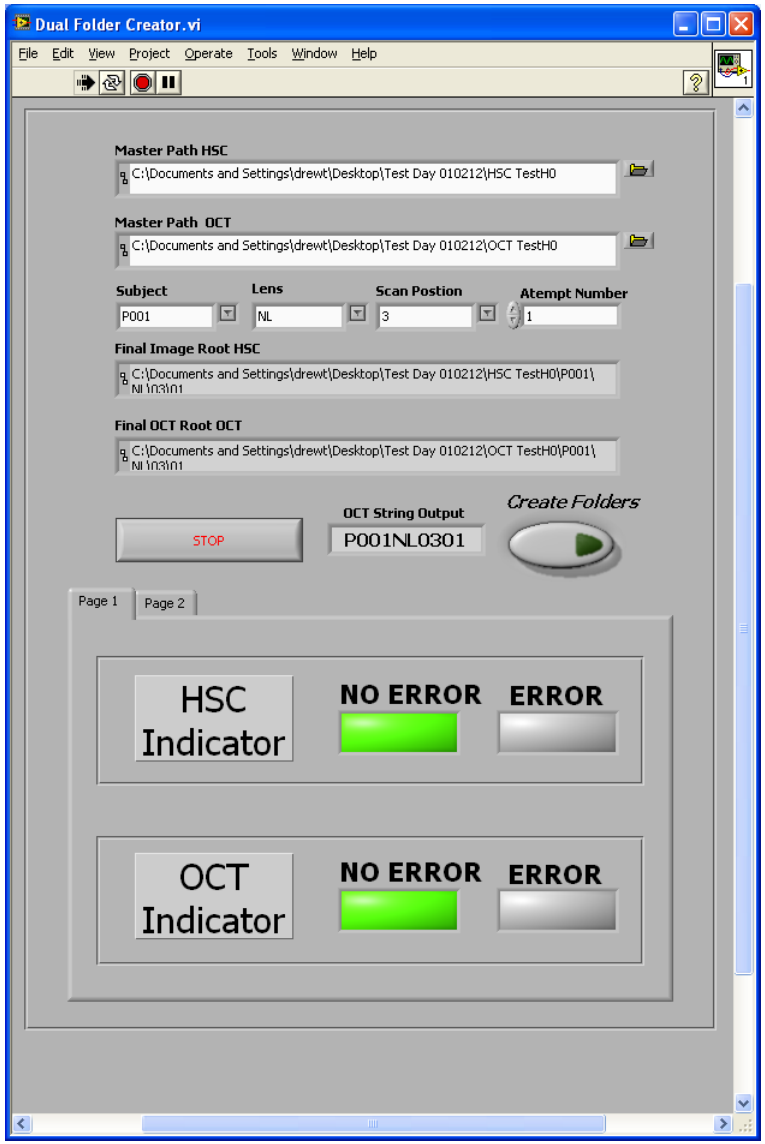

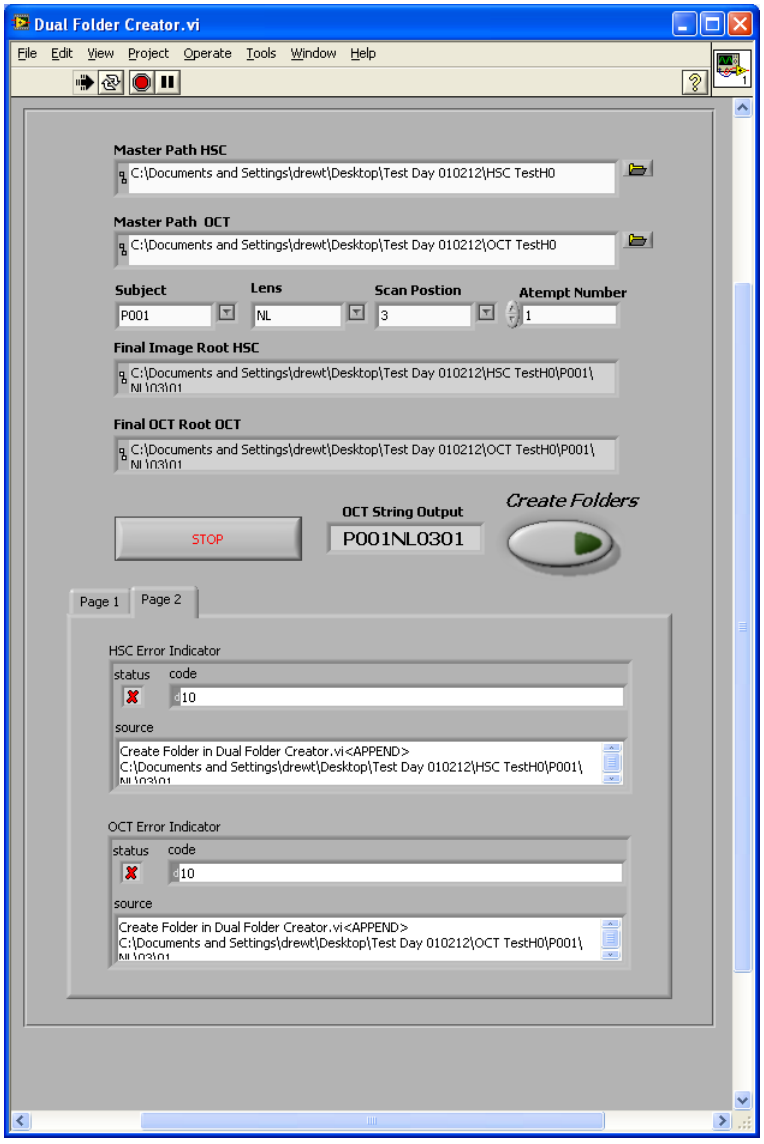

Figure 4.8: Front end GIU for the master data control system, indicators are clear, well presented, and self-documenting.

4.2.4 Void Analysis Program

The requirement to quantify voids formed at the contact lens / cornea epithelial interface and at the lower boundary of the Bowman's membrane necessitated the design of a custom analysis package. Specific zones of void formation were also designated. Voided scanning and analysis was to be performed with each lens at every time/lens combination and once with the absence of any lens on the eye lens. Figure 4.9 shows graphically these areas for the 'with lens' conditions. There were 5 point of inspection, categorised as follows.

Point 1: no lens void between stroma and Bowman's membrane in front of the lens edge.

Point 2: with lens' voids between stoma and Bowman's membrane interface less than 1mm from the lens edge.

Point 3: with lens' voids between Bowman's membrane and the contact lens interface

Point 4: with lens' voids between Bowman's membrane and the stroma greater than 1mm from the lens edge

Point 5: with lens' voids between Bowman's membrane and the contact lens interface

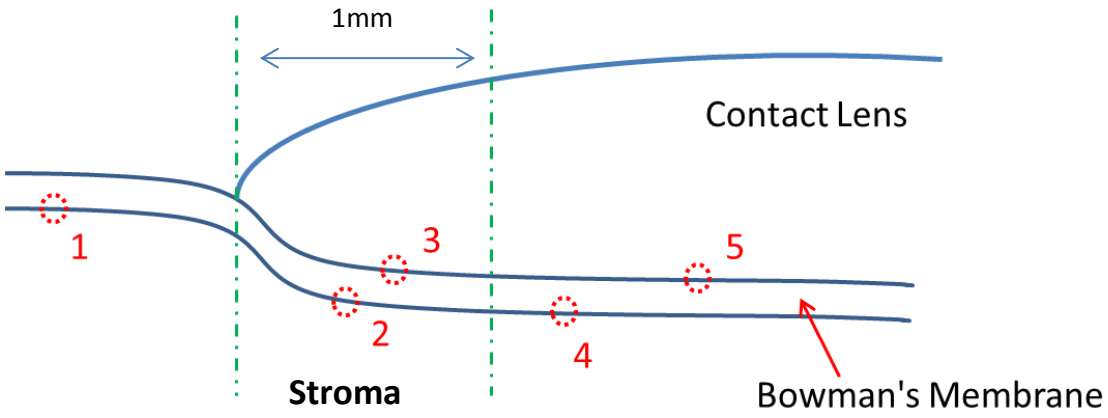

Figure 4.9: Indication of 5 positions and associated with void numbering system.

4.3 HSC Recording Software

The HSC provided a constant stream of images via the camera link capture card. A live image was displayed at a frame rate of 60fps with each frame dumped from the memory immediately after the image has been displayed on the screen. This provided the practitioner with a live view on the cameras data stream for alignment, focusing and calibration of the HSC. Upon triggering the data capture and recording, the software started to record each frame at a rate of 15Hz directly onto a 2GB partition on the computer Random Access Memory (RAM).

The software took advantage of multicore parallel processing delegating specific CPU cores to each separate task in the recording process. A single core ran the camera triggering and storage of the data in raw format to the system RAM as described in the data recording section. A second core ran the encoding of the images into the portable network graphics (png) loss less image format. The second task was of considerably higher computational intensity when compared to the first, requiring at least 2 orders of magnitude greater processing time depending on the image compression algorithms chosen.

After imaging was suspended the program took up to 30 seconds to continue the encoding process before completing its execution. The program also provided visual conformation of the recording process as well as progress on encoding and the number of frames recorded in total. Recording frame rate was also adjustable by the user but was pre-set at a default frequency of 15 Hz.Figure 4.10a shows the graphical user interface. The inclusion of separate metronome software was also integrated into the program. Figure 4.10b shows this program as a separate stand-alone system used for development. The metronome was user configurable to produce an audible tone so the subjects could maintain a regular blink interval with a finite number of repetitions. The use of a metronome where the users are requested to blink upon hearing the audible signal allowed for a more constant set of imaging data while reducing the workload on the practitioner. The program could also be configured to give a time delay before data capture to allow for individual response time to the audible signal. The metronome audible tone could also be triggered manually without imaging or recording so the subject could hear a demonstration so they were aware of what to expect.

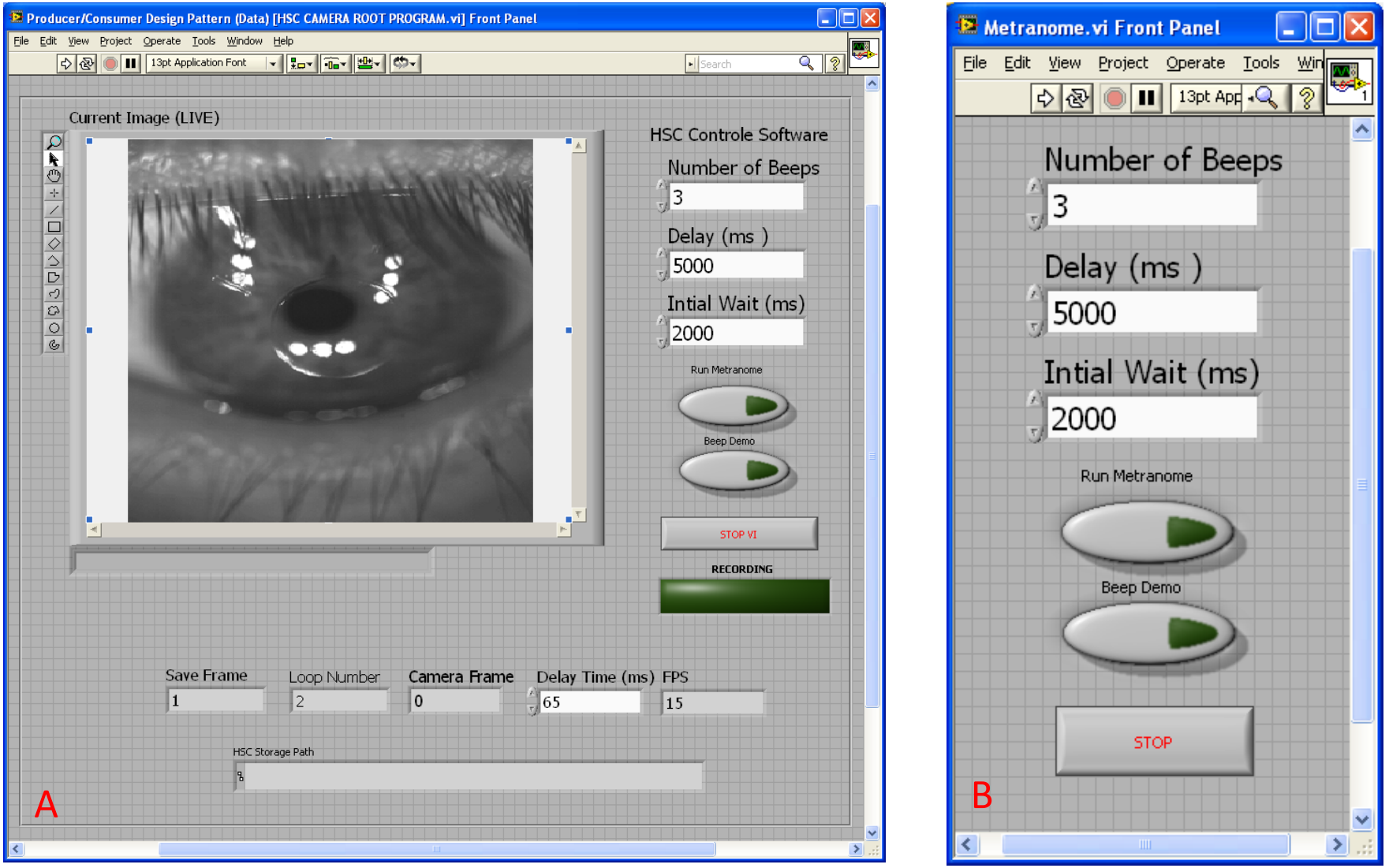

Figure 4.10: (a) GUI for the HSC recording and monitoring software with intergraed metronome **(b)** Prototype metronome system.

4.3.1 OCT Acquisition and Control

The OCT Acquisition and Control system software was based on demonstration software provided by Santec, but this was only really intended to show the capabilities of the OCT system. Considerable modification was required to fulfil the requirements of the scanning regime. The OCT software acted as the master trigger for the capture process. When imaging was started the program would synchronise the start of the HSC program and the metronome by passing commands though a data pipeline similar to the master data control program. OCT data capture was defaulted to 27fps and a horizontal pixel density of 1019 and a vertical of 500 pixels. Each individual frame was time locked to within 20ms of the reference source when accounting for the differences of capture frequency of both systems. The OCT was capturing at 27 fps and the HSC 15 fps so a beat frequency was needed to lock the timing together. The OCT program also provided master control for the length of the capture process; a series of 400 frames (25s approximately) was the normal capture duration. Three blinks were required to be imaged with the best two selected for further processing. The software displayed A and B scans simultaneously. A data player was included to check the quality of recorded data or confirm adequate recording of required features. A live image display mode was included to show a real time image of the target without recording data. Similar to the HSC program this was designed to allow the practitioner to align the subject before recording was commenced. Scan position (3 o'clock, 6 o'clock etc…) was also selectable involving both realignment of the system but also changing the sweep characteristics of the galvanic mirrors so the scan was perpendicular to the lens edge. Figure 4.11 shows the graphical user interface of the software.

4.3.2 User Control of the Imaging Process

The practitioner was required to observe both OCT images and HSC images simultaneously at the point of capture. This was best achieved by panning across a multiscreen desktop and glancing between each program while data was captured. The practitioner's hands were freed to control the slit lamp base to provide proper alignment give micro corrections and insuring adequate FOV throughout testing. With a single screen system it becomes difficult to navigate between windows effectively while correctly operating the alignment system. Figure 4.12 shows the multi-desktop arrangement

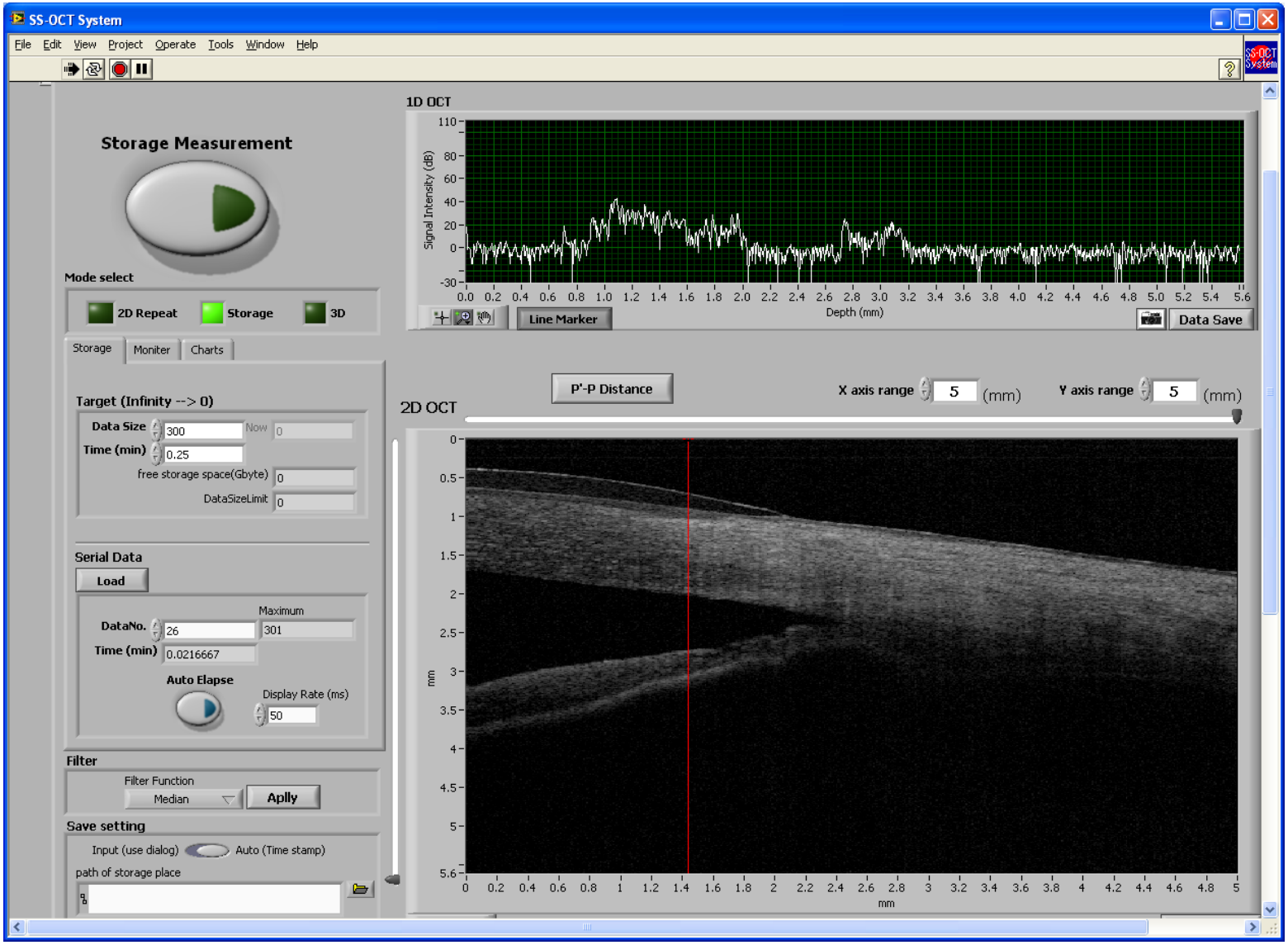

Figure 4.11: OCT control software GUI, B and A scans displayed.

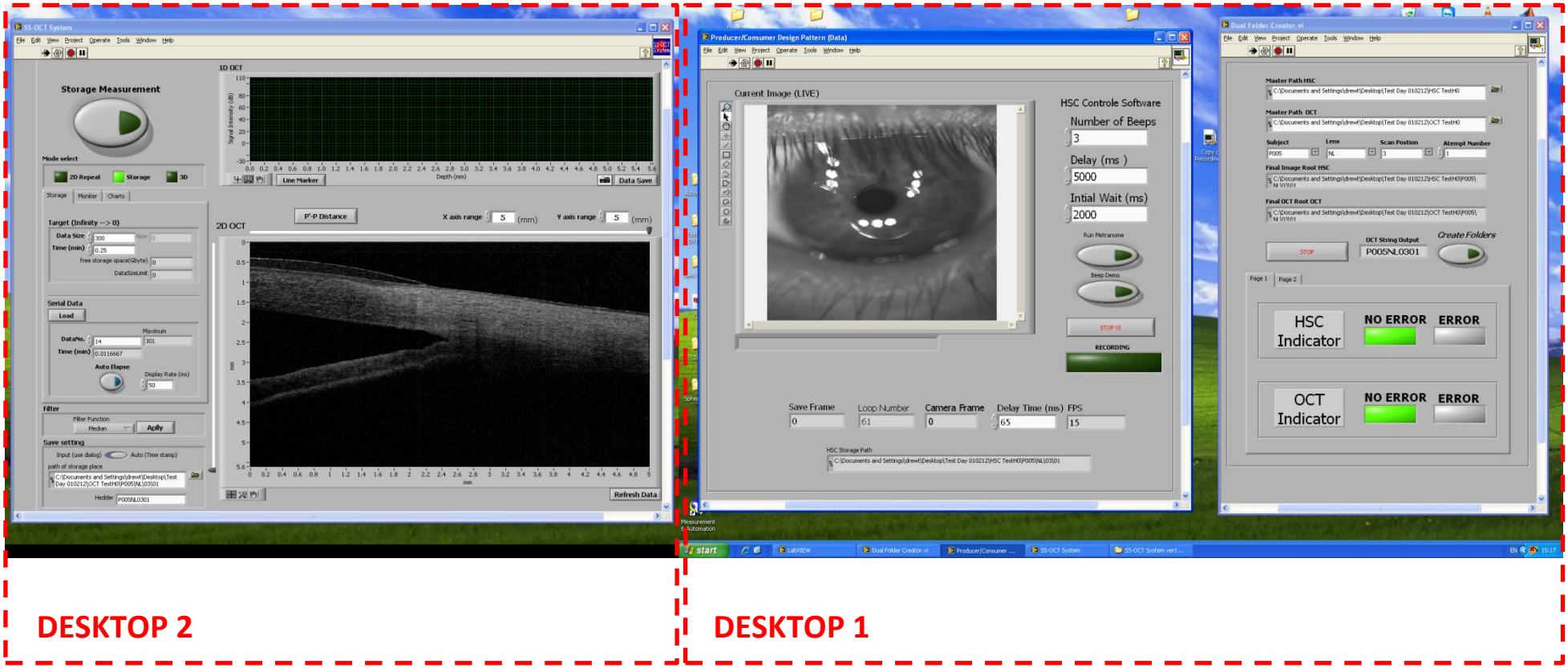

Figure 4.12: All three software systems running simultaneously, spanning across a dual screen system for ease of operator use.

4.3.3 Data Recording Speed and Random Access Memory Buffering

The HSC was required to record images with a frequency appropriate to match the temporal frequency of the B scans from the OCT system. A recording speed of 27 fps was the target for the HSC capture system. The recording of a data stream was limited by any bottle necks in the system, specifically in this case the digitisation and saving of the raw data to the system hard disk drive (HDD). Image compression and storage format can reduce image capture rate by consuming considerable processing overhead. A loss less PNG recoding format was selected after testing indicated good recording rate and minimal processing overhead.

Considerable bottlenecking was discovered in recording the images to the computer's hard drive. Figure 4.13 shows the recording speed in Hz and the types of media used. Initial testing with the standard 7200rpm mechanical hard drive supplied with the computer indicated a maximum recording speed of 3fps and a data throughput of 67Mb/s. A 120 GB solid state disk (OZC Vetex, OCZ technology, San Jose, California, USA) operating in the internal 3Gs/s Serial Advanced Technology Attachment (SATA II) channel was tested. A frame rate of 7 fps was achieved and a data throughput of 300Mb/s. Greater bandwidth was provided by directly accessing the high speed data bus. A 50GB Peripheral Component Interconnect Express (PCIe) Solid state HDD was tested on the 8 times second generation interface 8 Gb/s (OCZ RevoDrive, OCZ technology, San Jose, California, USA). Frame rate of 9 fps were achieve and a data throughput of 500Mb/s.

9fps was still deemed insufficient for HSC recording. A standard approach to increasing recording speed it to use networked parallel drives recording on different channels simultaneously to share the load. National instruments recommend a 10 disk Redundant Array of Independent Disks (RAID) allowing full frame rate capture. Such a system would add considerable cost and bulk to the solution. The fastest data throughput on a computer system is the RAM. A novel technique of buffering the data steam for the HSC was developed. Images were passed directly to a segmented section of the system RAM effectively buffering the data stream. Frame rates of 28fps were achieved with this method. As the RAM is limited to 4GB on a 32 operating systems such as Windows XP, only 2 GB of data could be diverted to buffering leaving a further 2GB for the operating system to index. Data capture was limited to 400 frames at a frame rate of 28 per second giving approximately 70 seconds of recording before the RAM will experience a stack overflow. After capturing, the data was recorded using the normal system HDD and the RAM purged. A final recording rate of 15 fps was chosen to reduce the burden on the RAM and free up more for the system memory. 60 seconds of recording space was deemed sufficient for scanning and provided no problems throughout subject testing.

4.4 HSC Analysis Software

The HSC camera produced vast amounts of image data. Each individual raw frame in an uncompressed state could consume 5mb of hard drive space. At a full capture frequency of 60fps there would be a requirement for 300Mb of space per second of recording. The frequency of 15Hz was determine to be affective for measuring contact lens fall as it was at least twice the capture frequency of many digital slit lamps (CSO CL990, CSO, Scandicci, Italy) . The novel RAM buffering discussed previously allowed a normal PC to handle the data throughput without significantly affecting the available bandwidth on the mainboards digital system BUS (bizarrely no definition of the acronym could be found!). Without sufficient bandwidth the OCT and HSC program would not be able to run in parallel.

The requirement was to be able to determine the fall of the lens over the eye and its associated movement in the X and Y plane with simultaneously mapping of the velocity profile. Both displacement and velocity profiles could be determined providing a complete definition of each lens types dynamic properties.

A datum was required to determine a coordinate system that will remain unchanged with time so lens fall could be compared to a stationary or affectively stationary reference (datum) point. Lenses were manufactured with a visible marking on the lens surface that could be tracked. Tracking was relative to either the pupil or limbus centre to allow for head and small eye movements. Tracking these features dynamical and correcting the coordinate system as required for each image provided a calibrated Cartesian coordinate system to measure lens fall against. Figure 4.14 shows the process of measuring fall and pupil centre position.

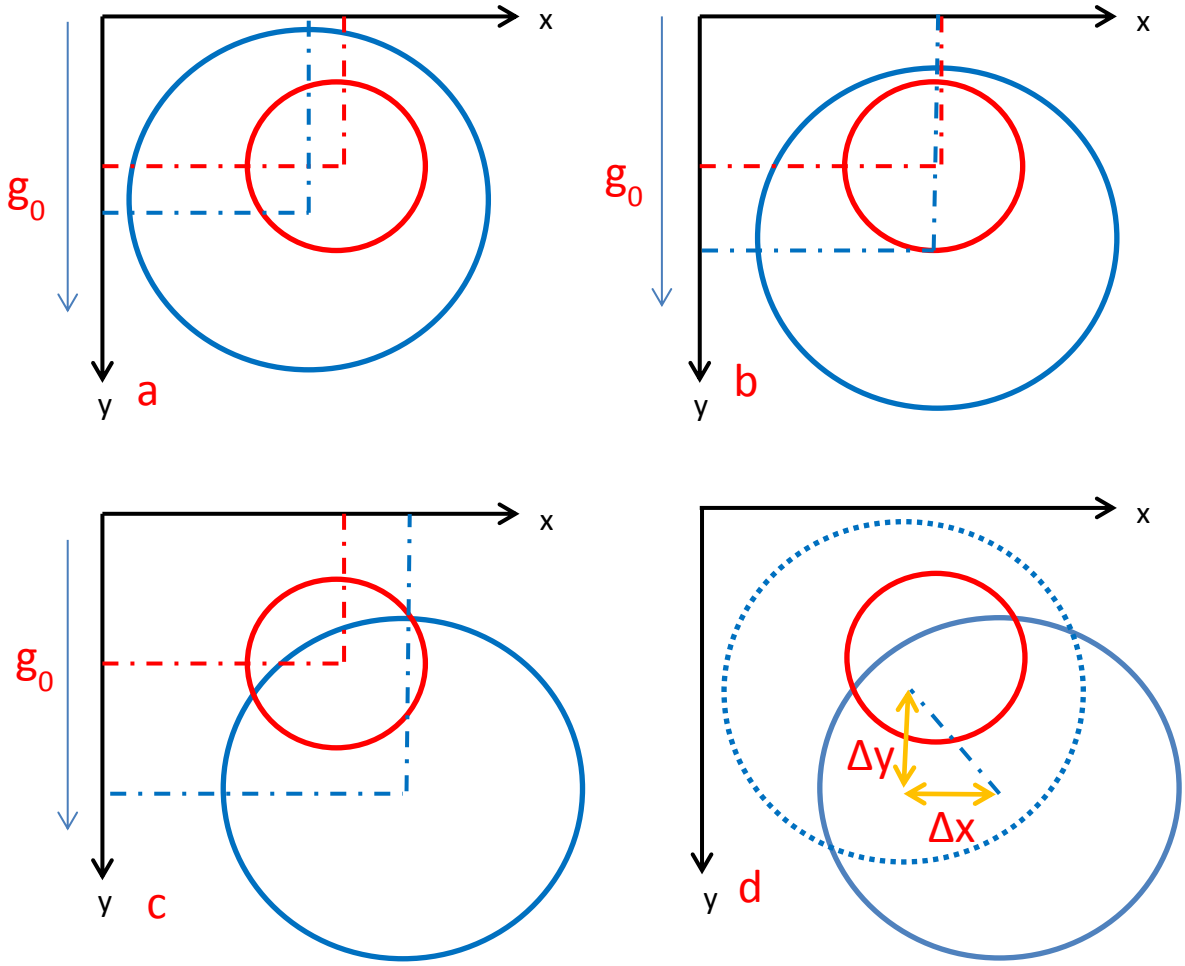

Figure 4.14: Algorithm developed for determining lens fall metrics. **(a)** Center point of both lens and pupil/iris is determined. **(b)** Lens starts to slip **(c)** Lens final rest position. **(d)** Change in both Y and X is determined and movement vector calculated. Start position is detailed by dotted circle.

A custom software package was developed that allowed an operator to define the lens marking and the pupil/limbus centre. The limbus center has been shown to be the more repeatable metric than the pupil center for determining central datum positions (Barry & Backes 1997). A set number of frames could be advanced through to the next image and the marking repositioned as required. The first frame was selected immediate post blink with the lens at its highest position and was measure

ed every 5 frames until the next blink was observed. Nine measurement points for lens fall coordinates were taken for each blink. Two blinks were recorded and analysed for each scan. The graphical user interface for the software is shows in Figure4.15. The software also included image manipulation tools for varying contrast, brightness and gamma of the displayed image allowing the operator to enhance the image if edges were difficult to see. The software allowed the operator to select each blink independently and to record the data to an external measurement file. After analysing two blinks the operator would write the files to measurement launching an external window where the mathematical analysis of the data being undertaken was displayed. The analysis program plotted the lens fall data with respect to time and fitted the data to an exponential function with the least squares method so decay constants could be determined. Equation 4.1 shows the fitted function with 'y' relating to time, 'a' relating to amplitude and 'b' to the damping coefficient.

$$\boldsymbol{y = a\, e^{bx}} \quad (4.1)$$

Figure 4.16 shows the analysis program with data and fit displayed. The analysis program returned damping for each coefficient, max lens displacement for the X and Y planes and time from onset of lens fall until the lens became stationary and no longer displayed any movement. The operators could check to see if the fit of the function to the data appeared good and if deemed to be insufficient, the image analysis could be repeated. As with the OCT data both programs were designed to be run in parallel and on a multi desktop machine to aid operator efficacy. Figure 4.17 shows the system running in full analysis mode on a dual screen system.

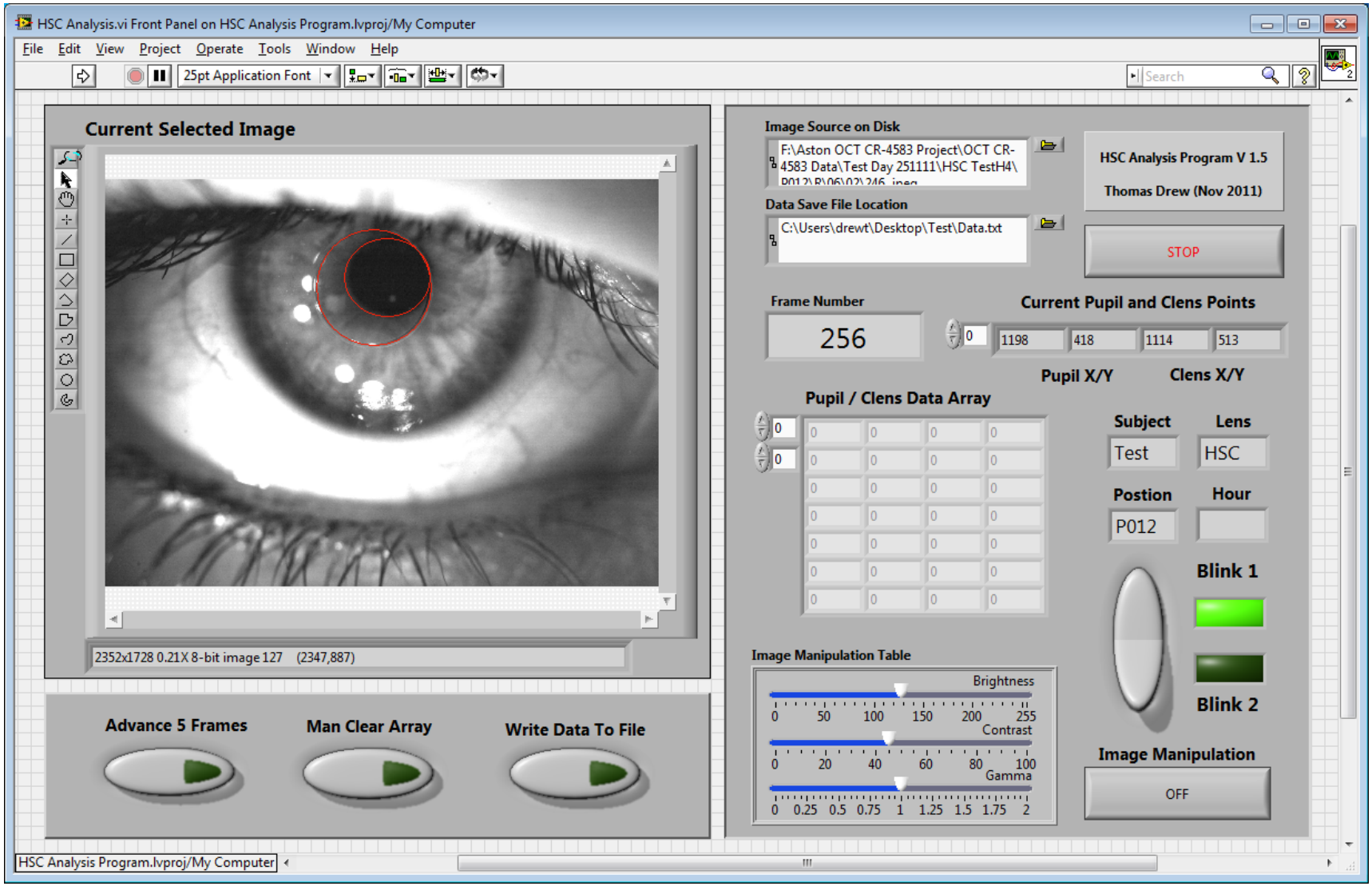

Figure 4.15: HSC lens fall analysis program, pupil edge and lens marking edge can clearly be seen. The program includes basics image manipulation tools to optimise the images for viewing.

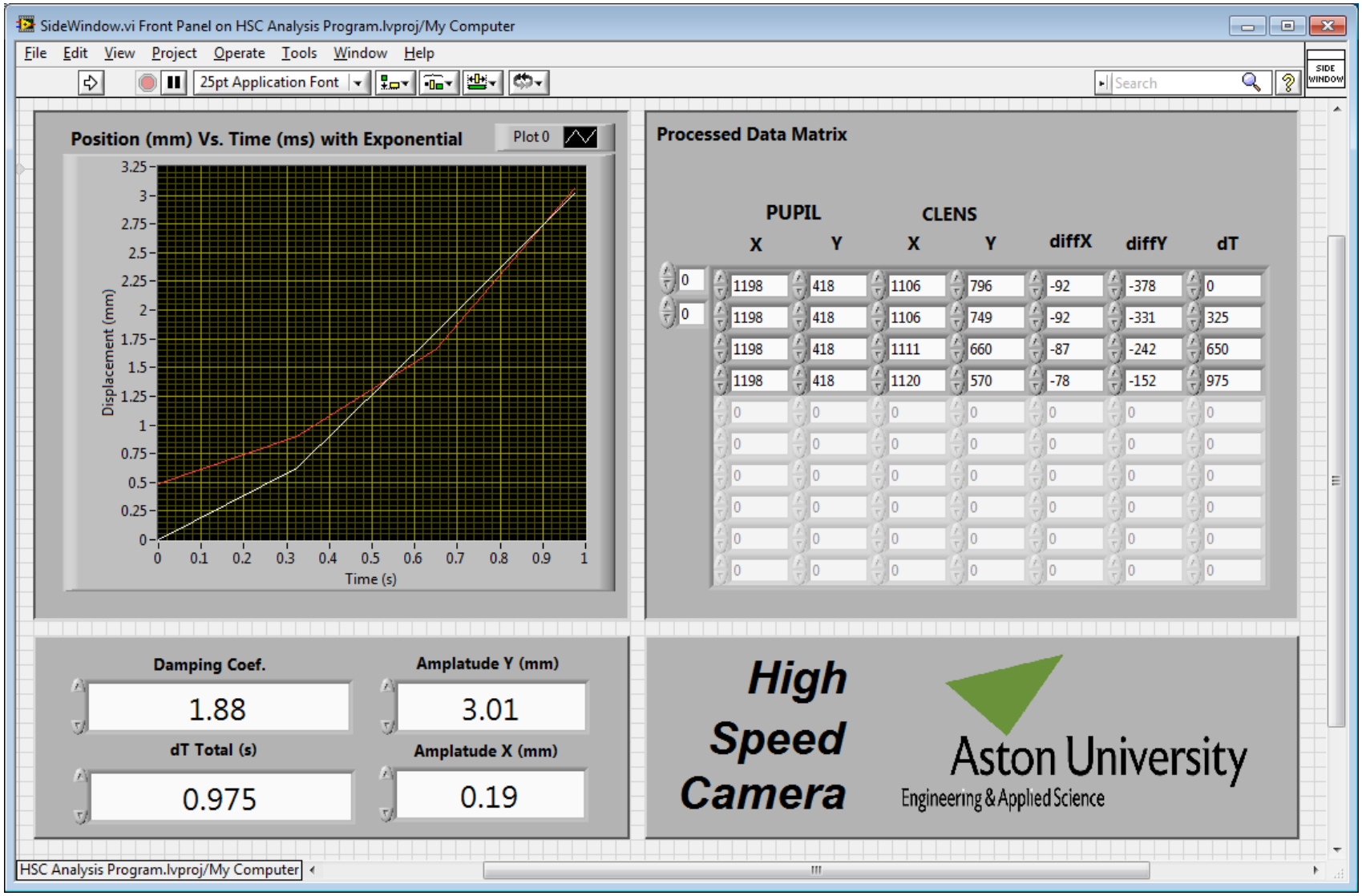

Figure 4.16: HSC companion program for fitting exponential curves to data.

Figure 4.17: Dual screen set up for HSC analysis program. The user can see both interfaces simultaneously aiding efficacy.

The no lens condition had only one relevant point that can be inspected between the stroma and Bowman's membrane. Any voids detected were measured for their maximum size and assessed for how long they lasted. If the void was still present at the end of imaging a not applicable grading was given stating the void lasted at least as long at the inter blink period of at least five seconds. A custom software solution was developed that decoded the OCT system data files and applied post processing as appropriate. Any frame from the image data set could be selected individually or viewed as a series of moving images. Upon selecting the appropriate start and finish points for the voids, the programme exported the required data to the analysis program where void size at its maximum size was assessed. The maximum size of the void in both the X and Y plain was recorded, the class of void and its duration. The final analysis program developed was to quantify the voids as discussed in the void section previously. Figure 4.18 shows the void analysis program GUI.

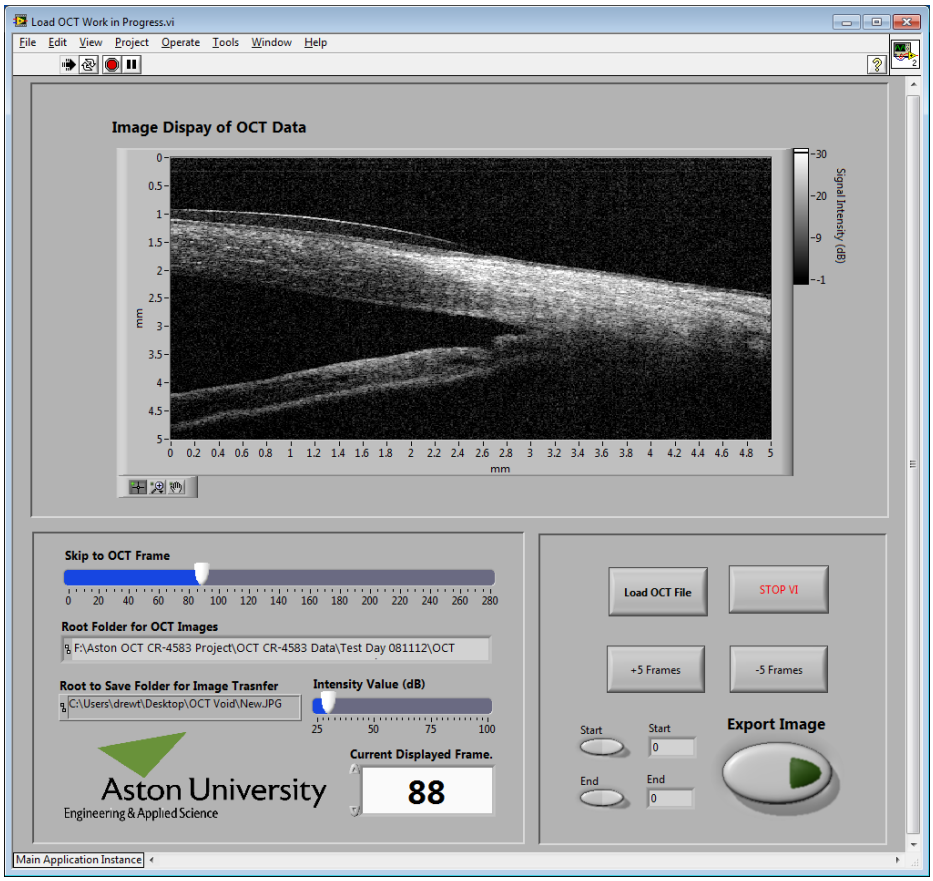

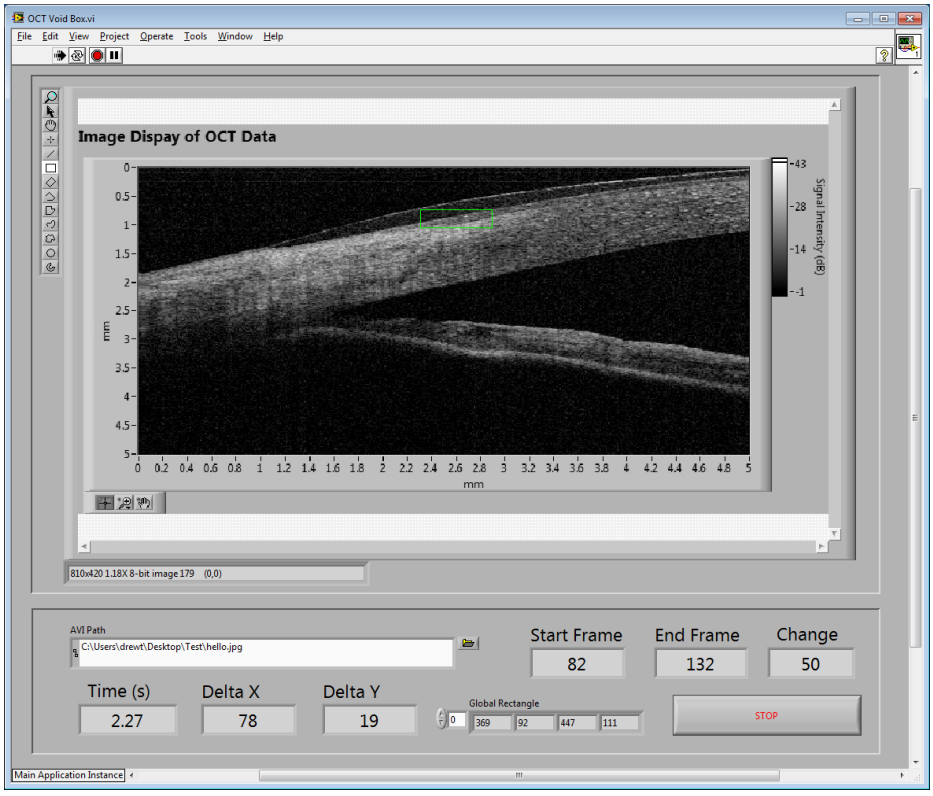

Figure 4.18: The void analysis program.

4.5 Image De-warping and Post processing

All OCT systems inherently suffer from some form of distortion in the images captured. Depending of the optical design of the system, errors can be segmented into four areas:

- Perspective correction (Imaging curved Surfaces)
- Non-linear lateral scanning (mirror correction)
- Non-linear laser sweep (different power output at different wavelengths)
- Refractive Index change at boundary Interfaces.

There of the above problems are discussed in detail by Volker Westphal's paper on the subject (Volker et al. 2002).Non-linear axis scanning is produced by a non-linear sweep of the reference arm. Santec's HSL-2000 is a high quality swept source laser, its primary design function was for the testing of optical fibre communication systems. A Study by Yoshiaki Yasuno (Yasuno et al. 2005) has investigated the suitability of the light source for use in ophthalmic imaging. It was concluded that the system is highly capable, displaying a central wavelength of 1310nm, a scanning range of 110nm and scanning rate of 20KHz. The light source was concluded to be stable, linear and suitable for ophthalmic imaging. A second study by Chanhgo Chong (Chong et al., 2008) assessed the linearity of the light source. They concluded that the sweep linearity had less than 0.25%, wavelength jitter was less than 0.1nm and the scan reliability was stable over a temperature range of 10-40 degrees centigrade over 8 hours. The light HSL light source is highly linear and requires no further correction for ophthalmic OCT imaging.

Differences between the refractive index of the media the light passes through in the sample under scan will cause refraction and reflection of light. Light traversing a refractive index boundary (representative of the soft tissues boundaries in the eye) will refract in accordance with Snell’s laws of refraction. In ophthalmic applications this means rays will refract towards the optical axis of the system. A study of distortions in OCT systems by Adian Podoleanu (Podoleanu et al. 2004) concluded that optical distortion is more pronounced towards the periphery of the scan range and that axial is worse than lateral error. In an ophthalmic setting some of these issues can be minimised. Primarily the combination OCT system is concerned with looking at the contact lens cornea interface and the corneal epithelium. Therefore correcting for errors that are only pronounced at deeper penetration depths of the scan is of less importance.

In the context of the OCT system and investigation requirements, de-warping will concentrate on the following areas: non-linear mirror sweep, refractive index differences and perspective correction.

4.5.1 Refractive index Correction

Commercial OCT systems such as the Zeiss Visante (Carl Zeiss AG, Oberkochen, Germany) have integrated refractive index de-warping based around surface detection and de-convolution algorithms. Detection of the corneal front surface, contact lens front surface and lens-cornea interface is required for full de-warping. Optical properties of the contact lens are taken as 1.42 (data from Chapter 5) and the corneal as 1.375 (Tuchin 2007) . After testing with phase 1 data, a similar approach of full surface detection was attempted. The Santec OCT systems high frame rate and contact lens movement made dynamic detection extremely difficult and sufficient algorithm robustness could not be achieved. A more simplified approach of simply correction for the path length difference for light transmission though media with different refractive indices. Although not perfect, the system will provide a good approximation to surface detection based de-warping.

As the outcome metrics of the study are relative differences with time and in the same person with different lenses, therefore the importance of precise de-warping of the whole image is less critical.

4.5.2 Calibration of OCT system

A system for calibration of OCT images and determination of the relationship between on screen apparent size and real word metrics was developed. Both lateral, axial and curvature deviance was assessed. Objects with known parameters can be used to de-warp the OCT image and relate positions, sized and curvatures to within a predicate level of certainty.

4.5.3 Lateral OCT calibration (X Axis)

It is known that OCT images can become distorted towards the proprietary of the image plane due to effects associated with de-warping. The normal X axis scan range was between 3 mm to 5mm for the study so a value of 5mm was selected for the dewarping testing.

Custom software was developed that allowed the measurement of distance between edge effects in OCT images to be determined with high accuracy and repeatability (>10µm). Figure 4.19 shows the software in use. A high accuracy, grade A, slip gauge set was used for testing. Accuracy of the slip gauge is at least one order of magnitude better than the OCT system resolution having a bilateral

tolerance of 0.15µm. A series of 9 gauges are used in testing ranging from 0.5mm to 4.5mm in 0.5mm steps, with each test repeated 3 times. A custom holder was developed allowing the gauge block to be held in place and attached to the slit lamp head rest aiding quick and uncomplicated testing and rapid gauge changing. Figure 4.20 shows the custom holder and selection of gauges. A specular reflection from the surface of the gauge is clearly visible in Figure 4.19. This confirms the block top surface is parallel to the X axis of the OCT system. This specular reflections drop off quickly when the block is not in good alignment. The software automatically compensates for small offsets between the X axis and the gauge block surface plane. Figure 4.21 shows the results graphically.

An average of 148 pixels per mm was determined to be the correct ratio for the OCT system in the X axis. The value was used in subsequent computer software when determining factors relating to contact lens measurements.

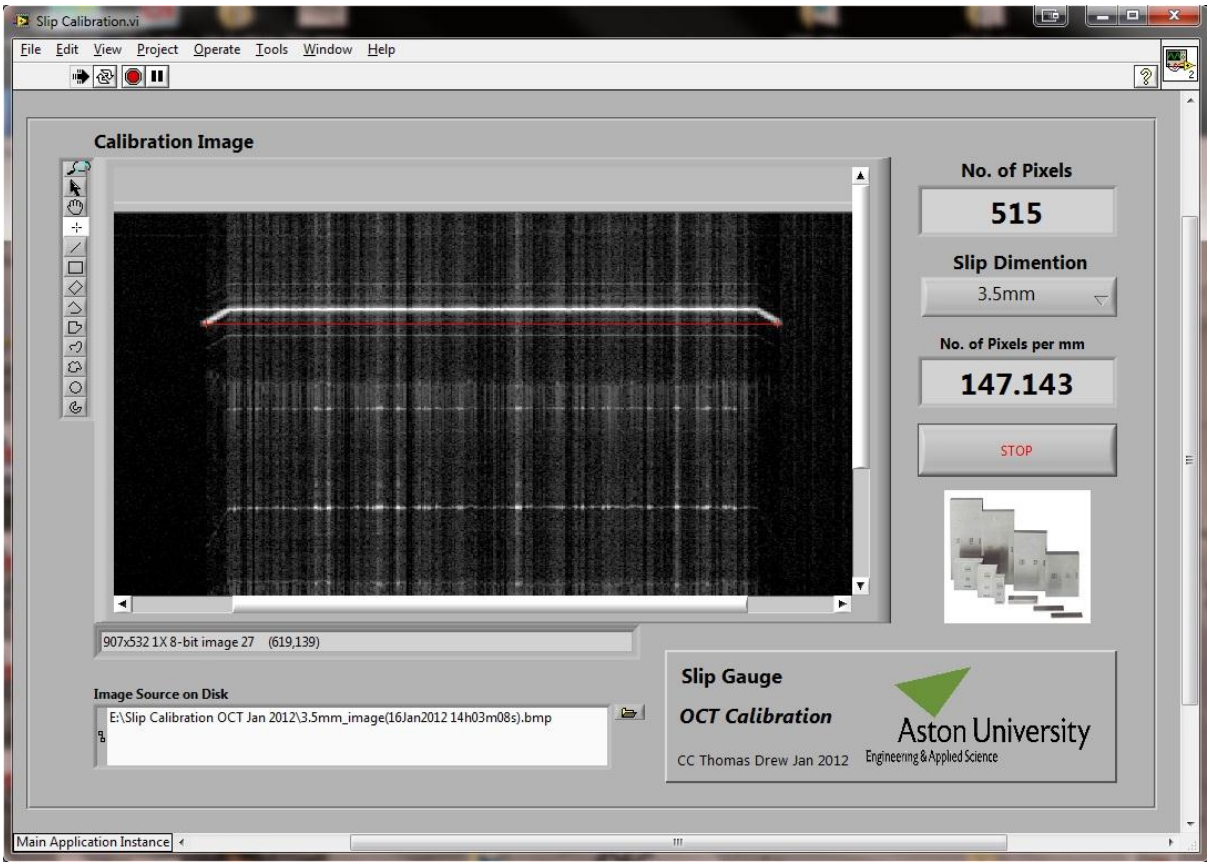

Figure 4.19: The OCT slip gauge calibration program imaging a 3.5 mm clip gauge. The specular reflection is also present in the image.

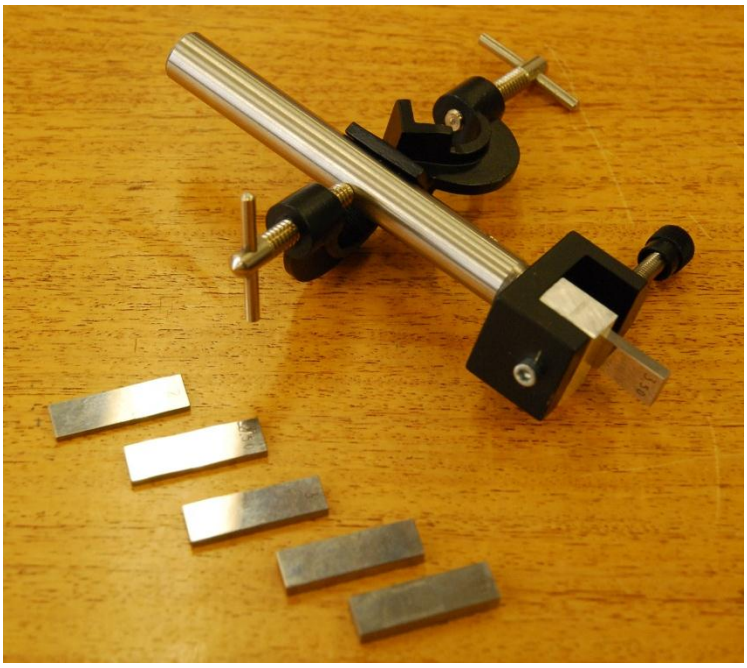

Figure 4.20: The slip gauge holding attachment and a selection of slip gauges.

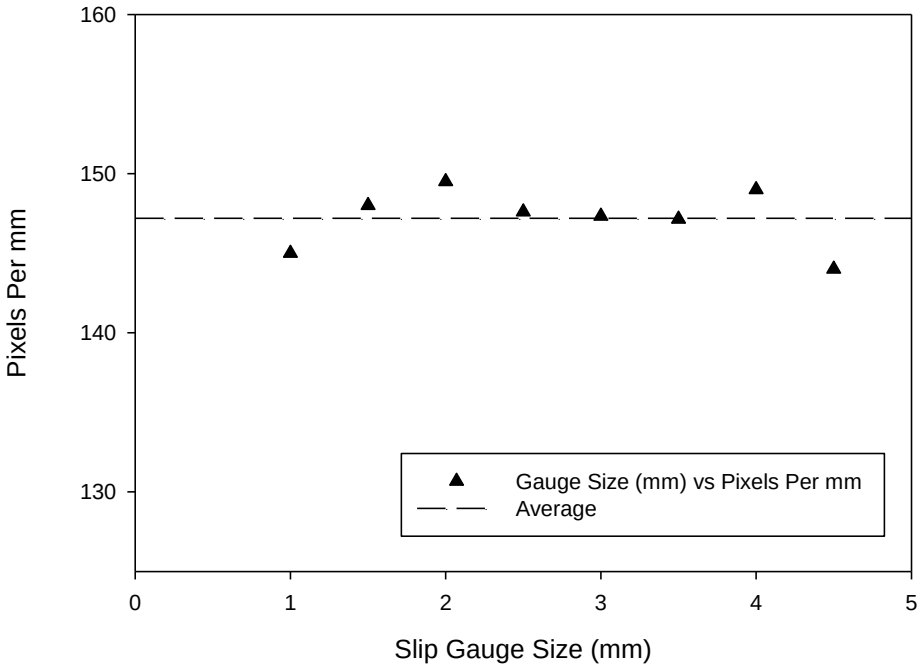

Figure 4.21: Graph of the calibration testing results, an average of 148 pixels per mm is indicated. Errors bars shows the error in OCT sampling resolution (7 microns).

4.5.4 Axial OCT Calibration (Z Axis)

Calibration in the Z axis is considerable more complicated than in the X axis. The requirement to both consistently image the penetration of the laser in sample, and measure artefacts of known size and geometry presents unique problems. Phantom OCT targets were developed in house giving a series of artefacts at known penetration depths that are visible when imaged with OCT swept source systems operating at the 1310nm wavelength. Typical phantom scans are shown in Figure 4.22. The phantom was fabricated from a Fused Silica substrate that had been selectively internally modified with a pulsed femtosecond laser. Highly focused laser light is fired into the internal structure of the BK7 material in a series of ultra-short but intense pulses. The extreme energy dissipated in the glass forms a small sphere (approximately 10 µm -20 µm in diameter) of new material. Specifically the arrangement of atoms in the structure is modified giving a material with a different refractive index change when compared to the surrounding medium.

When the OCT scan hits these spheres, refractive index differences produces a Fresnel reflection. Producing a strongly scattering artefact on the OCT display. Any series of lines, grids, helixes or matrix patterns can be drawn. Our device was a series of lines produced by overlapping spheres giving a tunnel or tube shape that extended into the Y axis of the OCT system (projecting into the page).

Patterns with a Z axis spacing of 50µm or 75µm were fabricated for testing OCT resolution in the Z plane. The lines are not always visible to the naked eye but are highly viable under cross polarized lights due to their strong bifingnence. Testing was repeated 3 times with each phantom and the data correlated. Figure 4.23 shows the results graphically. An average pixel to mm conversion factor of 140.95 pixels/mm was determined; this shows good coloration with the lateral calibration agreeing within 5%. A value of 141 pixels/mm will be used when referring to Z axis depth penetration.

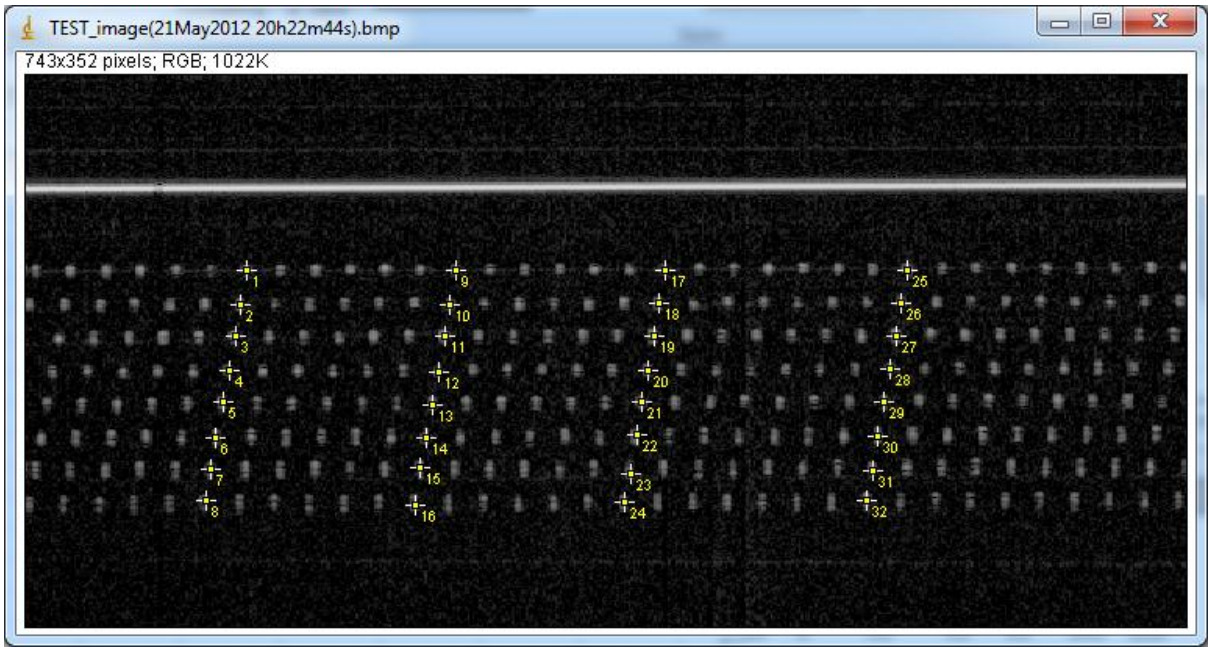

Figure 4.22: Custom designed phantom target with laser etched lines (moving though the page) line spacing is either 50 micron or 75 microns depending on requirements. Yellow numbers show point selections for later analysis.

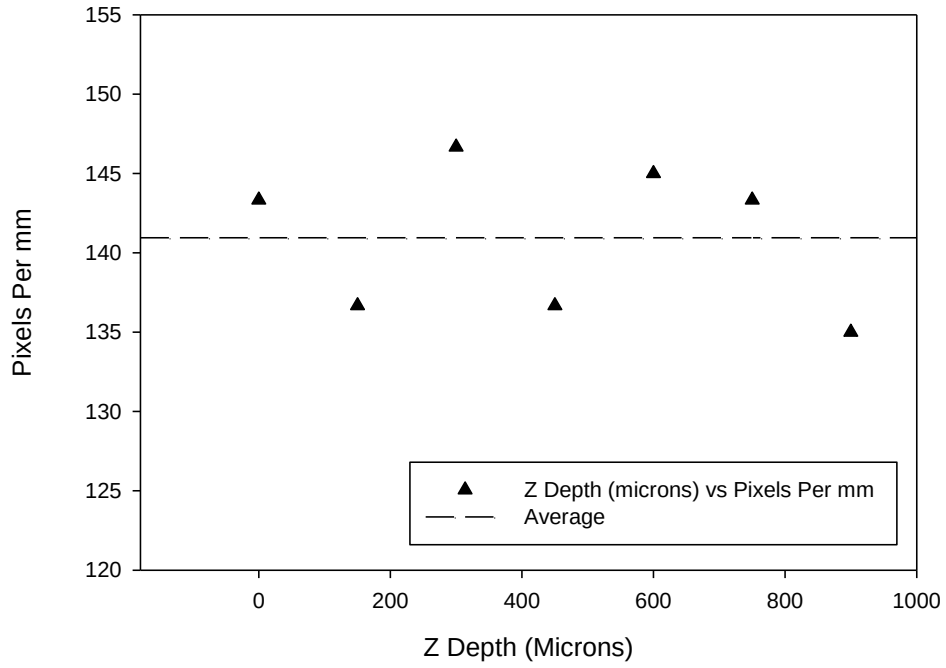

Figure 4.23: Z axis (depth penetration) calibration results graph, a value 140.95 pixels per mm average was indicated and will be used for calibration. Error bars represent know error of sampling system (7 microns).

4.5.5 Spherical Offset Calibration (Mirror Correction)

As described previously in the de-warping section, the changing length path of the light caused by mirror sweeping during the scan process will cause the OCT image imaging curved surfaces to flatten towards the periphery. With known lateral and axial calibrations it is possible to image reference spheres to assess the quantity of curvature offset present in the OCT system. Three chrome steel grade 10 precision ball bearings with radial tolerance of 1.3µm and surface roughness of 0.025 µm (Simply Bearings Ltd, Lancashire, UK) were chosen. Diameters of 12mm, 16mm and 20mm were used for testing. A custom magnetic self-centring holder was developed that aligned the apex of the ball bearing to the optical centre of the imaging system, shown in Figure 4.24 with the 20mm sphere attached. The device mounts in the same fashion and the slip gauge holder allowing for ease of use without removing the OCT system probe. The device was aligned with the probe using the specular reflection alignment technique discussed in the previous section. A custom software solution was developed that compared the scanned surface geometry of the reference spheres with an ideal mathematical model of the surface. Figure 4.25 shows the OCT scan of the sphere. Differences

between the ideal value and the images surface could then be assessed for different distances from the sphere apex. The green line in Figure 4.26 shows the ideal curvature of the surface that exactly matched the real world geometry of the calibration sphere. The vertical blue line represents the alignment to the specular reflection to the corneal apex. The orange vertical lines represent the points at which measurements of discrepancy were taken (300 µm spacing). As the mirror scans left and right sides of the apex (one full B scan represents a total sweep with the apex at the centre) both sides were assessed to make comparisons between each. Tests were performed 3 times with results shown graphically for the 12mm,16mm and 20mm spheres respectively in Figure 4.27. As expected the smaller radius sphere showed the most offset; 80µm compared to 45µm for 16 and 20 mm balls respectively as it represents the greater curvature relative to the image plane. The average cumulative error in microns for the total system over the X axis scan length of 3.0 ± 1.5mm. For contact lens scanning, the error between perceived and actual curvature should be less than 35 µm and is highly linear. The error represents less that 1/100% of the scan depth and therefore can be regarded as negligible when imaging contact lenses over such a small X sweep range. It should be noted, however, that the error will grow considerable when the X axis sweep range surface curvature ratio increases.

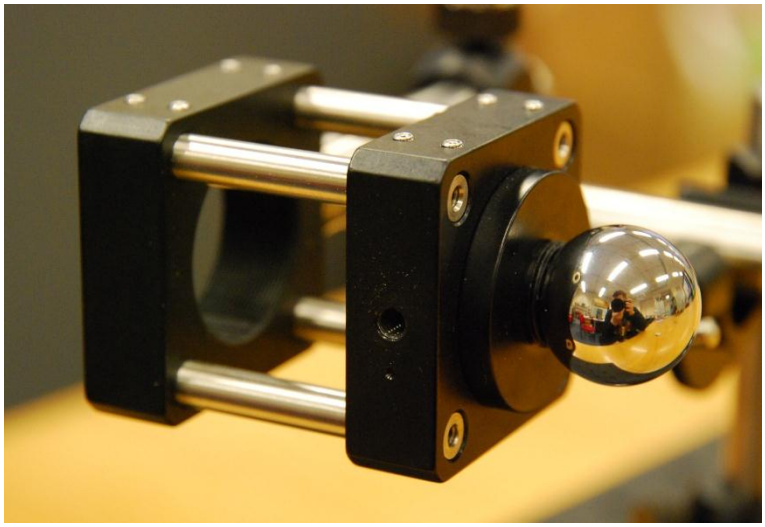

Figure 4.24: Self-centring magnetic calibration sphere mounting system. Capable of housing any size sphere required for system calibration.

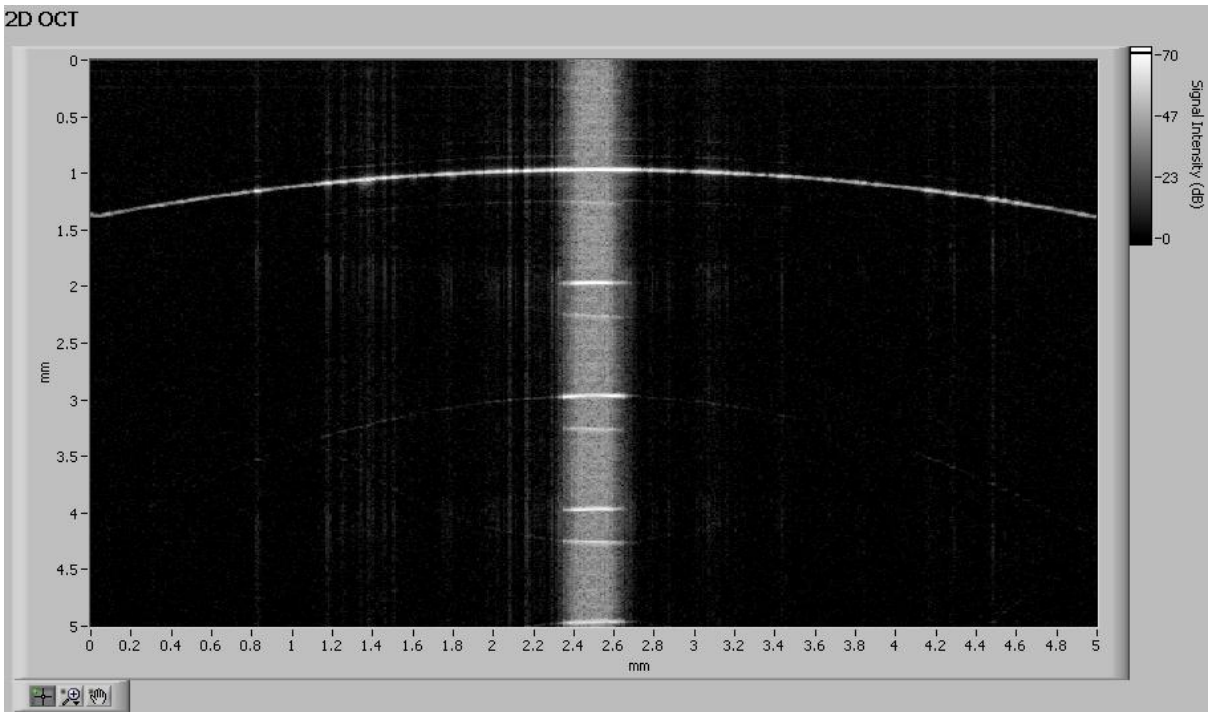

Figure 4.25: OCT scan of the 20mm calibration sphere; the specular reflection can clearly be seen.

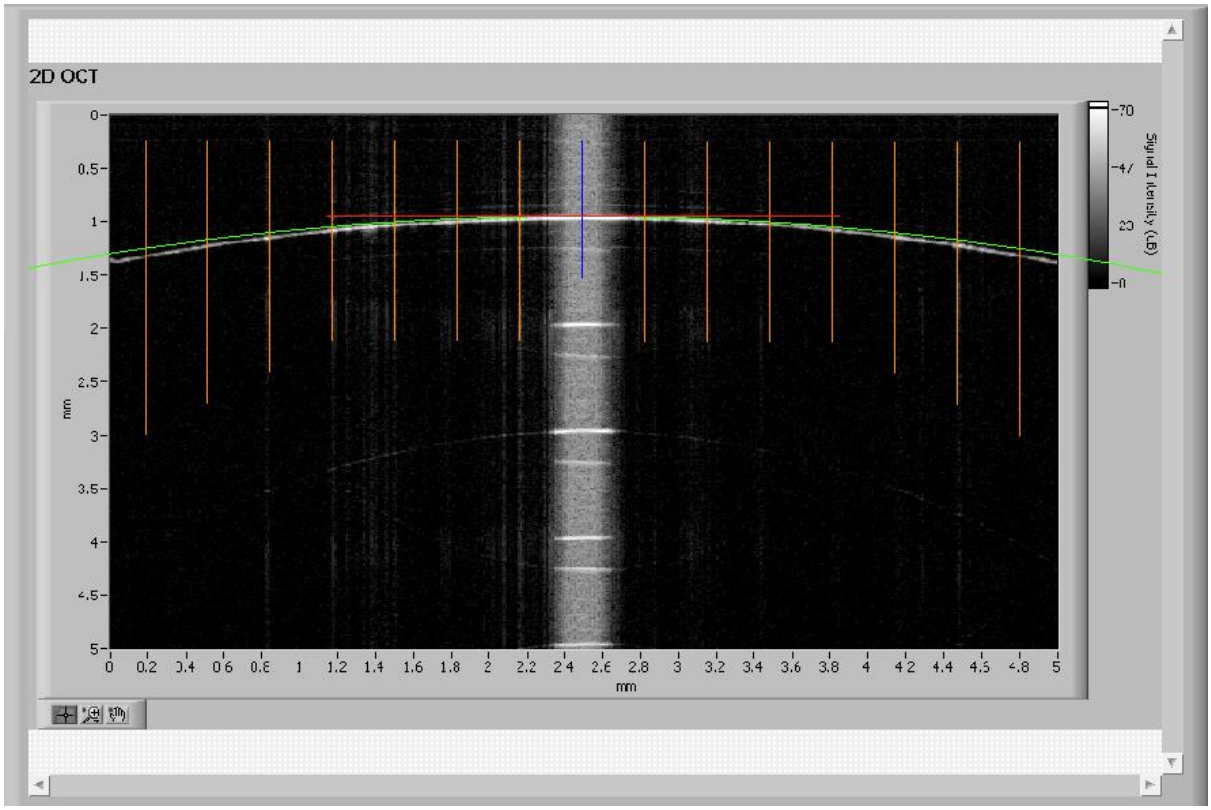

Figure 4.26: OCT scan of the 20mm calibration sphere (white line) and ideal curvature determine mathematically (green line). Vertical orange lines are measure locations.

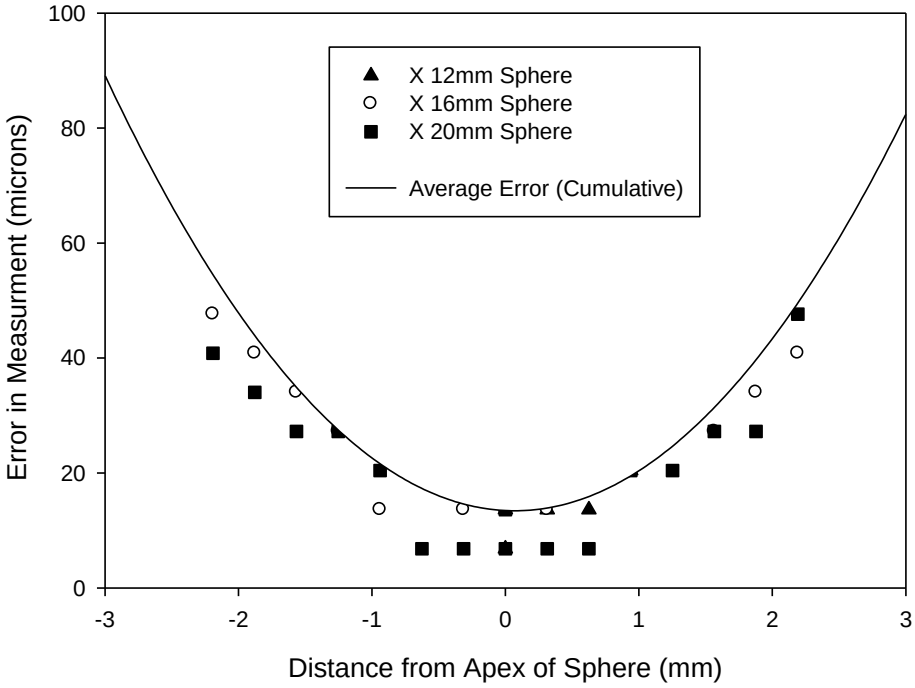

Figure 4.27: Sweep error for 12mm, 16mm, 20mm calibration spheres. The device shows consistent error that can be easily accounted for.

4.6 HSC Calibration

The HSC camera requires calibration to relate on screen features to real world measurements. The cameras focal length and magnification are fixed by using the lens retaining grub screws found on the focusing ring on the optics assembly. The cameras field of view (FOV) is changeable by altering the length of the extension rings. A minimum field of view of 12mm horizontally is achievable giving a pixel/mm ratio of 196pixels/mm equating to each pixel covering a section of 5µm-5.5µm over the cornea. However the depth of field is considerably reduced at this magnification. A minimum Nyquist limit of approximately 10µm-12 µm is achievable at this maximum resolution. Testing has indicated that a larger field of view and hence greater depth of field is more important than ultimate resolution for practical purposes. A FOV horizontally of 22mm and 19mm vertically was chosen after phase 1 results. Calibration regimes were required in the following three areas. 1.) Horizontal calibration, 2.) Vertical calibration and 3.) Elliptical off plane correction.

4.6.1 Vertical and Horizontal calibration

A custom calibration grid was developed allowing both horizontal and vertical calibration to be assessed. Figure 4.28 shows the calibration grid of white and black spots separated by 1mm spacing between centres produced on a professional CAD package (SolidWorks, Dassault Systems, Velizy-Villacoublay, France) and printed at high resolution and at a scale of 1:1. Custom software was used for image capture and ImageJ (Wayne Rasband, National Institute of Health, Bethesda, MD) for measurements each test was performed three times and averaged. Figure 4.29 shows the vertical grid calibration results.

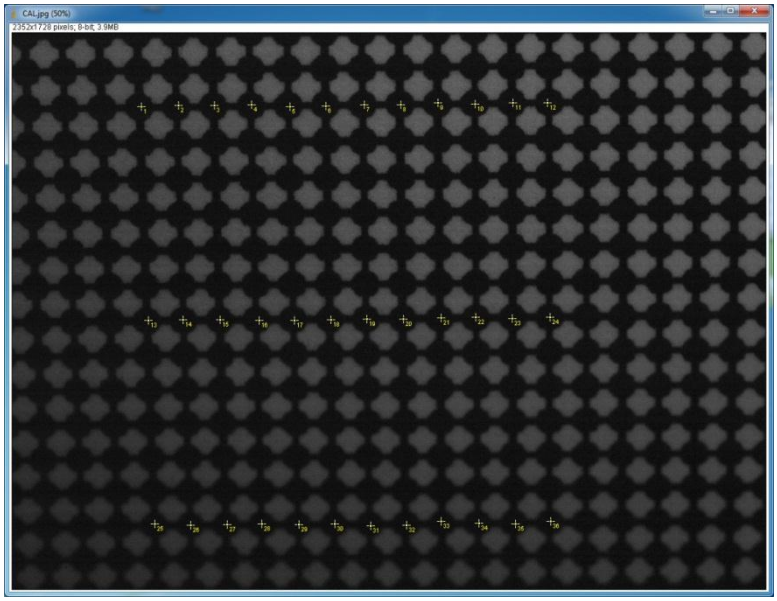

Figure 4.28: HSC calibration grid, yellow dots show measurement points.

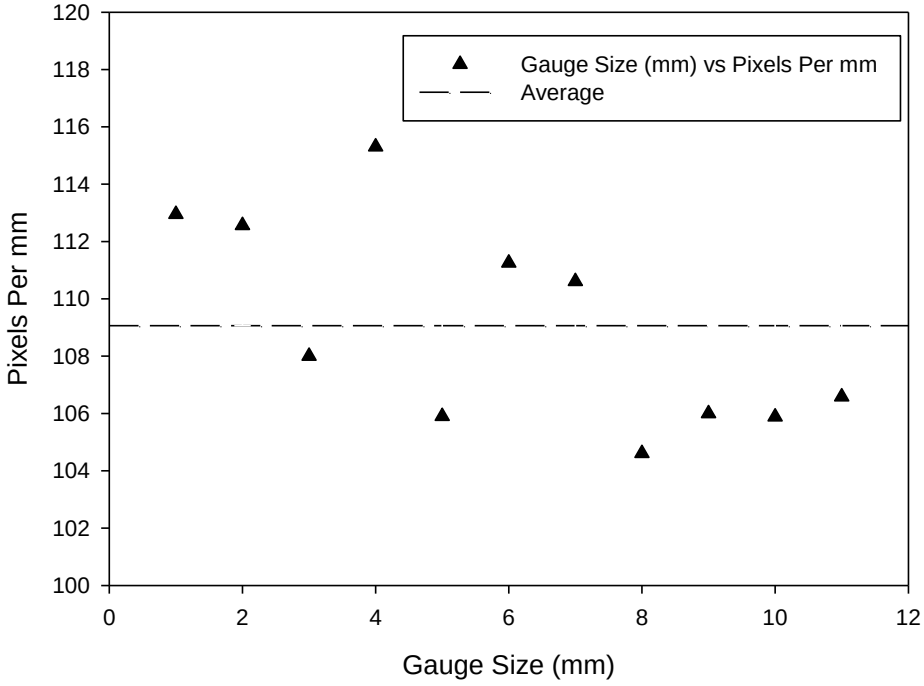

Figure 4.29: HSC calibration graph for vertical sections, average was 109.1 pixels per mm. Error represent error in measurement based on nyquist sampling limits (16 microns).

Vertical calibration shows an average pixel to mm ratio of 109.1pixels/mm that is in close agreement (<1%) with the theoretical results of 108pixels/mm at the stated horizontal FOV. Figure 4.30 shows the results from the horizontal calibration test. An average ratio was determined to be 114pixels/mm compared to a theoretical of 107pixels/mm, therefore results are in agreement with an error of 6%. The vertical calibration shows greater variation but this was expected because the camera is not imaging normal to the image plane hence the bottom part of the image plain is tilted away from the camera when viewing normally to the surface. The sensor plane is tilted away from the normal at an angle of up to 32 degrees when imaging, but only 8 degrees for calibration due to design considerations related to the dual imaging concept. Therefore magnification is not constant throughout the vertical meridian. An elliptical off plane correction factor was applied to correct for this error.

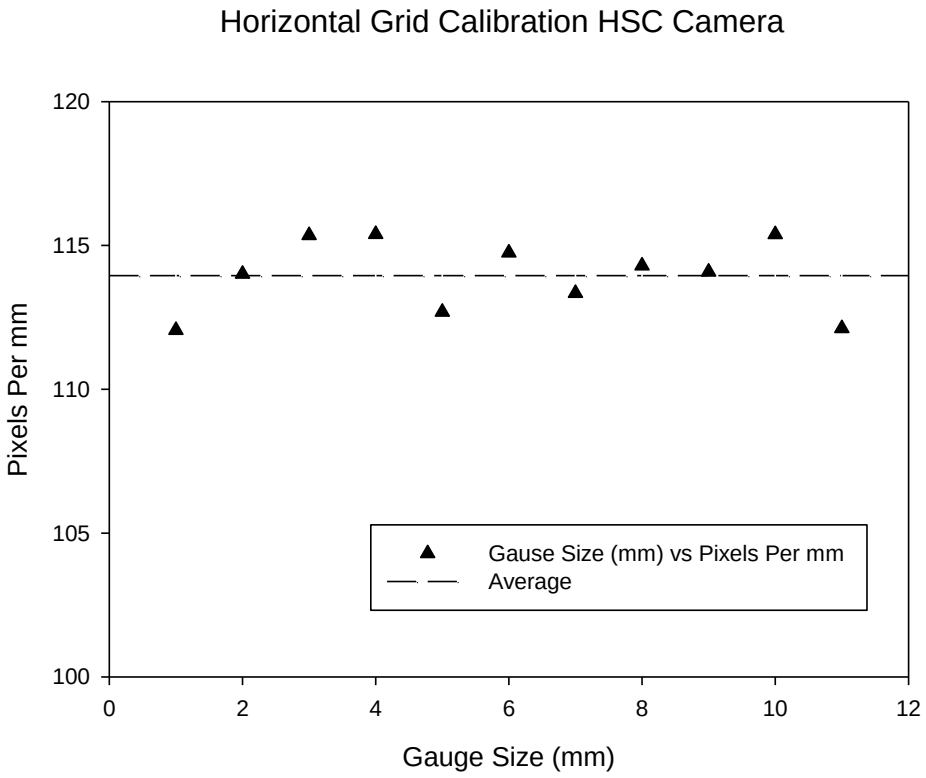

Figure 4.30: HSC calibration graph for horizontal sections, average was 114 pixels per mm. Error represent error in measurement based on nyquist sampling limits (16 microns). Horizontal was more stable than vertical as expected.

4.6.2 Elliptical off Plane Correction

The HSC camera system was located above the OCT probe and shared a common focal point and virtual pivot. Ideally both systems would be normal to the imaging surface (i.e. parallel sensor and image planes) at all times. Engineering constraints fitting both systems into a compact space make this an impossibility. The HSC camera was mounted on its own separate alignment platform, giving independent alignment and focus. An angle gauge gives an indication of the offset of the sensor plane with relation to the vertical position. This angle was noted in testing and was used to allow for subsequent image correction.

Apparent image size and true image size can be related via the plane offset angle. The greater the offset angle the greater the apparent distortion. When imaging a circular object the vertical meridian appears to become compressed while the horizontal remains unchanged. This turns a circle into an

ellipse. When applied to imaging the eye, circular contact lens markings and the pupil/limbus become elliptical and measurements and displacements made in the vertical meridian are no longer in scale with relation to horizontal measures. Figure 4.31a/b shows the effect of increasing offset angle on the eye imaging arrangement.

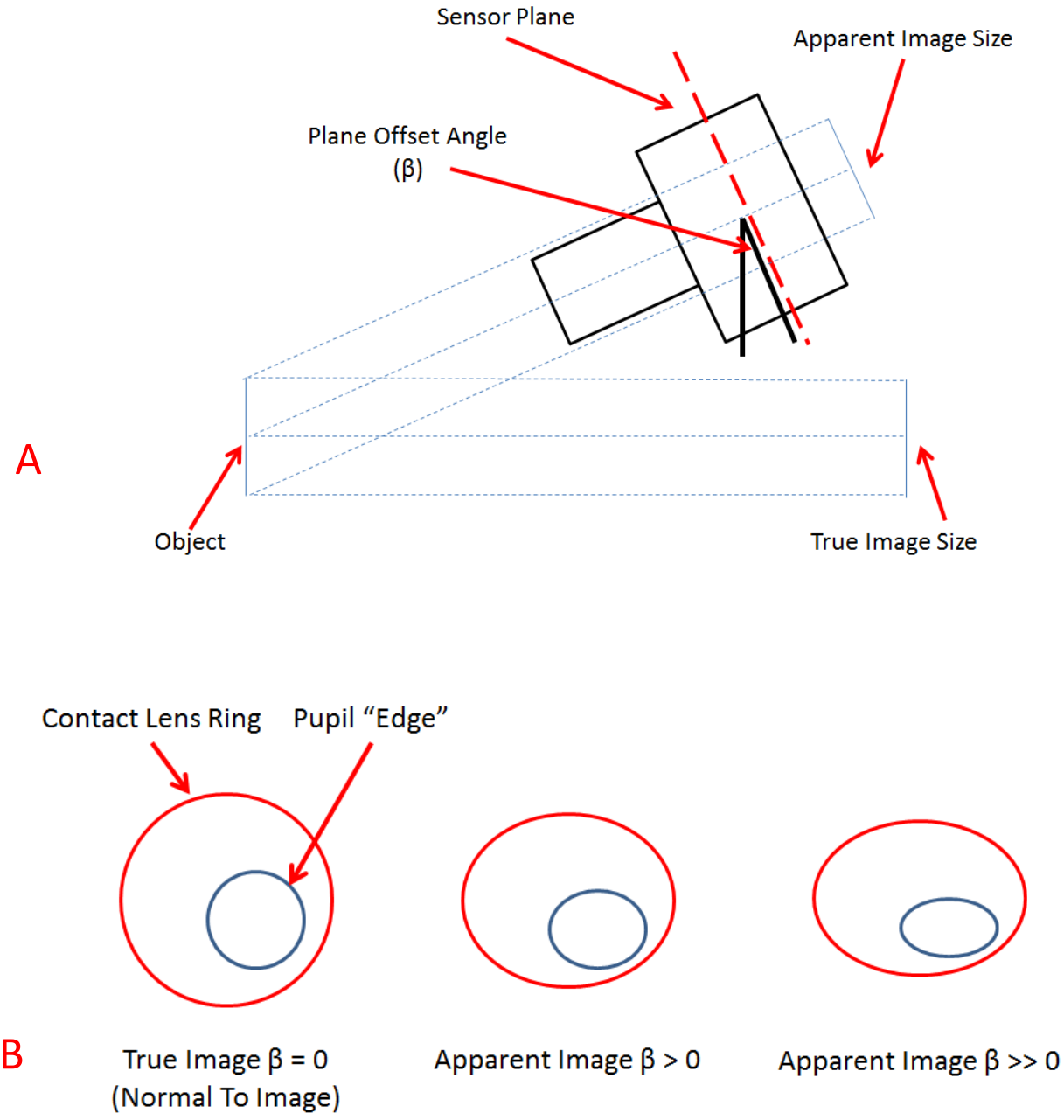

Figure 4.31: (a) Apparent image size change with plane offset angle and shows the coordinate system used. **(b)** Direct view of target (contact lens marking and pupil center), eccentricity is increases as plane angle increases.

It is necessary to create a calibration factor to relate apparent image size to true image size for the HSC imaging system. The relationship between sensor angle and eccentricity of the ellipse can be derived from first principles. Figure 4.32 shows the geometry of an ellipse and the arrangement of the major axis (a) and minor axis (b) with relation to the centre (C).

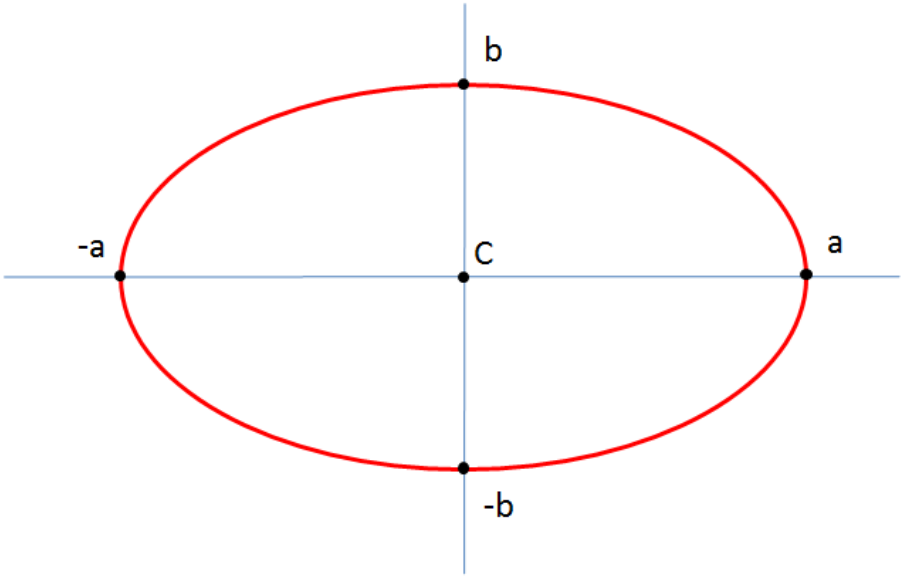

Figure 4.32: Geometric arrangement of an ellipse, the major axis "a" and minor axis "b" with relation to the centre "C".

The eccentricity of an ellipse can be can be related to the major and minor axis by the equation shown in Figure 4.33. Figure 4.34 the relation between sensor angle β and apparent size X /true size X is related by Equations 4.2/4.3/4.4/4.5. Sensor plane angle can now be directly related to eccentricity. The inverse transform relating eccentricity to sensor angle is stated in equation 4.5

$$\epsilon = \sqrt{\frac{a^2 - b^2}{a^2}} \quad \textbf{(4.2)} \qquad \bar{x} = x \cdot \cos\beta \quad \textbf{(4.3)}$$

$$\beta = \cos^{-1}(\sqrt{1 - \epsilon^2}) \quad \textbf{(4.4)} \qquad \epsilon = \sqrt{1 - \cos\beta^2} \quad \textbf{(4.5)}$$

Eccentricity to sensor angles can now be assessed over an appropriate range of sensor angles that are likely to be encountered in real world imaging conditions. Values between 0 and 45 degrees were chosen. Figure 4.33 shows calculated results and the near linear relationship. Physical testing has shown good results with theoretical conditions agreeing within 1%. It is more useful to assess the effect of sensor plane angle on the compression of the vertical axis of imaging. A calibration factor can be determined to transpose recorded displacements into real world values. Figure 4.34 shows apparent compression of the vertical axis with sensor plane angle. The relationship displayed is approximately exponential, but shows poor agreement when fitted with an exponential ($r < 0.75$) curve. A better description was a 3rd order polynomial ($r > 0.99$). Equation 4.6 and Figure 4.34 can now be used to correct measured values to real world conditions.

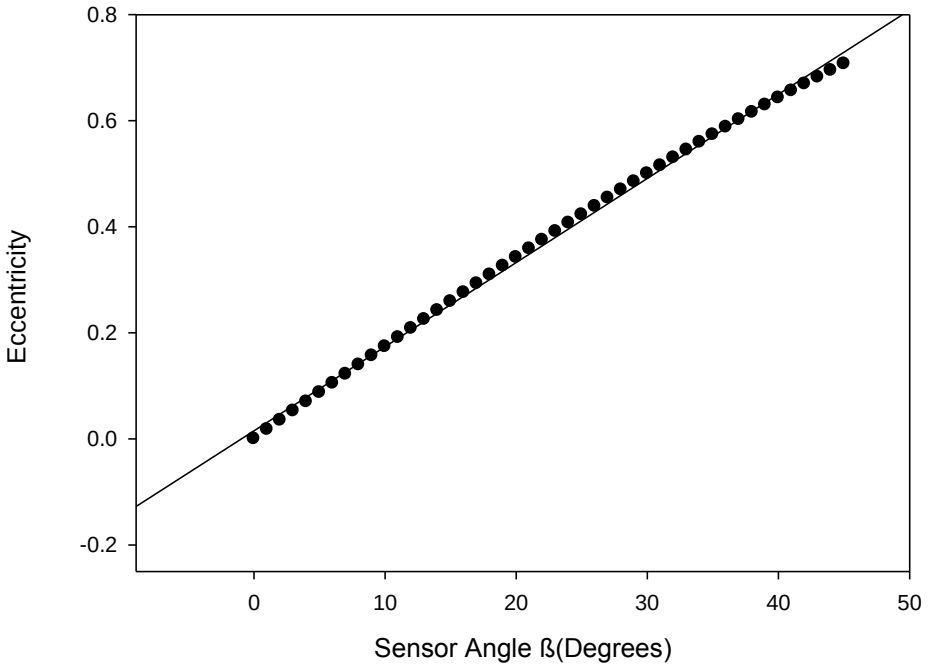

Figure 4.33: Effects of sensor angle on eccentricity of an eclipse is affected by sensor angle. Relationship is highly linear.

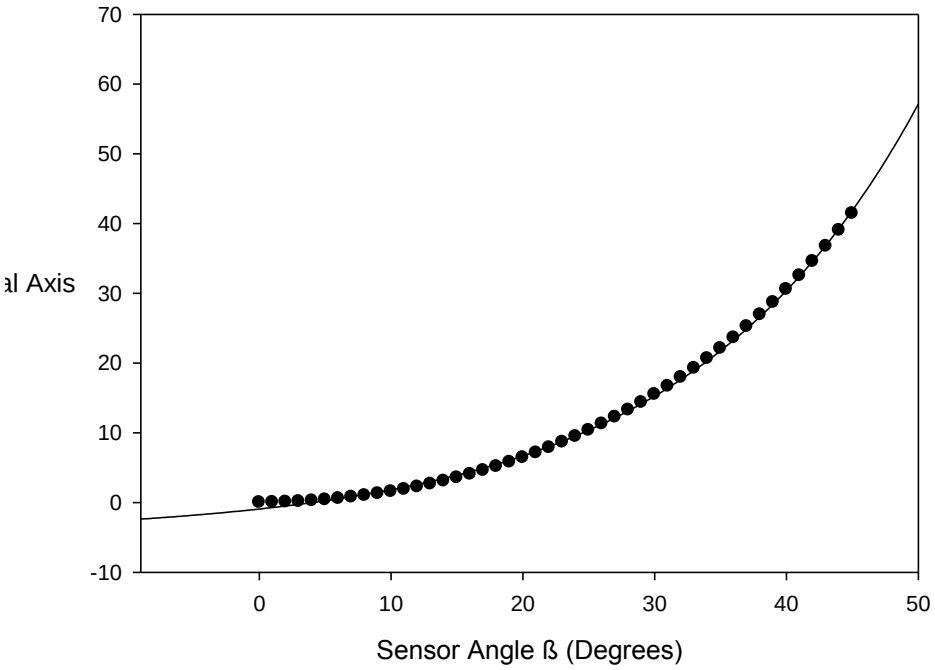

Figure 4.34: Apparent compression of the vertical axis with sensor plane angle variation, allowing for correction factors to be determined. A 3rd order polynomial accurately describes the system.

$$y = 3\times10^{-6}\beta^3 + 5\times10^{-5}\beta^2 + 9\times10^{-4} - 3.3\times10^{-3} \quad \textbf{(4.6)}$$

$$\{\beta \in \mathbb{R} \mid 45 \leq \beta \geq 0\}$$

4.6.3 Post Processing Algorithm

The OCT raw data tends to lack contrast when viewed on a computer screen. There are several methods for smoothing the OCT image data such as Gaussian filtering and frame averaging. On investigation of the data capturing functions provided with the OCT system it was discovered the Virtual Instrument (VI) assigns an image data matrix to captured images. However, the recording function does not utilise the full spread of the 14 bit image space. Figure4.35 shows the image space and the associated data histogram. Most of the OCT data seems to be present within the upper area of the histogram. Lower areas are predominantly OCT noise and speckle.

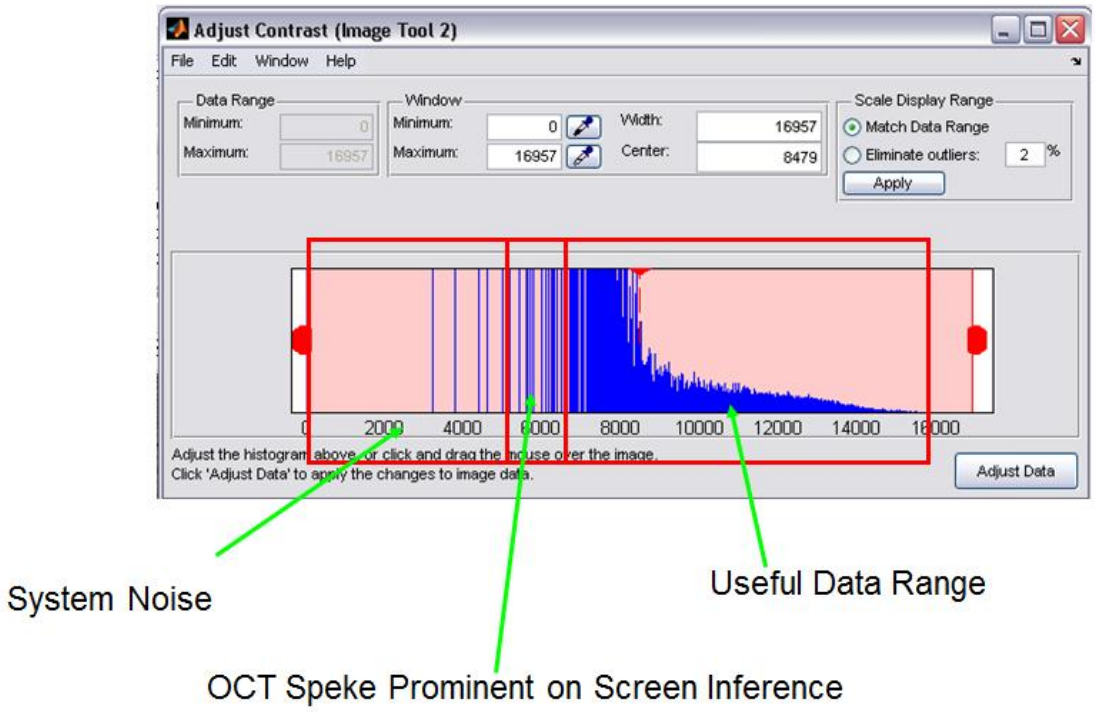

Figure 4.35: Image space (Histogram) of raw OCT data, note that the spread is very uneven.

A custom Matlab routine was produced that rescaled these data linearly over the entire 14 bit space giving much improved contrast. The algorithm also removed a proportion of the pixels values that fall under a certain threshold value setting them to a default value of zero (i.e. perfectly black). Overall the images show a better signal to noise ratio after processing. The results of different cut off points can be seen in Figure 4.36.

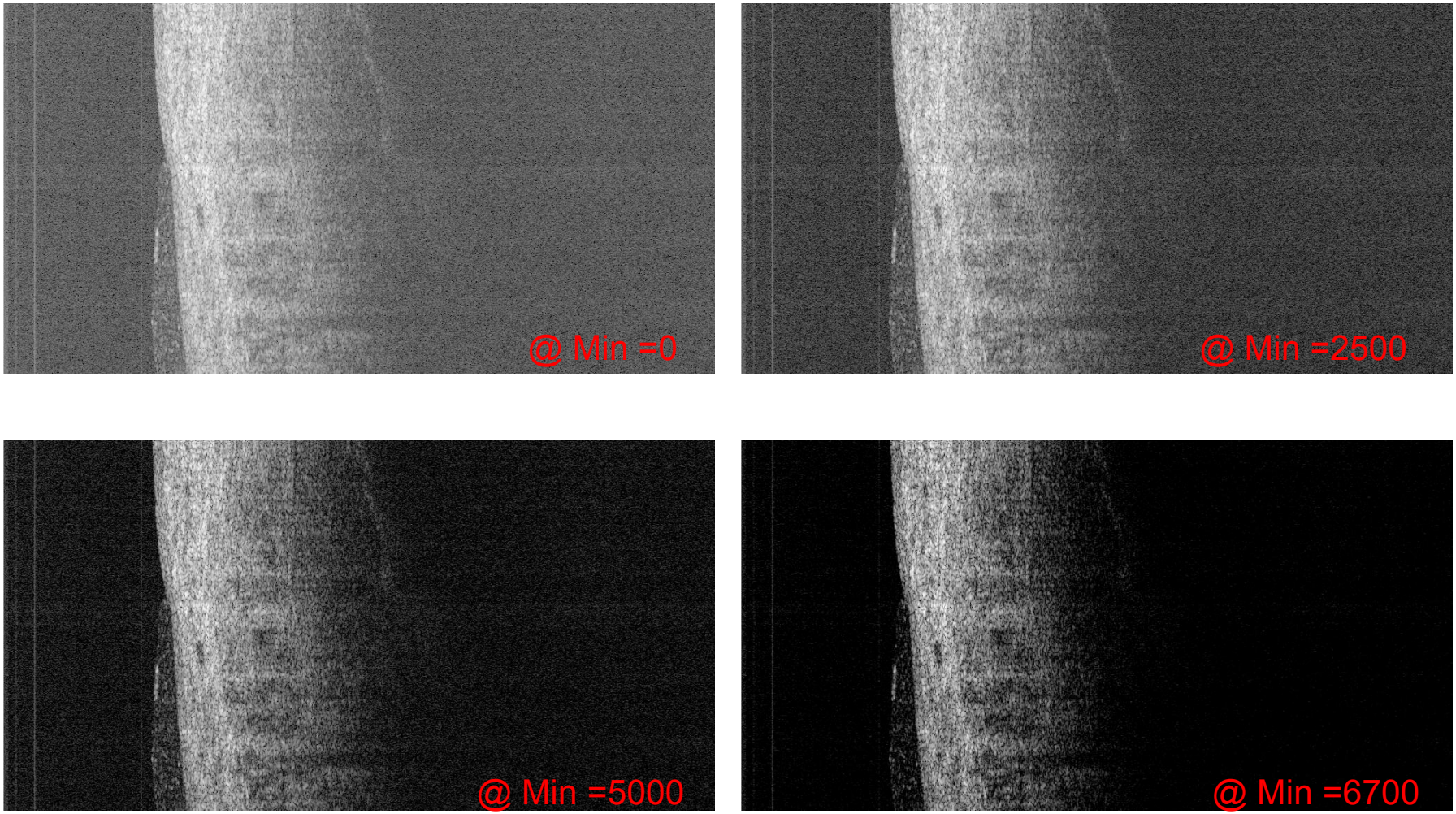

Figure 4.36: OCT data resamples at differing cut off positions. The greater the cut of position the higher the attenuation of noise, however loss of detail becomes more apparent as value increases. A compromise position of 6000 will be used as a starting point.

After the images were formatted into the .png format they could be viewed or recorded into .avi files by the custom player software. Viewing was essential after processing as data corruption was noted in the raw data output from the OCT system in approximately 1% of scans. Different cut of points could be used for different investigation areas, a higher point gave better edge selection results but void investigation tended to be optimised with less aggressive resampling.

4.6.4 Blink Removal Program

The removal of blinks from scans was essential as the eyelid moving though the scan path in imaging produced erroneous results with the tracking algorithms. Blink start and finish points (i.e. frames) were selected for each blink in an individual scan and inputted into the blink removal tool. This tool took the last non-blink image and copied it across all the following blink image frames until it reached the final frame. This produced the effect of pausing the image until the blink had passed. This process could be labour intensive and has been demonstrated to be automatable. The tool can also be used to remove corrupted frames of data using the same method.

4.7 Analysis Software and De-warping Conclusion

The software development for the OCT system was by far the most challenging and time consuming component of the project. The complete 26 programs developed consumed at least 75% of the project time and resources.

The measurement criteria developed for assessing lens coverage, indentation and thickness was highly successful and proved to be very robust when semi-automated with software developed in LabVIEW. Time required for analysis was reduced by at least 50% compared no specific analysis software such as imageJ when assessed in timed trials. A skilled operator can analyse a single 3-blink scan from the OCT system in less than 1 minute. Void analysis and quantification took similar amounts of time to complete.

Master timing and control software proved highly effective in managing the large data throughput generated by the combined imaging systems. Data entry for subject number, lens type, time and scan position could be entered in less than 10 seconds and repeat scan taken with a single mouse click. Timing staging and automatic folder creation proved very robust when tracking problems such as lost data (via user error) and for long-term storage/record keeping in compliance with Vision Care Research (VCR) policies.

On slide contact lens calibration proved easy to implement, novel way of determining true from apparent contact lens indentation into the epithelium. The slide holder was rapidly attached to the instrument at the end of subject scanning. As required the entire procedure could be completed in less than 10 seconds after removing the lens to preserve lens hydration. The indentation was rapidly assed with the customised software and date recorded accordingly.

The HSC recording software required constant monitoring of the execution process to avoided overloading the computer system. Timing procedures were successfully developed that allows simultaneous use of the OCT and HSC.

The HSC camera initialisation routine proved difficult to perfect. There appeared to be a specific hardware handshake on starting the camera that takes approximately 30 seconds to compete on first power up. If communications were interrupted, the system would not complete the correct initialisation and no images were transmitted to the capture card. The same applied if power was interrupted in the measurement process. A hardware reboot must be undertaken to reset the HSC.

HSC analysis was also successful and highly automatable. A single scan could be analysed in 3 minutes with full data and record keeping implemented. Even with the high automated analysis tools the size of the project necessitated considerable time for analysis. A total of 225 hours of analysis time was determined to be required for project completion.

HSC de-warping and calibration was quantified and minimised as a potential source of error. The highly novel RAM buffering system developed proved a conclusive solution to increasing imaging speed without adding significant cost or external hardware. As a stand-alone principle the concept has generated external commercial interest. The final device can now be regarded as the pre-production prototype put forward for testing as laid down in the block design pattern discussed previously and allowed the study describe in chapter 5 to be undertaken.

Chapter 5

Chapter 5 OCT Proof of Principle Clinical Trial

5.1 Introduction

Contact lenses need to move over the ocular surface with each blink to allow a healthy ocular physiology to be maintained. Greater fluorescein staining has been found with both loose and tight fitting lenses and higher levels of bulbar and limbal hyperaemia with loose fitting lenses (G Young & S. Coleman 2001). With an average blink rate of about 12 times each minute during time awake, a soft contact lens oscillates across the ocular surface approximately 11,500 times a day, travelling about 7m (Golding, Harris, et al. 1995). High resolution Optical Coherence Tomography (OCT) can be used to image the interaction between the contact lens edge and the corneal epithelium (M Shen et al. 2010).It has recently been shown using static imaging with high resolution OCT that contact lenses with a rounded edge worn for 30 minutes appear to indent the corneal epithelium more and underlying post-lens gaps near the corneal-scleral junction were more common than caused by lenses with angular edges (M Shen et al. 2011). Hence even apparently well-fitting soft contact lenses can impact the ocular surface which might link to comfort and future complications in some individuals. However, the indentation was only subjectively graded and commercially available contact lenses were used of differing lens material, so the effects of lens edge and shape profile were confounded.

Contact lenses parameters are traditionally selected based on central corneal curvature measured with a keratometer and the horizontal visible diameter assessed using a ruler. However, soft contact lens drape over the entire cornea, across the limbus onto the bulbar conjunctiva. As a result, peripheral corneal topography and the corneo-scleral junction profile determined by OCT have been shown to contribute to the prediction of lens fit(Hall et al. 2011). Hence the mismatch between contact lens design profile and underlying ocular surface shape should be considered in conjunction to the lens interaction with the corneal epithelium. Any indentation of the epithelium is a dynamic phenomenon, driven by the interaction between the contact lens movement, edge thickness profile and eyelid tautness. Hence the change in indentation with time together with the lens movement dynamics contribute to the mathematical modelling of the system. Finally, previous reports of OCT observed interaction between a contact lens and the ocular surface seem to have ignored the distortion effects of the contact lens curvature and refractive index on the underlying imaged tissues.

This effect will be influenced by hydration of the contact lens and hence may vary individual to individual. Optical distortion will naturally result in a rounder (thicker) lens edges appearing to indent the corneal epithelium more than an angular (thinner) edge and would magnify any post-lens gaps, resulting in them being observed more often, which could explain previous findings (M Shen et al. 2011).

Therefore this study combined a high resolution digital camera to capture contact lens movement with a custom built spectral domain OCT to dynamically capture the interaction between the contact lens edge and ocular surface. Four experimental lens designs were constructed from the same material to assess the interaction of lens base curve and edge design *in-vivo*. Hence the relationships between lens draping and edge-epithelial layer interactions, and lens movement and comfort could be elucidated.

5.2 Methods

The study was approved by the Aston University Ethics Committee and by Medicines and Healthcare products Regulatory Agency (UK) as the contact lenses were investigational products. The research followed the tenets of the Declaration of Helsinki. Signed consent was obtained from each subject following explanation of the study and possible consequences. Each subject was enrolled in the study if they were an adapted soft contact lens wearer, had refractive astigmatism of no more than 0.75 D, a corrected visual acuity of at least 20/30 in each eye, there was no evidence or history of ocular tissue anomaly, ocular surgery, ocular infection or inflammation, dry eye, allergy, or any ocular surface or systemic disease that might have affected the relationship between the contact lens and the ocular surface. None of the subjects were taking ocular medication.

Four different lens designs made from the same senofilcon A material were examined comprising of two different lens base curves (8.4 and 8.8mm) and two lens edge designs (chiselled and knife edge; Table 5.1). All lenses had a 0.00 ± 0.25 D power so that power related thickness profiles did not confound the study design and subjects could wear their spectacles to obtain appropriately corrected visual acuity, if needed.

Property	**Range**	
Modulus	5.10E+5 – 8.14E+5 Pa	
Tensile Strength	2.61E+5 – 1.07E+6 Pa	
Elongation	80-339 %	
Toughness	26 MPa/m^2	
Water Content	36-40 %	
Dk (edge corrected)	103 ± 21 $[10^{-11}(cm^2/sec)(ml O_2/ml \times mmHg)]$	
Refractive index	1.42 ± 0.02	
Diameter	14.00 ± 0.20 mm	
Base Curves	8.40 ± 0.20 mm	8.80 ± 0.20 mm
Centre Thickness	0.070 ± 0.017 mm	

Table 5.1: Senofilcon A design parameters.

A novel simultaneous dual imaging technique was developed as detailed in chapter 4 to assess dynamic contact lens movement and its effect on the ocular surface during blinking. The system comprised of a high speed swept source Fourier domain OCT system and a high resolution, high speed camera system (HSC). The OCT consisted of a Santec IVS-2000 (Aichi, Japan) customised to optimise its use in anterior segment imaging. Hardware customisation included the addition of a tuneable attenuation unit allowing power input to the ocular system to be controlled within eye safe levels. Additional attenuation between the return light path and the balance detector allowed optimisation of the signal-to-noise ratio and selectable sensitivity limited the negative effects of dropping output power to eye safe levels. The OCT delivered >15,000 A scans per second giving a frame rate of 27 frames per second (B Scans) with an axial resolution of 7 microns and a lateral resolution of 23 microns. Scan range was selectable between 1mm and 15mm. Scanning could be performed in any meridian and was changeable through software in real time by 1 degree intervals. The bespoke alignment system and headrest also allowed both the OCT and HSC to share a common focal point and image simultaneously. The imaging probe was mounted on a slit-lamp base with additional fine alignment from a 3-axis stage and vertical tilt platform as discussed in chapter 4. This allowed the imaging head to be positioned perpendicular to the ocular or contact lens surface at the point of highest sensitivity while keeping the HSC imaging colinear with respect to the optical axis of the eye.

The HSC comprised of the Flacon 4M60 camera (Teledyne DALSA, Thousand Oaks, California, USA) accompanied with a CameraLink frame grabber NI PCIe-1429 (National Instruments, Austin Texas) delivering 2352 x 1728 pixels with a capture speed up to 62 frames per second. A custom optical system from Schneider Optics (Hauppauge, New York, USA) captured a $16mm^2$ field of view at a resolution of 16 microns. A fixation target consisting of a Light Emitting Diode (LED) kept the subjects concentration fixed throughout scanning and allowed rapid eye alignment. Illumination was provided by a bespoke array of broad spectrum white LED's.

Custom software was developed using LabVIEW to control the OCT system and HSC system and maintain precision timing between HSC image and the Santec Application Programming Interface (API). The system relied on parallel processing techniques due to the high data throughput of the system. A novel system discussed in chapter 4 was developed allowing the HSC image data to be buffered in real time directly to the computers Random Access Memory (RAM) bypassing the normal method where data is written to the hard disk drive, allowing high image capture rates.

The study was a randomized, bilateral, cross-over, non-dispensing study in which subjects wore wear each contact lens type for four hours. Each lens was worn on a different visit, separated by at least one day, with subjects refraining from contact lens wear between visits. The study was conducted in a consulting room with controlled temperature (20 ± 2 °C) and humidity (40 ± 5 %). All subjects were scheduled after 10 AM to avoid the oedematous cornea and the alteration of the tear film induced by sleep, which could have affected the results (S Patel et al. 1988; M Shen et al. 2008).Twenty six subjects completed the study (28 enrolled and 2 discounted). Eye health was examined with a slit lamp biomicroscope. The randomly selected contact lens was fitted, centration and movement checked by a masked investigator. On insertion(H0), at 2 hours (H2)and 4 hours (H4) after insertion the lens en-face movement was imaged with the HSC simultaneous to the cross section of the contact lens edge interaction with the ocular surface being captured by the OCT (scanning perpendicular). At least three blinks were captured with the HSC and OCT systems and the two best were analysed. This was repeated at the 3, 6 and 9'o'clock lens edge positions in random order. Non-invasive tear break-up time was also measured three times with a Tearscope (Keeler, Windsor, UK).

5.2.1 Data Analysis

System calibration and de-warping was performed with a series of known precision reference spheres (Grade 10 stainless steel ball bearings with a diameter tolerance of 1.3 microns) with diameters of 7mm, 16mm and 24,mm (Simply Bearings Ltd, Lancashire, UK) and precision slip gauges (Mitutoyo, Kanagwa, Japan) . The process is detailed in Chapter 4, conversion factors were applied in software (axial resolution 141 pixels per millimetre). Each individual's contact lenses were imaged using the OCT system on a glass slide immediately on removal after the last on-eye scan to allow the distortion of the underlying structures caused by the contact lens to be measured and compensated for as show in Figure5.1a.

Further OCT image processing was performed with Matlab (The Mathworks Inc, Massachusetts, USA) by resampling the raw OCT intensity output and applying a custom rescaling algorithm to rescale the peak reflections over the 16 bit image space giving a superior dynamic range (contrast) and reducing high frequency speckle (noise) compared to standard OCT system output. A semi-automated image processing suite was developed using LabVIEW allowing epithelium thicknesses, lens thickness, gap sizes and indentations depths to be measured from the OCT data show in Figure 5.1b.

The HSC data were analysed with distance between the centre of a circle imprinted on the contact lens during the manufacturing process and centre of the limbus calculated in each frame to assess lens horizontal and vertical movement post-blink and the decay constant (λ) defined by the exponential equation 5.1:

$$N(t) = N_0 e^{-\lambda t} \quad \textbf{(5.1)}$$

As the lens movement and indentation data were normally distributed, repeated measures analysis of variance was conducted with time after insertion, position on imaging on lens edge, lens profile and pre and post blink as factors with the data averaged across two blinks.

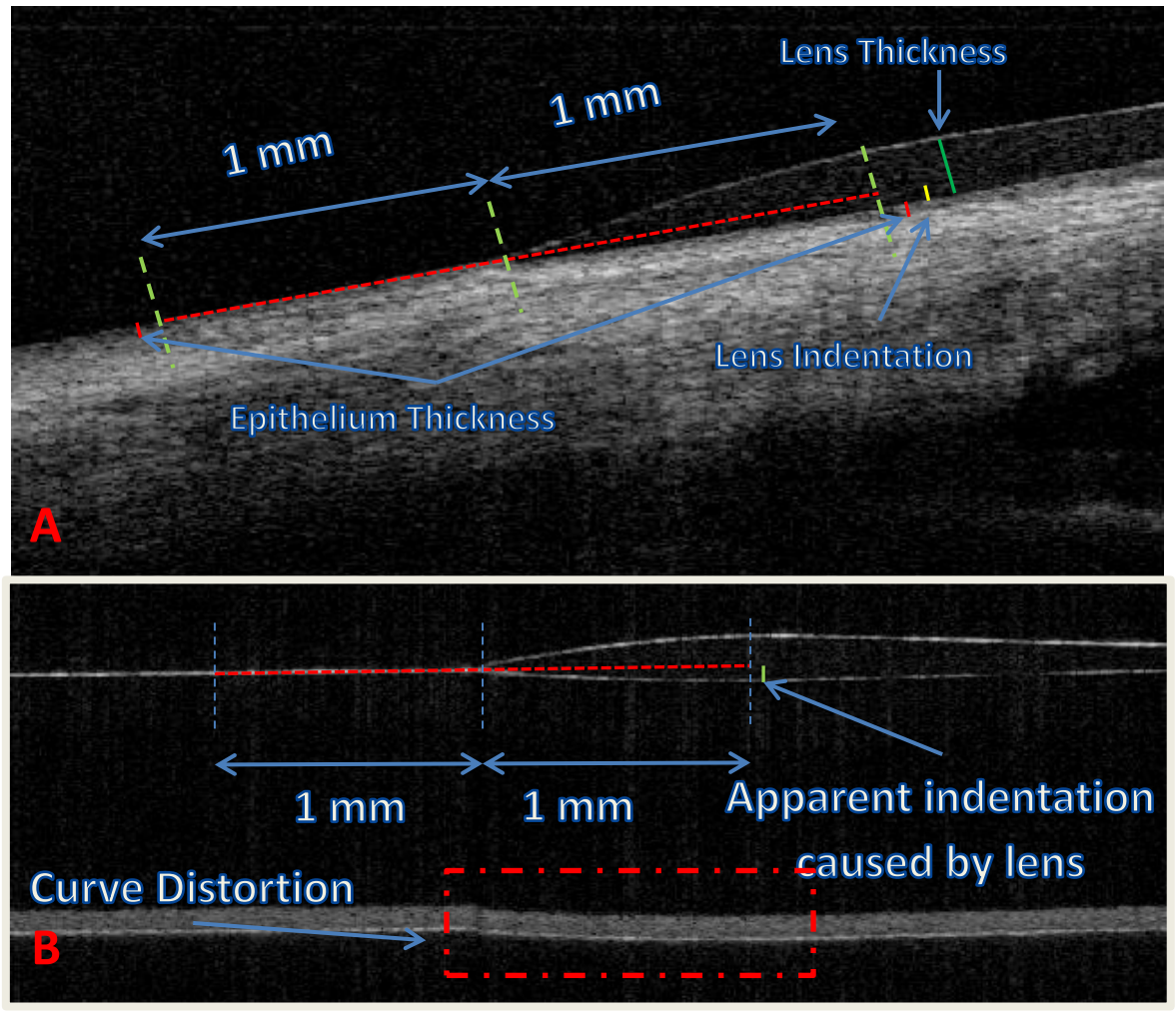

Figure 5.1: Image analysis of de-warped, calibrated and resampled OCT images to determine apparent epithelium indention **(a)** Measurements taken in real eye **(b)** on slide calibration.

5.3 Results

5.3.2 Epithelial Thickness

Epithelial thickness remained constant over time (on insertion 60.5 ± 17 microns; 2 hours 61.9 ± 17.7 microns; 4 hours 60.9 ± 15.7 microns; $F = 2.193$, $p = 0.115$), but varied with position on the lens edge (3 o'clock 63.6 ± 17.2 microns; 6 o'clock 64.6 ± 16.6 microns; 9 o'clock 55.0 ± 14.4 microns; $F = 44.642$, $p < 0.001$). There was no significant difference immediately after a blink to before the next blink (60.7 ± 16.8 microns vs 61.4 ± 16.7 microns; $F = 3.675$, $p = 0.059$), although there was an interaction with lens edge profile (knife edge before to after a blink 61.4 ± 17.6 vs 61.3 ± 16.8 microns; chisel edge 60.2 ± 15.9 vs 61.5 ± 16.5 microns; $F = 7.408$, $p = 0.008$). The epithelium under the contact lens appeared significantly thicker (66.4 ± 17.2 vs 55.8 ± 14.3 microns; $F = 88.815$, $p < 0.001$). There was an interaction between position on the lens edge and epithelial thickness immediately after a blink to before the next blink ($F = 3.921$, $p = 0.022$). There was also an interaction between edge design and epithelial thickness difference under the lens edge ($F = 3.204$, $p = 0.044$) and also with the additional variable of position of measurement along the lens edge ($F = 3.760$, $p = 0.005$). None of the other interactions were statistically significant ($p > 0.05$).

5.3.3 Lens Thickness

Lens thickness 1mm from the lens edge differed between the flatter and steeper base curve designs (104.1 ± 11.1 microns vs 146.5 ± 13.9 microns; $F = 803.079$, $p < 0.001$), but not with edge design ($F = 0.053$, $p = 0.818$), time ($F = 2.630$, $p = 0.076$), lens edge position ($F = 0.890$, $p = 0.413$) or pre and post blink ($F = 0.000$, $p = 0.993$) and there was no interaction between these variables ($p > 0.05$).

5.3.4 Indentation

Apparent epithelial indentation decreased with time (on insertion 60.0 ± 21.1 microns; 2 hours 55.8 ± 21.8 microns; 4 hours 54.7 ± 21.0 microns; F = 5.934, p = 0.003), varied with position on the lens edge (3 o'clock 48.1 ± 20.0 microns; 6 o'clock 57.9 ± 21.1 microns; 9 o'clock 64.7 ± 19.9 microns; F = 44.642, p < 0.001), changed after a blink (immediate after a blink 58.6 ± 21.9 microns to before the next blink 55.1 ± 20.8 microns, F = 21.034, p < 0.001), varied with base curve (flatter 52.3 ± 18.8 microns; steeper 61.2 ± 22.9 microns; F = 17.567, p < 0.001) and differed with edge design (knife edge 59.1 ± 22.4 microns; chisel edge 54.7 ± 20.2 microns; F = 4.916, p = 0.030). There were significant interactions between: position on lens edge with base curve (F= 4.139, p = 0.018) and with edge design (F = 6.490, p = 0.002); change after a blink with base curve (F = 11.711, p = 0.001); position on lens edge with change after a blink (F = 4.340, p = 0.015). None of the other interactions were statistically significant (p > 0.05).

When indentation was corrected epithelial indentation again decreased with time (on insertion 8.9 ± 2.5 microns; 2 hours 5.3 ± 2.4 microns; 4 hours 3.8 ± 2.5 microns; F = 4.731, p = 0.010), varied with position on the lens edge (3 o'clock 2.8 ± 23.6 microns; 6 o'clock 7.1 ± 23.9 microns; 9 o'clock 14.0 ± 23.2 microns; F = 59.180, p < 0.001), changed after a blink (immediate after a blink 7.8 ± 24.8 microns to before the next blink 4.3 ± 24.2 microns, F = 31.276, p < 0.001), but no longer varied with base curve (flatter 6.1 ± 21.3 microns; steeper 5.9 ± 27.4 microns; F = 0.026, p = 0.872) or with edge design (knife edge 7.5 ± 25.1 microns; chisel edge 4.6 ± 23.9 microns; F = 0.097, p = 0.757). There were significant interactions between: position on lens edge with base curve (F= 3.066, p = 0.049) and with edge design (F = 3.364, p = 0.037); change after a blink with base curve (F = 31.276, p < 0.001); position on lens edge with change after a blink (F = 5.500, p = 0.005). None of the other interactions were statistically significant (p > 0.05).

5.3.5 Lens movement

Horizontal lens movement did not change with time post insertion (F = 1.702, p = 0.185). It was significantly affected by base curve (steep: 0.31 ± 0.09, flat: 0.16 ± 0.05mm; F=88.285, p <0.001), but not by edge design (knife: 0.22 ± 0.10, chisel: 0.25 ± 0.12mm; F=1.712, p=0.194) and there were no interactions between parameters. Vertical lens movement was also unaffected by time post insertion (F=2.887, p=0.058), but was significantly affected by basecurve (steep: 0.41 ± 0.16, flat: 0.24 ±

0.12mm; F=34.692, p<0.001) and edge design (knife: 0.28 ± 0.11, chisel: 0.37 ± 0.20mm; F=10.308, p=0.002), but there were no interactions between parameters. Damping of the lens movement was not affected by time (F=1.337, p=0.265), but again was significantly affected by basecurve (steep: 0.28 ± 0.30, flat; 0.16 ± 0.19; F=4.543, p=0.036) and edge design (knife: 0.12 ± 0.15, chisel: 0.32 ± 0.30; F=14.632, p<0.001), but there were no interactions between parameters.

5.3.6 Relationship between lens movement and OCT parameters

The data was correlated for epithelial thickness under the lens edge and below the leading edge of the contact lens, and the corrected indentation caused by the lens for the steep and flat base curves, and chisel and knife edge designs investigated (Table 5.2). Greater horizontal lens movement was associated with a thicker epithelium under the lens with the knife edge design. Greater and more rapidly decelerating vertical lens movement was associated with a thicker epithelium under the lens with the chisel edge design.

Contact Lens Design	**Contact Lens Movement**	**Epithelial Thickness**		**Indentation**
		Pre - lens	***Under lens***	
Knife Edge	Horizontal	r=0.162; p=0.265	r=0.339; p=0.017	r=-0.015; p=0.916
	Vertical	r=0.114; p=0.437	r=0.118; p=0.421	r=-0.121; p=0.404
	Damping	r=0.062; p=0.671	r=0.038; p=0.793	r=0.075; p=0.605
Chisel Edge	Horizontal	r=0.046, p=0.749	r=0.166; p=0.250	r=0.002; p=0.988
	Vertical	r=0.215; p=0.134	r=0.335; p=0.017	r=0.114; p=0.437
	Damping	r=0.103; p=0.476	r=0.279; p=0.050	r=0.113; p=0.441
Steep Basecurve	Horizontal	r=0.219; p=0.127	r=0.271; p=0.057	r=-0.086; p=0.558
	Vertical	r=0.232, p=0.105	r=0.277; p=0.052	r=0.135; p=0.357
	Damping	r=0.060; p=0.677	r=0.211; p=0.142	r=0.114; p=0.437
Flat Basecurve	Horizontal	r=0.188; p=0.195	r=0.094; p=0.522	r=0.064; p=0.657
	Vertical	r=0.171; p=0.241	r=0.103; p=0.483	r=-0.029; p=0.843
	Damping	r=0.079; p=0.590	r=0.048; p=0.745	r=0.139; p=0.335

Table 5.2: The correlation between the epithelial thickness under the lens edge and below the leading edge of the contact lens, and the corrected indentation caused by the lens for the steep and flat base curves, and chisel and knife edge designs investigated; n=26.

5.3.7 Voids

No voids occurred when the eye was imaged without a contact lens in situ. Voids occurred in 18.5% of conditions, more often with the chisel edge (11.5%) than the knife edge (7.1%), more in the 3 o'clock (8.3%) and 6 o'clock (6.4%) than the 9 o'clock (3.8%) lens edge position and more commonly with the steeper (10.9%) than the flatter base curve (7.7%). 1.3% occurred beyond the contact lens leading edge, 0.6% around Bowman's layer and 3.5% between the lens and epithelium under the lens edge, 4.2% around Bowman's layer and 8.9% between the lens and epithelium under the lens bulk. The voids were present for on average 3.6 ± 4.6s with a maximum average width of 635.8 ± 304.0 microns and depth 95.8 ± 39.0 microns.

5.4 Discussion

This study for the first time coupled high resolution OCT with high speed en-face video to examine in detail the lens eye interaction, focused on the lens edge. The interaction between the ocular surface and the contact lens, especially around the lens edge, is of key interest in maintaining the health of the eye in contact lens wear and in terms of lens comfort. Characterization of the soft contact lens interaction with the ocular surface should enhance our understanding of current lens design parameters and allow improved designs to be generated.

Epithelial thickness with the bespoke OCT system designed for this study was similar to that reported previously for fourier domain OCT and in the periphery of the cornea with ultrasound(Reinstein et al. 2008; Parkash et al. 2012). Epithelial thickness remained constant over time, but varied with position on the lens edge, with the 9 o'clock position being thinner than the 3 or 6 o'clock. The increase in epithelial thickness in the nasal and inferior quadrants compared to other quadrants and centrally has been shown previously and relates to the differences in corneal topography in the corneo-scleral region as shown by (Hall et al. 2011). The chisel edge caused a thinning of the epithelium between blinks suggesting the blink movement thickened the epithelium during the blink motion and it subsequently recovered after the force of the lens edge was reduced. Further interactions with edge design were evident with epithelial thickness, but none occurred with lens curvature.

Lens thickness 1mm from the lens edge differed between the lenses of different curvature, but not with edge design which was unexpected. This is unlikely to be an artifact as the imaging was

performed perpendicular to the lens surface so the effect of curvature on lens distortion would have been negated. No other interactions were apparent with lens thickness, confirming the consistent repeatability of imaging this parameter.

When the epithelial indentation images were corrected based on the lens design worn and the effects of the individual's lens hydration and tear refractive index, the finding remained similar indicating the same trends, but the magnitude of the indentation decreased by an order of magnitude. Indentation from the contact lens (as none was evident over the duration in between blinking without a contact lens in-situ) reduced with time post lens insertion more over the first 2 hours (~3.4 microns) than over the subsequent 2 hours (~1.5 microns). This equates to about one twentieth of the epithelial and is less than the resolution of the OCT so is only evident through rapid OCT imaging speeds and averaging. Indentation was minimal at the 3 o'clock (nasal) lens edge and twice as great at the 9 o'clock (temporal) lens edge than the 6'oclock inferior position. The nasal cornea-scleral junction has been shown to have a greater angle than the other meridians, which might explain why the indentation differs in this meridian. The epithelium was thinnest temporally so the greater indentation in this meridian equates to approximately 25%. The reason why this meridian is particularly susceptible to lens indentation is unclear although the eyelid tends to close temporally to nasally, so the pressure may be greater on the cornea at this location and the pressure band induced by the upper lid appears to be lowest temporally (Shaw et al. 2010). Although lens design (basecurve and edge profile) did not impact on indentation overall, there was an interaction with the variation between the meridians and the indentation changes between blinks varied with lens base curve

The reduction in lens indentation with time was not related to lens movement as this remained consistent over the three time periods, although it is known to change over the initial hour of lens wear (Brennan et al. 1994; Golding, Bruce, et al. 1995). As well as the expected vertical movement which was on a typical magnitude expected for a HEMA soft lens (JS Wolffsohn et al. 2009), there was considerable horizontal slippage (equating to 78 ± 21% of the vertical magnitude). Great horizontal lens movement was associated with a thicker epithelium under the lens with the knife edge design. Surprisingly, the mobility of the steeper basecurve design was more than that of the flatter basecurve and it decelerated more rapidly, although clinical observation studies of modern designs have found little influence of basecurve on lens movement (Wolffsohn et al. 2009) and the difference of less than 0.2mm may not be subjectively observable. The knife edge design was less mobile than the chisel edge design and epithelial thickness was associated with greater and more rapidly decelerating vertical lens movement with this lens design. It is not possible with the

resolution of the OCT system to differentiate tear film under the contact lens from epithelial tissue so it is possible that the apparent increase in sub-lens epithelial thickness was greater tear flow, resulting in a more mobile lens.

Voids under the lens and at the epithelial-Bowman's membrane or conjunctiva-sclera interface, as reported and modeled previously (M Shen et al. 2011), only occurred with contact lenses in situ and were apparent in approximately one in five scans. These are thought to result from a mismatch between the lens and ocular shape and the resulting pressure variations in the post-lens region (M Shen et al. 2011). It is surmised that they could lead to compromises in ocular physiology and long term eye health (Martin & Holden 1986; Jenkins & Shimbo 1984). They occurred more often with the chisel edge, the design which also had most impact on the epithelial thickness between blinks and which resulted in the greatest lens mobility. Interestingly, voids were also more common in lens edge positions that had least indentation, suggesting a less deformable tissue (perhaps as it was thinner) causing the pressure to transfer to more inferior tissue. The voids were observed in different locations about two-thirds immediately under the lens edge or bulk presumably due to the stiffness of the lens and pressure forces of the lens on the epithelial surface (Shaw et al. 2010), but about one quarter at the level of the epithelial interface with Bowman's or sub-conjunctiva layer. For the first time these gaps have been dynamically quantified as lasting about half the duration between blinks and reaching a maximum average size of two-thirds of a millimetre by one-tenth of a millimetre. These values are thicker than the epithelium suggesting marked disruption of the ocular tissue as well as stand-off of the lens can occur.

This study was able to overcome many of the limitations of previous research to allow changes in the ocular surface to be quantified during contact lens wear, controlling for lens material properties and design differences between commercially available lenses. However, only one material was studied so the magnitude of the changes could vary with other materials of differing modulus. Our OCT system did not have the resolution to differentiate the tear film layer and tear exchange under the lens which is likely to be impacted by lens design and its conformity with the ocular surface could not be investigated.

In conclusion it is evident that studies that do not correct fully for lens thickness, curvature and hydration effects will grossly overestimate the effects of contact lenses on the ocular surface. However, dynamic changes do occur and these are affected by lens basecurve and edge design. This is the first study to objectively quantify these effects. The chisel edge caused greater lens mobility and appeared to have more impact on the epithelial thickness and in causing voids than the knife

edge, perhaps due to the extra bulk. Basecurve however, despite being related to lens mobility, had relatively little effect on the ocular surface and the two curves utilized encompass most of the soft lens designs commercially available. Hence the information gained from this investigation will allow improved modeling of the soft contact lens-eye system, including testing of current theories based on tear film expulsion and negative pressure effects (Martin & Holden 1986; Golding, Harris, et al. 1995) and will inform future lens design. The equipment built to image the dynamic movement of a contact lens simultaneously with high resolution cross sectional images of the lens-ocular surface interaction will allow these new lens designs to be better understood and may contribute to predicting those patients who will experience complications with certain lens designs.

Chapter 6

Chapter 6: Auto-Refractors Introduction and History

The auto-refractor is the logical application of technology to speed up and automate the refraction process. Some confusion appears to be present as to when the first devices became available (presumably due to prototype/production quantification). The first fully automated device appears to be the fantastically named “Ophthalmetron” developed in 1970 (Wood, 1987)

The first large scale commercial instruments were developed in the late 1970s (Dioptron autorefractor, Coopervision). Studies indicated the devices to have accuracy within ±0.5D spherical equivalent when compared to subjective refraction in 74% of subjects (Perrigin et al. 1984). The second generation device (Dioptron 2) reported a 50% increase in accuracy compared to the previous generation device (Mailer 1978). However the concepts of machines to measure refractive error are considerably older and can be traced back to the 1930s with Geofferys Collins “Electronic Refractometer” (Collins, 1939). No peer reviewed data could be found on the clinical effectiveness of the “Electronic Refractometer” and presumably technical limitations of the day rendered the device difficult to implement.

Auto-refractors can aid the optometrist by providing a quick and accurate measure of refraction providing a starting point close to the true level of refractive error present. Indeed some studies have indicated that the auto-refractors can be a more reliable refractive error assessment, however they rarely give better patient outcomes, with 51% of people preferring the optometrists prescription compared to 19% for an auto-refractor (Strang et al. 1998) .

Most auto refractors are based on three types of technology 1.) Image Quality Analysis (IQA) 2.) The Scheiner Principle (SP) and 3.) Retinoscopy. A detailed working description of each of these types of technology is beyond the scope of this thesis and can be found in the academic literature but the general operational principles are as follows.

IQA is a system where a reference signal is compared to a returned signal reflected from the retina of an eye. The signal is passed through an optical system which moves through the returning beam to locate the position of optimal focus which can be related directly to the vergence of the eye and hence the refractive error. SP or Scheiner Disk optometers measure the displacement of a spot from a known location (effectively the optical systems chief ray) due to the optics of the eye from which the light was reflected. Geometrical relationships can be determined to allow the computation of refractive error. The advent of photographic technology allowed this displacement to be objectively

quantified in real-time. Retinoscopy is the technique of determining refractive error by comparing the movement of a light source with the relative movement of the return signal. The subject's refraction is assessed at optical infinity as in accordance with Foucault's principle (Trusit 2004). The process can be automated, using with and against movements used to guide the instrument.

6.1 The Badal Optometer

A Badal optical system is an essential part of stimulating accommodation without the confounds of changing image size and luminance. Badal systems also reduce the space required to present a series of accommodative targets of different demands to the eye. The system was developed by J Badal in 1876 (Badal 1876). The perceived angular size of the target is independent of the target position and the scale of measurement is linear simplifying the measurement process.

The arrangement has some limitation, most notably the device can only produce negative (hyperopic) vengeance conditions. The single lens system also produces considerable chromatic aberration at the lens far focus point. Small targets must also be used to remain within the lens aperture as the target is moved back towards optical infinity (the focal point of the system). Studies have also indicated the system may induce proximal accommodation (accommodation due to the knowledge of the nearness of the target) (McLin & C. M. Schor 1988). Figure 6.1 shows the optical arrangement of a Badal optical system.

More advanced versions of the Badal system have been proposed (Atchison et al. 1995) that removed some of these issues by using series of virtual targets. Advances also include being able to produce hyperopic as well as myopic conditions.

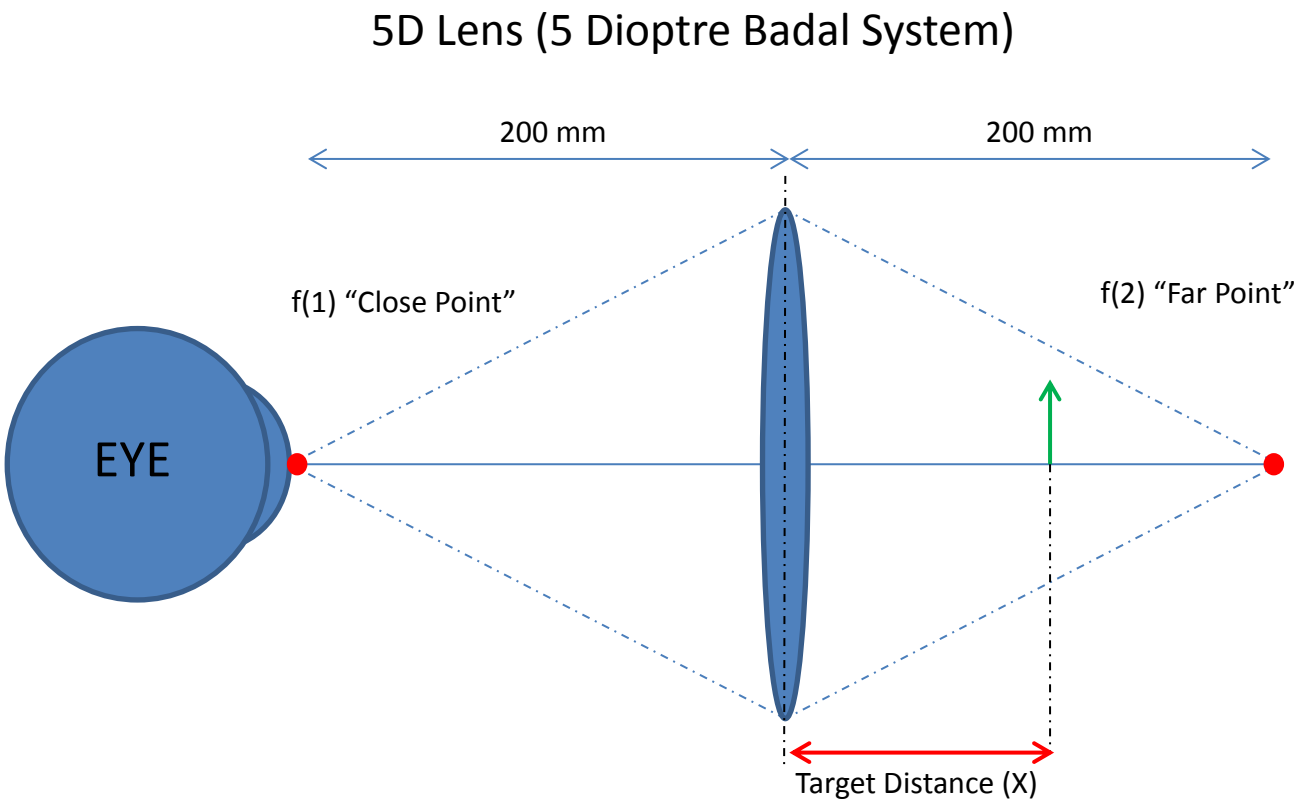

Figure 6.1: Optical arrangement of a 5D Badal system.

6.2 Open Field Auto-Refractors

Open field auto refractors are devices that measure refraction in same manner as standard auto refractors providing rapid information about the refractive state of the subject under test.

The advantage of an open-field of view is the added flexibility of subjects viewing stimuli binocularly and the ability to position targets at differing vengeance positions and angles. Most of the large ophthalmic instrument manufacturers produce an auto refractor, but open field versions are relatively rare.

The first production open-field auto refractor was the Canon Autoref R-1 (McBrien & Millodot 1985) first produced in 1980 but not in widespread use until several years later. The open-field device was verified and found to be comparable to other auto refractors (McBrien & Millodot 1985). The device spawned research in the area of dynamic accommodation, enabled by the open-field technology, however hardware modification to the standard instrument required for dynamic data capture, the range was limited to approximately 3.0D and alignment was critical making it difficult to use (Pugh & Winn 1988) (Heron et al. 2001).

Despite the advantages of open-field devices, subsequently developed auto refractors are virtually all closed-field, presumably as they are less complicated to use in a “non-research” environment. At the turn of the century, the Canon R-1 was no longer manufactured and those in existence were wearing out due to their mechanical nature. At this time, a new open-field instrument from Japan was released onto the market, branded by both Grand Seiko and Shin Nippon. Four iterations of the device have been sold to date, the Shin Nippon SRW-5000, Shin Nippon NVision-K 5001/Grand Seiko WR-5100K the Shin Nippon FR-5000 and the Grand Seiko WAM-5500.

The SRW-5000 was evaluated in 2001 and deemed to be accurate compared to a standard auto refractor and repeatable and hence a potentially valuable tool for accommodation research (E. A. H. Mallen et al. 2001). As sold, the device lacked any form of dynamic measurement and recording capability. Modification of the device was undertaken by directly tapping into the National Television System Committee (NTSC) output from the device and measuring the IR ring deformation directly with custom software developed with LabVIEW. The modifications were deemed highly successfully delivering a measurement frequency of 60Hz and sensitivity as small as 0.001D (J. S. Wolffsohn et al. 2001). The NVision-K 5001 was verified in 2003 as comparable with current devices with the addition of auto keratometry (L. Davies et al. 2003). However, the addition of the keratometry CCD made

conversion to dynamic measurement impossible. As of July 2012 it is unclear if the NVision-K 5001 is available for sale. The manufacturer appears to offer the device via their website, but with no indication of quantity, lead times and availability. Presumably refurbished units and construction for spare components are available in limited numbers (Wolffsohn et al. 2004)

The Grand Seiko WAM-5500 is the only device available for large scale supply with the device readily available from a number of global distributors. The device has a considerable smaller footprint that the SRW-5000 and NVision-K 5001. Part commonality is shared between all three components with the head unit appearing to share the same vacuum formed cowlings. The device underwent validation in 2010 and was deemed to be accurate compared to previous devices and reliable, the added feature of recording pupil size being noted as extremely useful (Sheppard & Davies 2010). For the first time a dynamic recording mode was added through the included WCS-1 software, which could record at a stated frequency of 5Hz (Sheppard & Davies 2010) The WAM-5500 has been used for both dynamic and static recording in research with slight disagreement in direct comparison between measurements (Win-hall et al. 2010).

6.3 Operation Principles of the WAM-5500

There is limited data on the operation principles of the WAM-5500, however it is understood that the system operates on very similar (if not identical) operation principles to the SRW-5000 due to the devices design hereditary. The WAM-5500 can be regarded as a modernised SRW-5000 with the advantage of better processing capability and faster optical movement capabilities due to high speed linear slides.

The operation principle for both the SRW-5000 and the WAM-5500 is the Grating Focus Principle GFP (Hung 2001) and a modified SP principle. GFP is a contrast based sensing algorithm where light returned from the retina is augmented with a series of movable optics until the best contrast is observed. The image received is an annulus shape whose deformation can be directly related to the refractive state of the eye under test. A ring provides a greater level of information that the standard dot used in normal SP systems. Assessment of magnitude change and elliptical displacement in different meridians yields both spherical and astigmatic refractive states. It should be noted that some versions of the instrument family use vertical and horizontal line separation rather than a ring, reportedly due to a patent infringement (Trusit 2004). Figure 6.2 shows the optical arrangement of the system.

6.4 Limitations of Current System

The standard WAM-5500 lacks proper accommodation stimulus targets or the structural mounting points to attach targets securely. Repeatability of measurement is affected by the lack of standard attachments for stimulus targets and/or Badal systems. The WCS-1 software only offers very basic functions and no ability to time external hardware or systems. The software does display the last received reading in real time, but shows no history of measurements received. The user is therefore given no indication of the successes of testing or instrument operation. The software requires the used to restart at the program for each successive testing sequence saving the data if different locations each time.

Part	Description
1	Eye
2	Large External Beam Splitter
3	Alignment Lights
4	Final Optic (View Lens)
5	Beam Splitter
6	Focusing Optic
7	Mirror
8	Target (Exteral)
9	Mirror
10	Mask
11	Optic
12	Mask
13	Light Source (IR)
14	Relay Lens (Movable)
15	Relay Lens (Movable)
16	Mirror
17	Focusing Optic
18	Beam Splitter
19	Aperture
20	Focusing Optic
21	CCD Sensor

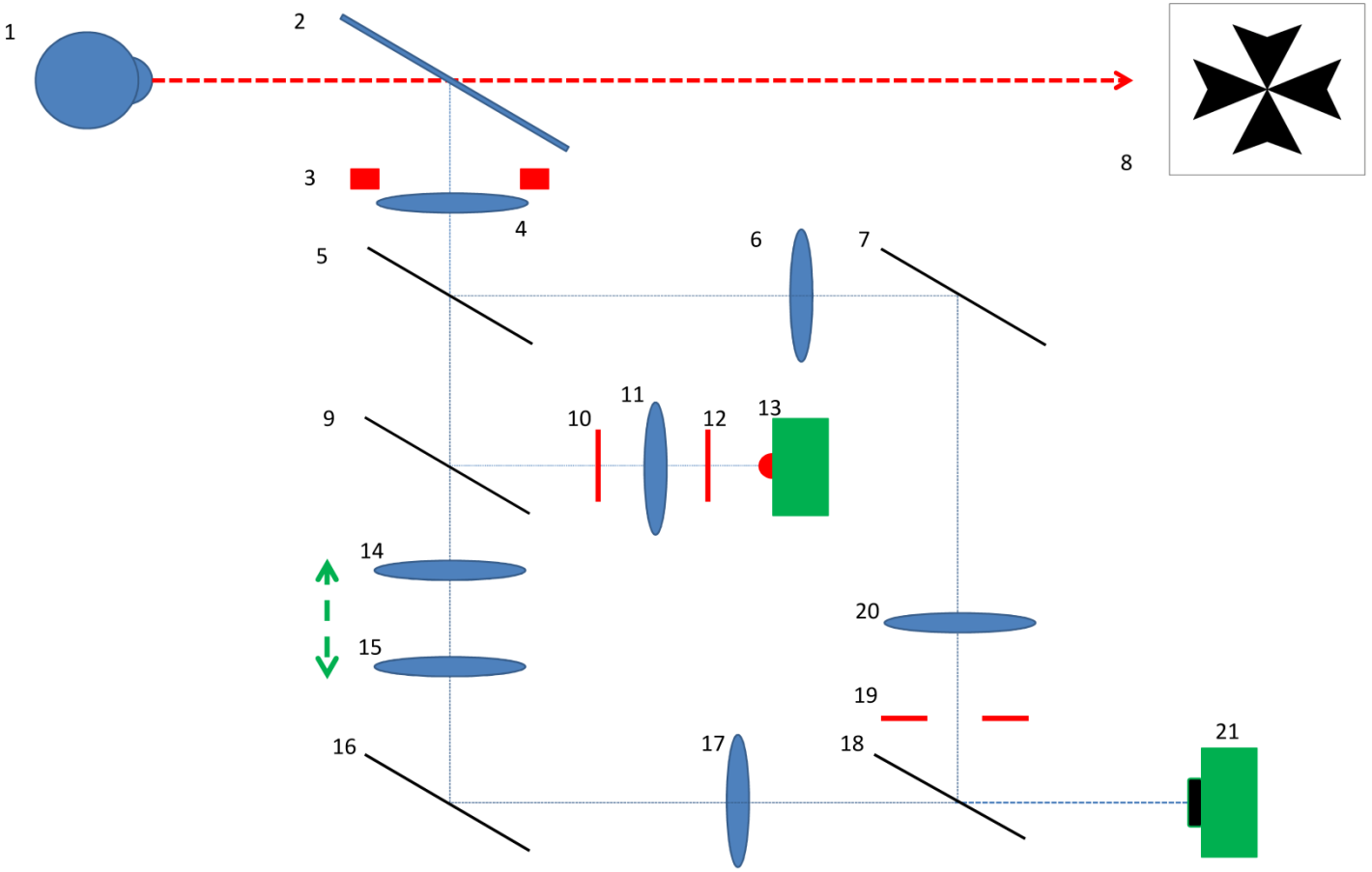

Figure 6.2: Optical arrangement the WAM-5500 adapted from (E. A. H. Mallen et al. 2001).

6.5 Block 1 Dyna-WAM

6.5.1 Hardware Development

The first device generation Block 1 device utilised a stepper motor to move a target in and out of the field of view mechanically. In line with current accommodation targets for the WAM the device was mounted on the top of the WAM-5500.

The lack of structural hard mounting pins on the WAM necessitated the design of a custom mounting system. A close fitting rapid prototyped plastic mounting fixture was designed, fabricated and bonded with epoxy resin to the cowling of the WAM. Epoxy was chosen because it would form a strong but non-permanent mounting.

Rapid prototyping was used extensively throughout the design of the Block 1 system. The motor mounts and shaft coupling were produced using the fused deposition modelling technique (FDM). FDM deposits layers of plastic forming a laminar structure. The tendency for delamination of components when under stress must be accounted for in the design phase. The material properties of the FDM substrate are equivalent to Acrylonitrile Butadiene Styrene (ABS) plastic giving good wear resistance and ultra-violet (UV) stability.

A small size 17 bipolar stepper motor (Nema Size 17, various manufactures) giving a step resolution of 1.8 degrees and a torque exceeding 3.4kg/cm when driven at 1.7A was selected. The motor could drive the target swing arm without reduction in speed or mechanical slip. Remaining plastic components were produced from laser cut perplex panelling. An electronics compartment box was included in the device to house the electronics and electrical connections.

A Badal system was produced on the FDM, housing a 5D meniscus lens integrated into the design, giving a range of accommodation stimulus from 0D to 4.5D.

6.5.2 Design and Fabrication

Following standard engineering principles, extensive computer aided design and computer aided manufacture was used throughout the development phase. A full professional CAD development environment with integrated Finite Element Analysis (FEA) and Computational Fluid Dynamics (CFD) was utilised (SolidWorks, Dassault Systems, Velizy-Villacoublay, France) CAD models of the system were developed allowing fits and tolerances to be assessed before manufacture reducing the need for physical prototyping; Figure 6.3 shows the CAD model of the Block 1 device.

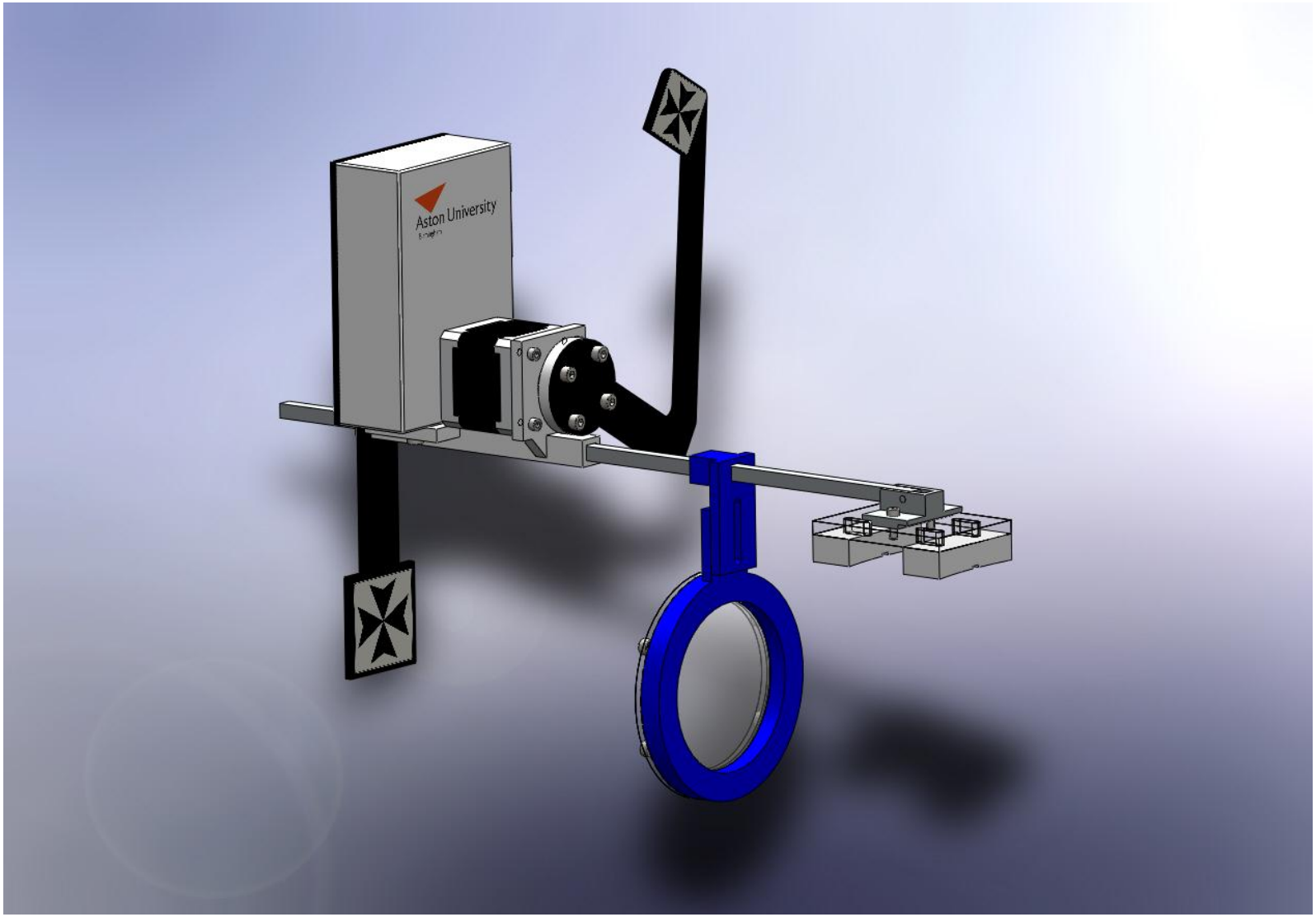

Figure 6.3: CAD model of the block 1 device.

6.5.3 Electronics and Firmware

The stepper motor required a current driving level of 1.7 Amps, voltage of 5V. A dual IC system was developed with a motor and control board and a communication and timing board respectively. Motor driving was controlled with a PICAXE-18 High Power Project Board (PICAXE, Revolution Education, Bath, UK) utilising a PIC16F1847 (Microchip Technology, Arizona, UK) microchip operating at 32MHz and a L293D motor drive IC. The PIC chip was programmed in basic allowing complete timing and control of the stepper motor with individual step resolution and bidirectional control. Full stepping was utilised, as micro stepping was deemed unnecessary because extreme accuracy (<1 degree resolution) was not required for the application. The coding was sufficiently advanced to reduce the holding current to the stepper motor when the target reached the required position, reducing resistive heating, allowing better thermal management of the L293D.

Communication between the PC motor driver was controlled with a Arduino Duemilanove (Arduino, Lvera, Italy) utilising a ATMega168 IC (Atmel Corporation, California, USA) operating at 20Mhz programed in C and complied with the AVR-GCC compiler (Atmel Corporation, California, USA) A custom communication protocol was used to communicate via asynchronous serial cable between the PC and Arduino board. Standard Transistor-transistor logic (TTL) communication between the Arduin and PICAXE board was utilised.

Separate power sources for the drive and control IC were used due to the required current for the stepper motor. Figure 6.4 shows the control and drive electronics on a laser cut Perspex mounting plate (Note, the Arduino Duemilanove was replaced with a Arduino UNO board in a later rebuild).

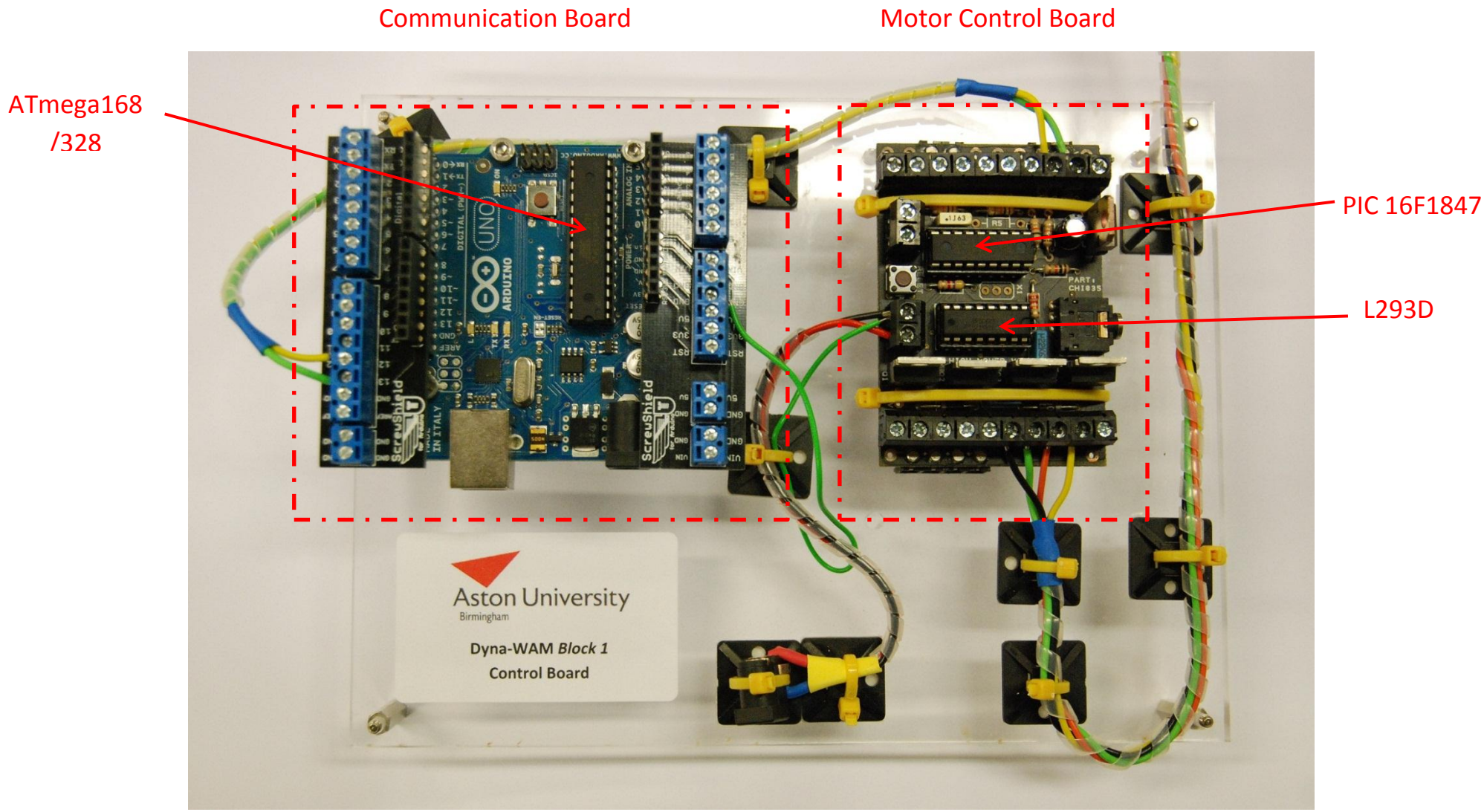

Figure 6.4: Control and communication electronics for the block 1 device.

6.6 Block 1 Typical Data

The majority of the hardware and software development was conducted using a model eye (OEMI-7, Ocular, Bellevue, USA) attached to the WAM-5500. The use of biological analogues in this fashion significantly reduces development times and provided clear indication of calibration errors. Initial *in vivo* dynamic testing was conducted on a small sample of five individuals for proof of concept evaluation. Figure 6.5 show typical scan with no post processing for a 25 year old pre-presbyopic male subject subjected to a stimulus of between 0D and 3D. Three seconds intervals between stimulus cycles were used.

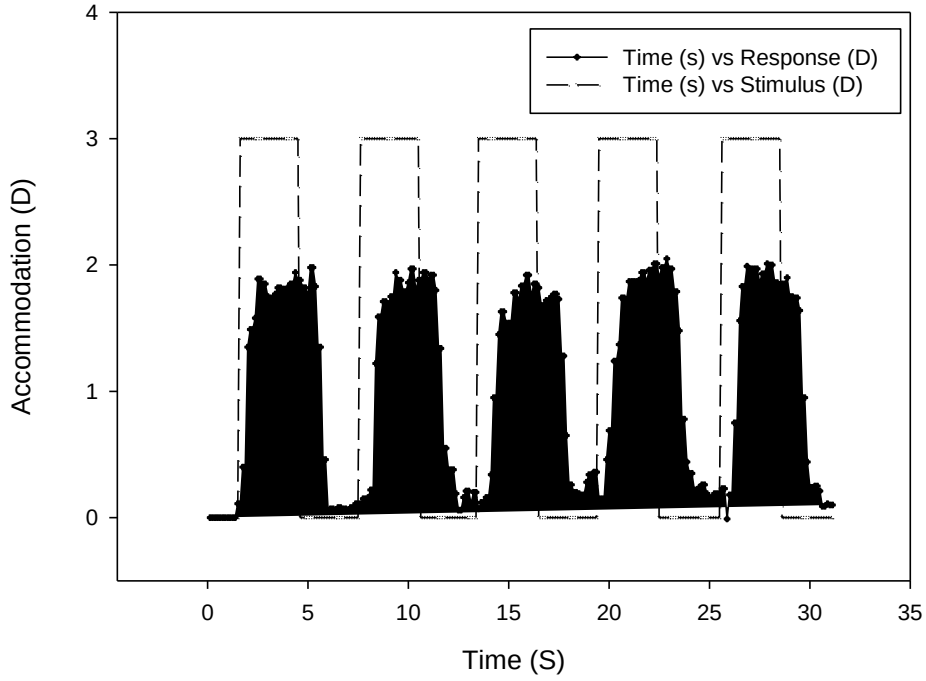

Figure 6.5: Typical trace from the block 1 system with 3 second stimulus between 0D and 3D for a pre-presbyopic subject.

The device showed excellent stability and the resulting trace appeared typical when compared to previous studies with pre presbyopic subjects having average accommodation amplitude of 1.92 ± 0.16D. Testing on a sub sampled group of 6 presbyopes implanted with a Tetraflex accommodating IOL was also undertaken to evaluate the stability and user friendliness of the device. Figure 6.6 shows

a typical (single subject) example of the trace output demonstrating little dynamic objective accommodation at 3 months after implantation average accommodation amplitude was less than 0.4D indicating the subjects were not accommodating. It was decided modification should be made to the device and more rigorous testing was carried out on the Block 2 Device.

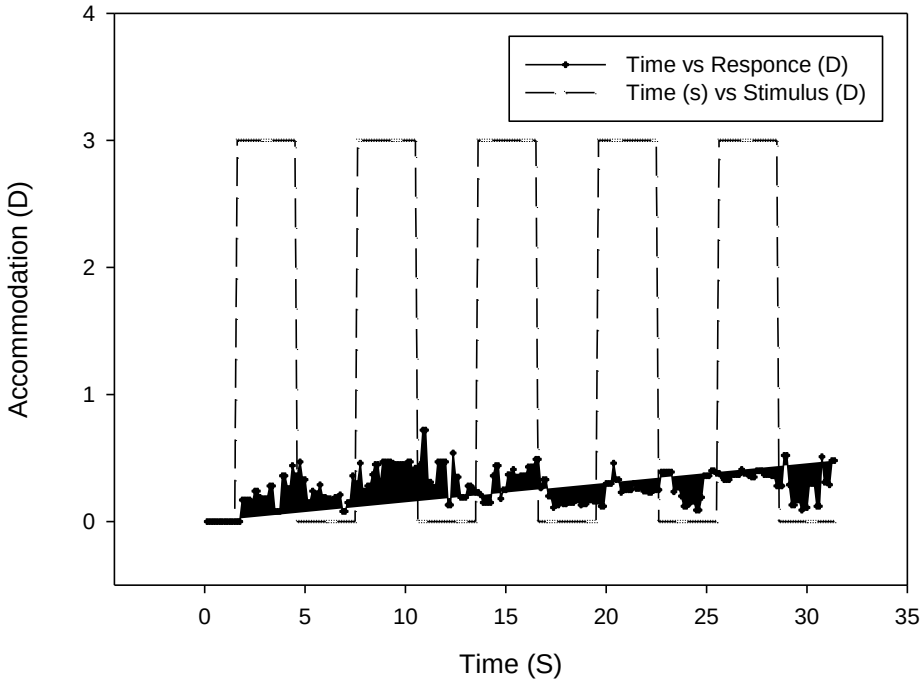

Figure 6.6: Typical trace form the block 1 system with 3 second stimulus between 0D and 3D for an older persbyopic subject

6.6.1 Timing and Accommodation Stimulus levels.

The block 1 device was designed as a proof of principle investigation into the possibility of developing a dynamic accommodation measurement facility for the WAM-5500. The major investigation focused on the software communication between the control PC and the WAM-5500. The first hardware developed was limited to a maximum accommodation stimulus amplitude of 3D. Start accommodation position could be between 4.5D and 0D and was variable to meet the researcher's requirements.

To swing the target into and out of the optical path of the system the target swing arm had to move 283 degrees clockwise then return 283 degrees counter clockwise. The bipolar stepper motor required 200 steps to complete a full revolution. Therefore 157 steps to complete the 283 degrees were required. The full step firing sequence provided maximum torque to avoid swing arm slip between pulsing. A backstop was provided so the target could be manually set to a common datum position before the testing sequence commenced.

The swing arm travel time from the datum position to the optical path was 1.45 seconds using a 9ms delay between each pulse sent. Testing indicated that reducing the pulse delay duration below 9ms reduced the torque provided by the motor beyond acceptable levels. The timing periods remained the same when retracting the swing arm. Figure 6.7 shows the finished device mounted on the WAM-5500.

6.6.2 Discontinuation of the Bloc 1 device

Design evaluation of the block 1 device indicated several areas where hardware improvements were required. Testing indicated the concept could be achieved and a second generation Block 2 device was commissioned to address the following concerns. The cantilever design of the attachment mount between the WAM and target hardware experienced repeated failures between connection interfaces. As the requirement for a fastener less attachment remained paramount a different approach would be utilised in future designs. The maximum accommodation stimulus of 3D was deemed too small for thorough testing; ideally a full range of 4.5D should be achieved. The target swing arm movement time of 1.45 seconds per movement cycle limited the minimum accommodation time possible to approximately 3 seconds. The delay between movement commands and presentation of the target stimulus significantly complicated the design of the control software. Reducing this time as much as possible to near instantaneous would provide much greater

flexibility. The requirement for recording pupil size simultaneously was also deemed useful, and was added to future design aspirations. A post processing system for the rapid determination of metrics such as lag, response time, growth function and accommodation amplitude could also be investigated.

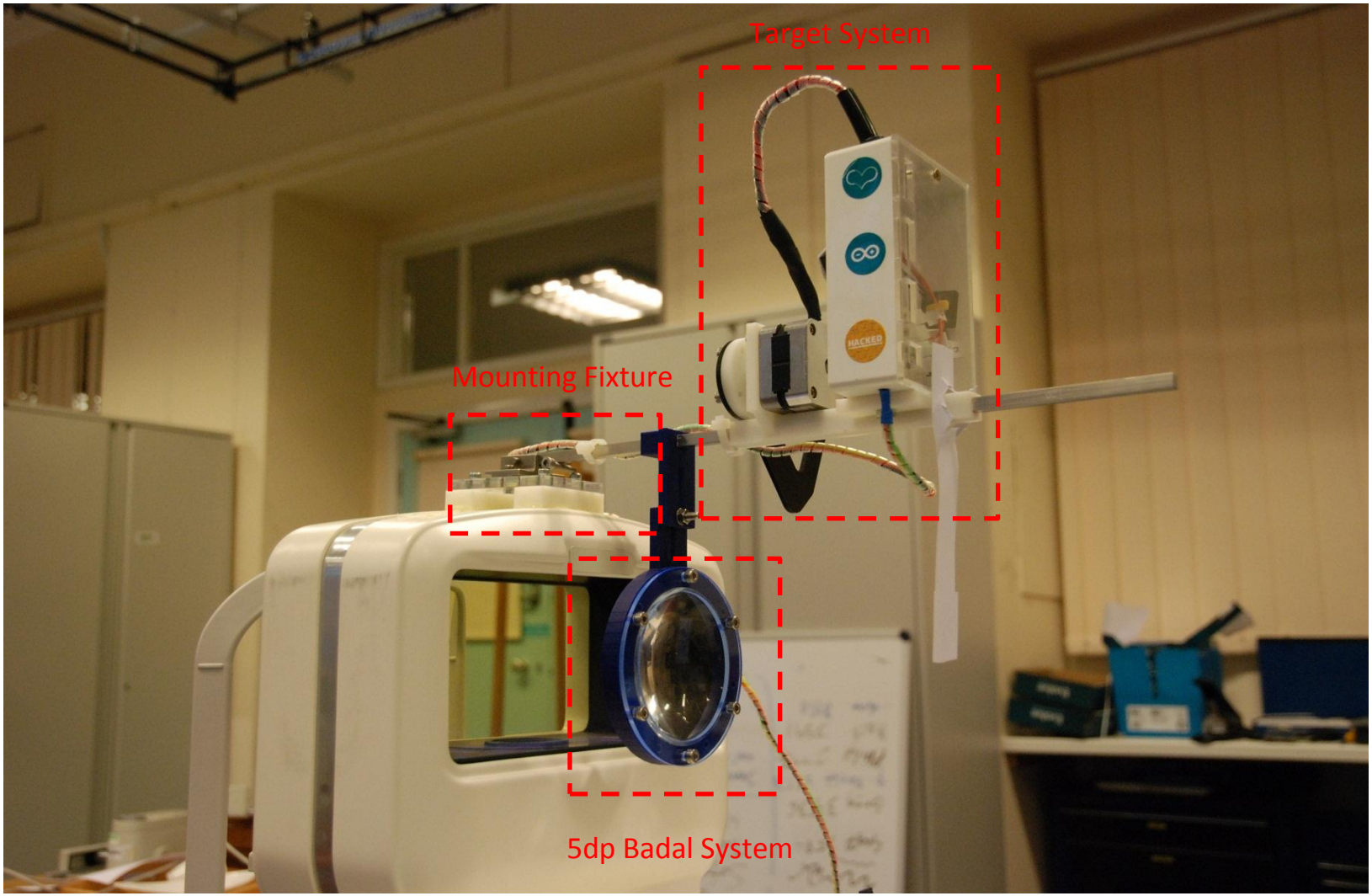

Figure 6.7: Completed block 1 system mounted on the WAM-5500.

6.4 Block 2 Dyna-WAM

The block 2 device was intended to address the design issues apparent with the first generation device. A complete redesign and overhaul occurred changing much if not all of the operational concept. Top mounting was discontinued in favour of mounting on the WAM-5500 shelf via a custom mounting bracket. Stepper motor technology was abandoned in favour of much quicker servo motors. Control electronics were simplified with part count and size reduction. Accommodation range was increased to 4.5D.

6.4.1 Hardware Development

The block 2 device was based around a common rail system where the Badal system, targets and movement hardware can be mounted and positioned independently. Figure 6.8 shows the WAM-5500 shelf and attached mounting plate. The mounting plate was bonded to the WAM-5500 with epoxy resin that will not form a permanently bond to polypropylene (B2012, Bondlock, Worcs, UK). A series of 6 M8 tapped though holes were located on the plate to provide points where pressure can be asserted to detach the place from the WAM-5500 in case there is a need for repositioning. As with the block 1 device a CAD model was produced for the device to reduce the design time and errors in measurement and design. Figure 6.9 shows the CAD model of the Block 2 device. The device comprises of four primary sub-assemblies and 134 separate parts consisting of the following; 1.)Rail assembly 2.)Lens assembly 3.) Target assembly 4.) Moving Target assembly. The rail assembly was manufactured from extruded aluminium profiles (Profile 5, Item Industrietechnic GmbH, Solgen, Germany) and precision laser cut Perspex. The assembly contained the mounting attachments for securing the rail to the WAM top plate, and the indicator ruler for stimuli positions and Badal lens position in dioptres. Accommodation level range was at least 4.5D to 0D. The lens assembly consisted of a 5D (f=200mm) plano-convex 100mm (diameter) lens on a precision machined aluminium rail carrier and laser cut Perspex lens carrier. The lens was repositionable in both height and lateral position on the rail. All aluminium structures were hand machined using 6082 high strength aluminium alloy with T6 temper (J. R. Davis 1993, p.482) allowing precise positioning with respect to the optical axis of the WAM-5500.

Figure 6.8: top mounting plate for the block 2 device.

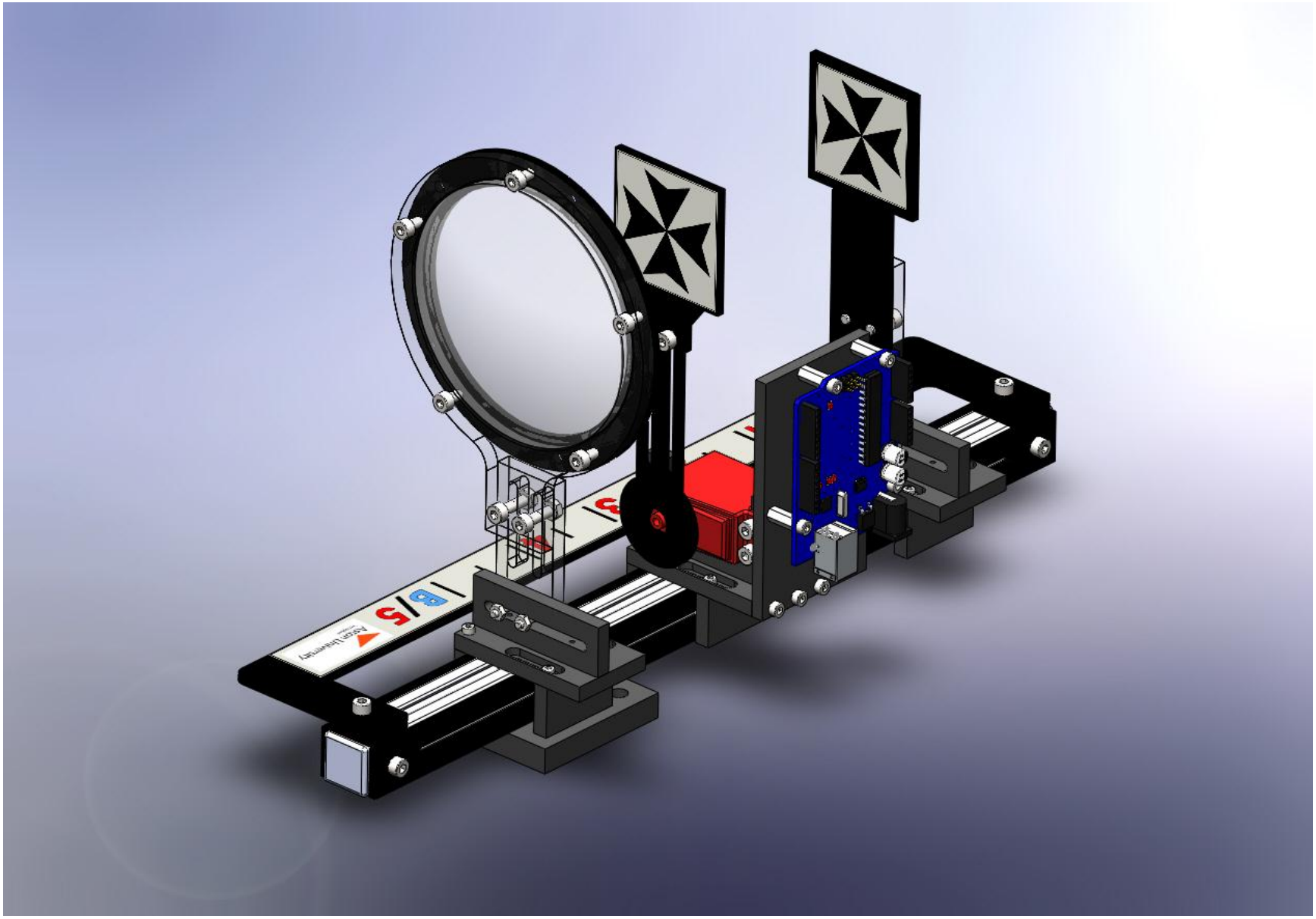

Figure 6.9: CAD model of the block 2 device.

The target assembly consist of an identical rail carrier and positioning system as with the Badal Lens Assembly. Both height and lateral position were tuneable giving the practitioner the ability to align targets in a perfectly overlapping manner, regardless of instrument alignment. Targets were produced by high contrast printing onto a dense card substrate (180 g/m^2) for wear-resistance and with 600x600 dpi printing for optimum clarity (HP 3505dn, Hewlett Packard, Palo Alto, USA). Target rendering and design was undertaken with a professional CAD package (SolidWorks, Dassault Systems, Velizy-Villacoublay, France) producing Maltese cross targets with a square profile of 45mm x 45mm. The CAD package allowed the target to be resized at different scales while maintaining identical geometry and profiles

The Moving Target Assembly was the most complex part of the Block 2 device, hosting the mechanical motive force for target movement and positioning. A high speed digital RC servo (DS650 Digital Servo, Align, Taiwan) was utilised to move the target swing arm. The servo could move the swing arm 60 degrees in 80ms when driven aggressively. Standard Pulse Width Modulation (PWM) was used to drive the servo electronics. The DS650 features titanium high strength low inertia gears for maximum performance. The assembly also features an electronics carrier plate hosing an Arduino Uno development board. A cable management system was also integrated into the plate. Figure 6.10a/b shows the finished device (note a later Seeedunino development board (Seeed Studio, Shenzen, China) is shown rather than an Arduino Uno).

6.3.2 Electronics and Firmware

Both the communication and control of the device was performed by the Atmega 328PU (Atmel Corporation, California, USA) microcontroller (MCU) on the Arduino UNO, later Seeeduino Board. The chip was driven at 20MHz by external oscillators, providing extremely accurate timings. In line with most AVR, MCU's have single clock cycle function executions.

Custom PWM functions are used to generate servo positions. If a pulse width of less than 1.5ms is sent to the servo, it will move anticlockwise, whereas a pulse width of greater than 1.5ms will result in a clockwise direction movement. The sub-routines allowed the servo to be positioned at 180 discrete points over its 180 degree rotation range, enabling tuning of the start reference position and end position. Later models of the Block 2 used a Seeeduino board as a replacement to the Arduino UNO board. The Seeeduino board is identical in operation and execution to the UNO, but features

surface mount technology (SMT) and low profile connectors, allowing better positioning of the USB communication cable figure 6.11a/b

All programming of the MCU's was performed in C and compiled with the AVR-GCC compiler. Custom serial communication protocols were developed allowing the control software to have complete control over the discrete positioning of the servo.

6.4.3 Discontinuation of the Block 2 Device

The Block 2 device solved many of the engineering problems of the Block 1. However it was noted that the digital servo was excessively noisy when holding stationary positions, to the point of startling subjects under test. The device could be improved both in environmental wear resistance and cosmetic appearance. A Block 3 device development was undertaken to address these issues.

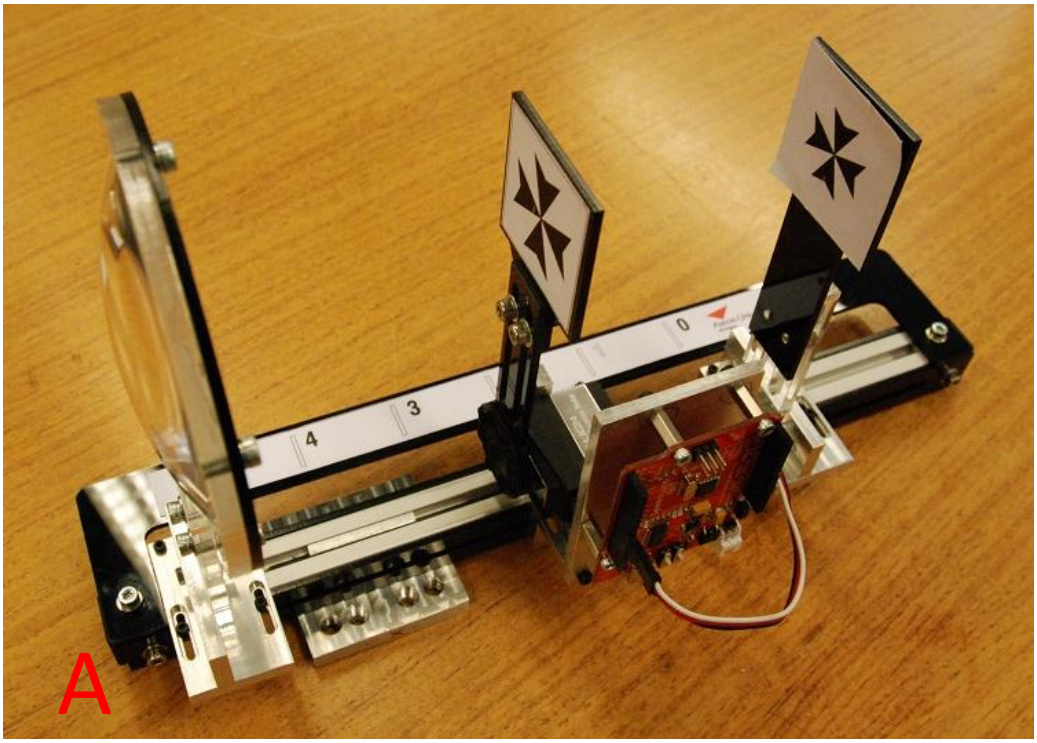

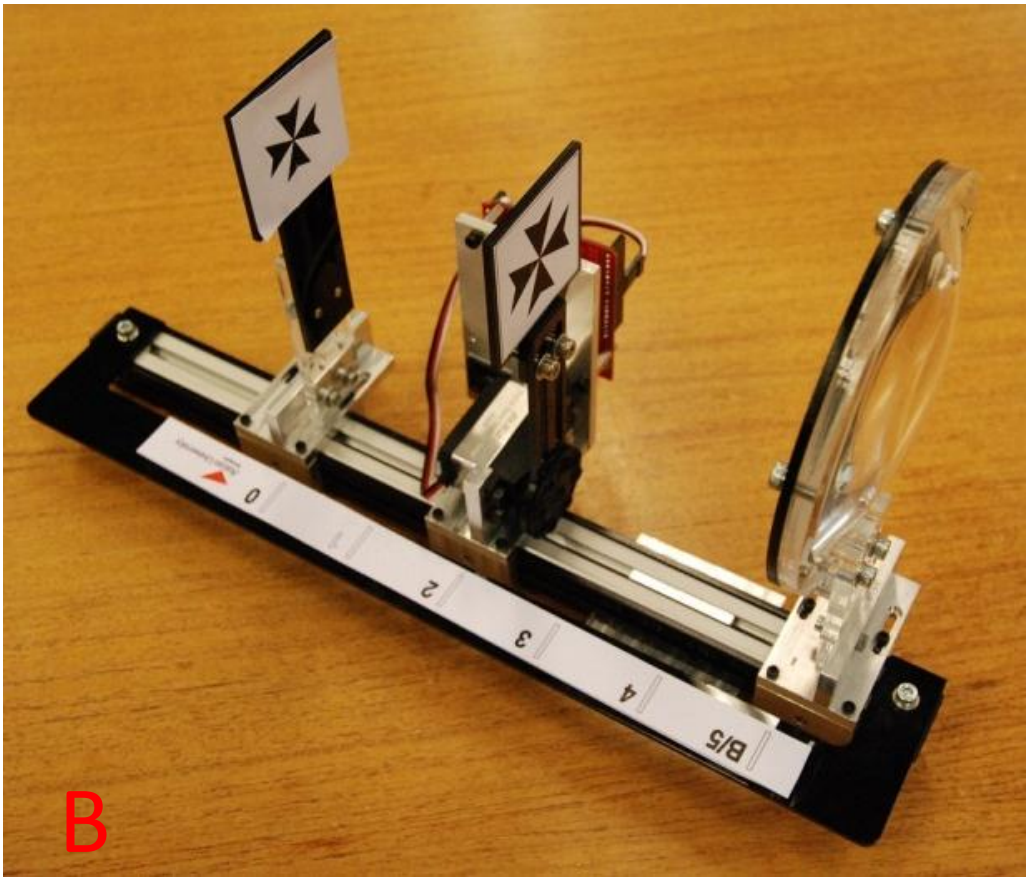

Figure 6.10: (a) The finished block 2 device right side **(b)** Left side of device.

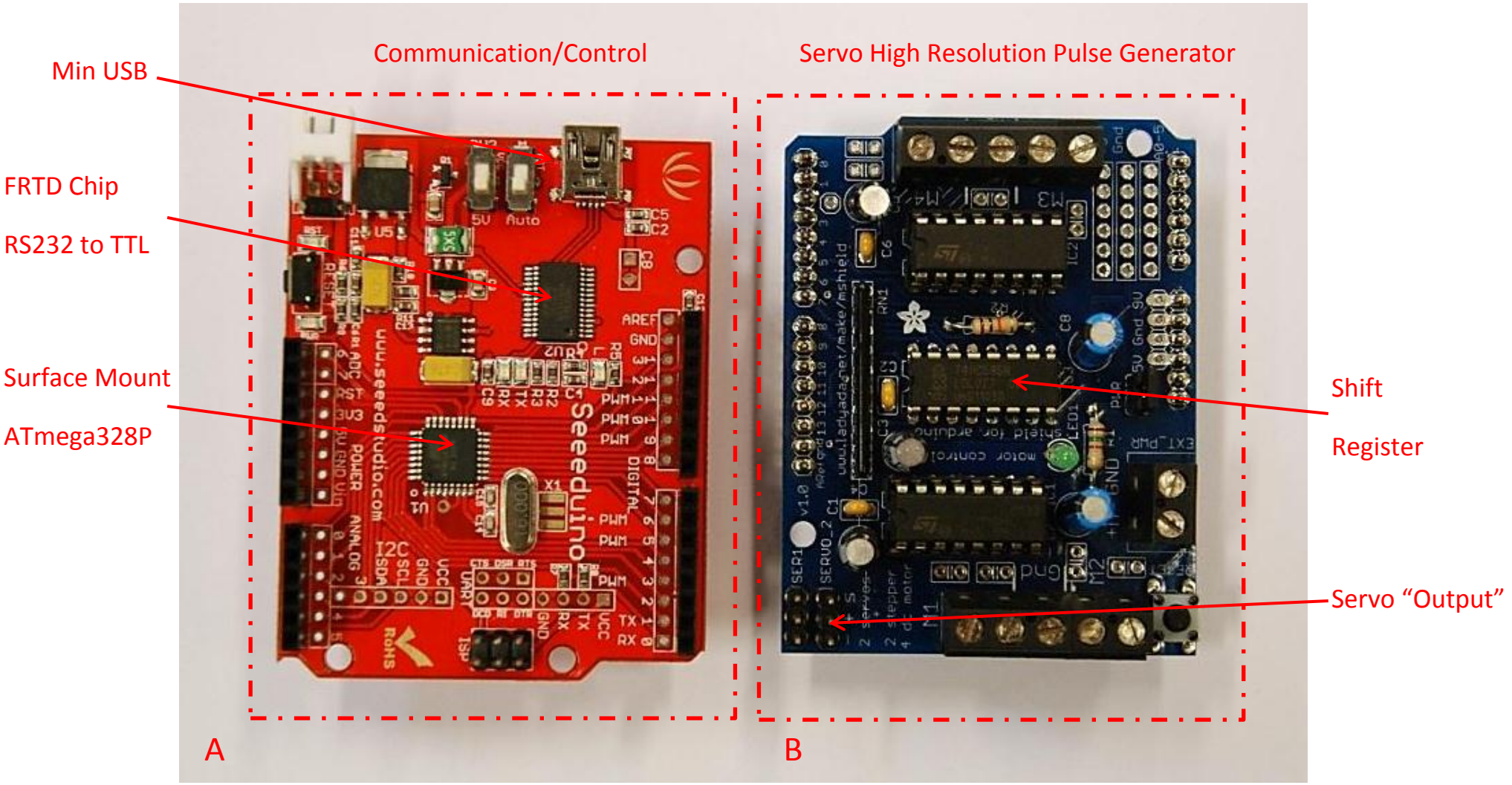

Figure 6.11: (a) The Seedstudio Arduino clone board in SMT conformation **(b)** Adafruit motor driver board.

6.5 The Block 3 Device

The Block 3 device features only minor upgrades in comparison to the progression from Block 1 to 3

6.5.1 Hardware and Firmware

Two major areas of hardware upgrading were undertaken.

1.) The addition of a high speed Adafruit servo/motor driving board (Adafuit Industries, New York, USA)

2.)Acid etching and anodising of all raw aluminium components.

The Adafruit Board is an additional “shield” attachment to the Arduino that provides extra driver hardware for controlling motors and RC servos. Figure 6.11b shows the Adafruit board. In the context of driving RC servos, a high speed digital line directly attached to the Atmega32 oscillator was provided. The addition hardware allowed the PWM signal to be driven at 16bit resolution rather than 8 bit, producing considerably smoother pulse trains. The better driver signal reduced servo ‘hunting’ and thus audible noise. The use of centre aligned PWM also reduced jitter by providing a more constant driver signal. Finally the addition of synthetic silicone high viscosity lubricant into the sealed servo casing helped dampen noise further. Overall noise volumes were reduced to acceptable levels for subject testing.

Acid etching of the uncoated aluminium components was undertaken to improve their corrosion resistance and durability with handling. Aluminium can dull and discolour over time in contact with common corrosive agents (sweat, humidity etc…). The acid etch process removes a few microns from the surface, removing minor scratches and surface imperfections. The anodising process provides a coloured protective coating on the surface, considerably increasing resistant to environmental agents and prolonging component life. A matt black coating was chosen to reduce unwanted surface reflection from the machines aluminium surfaces. Figure 6.12 gives an example of anodised and un-

anodised surface. Figure 6.13a/b shows the Block 3 Device and Figure 6.14a/b shows the final device mounted on the WAM-5500 left and right views respectively.

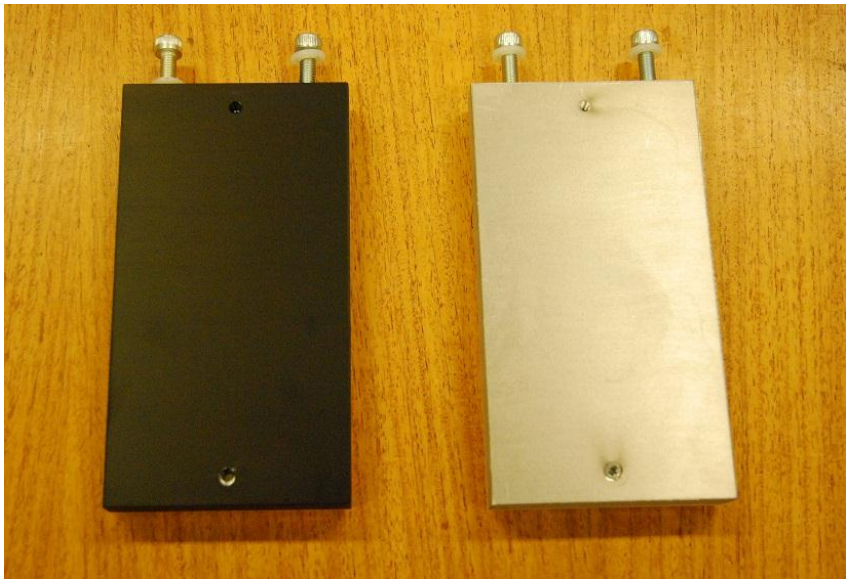

Figure 6.12: Side plate off the Dyna-WAS after and before anodising.

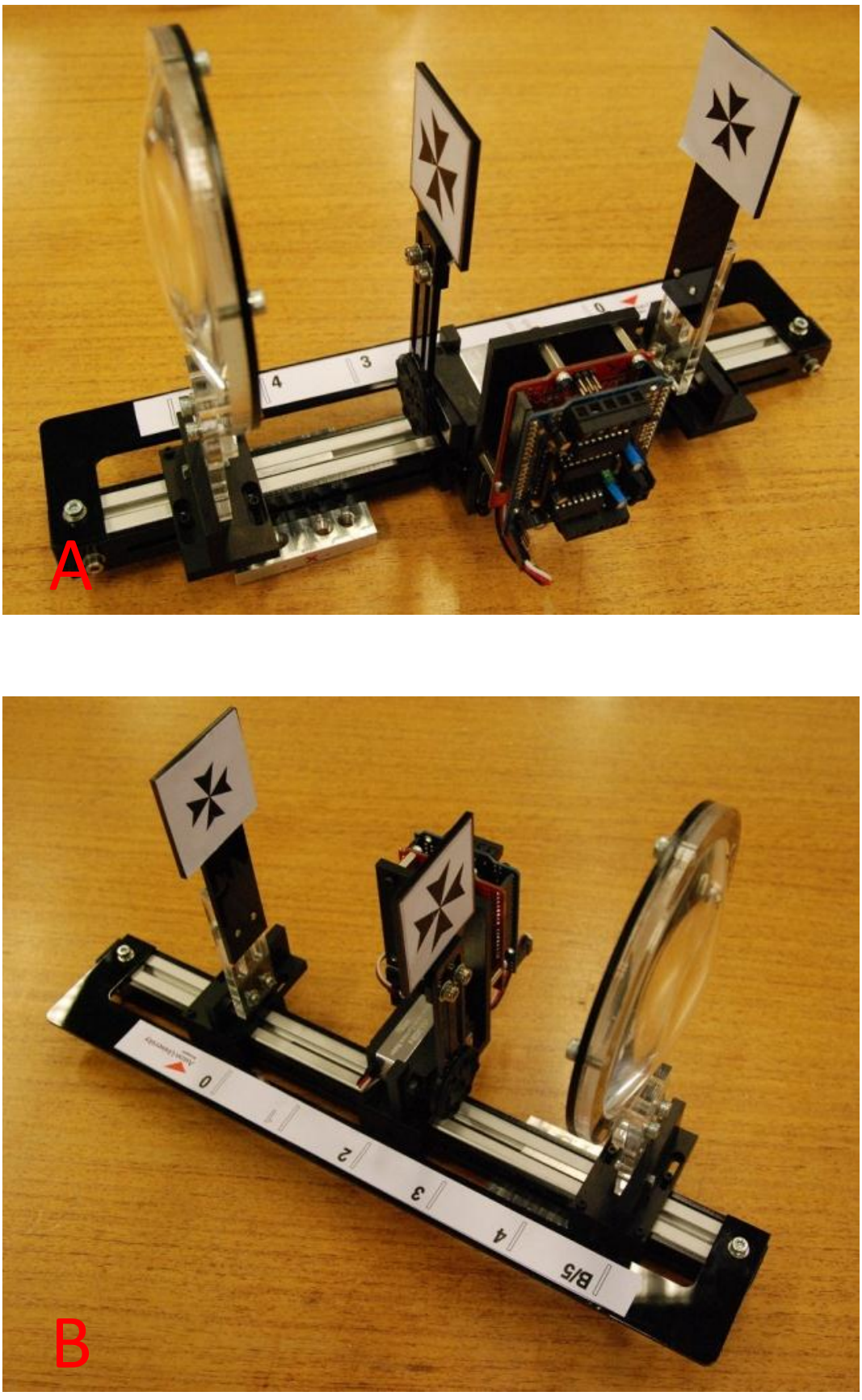

Figure 6.13: (a) Right side view of the block 3 device, note motor driver board and black anodised finish **(b)** Left side view of device.

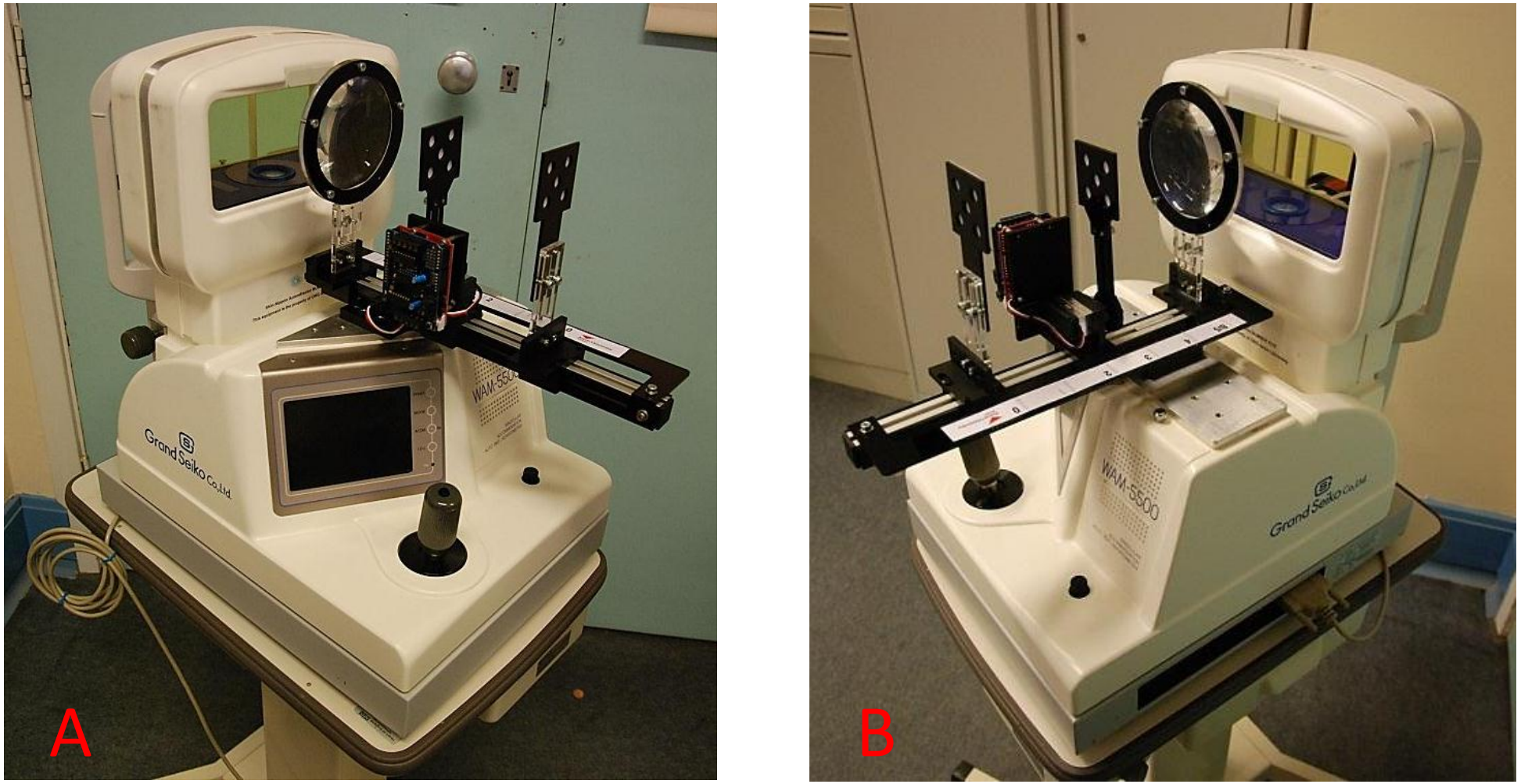

Figure 6.14: (a) Right side view of the block 3 device mounted on the WAM-5500 **(b)** Left side view of device.

6.5.2 Dyna-WAM Hardware Conclusion

The development of the Dyna-WAM hardware proved highly successful, novel and reliable. The use of high speed servo motors (specifically AC Servos) and microcontroller has proven itself appropriate in accommodation research. Currently there is no known competing device available that can provide such flexibility and capability for the testing of accommodation dynamically under controlled conditions.

The development process has highlighted a system of incremental design change and refinement that is highly applicable for the development and modification of custom ophthalmic devices and shall be used for a model for future endeavours. The 3rd generation device was put forward asses the dynamic accommodation response of individuals involved in the study of UV related eye damage. Without the Dyna-WAM device this part of the research would not have been able to be undertaken shows the value of knowledge transfer between the optometry and engineering fields.

6.6 Acquisition and control software

6.6.1 Hardware Interfacing

The WAM-5500 has a serial port (RS232- DB25) located on the right hand side of the instrument. Connection between the control PC and the WAM-5500 is though a standard crossover cable (Null Modem). The device outputs data in the standard RS232 EIA RS-232-C protocol (Seyer 1984, chap.1). The device can operate in manual mode and an automatic mode. Factory board rate is hardware limited to 9600bps, data output is continuous and is automatically triggered immediately after data acquisition.

Manual mode is the systems default setting. Automatic mode cannot be accessed manually from the machine. To activate the automatic data capture mode a set of serial commands are required.

6.6.2 Supplied Software

Grand Seiko supply two software programs with the WAM-5500 as optional extras designed to provide advanced data capture facilities. The Measurement Data Collection (MDC-1) program is designed to receive data directly over the serial directly from the WAM-5500 when operating in manual mode. When the activate measurement button is pressed on the WAM-5500 data is transferred to the MDC-1 program for later post processing.

The second program, the WAM Commination System (WCS-1), a standalone program designed for automatic high speed data collection. The system commands the WAM-5500 into automatic mode where the user can no longer control the data capture manually. A series of serial commands are exchanged between the WSC-1 and WAM-5500. Data capture is stated at a rate of 5Hz and can be saved as a Comma separated variable (CSV) file (Sheppard & Davies 2010).

6.6.3 Communication Protocol

Limited communication protocols are available for the decoding the MDC-1 incoming serial data stream. However no communication protocols are published by Grand Seiko for commanding the WAM-5500 into automatic mode and controlling data collection.

To determine the commands sent by the WCS-1 program a technique for intercepting the live data steam was devised. A combination of hardware port hacking with a logic analyser (Logic 8, Saleae, San Francisco, USA) intercepting communication protocols via custom RS232 to TTL device

(Figure6.15a) and software serial interception was used. Custom communication testing software was developed and is show in Figure6.15b

Three primary commands are required to control the WAM-5500 in automatic mode and are as follows (all transmitted in hexadecimal on transmission channel (TX) Channel)

Start automatic Mode (forces device into automatic mode): **IDO\sR\r\n**

Close automatic mode (set WAM back to manual mode): **IO0\r\n**

Read Command (request instrument to take measure): **S\r\n**

When the read command is sent the WAM-5500 returns a string of 'chatter' in the following format;

Output Data (Received on Rx Channel): **DR000C000**

The zeros are the output data stream. The following digit after the 'DR' marker are the refractive error of the subject under test in the form of the mean spherical equivalent. The three digits following the 'C' character is the pupil diameter in mm. When the WAM-5500 can gather no data for either metric zero values are returned.

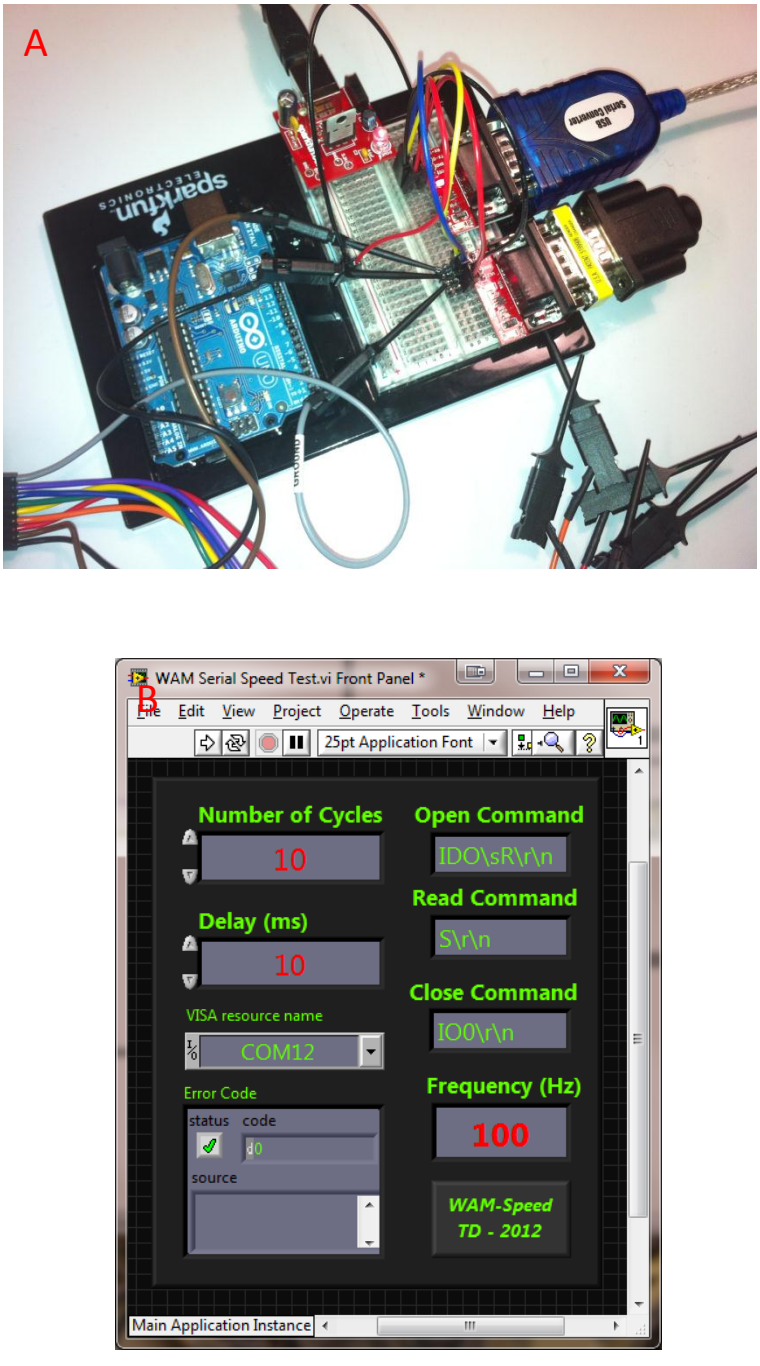

Figure 6.15: (a) Serial interception device RS232 to TTL to RS232, shown with bounce back device to echo commands **(b)** Timing software developed in LabVIEW to incrementally test the communication protocol of the WAM-5500.

6.6.4 WAM Data Acquisition Rate

Testing indicated that the stated data recording rate of 5Hz is not a true reflection of the operation frequency of the WAM-5500. The call and response relationship between the host computer and the WAM was assessed. Figure 6.16 shows the logic analyser traces for a single call request (**S\r\n**) showing an apparent period repeating pattern for calling data. Call requests are not spaced evenly in each cycle. Figure 6.17 shows the entire call pattern that repeats every 1.4 seconds sending 9 individual requests. The WAM-5500 will attempt to return a single reading for each one of these 1.4s second patterns sent. However true return frequency is difficult to determine as when no data is returned the system often falls out of synchronisation. If a call request is received simultaneously when data is sent, the WAM-5500 ignores this call and will only be ready to respond to a following request after transmitting has finished. Therefore the data acquisition rate is not constant throughout testing. The WSC-1 software appears to interpolate between missing data points to give a pseudo 5Hz operation frequency. Direct correlation between output data stream and WSC-1 Data display show little sign of one to one correlation between data points. Smoothing and averaging are obviously employed heavily.

Custom data acquisition software determined a maximum operational frequency of 4.3Hz when good data can be returned. Testing with a broad cross section of subjects determined the operation rate to be between 3Hz and the maximum 4.3Hz when testing under real word scenarios

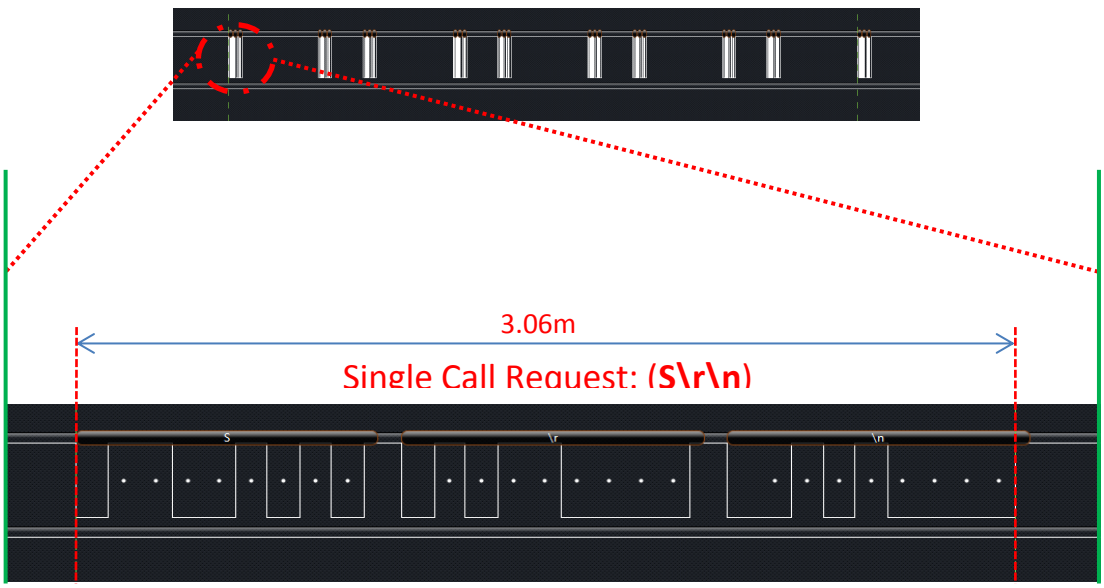

Figure 6.16: Single call for measurement @ 9600bps.

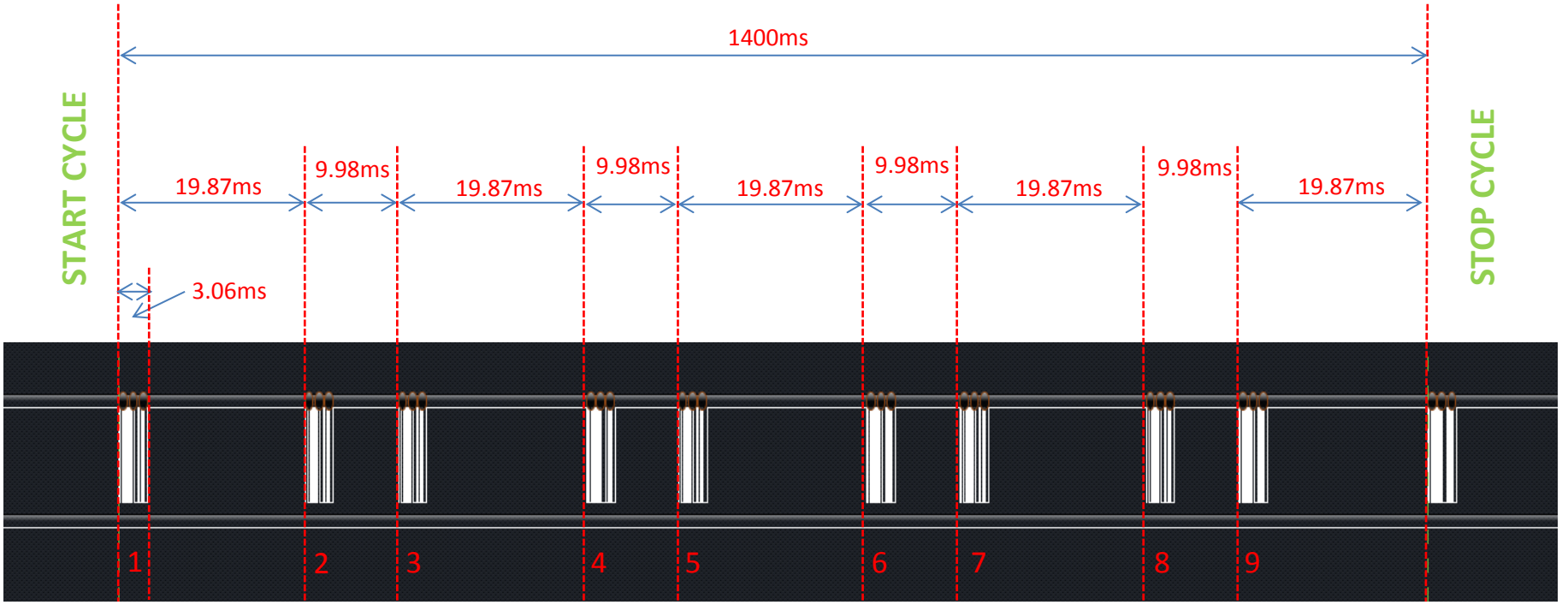

Figure 6.17: Detail of timings between call requests for the WAM-5500 for a single call request cycle form the WCS-1 software.

6.6.5 Block 1 Control Software

After the control parameters and commands were determine, a prototype control and acquisition program was developed. The Block 1 hardware required that there be significant delays in the timing routines for synchronising the data acquisitions and target presentation. Figure 6.18 shows the first generation software. The software is based on the producer and consumer design (PCD) architecture (LabVIEW, National Instruments, Austin, USA) and implemented in LabVIEW Software.

The PCD architecture is designed to allow efficient use of computer resources when multiple operations are taking place that have significantly different timing operations. The user inference displays the accommodation stimulus and measurement reading from the WAM-5500 in near real time. An averaging and interpolation sub routine is utilised to smooth the incoming data stream. When up to three data points are missed in the acquisition phase, data will be interpolated from the last known data point received and the next received data point. If more than three data points are absent, the program will not implement further post processing as the data could be skewed.

The Block 1 software allows the user to select the accommodation time stimuli starting point.
However the target starting accommodation magnitude has to be set manually by moving the Block 1 hardware device to the requited position.

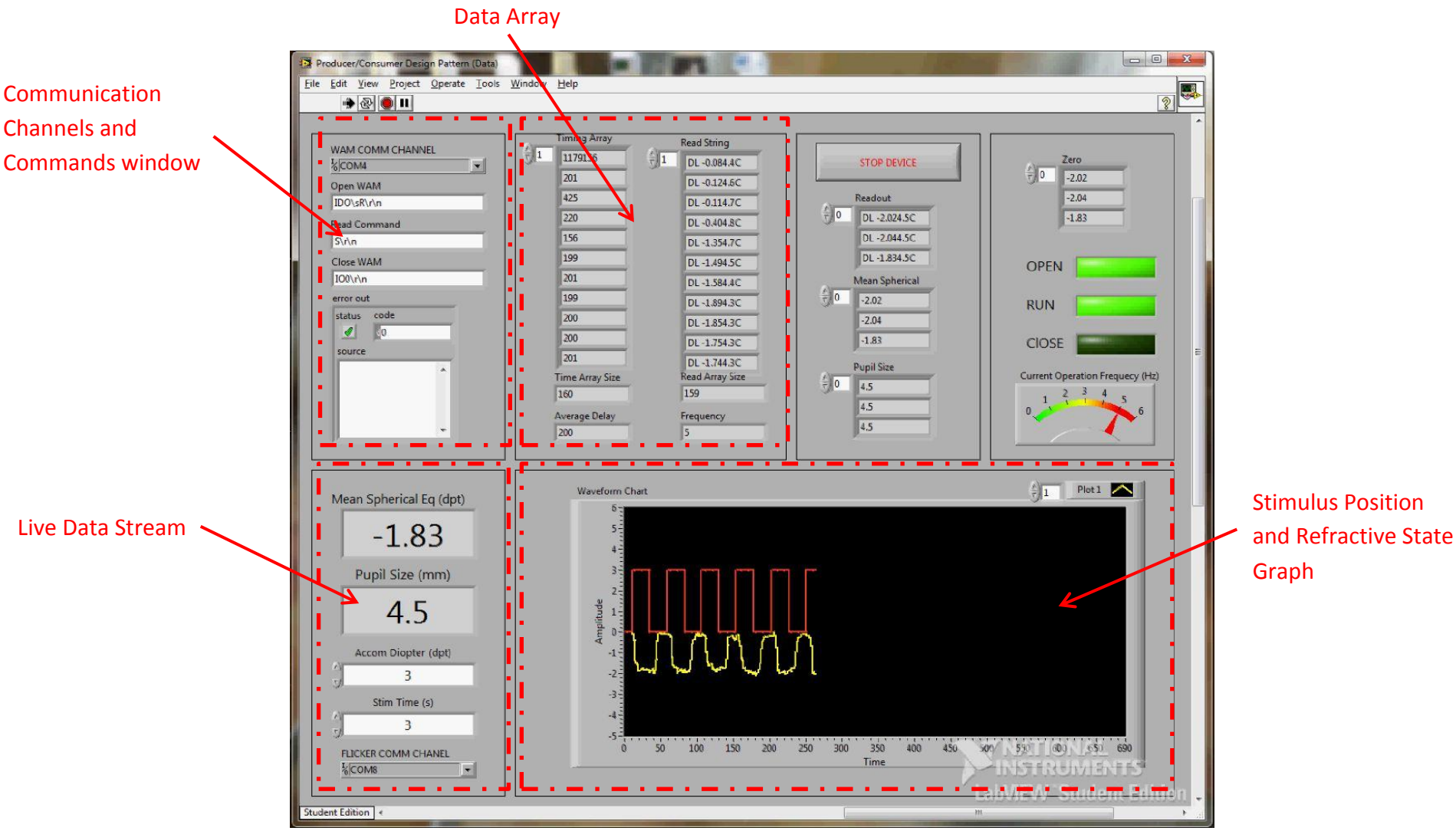

Figure 6.18: First generation software, not the extensive instrumentation for R&D purposes.

6.6.6 Block 2 Control Software

The second-generation software (V1.1) was an improved version of the original prototype software. Improvements were made in both form and function. Optimisation of the execution structure was undertaken with extra functions added. The code could now be stopped mid cycle and the hardware would return to its original default start position. A much simpler user interface was provided, reflecting the software's new requirement to be useable by a broader range of users. Figure 6.19 shows the second-generation software graphical user interface. Default set ups were included so that the user would no longer need to determine the WAM-5500 and Accommodation targets hardware communication channels.

Extra functions were added reflecting the faster operation of the Block 2 hardware and the greater operational range and capability of the device. Recording of pupil diameter, where available, was added. User selectable absolute or relative refractive error measuring was added. Absolute measurement mode overlays refractive error on top of the accommodation target stimulus displayed graphically. The user is provided with a quick straightforward view of the accommodative ability of the subject under test. The live view display still shows the raw refractive data stream from the system numerically. Data could be output to Microsoft Excel for later processing at the request of the user by following on screen instructions.

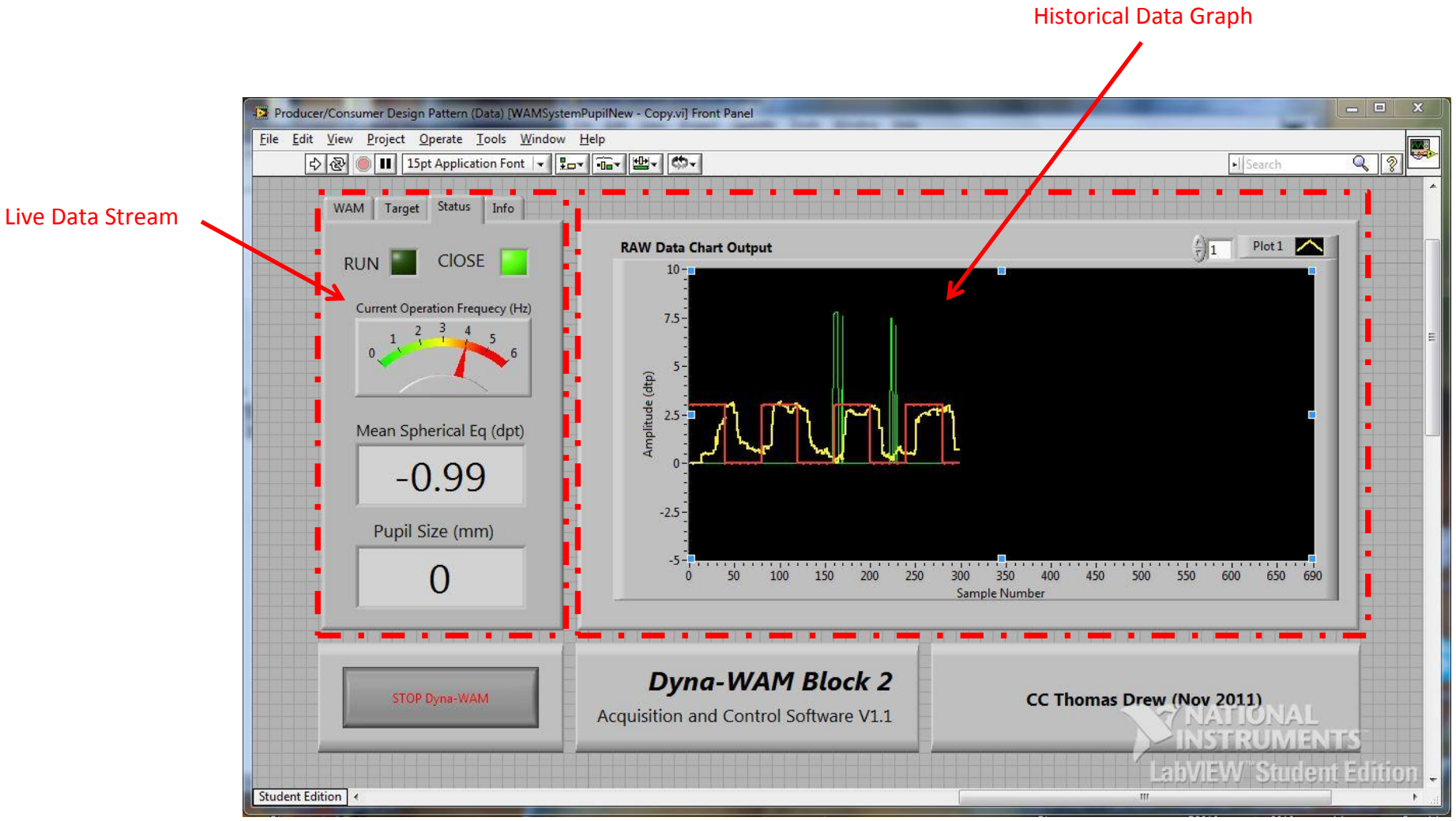

Figure 6.19: Second generation software, improved for user functionality.

6.6.7 Block 3 Control Software

The final generation software (V1.5) produced was the third generation. The increasing complexity of controlling the third generation device necessitated a redesigned coding structure. The producer consumer architecture was integrated within state machine architecture (SM). The SM is a software pattern where decisions at each stage control the next function the code executes (Travis & Kring 2007, chap.13).

Advantages are much-simplified workflow and a greater scalability. Extra functions and stages can be added without extensive re-coding as new states can simply be added to the list of states and the decision logic updated accordingly to give these new states links to previous states. A new dark style interface was added, reducing eyestrain in dark rooms where the device is most likely to be used in practice. All controls are now accessed from a series of tabs on the left hand side of the software GUI. Only relevant data is displayed to the user during testing to avoid unnecessary distraction. The software can now be produced as a standalone executable removing the need for LabVIEW to be installed on the host machine. LabVIEW will still be required for changing certain back panel software setting and is recommended when used in a research context. The software contained self-documenting controls that explain the default settings on the relevant control tabs aiding user interaction. Figure 6.20 shows the block 3 software

6.5.8 Disaccommodation Variant Block 3 Control Software

Further changes to the block 3 software were made to account for asymmetric accommodation and disaccommodation periods. A 1 minute linger time for the 4.5D (dioptres) stimulus followed by 30 seconds for the 0D stimulus was used to test for disaccommodation settling times. The software could be used to do repeat testing, but it was found that the subjects often had trouble concentrating for repeat measures due to the extended nature of the testing.

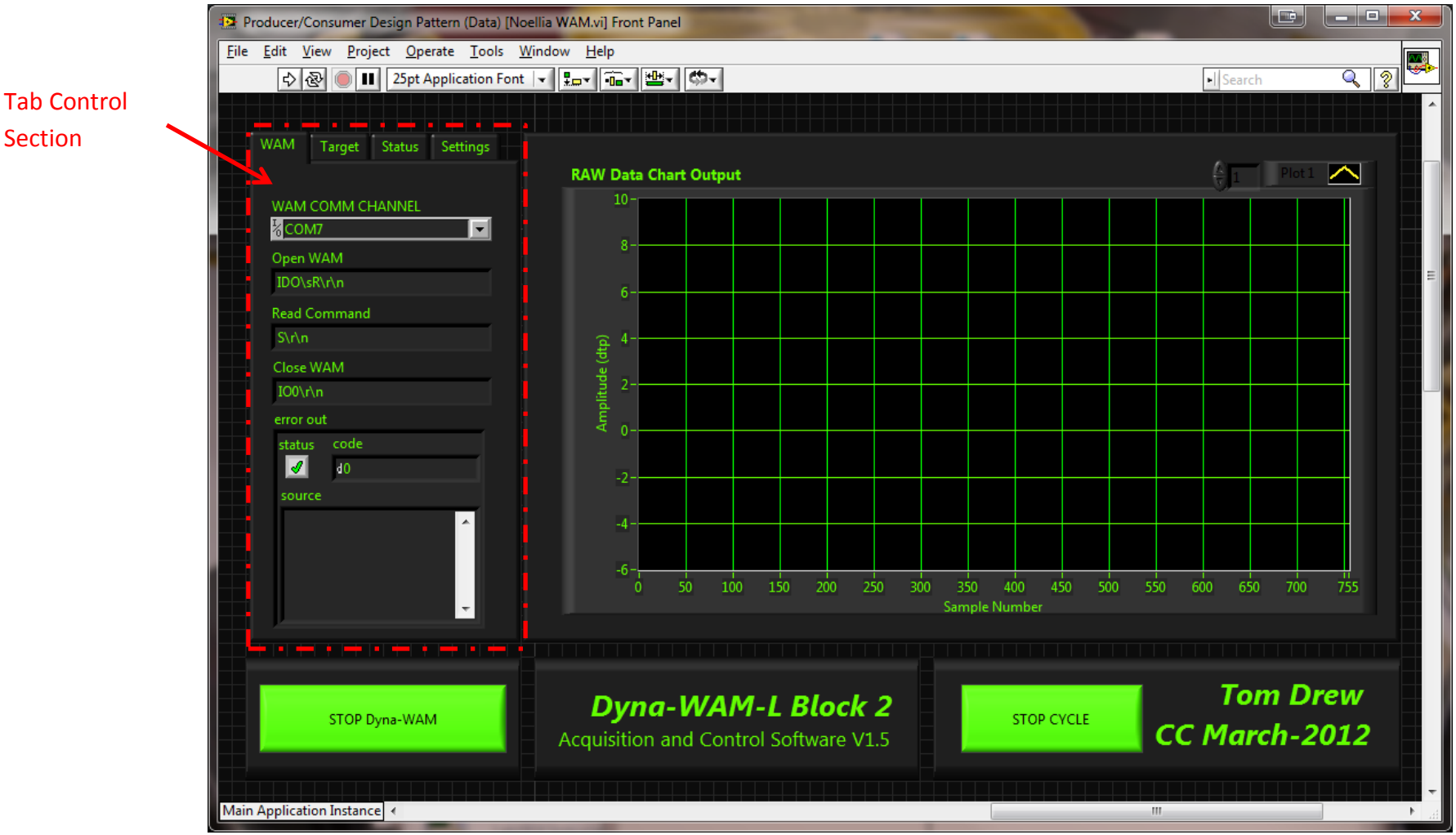

Figure 6.20: Third generation software, improved for user functionality and performance, note the dark style interface to reduce eye strain in low light conditions.

6.5.9 Dyna-WAM Software Conclusion

The Dyna-WAM software was arguably the most challenging part of the development untaken for the device. Three versions have been formally presented, but in reality there were over 10 different iterations developed with LabVIEW for the control and data acquisition software and 6 for the emended software in C for the ATMega328. Each succeeding generation showing incremental refinement of algorithms, improved operation speed and better user interfaces. This is an extremely important process as user feedback is paramount to develop optimum solutions. A close relationship between the engineer and optometrist is important to ensure the device meets practical requirements, something often lacking with commercial instruments.

The controls software gave great flexibility to the practitioner and allowed use of the WAM-5500 in new and novel implementations, expanding the equipment's usefulness beyond a standard instrument. Although the WAM-5500 is bundled with basic dynamic data question software (WCS-1) it lacks any useful form of historical display of data, thus giving very little real-time feedback to the user. It is believed that this is the first time such a comprehensive integrated aftermarket modification, involving both hardware and software, has been undertaken with the WAM-5500. There are further next generation devices planned to expand its capability further.

The bespoke tools and process developed to reverse engineer the communication protocols that control the WAM-5500 have proved very useful. These will be deployed in many future reverse-engineering projects involving instrumentation and in themselves represent novel devices and approaches. This work has strongly highlighted the potential for the cooperation between the engineering and optometry disciplines while developing successful routines for rapid development of instrumentation.

6.7 Clinical Trial Usage of the Dyna-WAM (Block 3)

The Dyna-WAM Block 3 was then utilized within a clinical trial. Although ultra-violet light is recognized as a risk factor for cataract, very little is known about its effect on presbyopia. However, a recent review has highlighted the potential of UV light to cause heat-induced denaturisation of proteins in the crystalline lens, resulting in a reduced ability to focus and cataract formation (Truscott 2009). A high incidence of presbyopia occurring at younger ages has been reported in countries with high levels of UV (Nwosu 1998)

Therefore the aim of this retrospective study was to examine the long-term (over 5 or more years) protective effect of UV filtering contact lenses on accommodative function. The primary hypotheses were that eyes that have worn UV filtering contact lens for >5 years will have a significantly better amplitude of accommodation, a significantly better range of clear focus and a significantly accommodative response for the same accommodative stimulus than eyes that have worn non-UV filtering contact lenses for >5 years.

6.7.1 Methods

Twenty healthy subjects from Birmingham, in the United Kingdom, who had worn UV blocking Acuvue contact lenses for at least 5 years and 20 age and gender matched controls who had worn non-UV blocking contact lenses for a similar period were recruited following informed consent. In order to be enrolled, each subject was wearing their contact lenses, on average, for a minimum of 5 days each week, had best corrected visual acuity of 6/7.5 or better in each eye and were prepresbyopic (aged between 18 and 43 years of age). In addition, subjects were free of ocular surface pathology, significant ocular tissue anomaly, did not have diabetes, had not had eye surgery and were not on any medication known to affect accommodation. The study was approved by the Aston University Ethics Committee and conformed to the tenets of the Declaration of Helsinki.

Investigators were masked as to the contact lenses the subjects wore. Subject demographics of age, gender, ethnicity, height and weight (to calculate body mass index = height x weight (BMI)), iris colour and general health (including smoking), medication, nutritional intake, exercise, body mass index (height and weight) and sunlight exposure were recorded.

Amplitude of accommodation was assessed by averaging 3 repeats of the push-up test. A RAF rule was held perpendicular to the subject's upright face, supported by the patient. With the slider at the extreme end from the patient, evenly illuminated to ≥85cd/m^2, the subject identified the lowest line of letters they could observe and was asked to view these letters, actively focus keeping them as clear as possible. Viewing the letters binocularly, the slider was moved closer to the patient at approximately 0.05m/s until the patient reported blurring of the letters. The slider was then withdrawn at approximately 0.02m/s until the patient confirmed they could resolve the letters clearly. The accommodative demand of this distance of the letters from the eyes was recorded in dioptres.

The range of clear focus was assessed over a range of +1.50D in 0.50D steps to the negative lens where the subject's acuity dropped below 0.3logMAR. Subjects wore their optimum distance correction and viewed an electronic letter chart at 3m evenly illuminated to ≥85cd/m^2. Visual acuity was assessed binocularly on a logMAR chart encouraging guessing and scoring each letter correctly read as 0.02logMAR. The logMAR chart letter presentation was changed for each lens and the acuity recorded. The range of clear focus was determined as the maximum negative lens that could be accommodated with an acuity drop of less than 0.04logMAR as previously described (Gupta et al. 2008).

The stimulus response curve for accommodation and pupil size was be measured from the right eye while viewing binocularly a high contrast Maltese cross at 0.0D, 0.5D, 1.0D, 2.0D, 3.0D, 4.0D and 4.5D of accommodative demand using a Grand Seiko WAM-5500 validated autorefractor in a Badal optical system(Sheppard & L. N. Davies 2010). The dynamics of accommodation were assessed by rotating a Maltese cross at 3D accommodative stimulus into and out of the line of sight of a second Maltese cross positioned at optical infinity, at 5s intervals. The pseudo 5Hz dynamic recording of the WAM-5500 autorefractor was captured by a personal computer which communicated and synchronised with the microcenter and AC servo controlling the presentation of the Maltese cross so the response time, speed of accommodation, response amplitude, and time to relaxation and speed of relaxation could be evaluated from three repeated accommodation and relaxation cycles. The device is explained in details within chapter 6. The dynamics of accommodation were determined using the algorithms of Kasthurirangan and colleagues (Kasthurirangan et al. 2003). The latency was determined from the time between the onset of the accommodative demand and the first point of three consecutive increasing data values, followed by four consecutive data values in which no two consecutive decreases occurred. The inverse algorithm was used to determine the start of the accommodative relaxation response. With the latency section of the trace removed, each accommodative and relaxation trace was fitted with an exponential function (APA Beers & Heijde 1994; AP Beers & Heijde 1996; T. Yamada & Ukai 1997) which iteratively found the best fit based on least squares weighting to equation 6.1:

$$y = y_0 + a \times (1 - e^{-t/\tau}) \quad \textbf{(6.1)}$$

6.7.2 Sample Size and Statistical Analysis

The variability (95% confidence interval) of the push up test is ±1.43 D so detect a 0.75 D change (80% power, 0.05 significance level) requires 15 subjects in each study arm (Rosenfield & Cohen 1996). The variability of defocus curves is not known, but the variability of the acuity measurement at each level of defocus is ±0.08 logMAR so to detect a 2 letter (0.04 logMAR) change would require at least 16 subjects (Rosenfield & Cohen 1996; Lovie-kitchin & Brown 2000). The variability of autorefractor measures of accommodation have been shown to be 0.18 D so to detect a 0.10 D difference requires at least 13 subjects (Sheppard & Davies 2010). Therefore 20 subjects were recruited in each group.

6.7.3 Results

The cohorts of subjects who had worn UV blocking or non-UV blocking contact lenses for at least 5 years were matched for age, gender, BMI, mean spherical equivalent (MSE) refractive error and best corrected visual acuity (BCVA).

	UV blocking lens wearers	**Non-UV blocking lens wearers**	**Significance**
Age (years)	29.6 ± 6.4	31.1 ± 7.4	p = 0.169
Gender (male/female)	5 / 20	5 / 20	
Ethnicity	3 / 20	5 / 20	
BMI	25.4 ± 6.0	23.3 ± 2.1	p = 0.194
MSE (D)	-3.6 ± 1.8	-4.0 ± 1.6	p = 0.110
BCVA (logMAR)	-0.14 ± 0.07	-0.14 ± 0.07	p = 0.766
Servings of fruit/veg	15.8 ± 12.3	22.1 ± 11.6	p = 0.091
Weeks of strong sunlight	2.1 ± 3.5	1.7 ± 1.3	p = 0.456
Smokers	6 / 20	1 / 20	
Using nutritional supplements	7 / 20	5 / 20	

Table 6.1: Overview of data form the clinical trial.

The amplitude of accommodation assessed with the push-up test was similar (p = 0.217) in eyes that had worn UV blocking contact lenses (9.91 ± 1.82D) compared to eye that had worn non-UV blocking contact lenses (9.50 ± 1.98D) for at least the previous 5 years shown in Figure 6.21

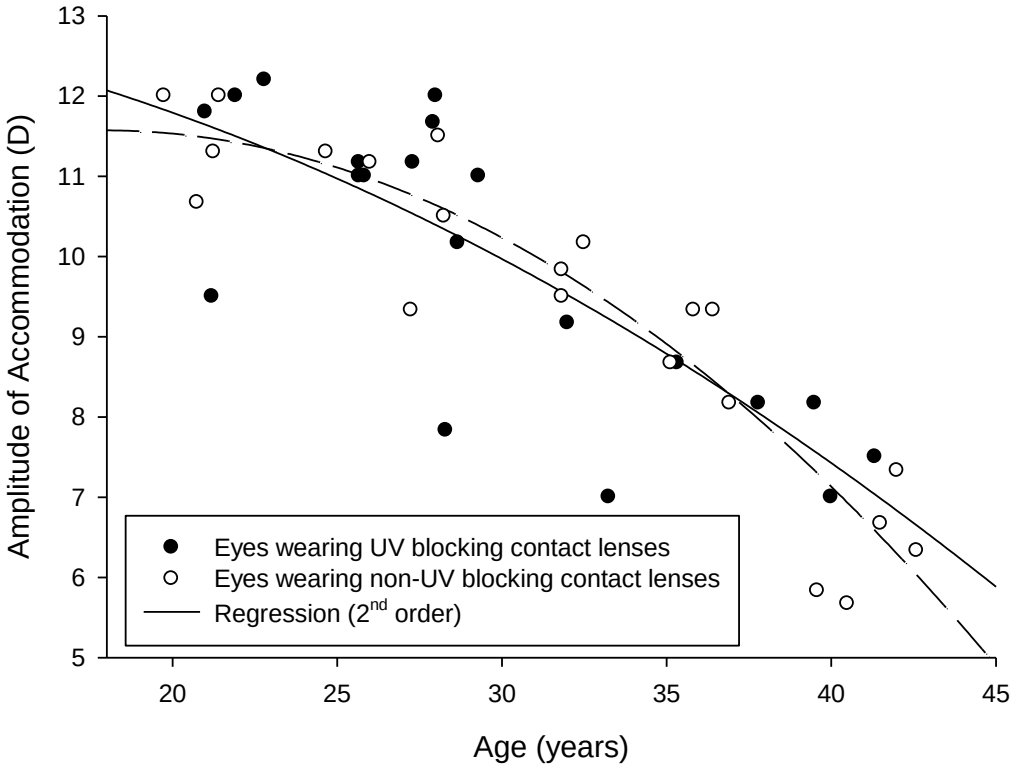

Figure 6.21: Subjective amplitude of accommodation with age for eyes wearing UV blocking contact lenses (solid symbols and line) compared to eyes wearing non UV blocking (open symbols and dashed line) contact lenses for at least 5 years n=40.

The range of clear focus assessed with defocus curves was similar ($p = 0.783$) in eyes that had worn UV blocking contact lenses (4.28 ± 2.22D) compared to eye that had worn non-UV blocking contact lenses (4.20 ± 1.81D) for at least the previous 5 years. No significant difference at any accommodative demand level was found (Repeated measures ANOVA $F = 0.309$, $p = 0.586$; shown in Figure 6.22).

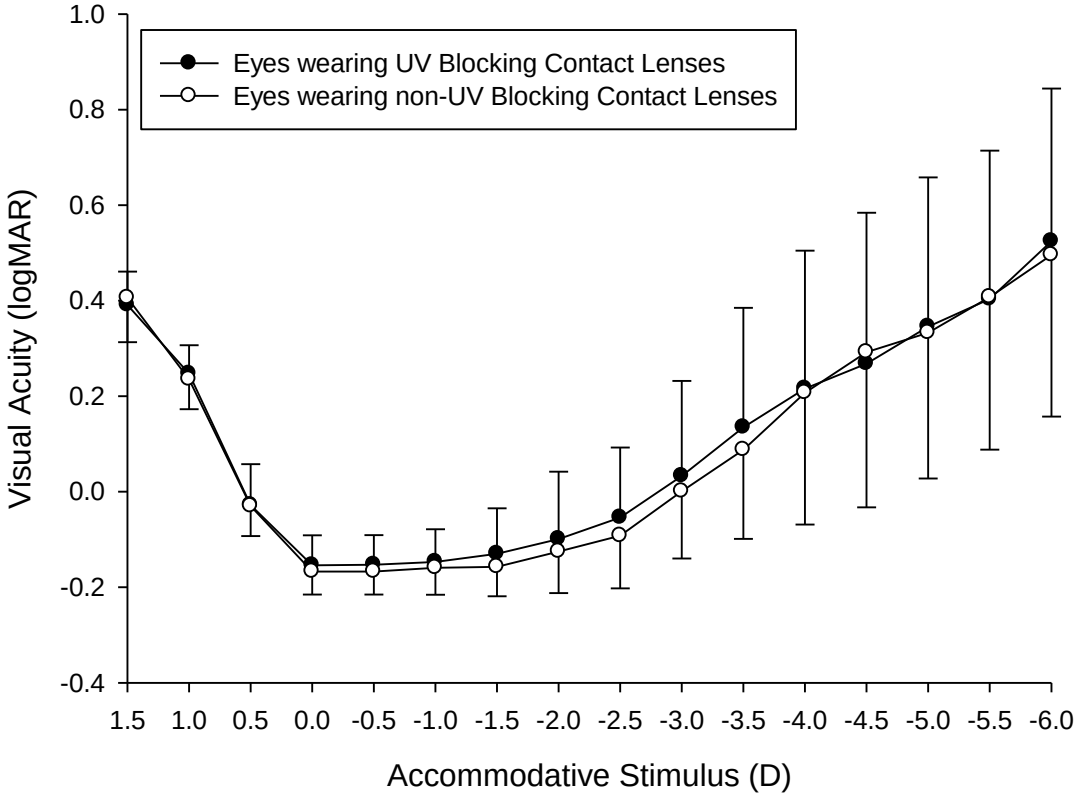

Figure 6.22: Defocus curve for eye wearing UK blocking contact lenses (solid symbols) compared to eyes wearing non-UV blocking (open symbols) contact lenses for at least the last 5 years. Error bars = 1SD n =40.

The accommodative response measured with an open-field autorefractor increased with the accommodative demand of the stimuli from optical infinity to 5.0 D ($F = 225.31$, $p < 0.001$), but did not significantly differ between eyes that had worn UV blocking and non-UV blocking contact lenses for at least 5 years (Repeated design measures ANOVA $F = 1.926$, $p = 0.181$; shown in Figure 6.23). However, the average accommodative response was consistently higher in eyes that had worn UV blocking contact lenses for at least the last 5 years (on average by 0.25±0.15D; $p=0.010$). Pupil size significantly decreased with increasing accommodative demand (ANOVA $F = 636.939$, $p < 0.001$), but did not significantly differ between eyes that had worn UV blocking and non-UV blocking contact lenses for at least 5 years (Repeated measures ANOVA $F = 0.044$, $p = 0.836$) with no interaction between them (Repeated measures ANOVA $F = 1.595$, $p = 0.155$; Show in Figure 6.24).

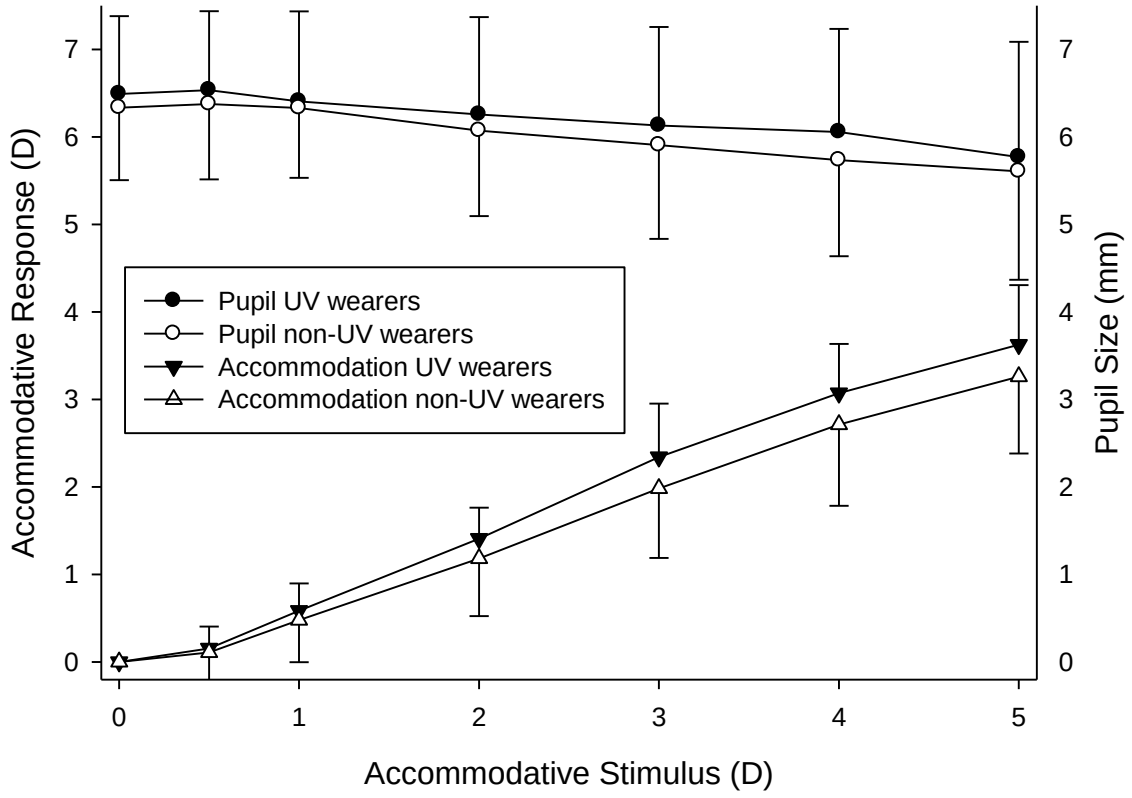

Figure 6.23: Accommodative (triangular symbols) and pupil (circular symbols) response to accommodative demand for eyes wearing UV blocking contact lenses (solid symbols).

The exponential algorithm used to describe the dynamic accommodation and relaxation (Figure 6.24) described the data well for both eyes that had worn UV-blocking contact lenses (r^2 = 0.870 ± 0.085; r^2 = 0.924 ± 0.137; respectively) and eyes that had worn non UV-blocking contact lenses for at least 5 years (r^2 = 0.823 ± 0.139; r^2 = 0.908 ± 0.072; respectively). Accommodative latency was shorter in eyes that had worn UV-blocking contact lenses (0.288 ± 0.128s) than eyes that had not worn UV-blocking contact lenses for at least 5 years (0.363 ± 0.068s, p = 0.044) but relaxation latency was similar (0.326 ± 0.023 vs 0.338 ± 0.043s, p = 0.456). Initial accommodative level (p = 0.812) and the amplitude of the change (p = 0.271) was similar between the two groups, but the speed of response for both accommodation (p = 0.026) and relaxation (p = 0.027) described by the time constants was greater in eyes that had worn UV-blocking contact lenses (3.754 ± 2.184;3.985 ± 2.559; respectively) than eyes that had not worn UV-blocking contact lenses for at least 5 years (2.700 ± 1.985; 2.300 ± 1.094; respectively).

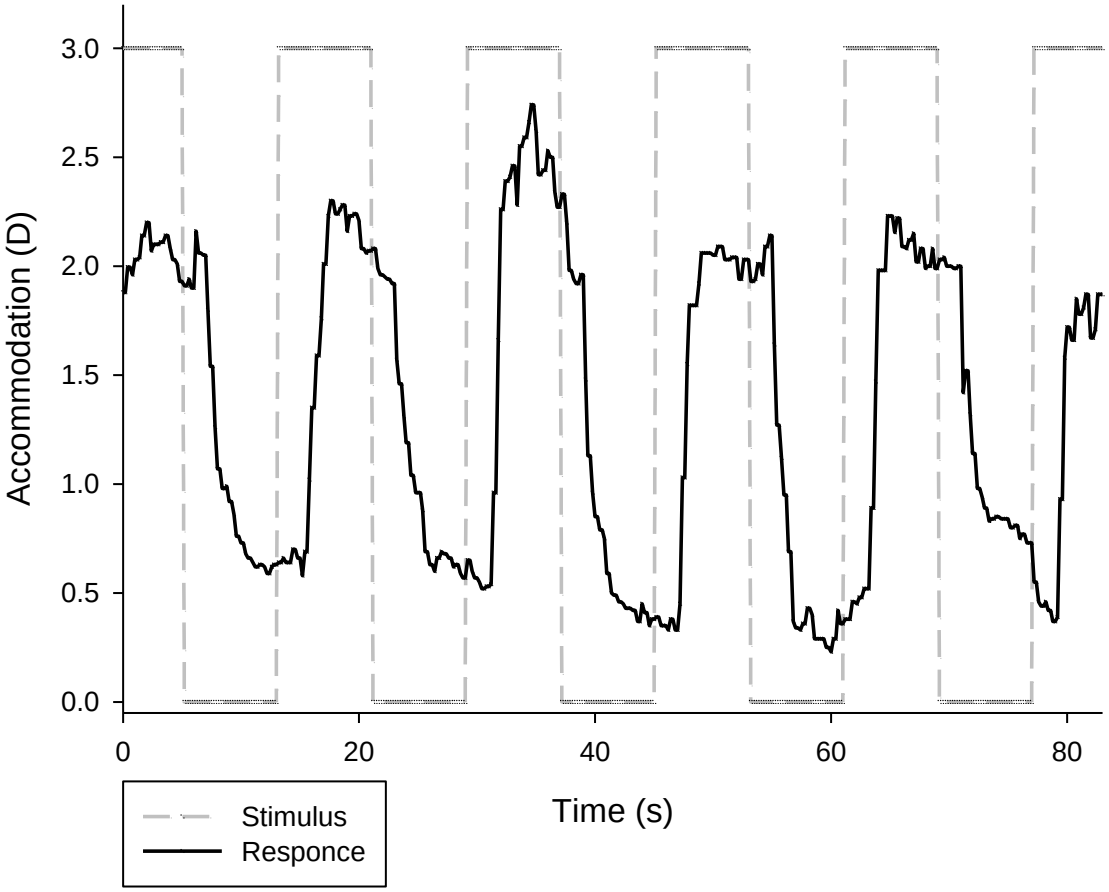

Figure 6.24: Example of dynamic trace of accommodative stimulus for a 0D to 3D stepped accommodative demand.

6.7.4 Study Discussion

Although there is strong evidence that shielding the skin from UV is beneficial, there is no conclusive evidence for the eyes. Therefore this study examined the retrospective effects of wearing UV compared to non-UV blocking contact lenses on ocular accommodation. The cohort consisted of 40 subjects, 20 who had worn UV blocking contact lenses at least 5 days a week for the past 5 years and an age and gender matched control group of 20 subjects that had worn contact lenses at least 5 days a week for the past 5 years, but whose material transmitted exposed UV to the ocular surface. These groups had similar ocular and physical characteristics although it was interesting that those patients that wore UV blocking contact lenses generally took less care of their health, with more smokers and less fruit and vegetable intake in this group, although this did not reach statistical significance.

UV has the potential to reduce the ability to focus through heat-induced denaturisation of proteins in the crystalline lens (Truscott 2009). The subjective assessment of the range of clear focus in this study did not find any significant difference in absolute accommodative range with UV protection. This could have resulted from the lower exposure to strong sunlight (on average about 2 weeks a year) compared to countries with higher levels of UV where a high incidence of presbyopia occurring at younger ages has been reported (Nwosu 1998). The, on average, 0.4D difference in amplitude of accommodation between the two groups could delay presbyopia by about 5 years extrapolating from Figure 6.21 which would be clinically significant to patients. Interestingly, the objective assessment with an autorefractor consistently showed more accommodative response to increasing accommodative demand in those eyes that had had UV protection, although the differences between individuals rendered the different at each level statistically insignificant. Dynamic assessment of accommodation confirmed that absolute levels of accommodation were similar regardless of ocular UV protection, but dynamic aspects such as accommodative latency and speed of response for both accommodation and relaxation were faster in eyes that had worn UV-blocking contact lenses for at least 5 years. Speculating, this could relate to a reduced ability of the lens fibres being able to slide past each other with oxidative UV damage, whereas amplitude of accommodation could be more dependent on the lens bulk which is not affected by UV Hence it would appear that there are UV related lens changes that could be protected against to reduce the impact of presbyopia.

Chapter 8

Chapter 7.0 Aston Tearscope Replacement

7.1 Introduction

The Aston Tears is designed to help with the diagnosis of dry eye and enhance the practitioner's ability to fit contact lenses. The aim of the project is to enhance the patient experience by producing a more functional hand held device addressing some of the shortcomings of Keeler's now defunct Tearscope (London, UK). Aston Tears will not be limited to range of functions of the current Tearscope as advancements in illumination and imaging technology have given the potential for a new generation of hand held device in an extremely compact footprint.

The Keeler Tearscope Plus is a hand held device designed to allow the practitioner to assess the quality of the tear film. It uses a broad spectrum cold cathode source that is diffused via a filter. The Tearscope produces a diffuse illumination of the cornea, reflected from the tear surface and produces coloured interference fringes from the lipid interface. A grid pattern can also be fitted to the illumination source that produces a set of reflected concentric circles (mires) on the surface of the film. This allows the practitioner to visualize the shape of the cornea and how the tear film is interacting dynamically with the corneal surface. A timing device is included that is simply a push button stopwatch that allows the timing of the non-invasive tear break up time (NITBUT) to be recorded. It has no internal memory for storing data and no camera for capturing images. A mounting kit is included with the Tearscope that gives the flexibility for it to be attached to a slit lamp biomicroscope. The capabilities of the slit lamp provide better viewing optics and stable manoeuvring for the Tearscope and if a digital slit lamp is available, images or video may be captured. The Tearscope is used in conjunction with coloured fringe charts that show what kind of colours and patterns are formed by patients with different types of dry eye and ocular pathology (Guillon 1998). With practice the Tearscope can be very useful in contact lens fitting and assessment (Guillon 1998). Because all measurements are performed by eye they are susceptible to human error and are subjective. Studies have shown that different people can often disagree on the particular point of NITBUT (J. J. Nichols et al. 2002) a major drawback of the Tearscope. By digitising the image with the Aston TearMaster it is hoped that viewing on a larger screen and the ability to review the video captured will improve the reliability of the measurement of NITBUT, improving the sensitivity of detecting changes with pathology and contact lens wear. Contact lens fitting is one of the core businesses for optometrists but studies have shown that as many as 50% of contact lens wearers suffer from some form of dry eye which is considered to be one of the major reasons for

discontinuation of contact lens use (J. Wang 2003; Graeme Young 2004). Producing instrumentation that could increase the take up and continuation of contact lens ware can add profitability for the practitioner. The Tearscope can be used with sodium fluorescein staining but is not optimised for molecular excitation.

Hence the aim of this study was to show the advantages of collaboration between engineering and health professionals to develop a novel, inexpensive solution to replace the Keeler Tearscope which is no longer in production and perhaps improve on its reliability.

7.2 The Tear Film

To develop a modernised version of the Tearscope it was first required to investigate the physics of the tear film and the operation principles of the device.

The pre corneal tear film (PCTF) is most commonly described as a three layer system, comprising of a mucus, aqueous and lipid layer. Each layer has specialised functions. The tear film smooths the surface of the cornea (epithelium) filling in small irregularities improving the surface quality of the eye thus improving the optical performance of the cornea (Rieger 1992).

7.2.1 The Mucus Layer

The mucus layer is the layer directly in contact with the surface of the cornea and sclera primarily composed of mucin. Mucin is produced in all vertebrates and contains various proteins, carbohydrates, vitamins and micronutrients (Patel & Blades 2003). In the context of the eye it is produced by goblet cells to provide hydration, oxygenation and nourishment to the cornea(Heald & Langham 1956). The mucus layer helps the tears spread and cover the eye during blinking, keeping the eye lubricated, helping the eyelid glide over the surface of the eye ball (reducing friction). The mucus layer is viscous in nature helping carry foreign bodies and contamination away from the corneal epithelium while enhancing wettability of the corneal epithelium. There is some considerable variation between accepted thicknesses for the layers of the tear film (King-Smith et al. 2004). Measurements tend to differ, often considerably, between measuring techniques. However an excepted value for the thickness of the mucus layer is 5-7 µm, it is also accepted to be between 10-100 times more viscous than the aqueous layer (Braun & Fitt 2003)

7.2.2 The Aqueous Layer

The aqueous layer, generally modelled as the middle layer of tear film, is produced by the lacrimal glands and is the largest component of tears by volume (Patel & Blades 2003). Composition is mainly water and a mixture of proteins. Its primary purpose is to aid the wetting, spreading and stability of the tear film, allowing the eyelid to glide smoothly over the eye surface without causing friction or contact damage. There are also anti infection components contained within its composition, supplied by the body's immune system, helping retard the growth of bacteria, reducing the eyes susceptibility

to infection. Accepted thickness is between 4-10 µm (King-Smith et al. 2004). The aqueous layer has a high purity, only 2% solids by volume, and is often modelled as pure water (Braun and Fitt 2003). This supports the 3 layer model of the tear film as there is minimal cross contamination from the mucus or lipid layer into the aqueous layer

7.2.3 The Lipid Layer

The lipid layer is the outermost layer of the tear film, in contact with the environment, and is comprised of lipids (oils) which due to their lower specific gravity, float on the aqueous layer. The primary purpose of the lipid is to seal the aqueous and mucus layers from environmental exposure to prevent excessive evaporation. The surface tension and elastic nature of the lipid layer stabilises the tear film and smooths out surface irregularities while resisting environmental factors such as surface tension induced flow and humidity differences. Surface tension between the lipid layer air interfaces has being measured between 43.3 – 46 mN/m, which is considerably more than the pure water air interface 72.3 mN/m. An excepted value for the lipid layer thickness is 0.1-0.2 µm (Sudi. Patel & Blades 2003)

The melting point of the lipid layer varies and is primarily determined by the different proportions of intermixed lipids resulting in a material with a liquid and solid phase. (Driver & Michael A 1996) found eye lid surface temperature is approximately 30 degrees centigrade with corneal surface temperature ranging from 32-36 degrees centigrade (Purslow & JS Wolffsohn 2005). The melting points of normal secretions were believed to be between 32-33.8 degrees centigrade. Melting points of subjects with Meibomian Gland Dysfunction (MGD) were stated to be higher than this but this was not quantified.

7.2.4 The Role of Eyelids in Tear Film Production

The lacrimal glands are located above and temporally to the eyelids and are primarily responsible for providing the aqueous components of the tear film to the upper lid via the excretory ducts (Braun & Fitt 2003). The Meibomian glands ducts, located on the rims of the eye lids, excrete the lipid layer and the mucus layer is produced by the goblet cells on the conjunctiva. The upper and lower lids both have tear menisci which are the primary storage location for the tear film. The tear film is spread over the corneal surface by blinking. A typical blink lasts about a third of a second and covers approximately 1cm (Braun & Fitt 2003). The tear film adheres to the corneal surface and eyelids via

surface tension and pressure differentials menisci are formed between at the interface between the tear film and lid margins with gravity plays a role reducing meniscus size on the upper lid interface while increasing the size of the lover lid (King-Smith et al. 2004) . Pressures under the eyelids on closure during blinking have being showed to be 10-51 mmHg (Prydal et al. 1992). Blinking has also been shown to be affective in mechanically removing particles and cellular debris (Wolkoff et al. 2005).

During the post blink period, particles in the tear film can be seen moving upwards towards the upper lid. This effect may well be a combination between the momentum transferred to the fluid by the upstroke of the eye lid and pressure differentials caused the establishment of meniscus between the tear film/tear layers and the ocular surface/eye lids post blink (King-Smith et al. 2004). Studies have shown that the average settling time for the tear film in healthy eyes is approximately 1 second and is slower in patients with dry eye (Norihiko Yokoi et al. 2008). It was theorised that this slowing in tear movement is a result of altered viscoelastic properties due to gland deficiency affecting the composition of the layers and this mechanical properties of the tear film.

7.2.5 Optical Properties of the Tear Film

The tear film is often modelled as being a single structure with a single refractive index of n=1.337 (Barbero 2006). However, due to the relative difference between refractive indices being the major factor governing the reflection between mediums, ignoring the lipid layer could cause inaccuracies. Lipid layer refractive index has been found to be 1.482 (J. M. Tiffany 1986) and the aqueous 1.334 (Craig et al. 1995) Values for the mucus layer were not quantified due to their similarity with the aqueous layer.

7.2.6 Six layer model of the tear film

The three layer tear film had being accepted as an accurate representation of the tear film, with many researchers basing their rational on its acceptance. The primary assumption in the three layer system is a clear and well defined contrast between layers. A six layer system has being suggested as a more realistic possibility where the three layers remain the same as the standards model but contact points between each layer are interfaced by a zone of gradual change from one medium to the next (Korb 2002, p.20). The effect of this change is that reflections from the boundaries are not

as easily quantified due to Snell's law of refraction assuming instantaneous infinitely small boundary layer between the two substrates. For practical purposes, the difference may actually have very little effect on the magnitude of measurements generated. The tear films aqueous and mucus layers have such similar refractive index that they could be assumed to be a single phase of the tear film.

7.2.7 Tear deficiency and Testing

Each layer of the tear film provides a role in stabilising the overall system; each is susceptible in different ways to causing the onset of instability. Dry Eye Syndrome (DES) is a medical condition that affects millions people in the worldwide (DEWS 2007) Dry eye is the general term given to deficiencies in tear film that can cause medical problems and complications to the individual. It is often described by a patient as discomfort such as, itching, soreness, tiredness of the eyes or similar. In fact, most people have experienced this condition often when working for extended periods of times with computers and visual display units (VDU) due to a reduction in blinking when concentrating (Wolkoff et al. 2005). Dry eye can be explained by evaporative water loss from the eye linked to gland and blinking deficiencies (Shimazaki et al. 1995)

The DEWS report was generated by experts in the field and provides a consensus as to the current definition, proposed mechanisms and validity of diagnostic techniques (DEWS 2007). Dry eye related tear deficiency was separated into Aqueous Tear Deficiency (ATD) affecting the middle aqueous layer of the tear film and Lipid Tear Deficiency (LTD) affecting the outermost lipid layer of the film. Tear Film evaporation rates have being shown to vary between 0.24 and 1.45 μm/min with a healthy intact lipid layer and 7 μm/min with a compromised one (J. J. Nichols et al. 2005). Estimates for volumes of tears covering the ocular surface range from 2.75 μL to 7 μL (Sudi. Patel & Blades 2003).

Establishing which layer is causing the problems for the patient can help guide treatment. Two principals conditions causing dry eye are Meibomian Gland Dysfunction (MGD) and Sjogren's Syndrome (SS). MGD manifests itself as a reduction in thickness of the lipid layer of the tear film. MGD is caused by blockage of the Meibomian glands resulting in reduced secretion of lipids into tears. The second condition, SS is an autoimmune response deficiency in which the body's immune system attacks the body's moisture producing cells. Specifically the lacrimal glands when referred to in an ophthalmic scenario. The lacrimal glands can be severely affected diminishing there capability to produce the aqueous components of the tear film. SS is the leading cause of severe dry eye and can still remain somewhat resistant to treatment (DEWS 2007; Goto 2004).

7.2.8 Testing For Aqueous Tear Deficiency

Aqueous tear deficiency is currently assessed in vivo by techniques with differing levels of invasiveness.

2.8.1 Tear volume Quantification

The Schirmer Test (ST) is designed to infer the production rate of aqueous components of tear film by assessing the volume of tears present. The process involves placing a strip of filter paper (35 mm wide and 5 mm wide) into the lower conjunctival sack. The filter paper wicks moisture away from the tear reservoir via capillary action. Aqueous quantity of the tear film is assessed by measuring the spread of fluid along the length of the paper. Over a five minute time period a transit distance of less than 5mm is regarded as ATD, between 5-10 mm is borderline ATD and greater than 10 mm is regarded as normal (Korb 2002, p.70; Rieger 1992). Care must be taken when placing the test strip into the eye to avoid causing a reflex tear response that would render the test void requiring a rest period and reapplication. A local anaesthetic can be applied to the eye beforehand to minimise this risk of reflex tearing, although the resulting change in ocular surface osmolality can affect measurement (A. Bron 2001).

The phenol red thread (PRT) test is similar to the ST. It involves placing a cotton thread impregnated with phenol red PH into the lower conjunctival sack. The alkaline nature of the tears will cause the phenol to react and display a red colour change, clearly showing the distance wetted along its length. The advantage of this method is that it is only required to be placed on the ocular surface for fifteen seconds producing the required wetting in the majority of healthy eyes, rather than five minutes with the ST, thus reducing the invasive nature of testing. A secondary advantage is the reduced size and thus required tear volume to saturate the thread compared to the ST a longer distance is wetted making it easier to determine borderline cases of ATD. FRT is less rigid than the ST reducing its chance of causing irritation to the eye. Less than 10 mm of wetting in 2 minutes is required as an indicator of ATD (Sudi. Patel & Blades 2003)

The tear meniscus height is another indicator of tear volume. A greater radius of curvature of lower tear meniscus indicates a greater tear volume and has been used in the diagnosis of dry eye and the determining the effectiveness of punctual occlusion (N Yokoi et al. 2004). It is estimated that between 75-90% of the tear volume is stored in the upper and lower menisci (Holly 1986).

7.2.9 Tear film visual enhancement

It is often problematic to image the tear film due to its thin and transparent nature. Sodium fluorescein (SF) is a water-soluble yellow dye. In the presence of blue light with a peak emission of 495 nm, the molecules are exciting and fluoresce, emitting a wavelength of 510-520 nm (Peterson et al. 2006). When used for slit lamp examination, fillers can be used in both optical paths of the system; in the illumination system (traditionally a cobalt blue) and the viewing optics (traditionally a Wratten no 12- yellow) are used to increase the intensity and visibility of the dye to visualise the tear film. It is also noted that the addition of SF reduces TBUT though altering the fluid properties of the tear film, potentially skewing the measurement (Pflugfelder et al. 1998).

7.2.10 Ophthalmic dyes for examining dry eye induced ocular surface damage

It has long become common practice in biology to stain cells for better viewing. The first use of fluorescein due in ophthalmology was in 1886 by Paul Ehrlich (Erlich 1886). There are currently three primary stains used in tear film imaging. These are Sodium Fluorescein, Lissamine Green (LG) and Rose Bengal (RB). SF accumulates in the interstitial spaces created by discontinuities in the corneal epithelium. Tear film thickness can be assessed by the intensity of the colouration over the corneal surface (Goto 2004). Hence SF can be used to determine when characteristic holes form in the tear film appear, following a blink, referred to as the tear break-up time (TBUT). Very small quantities are used (1 mg, approximately 1 ml) and it is generally non irritating in most patients. Application can be via controlled solution, but is more commonly now purchased in disposable dry applicators (fluorets) for ease and convenience of use and reduced risk of cross contamination (Peterson et al. 2006). The use of hermetically sealed units also reduces the risk of contamination of a bulk solution. SF is widely used in optometry but some studies indicate that its addition to the tear film alters its physical properties such as its viscosity and dynamic behaviour (studies have shown the tear film to be behave as a fluid whose viscosity is dependent on level of shear forces present i.e. a Non-Newtonian fluid) (Prydal et al. 1992; Kaura & J. Tiffany 1986; J. Tiffany 1991). The rationale behind the tear film behaving in this method is to aid its spreading and adhesion on the eye. The increased pressure placed on the tear film by the lid closing (i.e. a sheering force) causes a reduction in the viscosity of the fluid, allowing it to spread better under the closed eye lid condition. After eyelid contraction the viscosity of the fluid increases, producing a more stable and reactive tear film (Németh et al. 2002).

Rose Bengal is water-soluble staining agent that shows the location of dead or damaged cells mainly on the conjunctiva overlying the sclera and the corneal epithelium. It is used in contact lens fitting to see if any superficial damage has being caused to the surface of the cornea with prolonged wear and if prolonged dry eye and discontinuities in the tear film with the related loss of lubrication and nutrition have caused problems. RB can be a highly irritating substance to the surface of the eye and a concentration higher than 1% can cause very noticeable discomfort (Korb 2002, p.68).

A third type of increasingly used stain is LG, a replacement for RB, designed to have the same properties showing where cells have being damaged on the conjunctival surface (Feenstra & SCG Tseng 1992). However LG has much lower irritation effects than RB (Korb 2002, p.67). LG has a low linger time in the eye (no more than 4 minutes for optimal viewing) and also require a relatively large volume of agent for staining (10-20 ul). It is not a fluorescent dye, but some investigators do use a red coloured filter to increase the contrast of the green stain against the off-white sclera (Peterson et al. 2006).

7.3 Observing the Tear Film

7.3.1 Imaging of the Tear Film

Due to the small thickness of the tear film and in particular its transparency, it can be very difficult to measure the tear film directly, particularly the lipid layer which is much thinner than the aqueous. The best method of observing its behaviour thereby is via direct imaging. A helpful way to visualise the tear film is by assuming it is a multilayer system with each layer floating upon the previous. There are four primary methods of imaging the tear film, these are: fluorescein dye (see section 8.8.10); Interference methods (such as specular reflection); Confocal Microscopy (CM), and OCT. The interference method can further be broken down into to two sub methods; Narrow spectrum (i.e. illumination by monochromatic laser light) and broad spectrum (illumination by broad spectrum white light, traditionally a cold cathode source).

A useful approximation of the tear film would be a bubble having both a curved inner and outer surface. Light passes from the atmosphere into the bubble medium travelling through it before exiting from the bubble's posterior surface. Light, therefore travels, from a less dense medium (air, n1) to a more dense (bubble medium, n2) back out to a less dense medium (air, n1). Light travelling from n1 to n2 material will have an associated reflected and transmitted component because n1 is less than n2 Fresnel reflection will be produced causing a 180 degree phase change for the reflected beam. Light travelling through the n2 material will be refracted and then strike the n2/ n1 barrier before exiting the medium. Due to the difference in refractive index a reflection will be produced, however because the light is travelling from a more to a less dense medium (i.e. n1>n2) there will be no Fresnel reflection. The reflection will be in phase with the refracted beam. The light reflection from both of these surfaces will cause interference. The narrow spectrum method will produce monochromatic interference fringes (shown as areas of varying pixel intensities if imaged with a camera system) to be formed on the tear film's upper surface (lipid/air interface). The broad spectrum model interference will be visible as coloured patterns on the upper-most surface.

7.3.1.1 Lipid Layer Imaging

As reflection properties are known at each surface and the nature of refraction in the lipid tear medium is quantifiable, the only variable will be the thickness of the tear film. The changing intensities or colours in the tear film are therefore directly related to the thickness of the tear films lipid layer (Goto et al. 2003). In addition, the reflection can be used to observe the presence of the

tear film. This model can be assumed to be thin film reflection. Thin film optics are well understood and defined (Grunwald 2007, pp.39–58). The lipid layer of the tear film floating on the aqueous layer can be modelled accurately in this fashion.

Curvature of the lipid layer will however cause problems. Illuminating a curved surface is difficult with a single point source because light rays will not strike at normal to the tear films surface. Diffuse illumination will be required to reduce specular reflections. Two imaging systems currently use this diffuse broad spectrum illumination method; the Keeler Tearscope Plus (Windsor, Berks, United Kingdom) and the Kowa DR-1 camera (Kowa CO., Nagoya, Japan) (Goto et al. 2003)

7.3.1.2 Specular Reflection Based Non-Invasive TBUT

Non-contact methods for measuring the tear film (primarily interference techniques) are noted with the prefix non-invasive (NI); therefore many studies assess the non-invasive tear break up time. NITBUT is an important measure of the stability of the tear film, giving a metric of quantification for the time taken for the tear film to become unstable and break up after blinking has occurred. Metrics can be cross compared and stored for later comparison, giving some measure of disease progression or treatment strategies. Determining the point of NITBUT can be difficult; an excepted practice is to study interference fringes covering the cornea and determining at what time after blinking the lipid layer of the film loses its evenness of reflection. Holes may appear as the meniscus holding the lipid layer intact degrades. A NITBUT of less than 5 or 10 seconds is typically classed a dry eye (Korb 2002, p.66) . With many cases of severe dry eye NITBUT can be considerably reduced. The NITBUT is an essential measurement for assessing a patient's suitability for wearing contact lenses and along with tomography is required for advanced contact lens fitting.

7.3.2 Interferometry Theory

Interferometry is the technique of studying the patterns caused by two waves interfering with each other constructively or destructively. The interference patterns created are caused by the principle of super position (Serway & Jewett 2004). Waves intermix together producing a new wave with different properties to both of the original waves (assuming the waves are not at the extremes of magnitudes to each other, respectively). The physical properties of this new wave will depend on the phase and amplitude of each of the waves mixing. When waves are in phase they add together producing a new wave with greater net amplitude than either individually, and vice versa when they

are out of phase producing a wave with net smaller amplitude. Any combination from complete addition of amplitudes to complete cancellation can be formed. Observing the perturbations of resulting waves can lead to conclusions about the original wave's amplitude and phase components.

7.3.3 Producing Digitised Measurements of Tear Film Thickness

White light interference methods for determining lipid layer thinness such as used by the Tearscope are subjective and thus have poor repeatability. The study by (Goto et al. 2003) attempted to produce mathematical models relating to observed primary colours red, green and blue (RGB) and pixel intensities. The aim was to produce quantifiable colour mixing functions. The variation in thickness of the lipid layer can be directly and predictably related to colours observed on its surface. If factors such as refractive index, absorption and reflection coefficients are know it is possible to determine the thickness of the layer that can produce any given colour and contrast combination.

Different colours are a result of variation in optical path difference between rays of light interfering on the lipid layer surface. Due to the relatively small difference in the wavelength of light between the extremities of the visible spectral (i.e. violet and red) and the proportionally large change in lipid layer thickness, the same colours will be observed for many different combinations of lipid layer thickness.

The repeated nature of this relationship can be visualised as different octaves of the same colour spectrum. The human visual system perceives the higher octaves as being lower contrast compared to lower octaves. It will be more difficult to see the changes between the colours as their bands become more spaced out. The lower contrast colour octaves represent a thinner tear film. Goto *et al* produced a model ranging from 0 nm to 1000 nm of lipid layer thickness and synthesized what colours this would produce. As the tear film increases in thickness, the intensity of the RGB signals reduces (this is why there is a perceived loss in contrast). Blue light is clearly more affected than red, most likely due to the lipid layer acting as an interference band stop filter at this wavelength. (Goto et al. 2003) produced a colour chart by normalising the colours using the CIE colour space diagram, producing a realistic representation of what the eye would see (or more precisely how the observer would perceive the colours). The Kowa DR-1 camera was used for this research. Very little information is available of the design of this device. However, it is this author's opinion that it uses

some form of polarising beam cubes to remove specular reflection from the lipid layer, most likely using multiple cameras and digital manipulation with subtraction of one image from the other to maximise the information gathered from the colour patterns on the surface of the tear film.

7.3.4 Spectral Power Distribution and Reflection

Every light source will have a specific Spectral power Distribution (SPD). The SPD indicates how the energy produced by the light source in the visible spectrum is distributed with reference to the frequency range. Knowing the specific SPD of an illumination source provides enough information to produce the luminance and chromaticity diagrams. This allows the perceived colour of light sources to be estimated when adjusted for the relative sensitivity of the human eye given the unequal sensitive of the cones to differing wavelengths of light (the gamut of human vision). The CIE colour space has been developed based on group observation of normal individuals and their responses to know colour stimuli (Fairchild 1998). The CIE colour space represents the colour perception and brightness of light. The SPD can be converted into coordinates on the CIE diagram by use of colour matching functions (Sangwine & Horne 1998, p.40). Two values will be determined called tristimulus coordinates (i.e. chromaticity coordinates). When represented on the CIE diagram information such as perceived white point can be estimated for the given illumination source. SPD are often normalised, allowing for better representation of the spread of energy versus frequency (Sangwine & Horne 1998).

Reflection will also affect perceived colour perception. Any physical medium will have properties that govern its reflection and absorption of light. If a material absorbs all wavelengths of light in the visible range other than red and is illuminated with a broad spectrum source, we perceive that object to have a red colour. If the same object is illuminated with pure green light we would perceive the object to be black. This is because all the green would be absorbed and no light would be reflected into the eye. In reality this is not possible because no material is a perfect absorber or reflector. For any given wavelength a material will have an emissivity coefficient. The coefficient varies from 1 to 0 with 1 being a perfect black body (i.e. absorbs all energy) and with 0 being a perfect reflector (radiating all energy back out); (Serway & Jewett 2004) Reflection will also be caused by a refractive index boundary. When light travels from a substance of higher to lower refractive index a reflection is produced. The magnitude of these reflections is proportional to the change in refractive index between the media, the greater the change the greater the magnitude of the reflection. Part of the light will be reflected and part absorbed deeper into the material (Sharma 2006, p.32). The reflection/absorption quantities can be assessed using Fresnel equations and reflection (R) and absorption (T) coefficients. R and T will be affected by polarisation of light and angle of incidence (Sharma 2006). The conceived colour of a substance can be completely changed by the SPD of light striking its surface. The different R and T coefficients for each wavelength will change the effective

SPD of the light reflected of the surface of an object and into the eye. Therefore, any system that aimed to quantify the colours produced by broad spectrum interference will need to allow for changes in SPD between incident and reflected rays and relative intensities of the R and T coefficients changes throughout the layers of the system.

When producing board spectrum interference systems it is important to take into account how the light source will be perceived by the eye. Each individual will have slightly different colour perception. Colour can also be misrepresented by photographic capture on chemical film, electronic capture devices such as charge coupled devices (CCD) or complimentary metal-oxide-semiconductor (CMOS), each of which will have different gamuts than the human eye. Therefore their perceptions of colour will not match that of the human eye (Sangwine & Horne 1998). Displaying of images will also have similar effects. Electronic display formation, such as VDU and projectors, also have limited capabilities in colour space. Further inaccuracies could be introduced with digital storage and compression of images with algorithms often simplifying the colour information when storing images and interpolating the information when displaying, producing a net loss of information (James S Wolffsohn 2008, p.14; Cosman et al. 1994). Inaccuracies can be minimised by using calibrated monitors and loss less compression formats to produce truly accurate representation. Loss factors must be quantified and allowed for in design (Sangwine & Horne 1998). Therefore any system that is designed to detect interference patterns from broad spectrum light need to minimise the effects of colour representation and human subjectiveness from the decision making process.

7.3.5 The Role of Specular Reflections

The reflection of light from a surface can be split into specular and diffuse. diffuse reflections are produced when an incident ray hitting a surface is scattered and reflected in multiple differing directions, this is usually due to inaccuracies in the surface finish of materials. Natural undulations in the surface will cause light to be reflected at different angles proportional to the angle at which the light strikes the reflective medium. Diffuse reflections are of lower intensity than the incident beam. Specular reflections are where the light is reflected off in a more focused and coherent direction. A good example of this is how light reflects off water producing a very strong reflection at certain angles (i.e. Brewster's angle; Sharma 2006).

Specular reflections are strongest when striking a surface of high quality finish and high refractive index differential. Fluids can be regarded as surfaces with extremely good surface finishes due to surface tension producing a flat high quality uniform surface. Specular reflections are also maximised when incident the light is highly collimated (i.e. has highly parallel wavefront propagation).

Specular reflections can be minimised with use of polarising filters due to their more uniform and ordered wavefront propagation when compared to diffuse reflections. Much of the light produced by specular reflections will lie in a single plain of propagation and using polarising filters to remove unwanted polarization components can be helpful in reducing the intensity of specular reflections. Digital methods can also be employed to remove secular reflections. Most systems seem to use multiple images and use subtraction algorithms to remove a background or a foreground from one or multiple images. However useful this system, the tendency to lose information could be great, therefore careful investigation and testing is required.

7.3.6 Note on Optical System Design

It is important when looking at any optical system to be able to compare systems in a like for like manner. Many people state that the performance of an optical system is simply the resolving power of its weakest component. However this is not an ideal method of representation. Each component in an optical system (lens, camera, reflectors, prisms etc…) will have limiting optical performance characteristics. Combination of these factors can lead to a system that actually performs significantly different than any of its individual parts. The vector nature of aberrations (have both a magnitude of aberration and a direction of action i.e. positive and negative component) may produce images both of better or worse resolution than presumed, to image at the resolution of its weakest principle part, primarily because destructive or constructive interference between image degrading elements occurs.

The importance of the assessing an optical systems performance is to understand the nature of how systems collect and image light. This is paramount to designing a system that is capable of resolving the smallest detail you wish to detect and understanding and correcting for how the inherent nature of the optical system will distort the light it collects.

For every optical system there is a limit to its performance. Assuming perfect lenses (no aberration whatsoever) and image capture devices are operating at their maximum theoretical performance

(CCD, CMOS etc…) the resolving power of the optical system will be limited to the diffraction limit (DL). The DL of a system is primarily governed by the aperture present in the optical path. Diffraction will cause a point of light to interfere with itself as the waves that make up the column of light representing the point are modified by the aperture, an airy disk will be formed. The airy disk is a unique pattern formed by interfering light, taking on the general shape of the aperture that caused the diffraction in the optical system (Hecht & Zajac 1974, p.174). Taking a line profile across an airy disk shows how the energy of the light source is distributed. The smaller the aperture the less a system will be diffraction limited. Therefore the design of an optical system must take into effect the size of the aperture the image system needs. In reality most optical systems never come close to their diffraction limit aberrations as the lenses are usually far more detrimental to image quality.

7.4 TearMaster Hardware Development

The tearscope replacement project was designed to determine if a digitised tearscope could be developed offering the advantages of digital recording and recordkeeping. A market price point of sub $1000 (USD) was to be used for an aim point retail price. Fabrication costs should be approximately 1/3 of this price. The project cycle consisted of the development of three concept devices (Block 1,2,3 etc.).

7.5 The Block TearMaster 1 Device

7. 5.1 Illumination Selection

The block 1 device was a simple first generation concept designed to assess the requirements for a digital tearscope. The principle of using reflection mires and assessing the stability of the tear film by relating it to the perturbations observed as the tear deteriorate on the cornea was utilised. The tearscope utilises a cold cathode fluorescent lamp (CCFL) light source for the illumination of the corneal surface. The tearscope was developed in 1997 by Jean-Pierre Guillon. The developement of the device, operation principles and testing routine, were detailed shortly afterwards (Guillon 1998; Guillon 1997).

Use of CCLF light sources was driven by the technological limitations of the technology available when the device was developed. CCLF sources provide a broad spectrum white light sources capable

of producing interference fringes, however they do have limitations. There luminosity is poor compared to more powerful modern light sources such as LED and Laser Diodes (LD). A custom CCLF was designed for the tearscope, physically wrapping the CCLF tubing around the illumination cone producing the effect of back illuminating the reflection mires. The development of the custom CCLF source would most have likely contributed the majority the development cost for the device. There are also design limitations of the CCLF sources that can be summed up as follows: 1.) Fragility, they are fragile and susceptible to damage via drops and falls, especially considering that the device is hand held and portable; 2.) They have to be driven with AC voltages requiring complex, expensive and energy inefficient inverters, dimming capabilities further complicates the design of the electronics; 3.) Their physical bulk places excessive limitations on the design of a highly compact system. A more modern, power efficient, high luminosity, illumination system was to be developed, giving the device the capability to be very small footprint and the ability to work off batteries. Two types of light sources were considered (in no particular order), High power LED's and the new generation of flexible light emitting materials working via the principles of Electroluminescence (EL).

7.5.2 Electroluminescence Technology

A new generation of highly flexible light sources has been developed by Electro-Luminx Corporation (Chester, Virginia, USA). Figure 7.1c shows the "Light Tape" product in the TearMaster block 1. Light Tape (LT) is a highly flexible plastic based material 500 microns thick that emits light from its surface . The LT can be bent or wrapped around anything with a bend radius of 25mm or greater. Currently 18 different colours are available as of July 2012 (All data proved by LiteTape UK). Testing was undertaken to determine the SPD of the light source, conducted with a SpectraScan 650 Instrument and the associated SpecraWin software (Photo Research Inc, Chatsworth, California, USA). Figure 7.2 shows the SPD of the system.

Figure 7.1: (a) Rear left view of the bloc 1 system. (b) Front right view of the block 1 system. (c) Close up of the active LiteTape illumination.

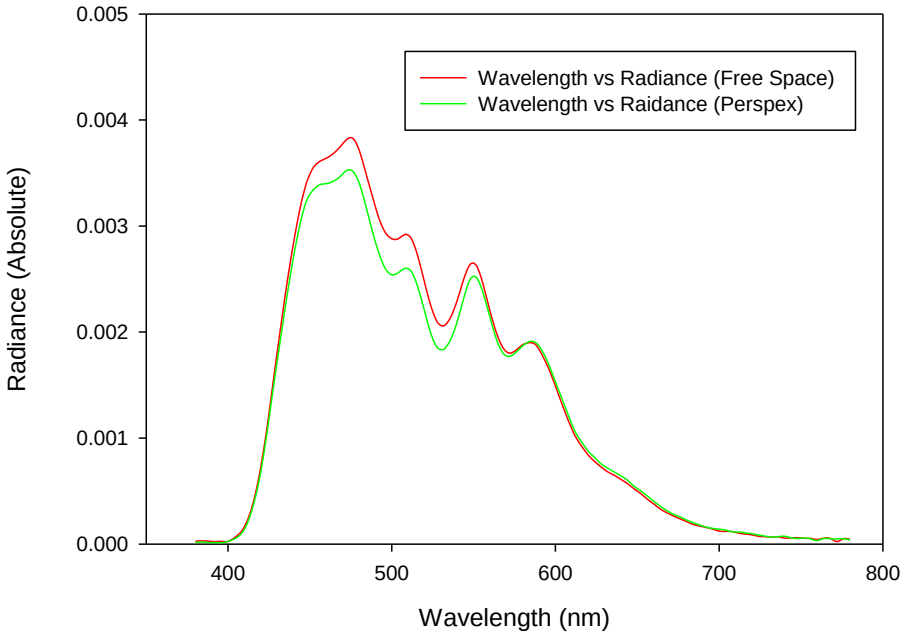

Figure 7.2: SPD of the LiteTape both in free space and when filtered through a Perspex medium to simulate the Perspex tube used in the system.

A direct backlighting technique was developed wrapping the LT with the illumination surface pointing inward around a translucent Perspex tube. A series of differing mires could be printed on transparent plastic sheet and inserted into the tube in a similar fashion to the tearscope. The LT is driven by a high voltage high frequency inverter, however portable units capable of running of batteries are available (PDC60, Eectro-LuminX, Virginia, USA).

7.5.3 Imaging System Selection

Selection of an appropriate digital imaging system was undertaken. The decision not develop a bespoke imaging solution for the block 1 concept device in favour of a commercially available solution was taken. The ideal device appeared to be some form of hand held video or still camera. A hand held device would have self-contained power and the capability to record still and/or moving images, ideally with an external fold out LCD display. Initially a Supacam Pro (SupaCam, Sana Monica, California, USA) device was chosen, primarily because the unit had a compact but blocky, straight edged design that would provide easy structural mounting points. The Supacam Pro provided an imaging resolution of 720x480 pixels and the capacity to take still images at 3072x2304 pixels (7mp). Testing the device was ultimately deemed a failure because the cameras automatic focusing system could not be disabled or set to a constant focal point manually. In still imaging mode the inbuilt flash unit could not be disabled, severely limiting functionality. Upon contacting the manufacture it was found to be imposable to disable the features without developing a custom firmware solution. To do so would have been feasible in house, but would require considerable time and resources. A better alternative was therefore sought.

After investigation of nearly every hand held camera on the market, a second device was chosen the Sanyo Xacti. The device was capable of imaging at 1920x1080 with a frame rate of 30fps and could take still images of 4000x3000 pixels (12mp). The autofocus could be controlled manually and featured a close up mode where focusing could be as close as 50mm from the front optic. Flash and illumination could be controlled independently and disabled as required.

7.5.5 Final Hardware

The block 1 system consisted of the Sanyo Xacti camera and precision cut Perspex tube of diameter 38mm externally wrapped with EL tape with a top mounted rail system. The rail system allowed the operator to move the light tube back and forth (allowing some minor focusing) and side to side to produce a full field image frame. Figure 7.1c shows the device with the EL tape switched on.

7.5.6 Conclusion and Discontinuation of the Block 1 Device

The block 1 device proved the principle of using EL tape for producing interference fringes and reflection mires on the corneal. Figure 7.3a/b shows a typical image of the reflection mires on the cornea from both the block 1 device. Figure 7.4 shows a 20mm calibration sphere with a ring mire with equal spacing for assessment of corneal curvature. The change in curvature can clearly be seen and with appropriate software the device could be used to determine corneal curvature. From initial testing problems with the design were apparent, focusing was non optimal, and had to be adjusted for each subject individually, a time consuming process. The differing sizes of subjects eyeball showed the Perspex tube to be too large to securely fit smaller eye sockets. A second generation device was commissioned to address these concerns and investigate the concept of LED light sources.

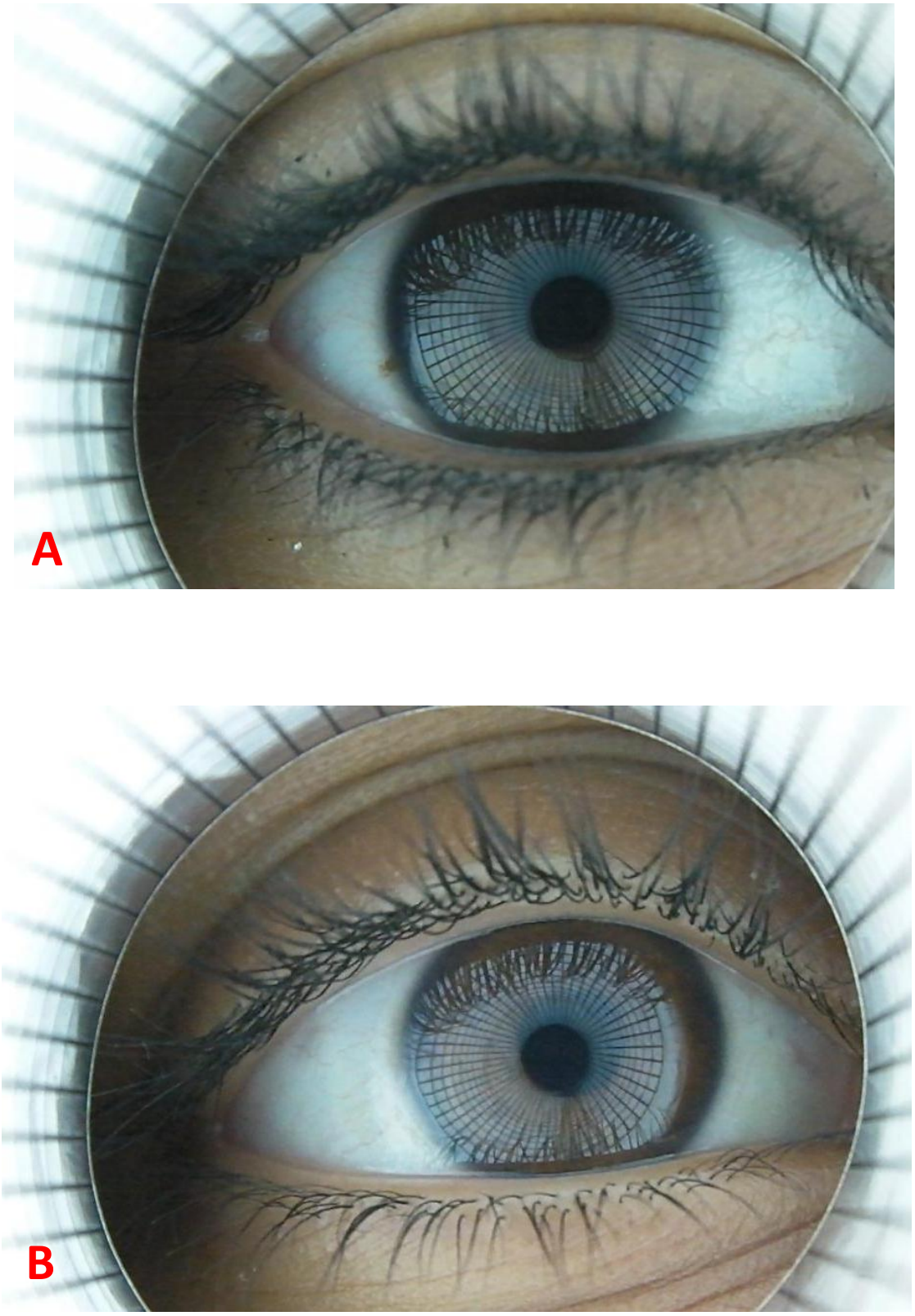

Figure 7.3: **(a**) Typical view of reflection mires from the block 1 system (female subject) **(b)** Typical view from a male subject with a lighter coloured iris.

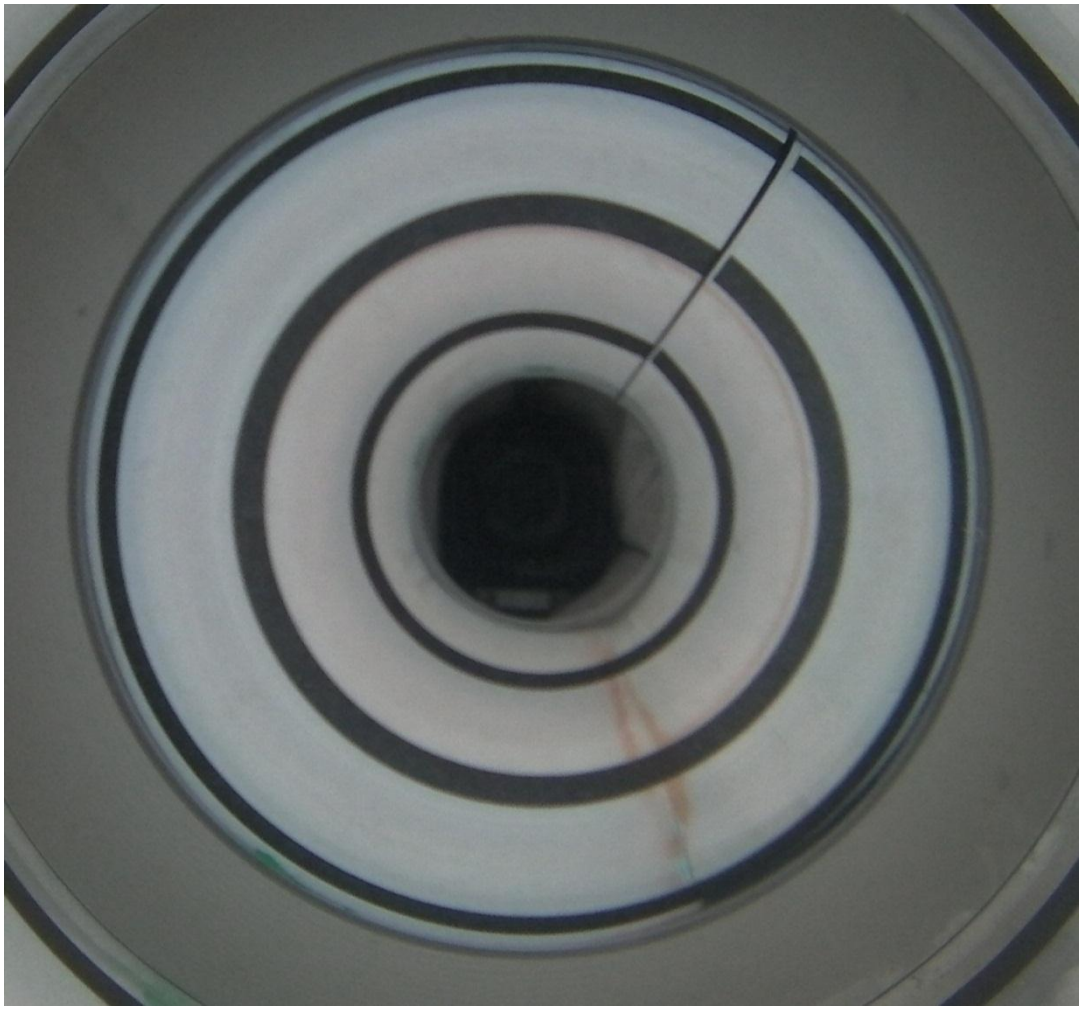

Figure 7.4: Close up view of a 20mm calibration sphere from the block 1 system.

7.6 The Block 2 TearMaster Device

The Block 2 device was designed to address the problems that were encountered after testing the first block 1 unit. In line with modern engineering principles a CAD model of the system was developed to aid rapid development and fault finding.

7.6.1 Hardware Development

The block 2 developments followed the same design layout as the block 1 device, primarily utilising the Sanyo Xacti camera and EL illumination. The addition of four major new design concepts were tested, listed as follows: 1.) Linear rail focusing system; 2.) Lens addition system; 3.) Optical waveguide concept; and 4.) Dual fluorescing imaging system. A CAD model of the design with components identified and highlighted is shown in Figure 7.5a/b (note, electronics are not shown)

7.6.2 The Linear Rail Focusing System (LRS)

The LRS was designed to provide positioning for the camera in 3 axis for alignment and focusing. Figure 7.5a shows an image of the system. The rail system is a lightweight polymer unit developed by IGUS UK (IGUS, Northampton, UK). The unit utilises maintenance free polymer bearings and will not require lubrication under normal operation conditions. Figure 7.6 shows the breakdown of the axis of movement. Axis 1 provided focusing for the system allowing the fixed focus of the camera to be overcome by moving the entire imaging system; depending of the size of the slide used, travel distance was in excess of 50mm if required. Axis 1 and 2 provided positioning between the camera and waveguide allowing the aligning of both the optical system and illumination system to be concentric with the pupil centre. Axis 2 and 3 are locked off after positioning, and require tools to alter their alignment. Axis 1 is variable via a through screw on the linear slide. Depending on configuration, axis 2 and 3 are moveable over distances of up to 20mm from the central position and repositionable (via a thumb screw). A brow rest similar to portable slit lamps was also included to allow the device to be aligned with precision to the eye.

The Sanyo Xacti was attached to the LRS via an aluminium conversion block bonded to the plastic case of the camera. Initially the bonding process proved difficulty to perfect with the first two attempts to provide a strong bond with structural epoxy adhesive (B2012, Bondloc, Bewdley, Worcestershire, UK) failing after initial testing. After consultation with the manufacturer they, could not, or would not, disclose the specific type of plastic the case was fabricated from. Comparative

testing indicated it is most likely a type of polypropylene (PP) or Polyethylene (PE), both highly restive to bonding. Consultation with specialist adhesive manufactures Loctite (Henkel Corp, USA) provided a surface preparation and adhesive was recommended for forming bonds between PP or PE and aluminium. The final chosen surface preparation was Polyolefin Prymer770 (Loctite,Henkel Corp, USA) and adhesive Loctite 480 (Loctite,Henkel Corp, USA). Testing indicated the bond was extremely strong with destructive testing indicating the camera case would break before the bond fails. This allowed a high degree of confidence the device would stand up well to hand held use.

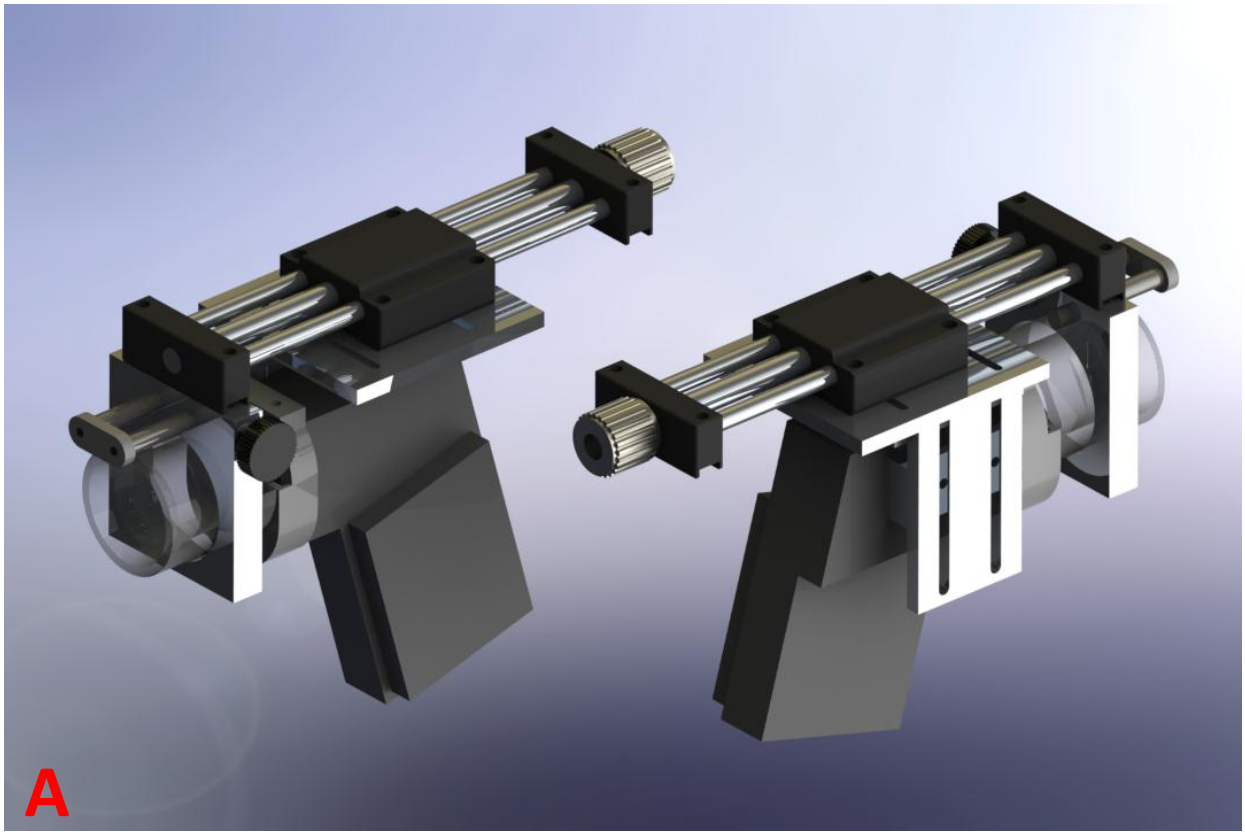

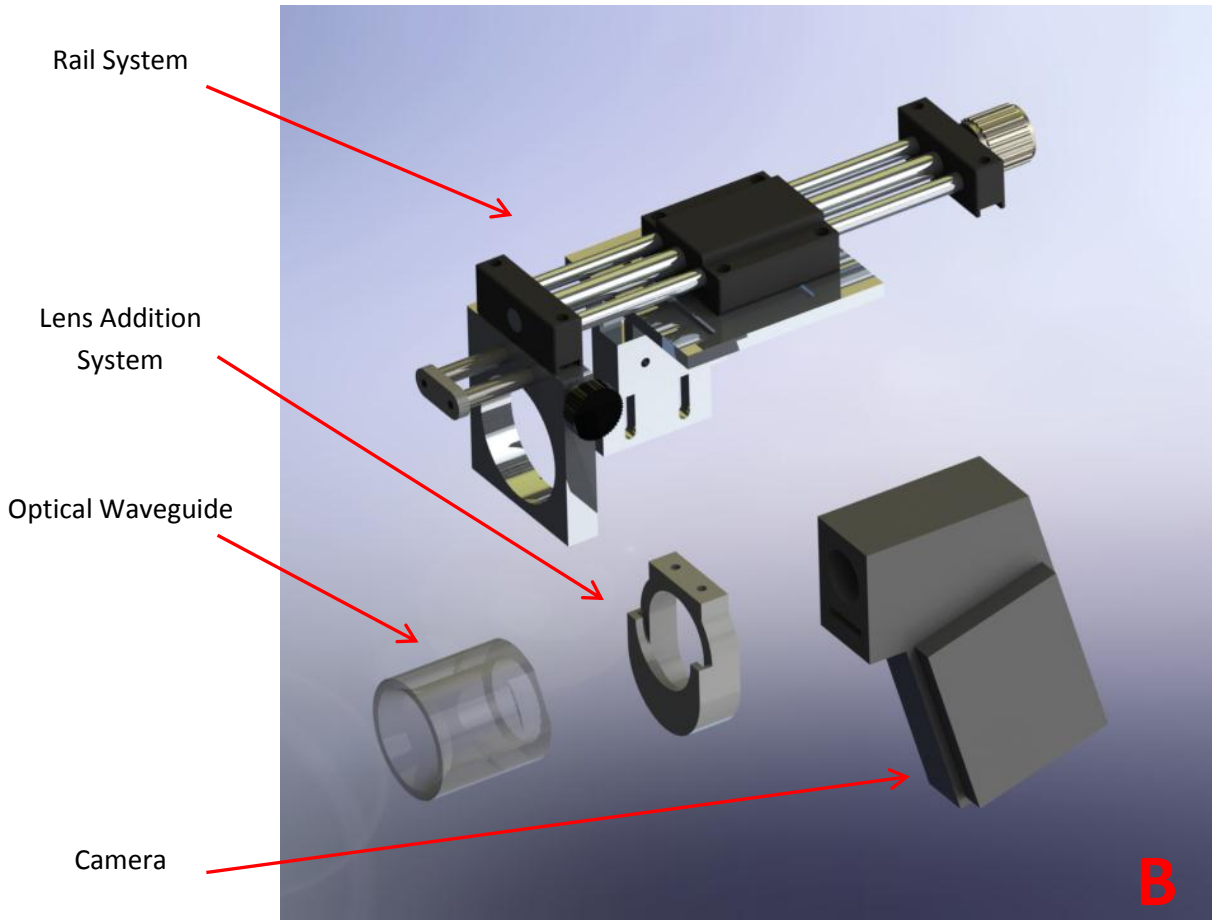

Figure 7.5: (a) CAD model of the bloc 2 device, front and back. (b) Individual parts the block 2 system in exploded diagram.

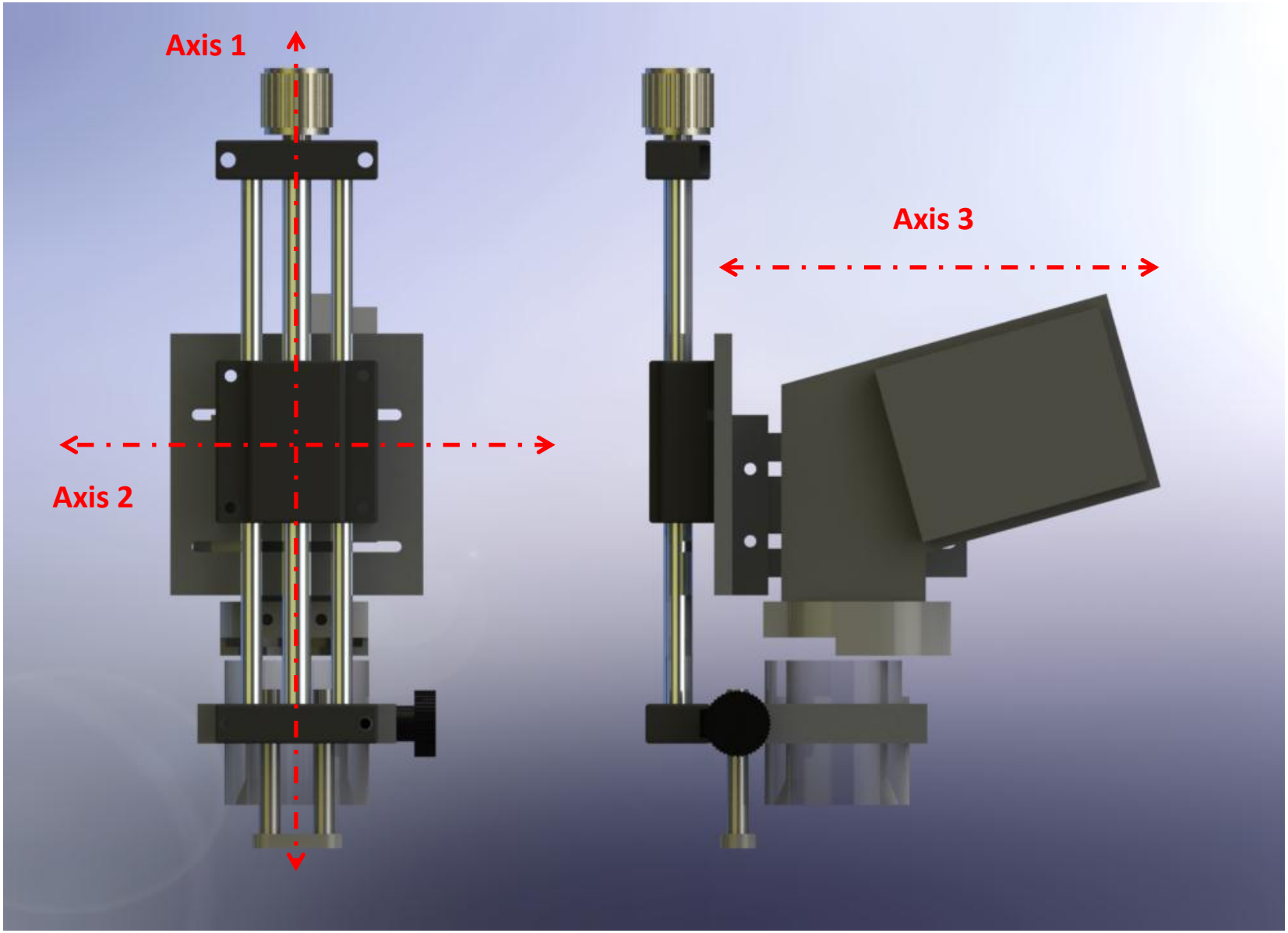

Figure 7.6: Breakdown on the 3 axis of movement for the block 2 system. The system can be aligned with precision to the cameras optical axis.

8.6.3 Lens Addition System (LAS)

The LAS was intended to provide the ability to add additional optical elements in the optical path of the system. Using scaled photographs of the front portion of the camera system and layout sketching, CAD was used to generate a geometry that would provide interference fit between a holder and the camera system.

An attachment was developed to fit onto the camera system and hold a full aperture trial frame lens. A series of tests were undertaken to produce the correct interference fit for both between the holder and camera and also the holder and trial frame lenses. Figure 7.5b shows a exploded CAD model of the device clearly indicating the LAS.

8.6.4 Dual Fluorescing Imaging System (DFI)

The Keeler Tearscope can be used with a inserted but filter and fluorescein dye to image the tear exchange under the contact lens. However the tearscope is not optimised for producing stimulated emission of fluorescein. The use of modern illumination technology allows for the optimal selection of light sources for the production of stimulated emission. The problem associated with normal incandescent light forces and filtering has been discussed previously in the introduction.

The absorption and emission spectral of SF is displayed in Figure 7.7. Peak absorption wavelength is 490nm and peak emission 520nm. Cut off levels for imaging return (reflected light) spectra while attenuation the emission should be between 500nm and 510nm. High pass filters should be utilised as the emission spectrum will dominate returning light providing better imaging of the fluorescein dye.

A system that could provide dual light sources would be advantageous, allowing a practitioner to image the corneal surface both in diffuse white light and light optimised for fluorescein imaging. Producing two distinctly different light sources in a compact instrument presents challenges for miniaturisation and heat dissipation. Traditional methods such as beam splitters or optical combiners are capable of combining beam paths from different light sources, but are very expensive precision devices, not well suited for a low cost mass produced device. Building on the illumination system developed for the block 1 device a novel dual imaging system was developed.

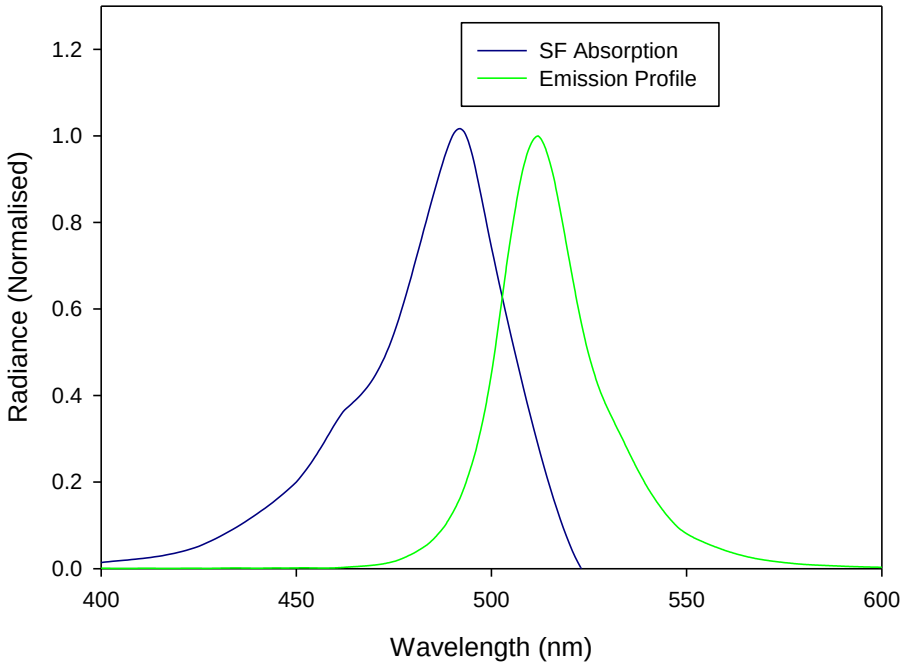

Figure 7.7: Sodium fluorescein absorption and emission spectra.

7.6.5 Optical Waveguide Concept (OWC)

The OWC is a novel device for combining the light from two separate light sources in a compact and controllable manner. The OWC is based on the principle of total internal reflection producing a waveguide for LED lighting and a straight pass though for the light EL source. Figure 7.8a shows the device and operation principles. The light guide is fabricated from Perspex and precision machined and polished (the first prototypes took 35 hours of matching and polishing to complete). Similar to optical fibres, the LED light source needs to be positioned to take effect of the total internal reflection angle between air and Perspex (42 Degrees, for n=1.49 (Serway & Jewett 2004)). The LED's are positioned towards the back of the device with light guided though the material and exiting at the chamfered edge directly opposite the corneal surface. The chamfer is not polished to a mirror finish but left "frosted" to provide a surface to scatter emitted light. The LED's chosen had up to have a 170 degree dispersion angle (Golden DRAGON, Osram Opto Semiconductors GmbH, Rogensburg, German) so they could be placed parallel to the Perspex surface and still provide considerable internal reflection, reducing the machining required for the waveguide. Figure 7.11a shows the waveguide proof of principle device and a sample of fluorescein.

7.6.6 LED selection for Fluorescein Imaging

Attempts were made to source high power LED's that could provide peak emission wavelengths centred at 490nm required for optimum SF stimulation. Devices manufactured in limited quantity, LED490-03U (Roithner Lasertechinik GmbH, Vienna Austria) were source, but proved to be extremely expensive and low luminosity compared the latest generation high power devices provided by leading suppliers such as Osram Opto Semiconductors GmbH (Rogensburg, German).

High power LED's require high current drives to the devices at full luminosity but they will produce considerable light levels even at very low current driving. The Golden Dragon LED can be driven with currents up to 350mA but there will be the requirement to uprate the junction cooling if the device is not to be overheated with prolonged use. Both optical and thermal testing of the LED indicated potential problems. When driving the LED with a current of 40mA (maximum standard output from the standard I/O channel) it was noted that the light produced appeared to be off colour. Photospectrometer testing indicated that there was a phase shift phenomenon that could be related to drive current. Figure 7.9 shows the phase shift for a green LED with a stated peak wavelength of 504nm been drive at 20mA and 350mA. A positive phase shift of 9nm can be seen, with a peak at 513nm observed. It was also noted that the emission profile differed from the stated clause on the

data sheet provided by the manufacturer. Figure 7.10 shows the emission profiles for the same LED with SF absorption, data sheet profile and driving at 20mA and 350mA. The data sheet values shows close coverage for the requirement for SF excitation. The values produced by driving at 20mA were phased shifted to the right, showing much poorer excitation. A different approach was taken by selected LED's with stated emission profiles lower than required and using the phase shift to push the profile into the SF excitation range. LED's with stated peak emission of 470nm were chosen and displayed good SF emission under testing.

7.6.6 System Testing

The device was tested under a variety of conditions. Figure 7.11a/b shows a sample of sodium fluorescein test with the waveguide illumination concept and figure 7.12a/b/c/d shows subjects under test.

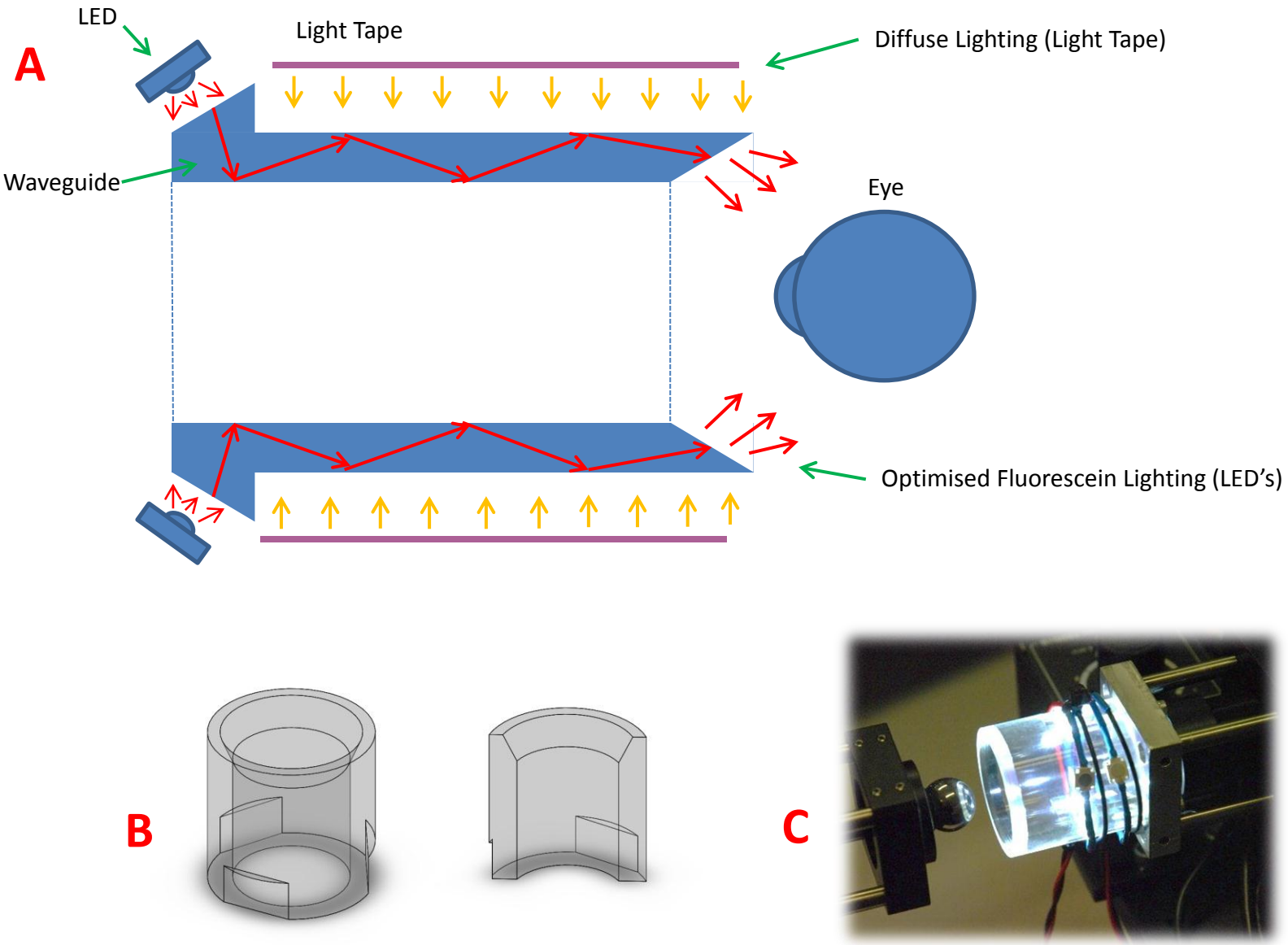

Figure 7.8: **(a)** Total internal reflection principle for the waveguide concept. **(b)** Translucent CAD models showing structure of the waveguide. **(c)** Device in operation on test rig.

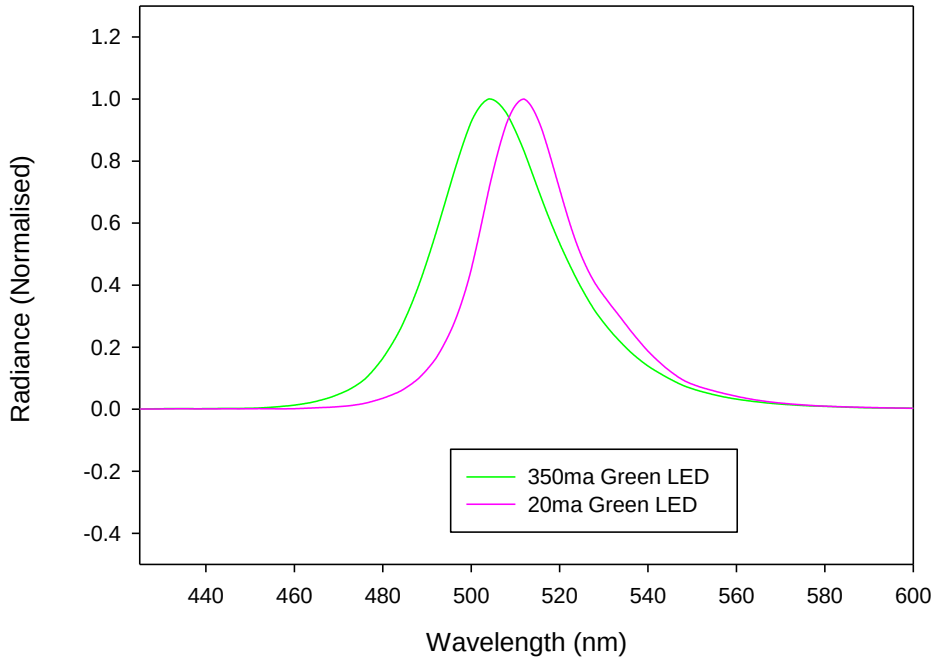

Figure 7.9: Phase shift phenomenon for current under driving, a 9nm peak shift is observed.

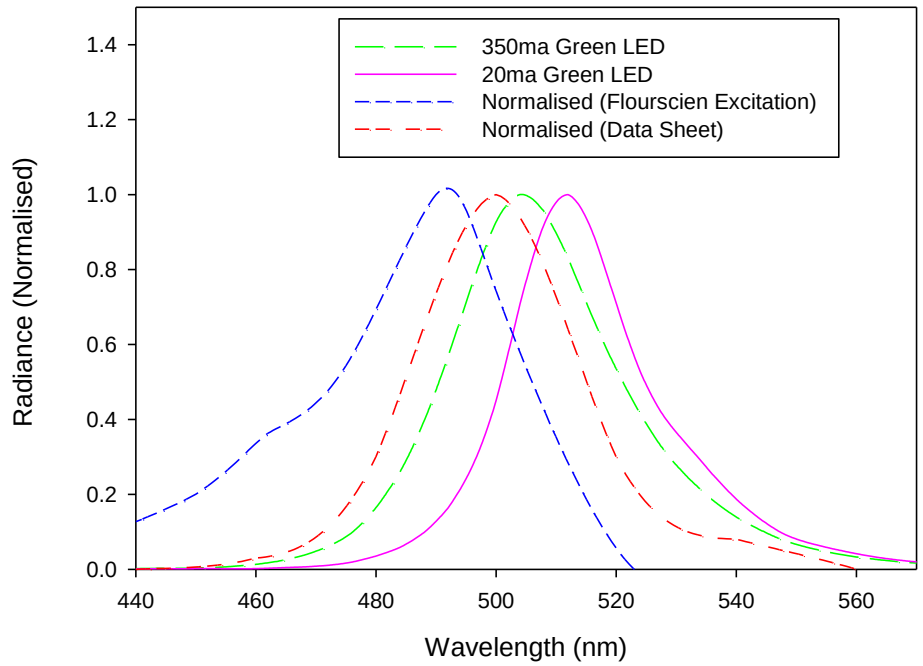

Figure 7.10: Differences in emission profiles indication the requirement for physical testing of illumination systems in the design phase of the project.

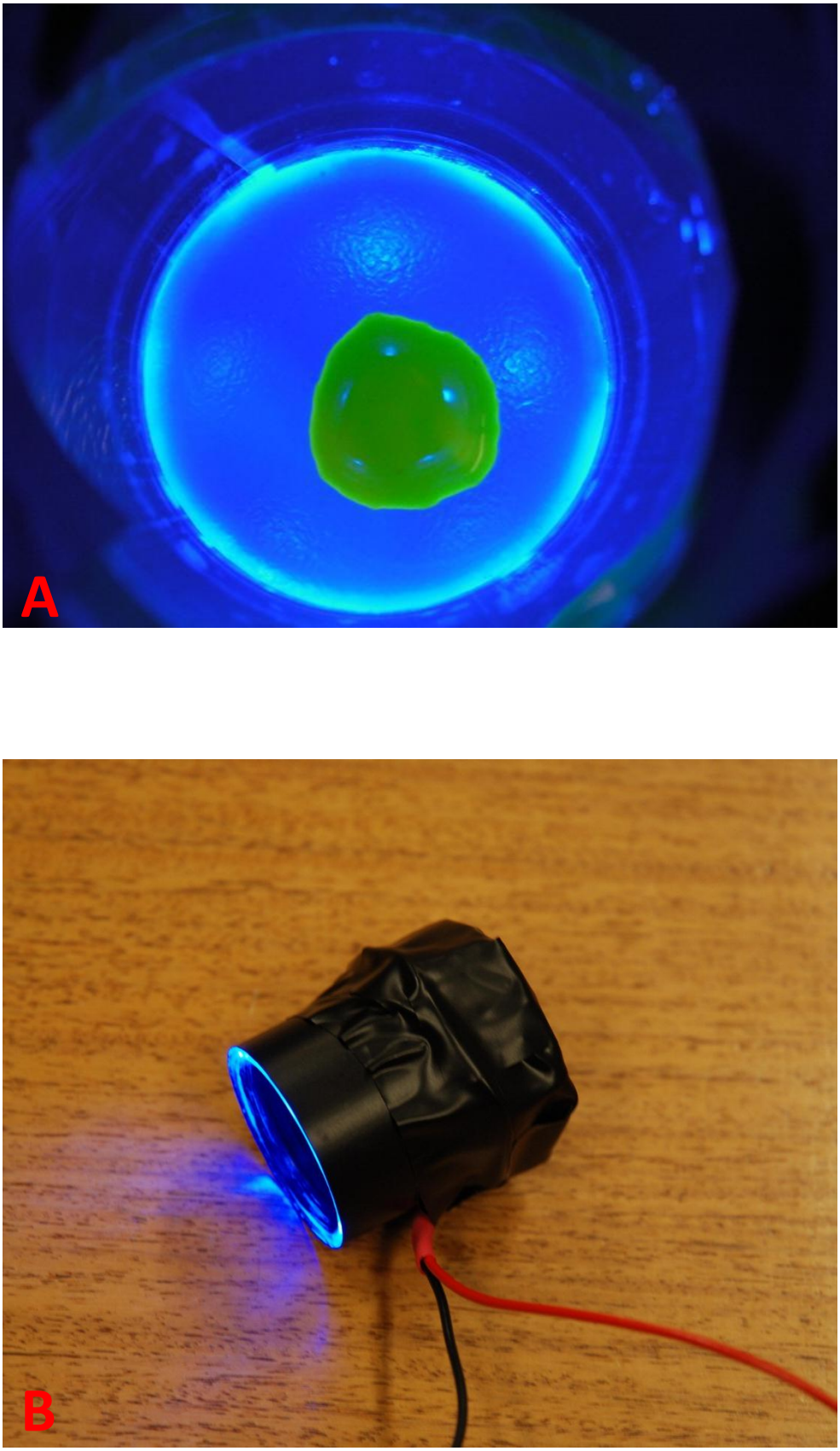

Figure 7.11: (a) A drop fluorescein under test, the illumination can clear be seen emanating from the front edge of the device. **(b)** The prototype waveguide device.

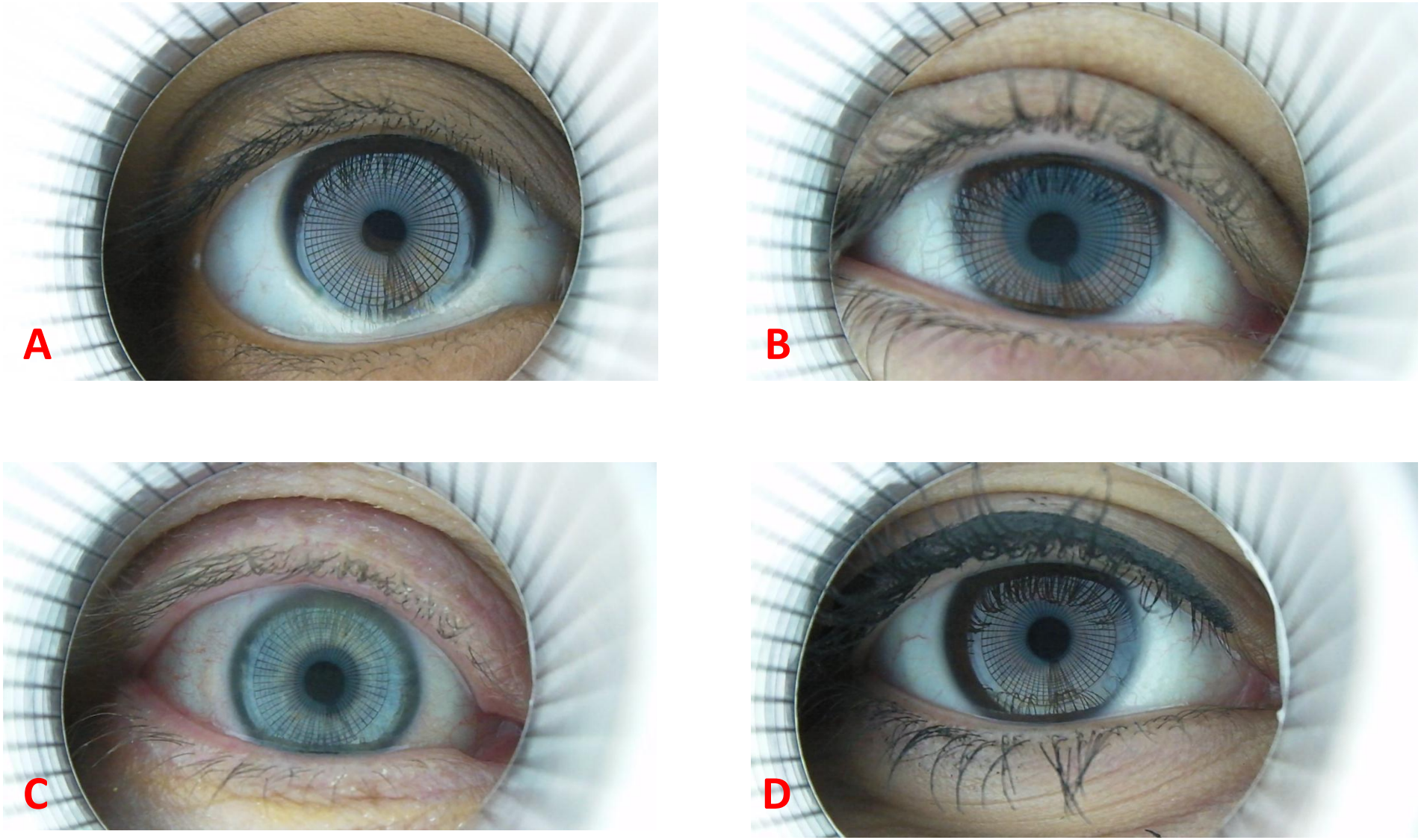

Figure 7.12: (a/b/c/d) The block 2 device under testing with different human subjects. Note lighter coloured irises are more difficult to image.

7.6.7 LED Driving

LED's require constant current driving to produce consistent illumination. Traditional power packs provide a constant voltage source and dim light output by reducing the voltage available (i.e by reducing delivered power). Using switched mode power or pulse width modulation is a better way of providing dimmed illumination sources. Multiple different types of driving sources were used thought the tearscope replacement projects, including custom developed integrated circuits and MCU's to stand-alone PWM LED drivers. High power LED's provided extra complexity for powering due to their extreme current consumption requiring more complex drive electronics. An off the shelf solution was used for the majority of testing for Block 1 and 2 devices. The LEDD1B Driver (ThorLabs, Newton, New Jersey, USA) proved very useful due to its very large current supply of 1.2A providing considerable flexibility for serial connection of LED's. The device can be controlled by an external TTL logic and PWM input if required.

7.6.8 The Final Block 2 Device

A comparative study of the Block 2 device against the Keeler Tearscope Plus, Slit Lamp Imaging, Keratometry Mire imaging and Fluorescein break up was undertaken. Figure 7.12 shows the finished device assembled.

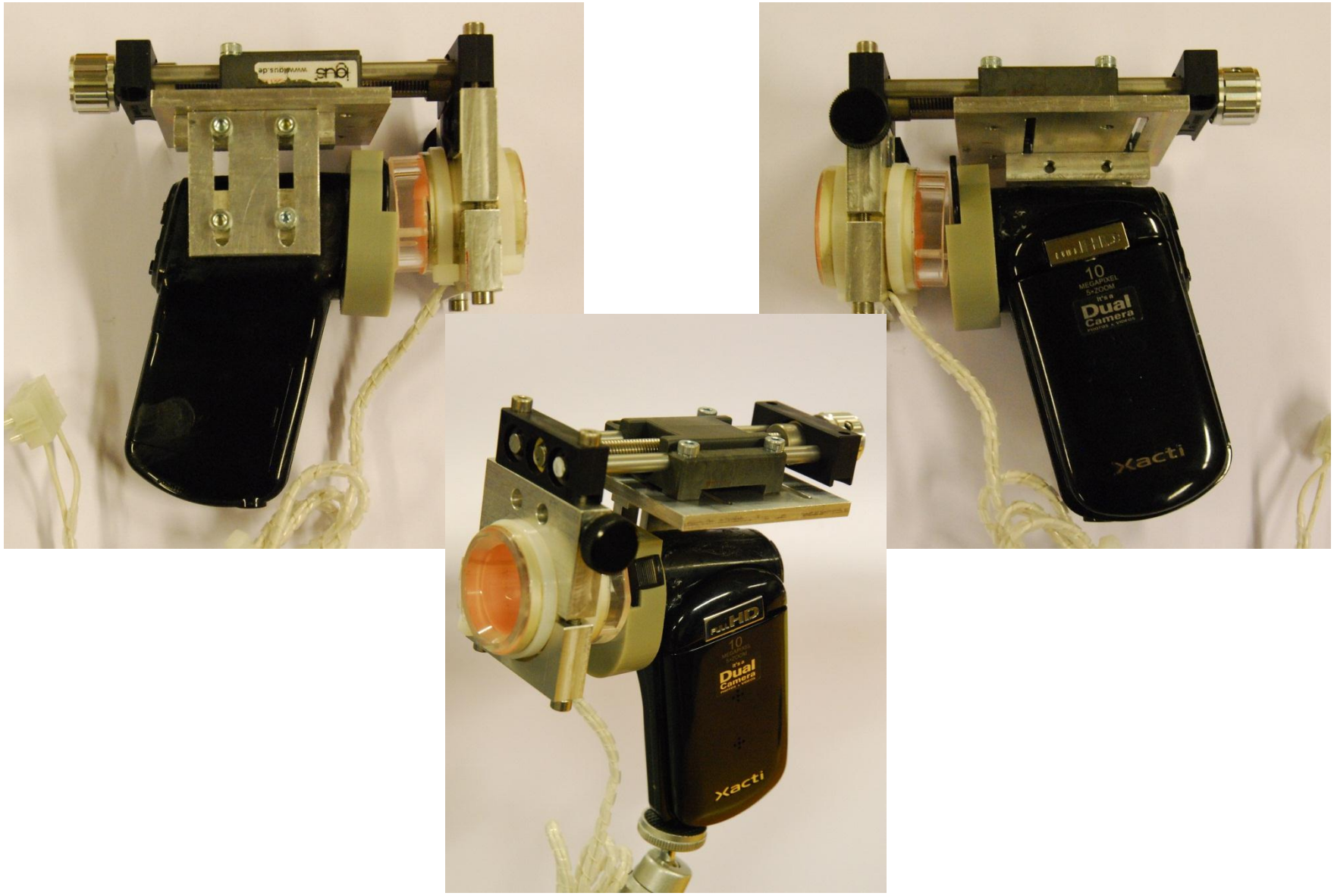

Figure 7.13: The final block 2 prototype put forward for testing in clinical trials.

7.6.9 Conclusions for the Block 2 Device

The block 2 device operated well, but some problems were apparent. Images produced are clear and of good quality but because of the straight geometry of the waveguide it is not possible to produce reflection mires over the central part of the cornea without using an excessively long tube. The reflection produced by the front optic of the camera filled much of the subject's pupil, again removing the possibility of assessing data in the central region. Magnification could not be optimised for full frame viewing of the corneal due to the limitation of the camera built in optics.

The use of an off the shelf camera system also limited the scope of possibilities for working with images after capture. The Sanyo Xacti can output a live feed to a computer system, but it requires further digitisation equipment. Currently images or videos have to be saved and transferred to the computer for post processing manually, a time consuming process. Problem with imaging SF emission were also noted. No matter what the position of the focal point images saturated with blue illumination and green emission wavelengths always appeared blurred regardless of adjusting the focal position. Initially it was thought that the narrow wavelength range of light was producing some form of chromic aberration and was not being focused completely onto cameras sensor plane. After investigation and noticing that green light produced a less noticeable effect, it was determined the Bayer filter and reconstruction algorithm were likely responsible. Bayer filters on Complementary Metal Oxide Semiconductor use a single sensor to reproduce a colour image. The sensor plane is split into pixels with alternating ones having sensitivity to either Red (R) Green (G) or Blue (B) light. However, these pixels are not evenly distributed with 50% Green and 25% red and blue respectively depending on specific configurations. The post processing algorithm (PPA) interpolates across respective pixels to produce a pseudo full resolution image. When imaging only with the blue light, only blue sensitive pixels are effectively quantifying the actually resolution of the system. The PPA produces an image of much reduced contrast as an effect. All colour imaging system based on this technology are susceptible to this error, so micropunctate staining observed by the practitioner's eye may be missed in the recorded digital image. Monochrome cameras will not display these kinds of problems. If there is a requirement for colour specific imaging, cameras with tri-sensors (3-chip), colour wheels or similar should be utilised.

The waveguide concept was deemed very promising, successfully demonstrating the concept, however it proved very difficult to perfect. Optimising the transition of light while minimising the specular reflection caused by the LED was the most difficult design criteria. To progress to the next

generation design it would be preferable to use advance computer aided design and ray tracing to optimise the optical properties of the waveguide.

7.7 TearMaster Block 2 Clinical Study Aims

To compare the accuracy of the Aston Tears compared to other methods of measuring tear film break-up time and to assess its intra-session repeatability.

7.7.1 Methods

Forty-one students from Aston University with ages varying from 19 to 53 years with an average age of 21.7± 5.4 years (29 female and 11 male) were recruited. Subjects were healthy and free from known ocular surface pathology and have had no know eye surgery or significant ophthalmic intervention. Subjects consented to take part in the study after a detailed explanation of the procedures. The study was approved by Aston University Ethics committee and conformed to the tenet's of the Declaration of Helsinki.

A series of five ways of measuring the tear-film break up time were conducted in random except for fluorescein which was instilled as the last method to prevent the invasive nature of the test impacting the other methods. The tear film break-up techniques, which were each carried out by a different investigator for consistency, were:

1.) Tearscope Plus (TS) mounted on a slit-lamp assessed until 10x magnification (Guillon 1997).
2.) Standard slit lamp Purkinje I tear break up time assessed in white light specular reflection under 10x magnification (SLP1)
3.) Keratometery mires (KTM) using a Javal Schiotz keratometer
4.) Testing with the novel Aston University TearMaster (TM) Block 2 device
5.) Sodium fluorescein (FL) dye instilled, illuminated with a slit lamp with blue light source and yellow enhancing filter(Lemp & Hamill 1973; Peterson et al. 2006).

All testing was performed on the same day with subjects rotated between testing stations at 5 minute time intervals. For each measuring technique three separate tear break up times were recorded. The first 3 and last testing techniques (TS, SLP1, KM and FL) were assessed (analysed) at the time of the measurement been taken (i.e. as the practitioner was testing) with the results, tear break up time in seconds, noted down. The processes involved watching the surface of the tear film and determining the time when the film has appeared to deteriorate. Assessment on TM was

undertaken later as the device recoded images of the tear break up in real time at 30fps. The assessment criteria were the same, with the same types of features observed. TM recoding could be re-watched at the practitioner's leisure and was done so when the breakup point may not have been obvious, giving the practitioner a second, third etc… chance of catching the exact breakup point.

Statistical Analysis was undertaken to determine the relationships between metrics. Each metric, TS, SLP1, KM, FL and TM were analysed using the One Sample Kolmogorov-Smirnov Test to determine if the data was normally distributed. All five dater sets were determine to be normally distributed and thus can be treated as a parametric variable (Armstrong et al. 2011). As the sample size was relatively small and all metrics were directly comparable, a Pearson's correlation was used to determine whether there was statistically significant correlation between variables (Pearson & Lee 1903). Finally comparisons directly between the TM and the four competing measurement techniques was assessed using the Bland-Altman test of agreement (Bland & Altman 1986).

7.7.2 Results

Metric	TearScope (TS)	Slip Lamp P1 (SLP1)	Kera Mires (KTM)	Fluorescein (FL)	Tear Master (TM)
Sample Size (N)	41	41	41	41	41
Mean TBUT (s)	11.72	9.80	10.31	9.47	13.41
STDev	5.55	3.17	3.77	3.09	4.06
Kolmogorov – Smirnov	.119	.927	.846	.782	1.055
Significance	.119	.972	.471	.573	.215
H0	Reject	Reject	Reject	Reject	Reject
Distribution	Normal	Normal	Normal	Normal	Normal

Table 7.1: Statistical analysis of the TearMaster trial data for determining parametric/non-parametric compliance.

The TearMaster was significantly correlated with the TearScope results (r=0.505, p < 0.001), but was only borderline significant with the Purkinje image (r = 0.300, p = 0.057), keratometer mires (r = 0.308, p = 0.050) or fluorescein (r = 0.318, p = 0.043) tear break-up time.

There are statistically significant differences between groups determined by a one–way ANOVA (F= 6.67, P<0.001). A Tukey post-hoc assessment of TBUT between groups indicated that there is significant relation between the TM and TS (11.72 ±5.55, *P*=.380) but not the SLP1 (9.81±3.72, *P*=0.001), KTM (10.31±3.77, *P*=.050) or FL (9.47±3.08, *P*<.001). As was expected the TS showed the greater variability in recording TBUT with the largest observed SD. FL showed the lowest average TBUT as expected (Mengher et al. 1985).

To allow comparison between the TM and the four other methods Bland and Altman plots were produced for each case. Table 7.2, Figures 8.14 and Figure 7.15 shows a summary of the results.

In all cases TM TBUT showed higher values than the other techniques and generally a positive bias (except with the TearScope) where the difference was larger with larger average values.

	TearScope (TS)	**Slip Lamp P1 (SLP1)**	**Kera Mires (KTM)**	**Fluorescein (FL)**
Sample Size (n)	41	41	41	41
Average difference(s)	1.69	3.61	3.10	3.94
95% CI Upper	11.60	12.39	12.33	12.43
95% CI Lower	-8.21	-5.10	-6.13	-4.56

Table 7.2: Statistical data derived from Bland and Altman testing method.

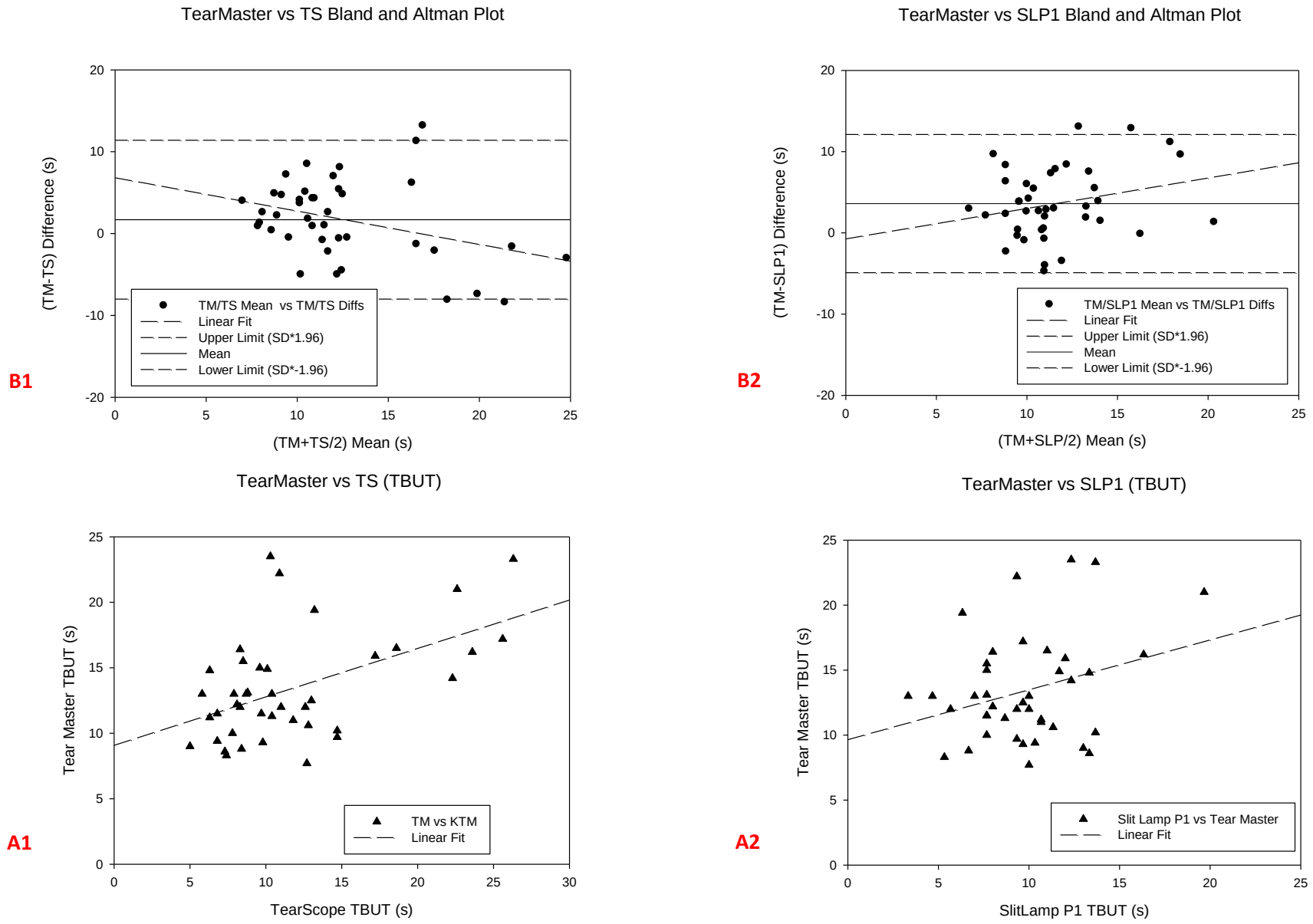

Figure 7.14 B1/A1 Apparent underestimation by the TearMaster compared to the Tearscope at longer TBUT's A2/B2 Apparent over estimation of TBUT by the Tearmaster compared to the Slit Lamp method.

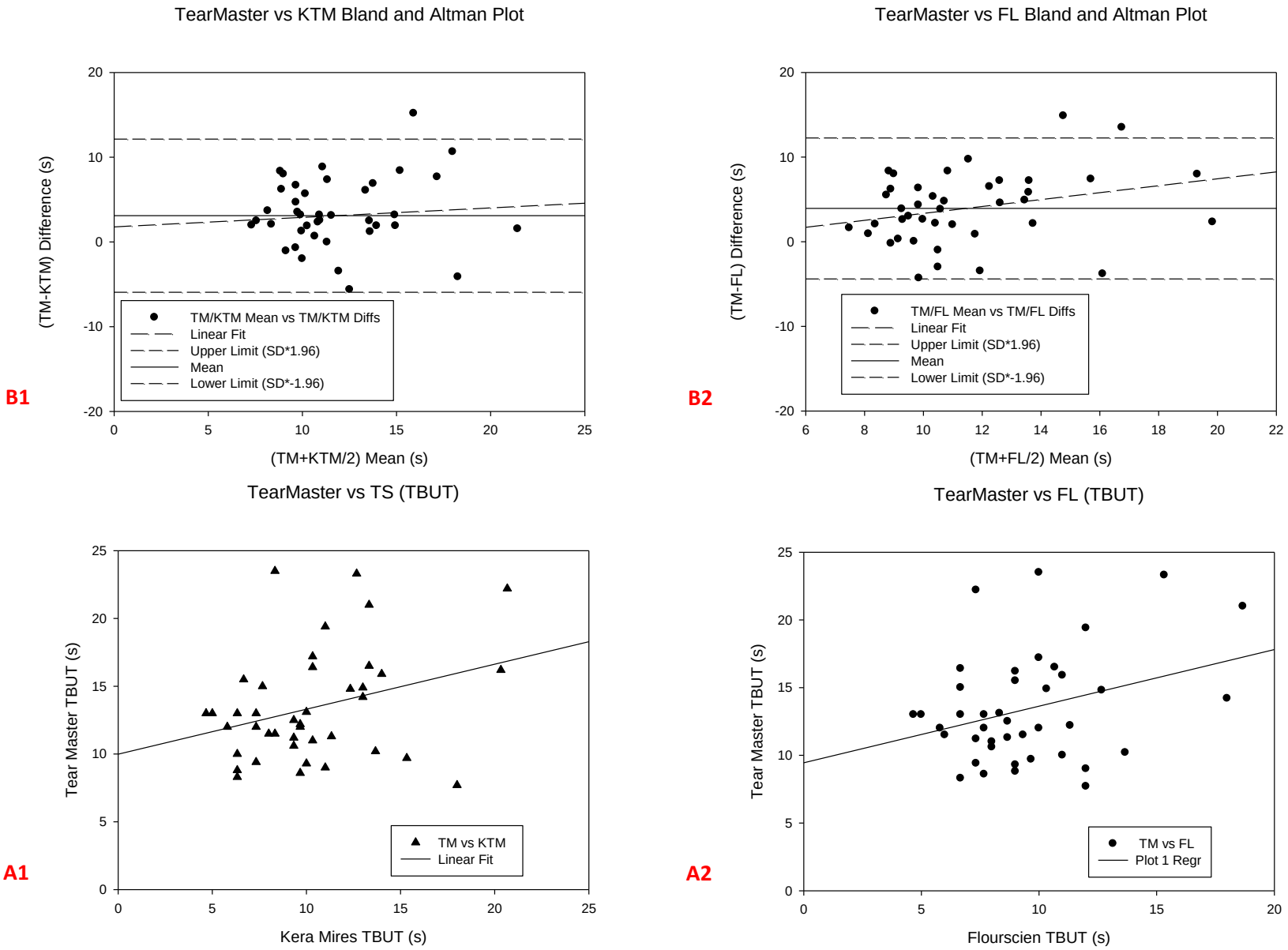

Figure 7.15: A1/B1 Comparison between TearMaster and Keratometry method, small positive trend evident with greater variation at longer TBUT's A2/B2 Comparison between TearMaster and Fluorescein methods again slight tend for TearMaster to overestimate at longer TBUT.

7.7.3 Discussion

There was strong correlation between the measured TBUT with the TM and the TS with this study suggesting that the TM is an effective tool for measuring and quantifying the tear break up process. There was a far weaker coloration with the SLP1 and keratometry methods and this was concluded to be because of the smaller field of view of assessment when using these techniques. The instillation of fluorescein for the FL TBUT method has been shown to destabilise the tear film due to the addition of liquid with the fluorescein molecules on the fluoret in addition to the molecules themselves changing the physical properties of the tear film (Mengher et al. 1985). The longer measured tear film break up time with the larger field of view and ability to watch the video frame by frame with the Tear Master was unexpected. If the tear-film break-up occurred in the periphery first the TearMaster values should have been shorter than the central imaging techniques (SLP1 and KM) whereas if the distortion occurred first centrally there should be no difference between them. Instead the result suggests that the observer could have been more lenient on their definition of what constituted a break (a potential limitation of the study having more than one investigator) or that breaks were recorded with the small mire area of the SLP1 and KM techniques, where the larger image showed these to be tear debris floating across the field or transient and small compared to the overall tear film stability.

The Sanyo Xacti hand held camera was able to provide clear and well exposed images of the tearfilm during the interblink interval. However it was noted that the system lacked sufficient battery life for a full testing cohort, falling after approximately 20 subjects. The standard 2GB storage also lacked sufficient space and provides only enough storage for 30 subjects. A commercial system should be able to offer better battery life and storage efficiency. Approximately 4 hours of continuous recording and data storage is required for assessing 200 Subjects. The TM is therefore determined to be a useful, novel and practicable device for imaging tearfilm break up-under conditions found in everyday environments. The device could be made even more effective by the development of software to automate both the recording process but the post processing and analysis. Although outside the remit of this investigation the process of developing imaging software should be untaken in future versions of the device. This project has demonstrated how modern technology can be used to create small, portable and potentially more objective devices for assessment of the eye through collaboration between ophthalmic practitioners and engineers.

Chapter 9

Chapter 8 Thesis Discussion

This thesis set out to demonstrate the potential of combining modern engineering expertise with ophthalmic applications to allow enhanced eye care through better imaging, detection and monitoring of ocular changes. This was to be showcased by examples of how high-end technology can enhance the understanding of *in-vivo* the interaction between medical devices and ocular tissue, how existing commercially available equipment can be enhanced to increase its functionality and finally, the ability to recreate and expand the functionality of an existing instrument, but in a smaller, portable and lower cost device.

8.1 High End Technology Development: OCT Systems and Ophthalmic Imaging

Chapter 2 identifies the historical development of OCT and its application in ophthalmic imaging, The research involved demonstrating how high-end technology can enhance the understanding of *in vivo* the interaction between medical devices, in this case a contact lens, and ocular tissue in a dynamic in-vivo clinical environment. A dual imaging Optical Coherence Tomography / High Speed Camera system was developed to study the dynamics of contact lens movement over the cornea under varied conditions.

The customisation of the Santec OCT system was successful and highlighted the possibilities for using off the shelf hardware (OTS) with the addition of extra modifications to develop a device that is unique and highly specialised. Without the use of OTS instruments construction of instrumentation would be extremely expensive and time consuming. The design modification of the OCT to be suitable for ophthalmic use took 18 months and two full hardware iterations before the device was fit for purpose.

The seven-axis alignment system was the most mechanically demanding part of the physical design process, but offered unprecedented flexibility. As of August 2012 no other OCT system is known that can be aligned with the eye with such precisions and repeatability. Without the development of this custom hardware the clinical trial could not have taken place.

Calibration and de-warping of the OCT images proved successful removing the distortion inherent in such a measurement system. After calibration and de-warping epithelium thickness was measured to be approximately 60 microns, in close agreement with literature giving validity to the technique

(Parkash et al. 2012; Reinstein et al. 2008). The methods and approach discussed in chapters 2,3 and chapter 4 denoting the hardware design phase has proven itself to be effective in the construction of advanced ophthalmic instruments. They will be expanded upon in succeeding instrumentation design sections.

In retrospect most of the project was actually more closely focused on the software development. Although the Santec OCT system was a capable device it lacked considerably with regard to software capability. The Santec OCT control software was only designed to demonstrate the operation principles of the OCT system. It had poor provision for saving and exporting data. The system wasn't even provided with a stand-alone viewer for data. Data could only be viewed on the actual OCT system with the entire unit (including laser) powered up. A total of 26 full stand-alone programs were developed for the OCT project, including external data viewer deployable to any windows X86 or X64 based machine and full analysis packages for OCT and HSC data.

Custom software allowed the OCT system to be utilised in novel ways with complete control over the capture process and timing. The system was not limited like commercial systems to sets of specific routines or timings. Using the HSC and OCT simultaneously utilising the capability of desktop computers, pushed them to the limits. Though careful handling of the execution process and use of coding optimised for multithreaded operation, the entire acquisition process could be performed from a single Central Processing Unit (CPU). The use of a multithread design is becoming more popular as modem computer chip designs increasing taking this route to add ever more processing power and keep up with Moore's law (Geer 2005). These techniques will be applied to future work at Aston when developing customised software solutions to take advantage of the most modem processor technology.

The laser safety assessment process was far more complex and involved than had previously been planned or budgeted for, consuming nearly 6 months of investigation time. Experience with such a complex system has proved useful in developing methods and approaches to future safety assessments. Generic documentation have been developed and specific testing equipment has been purchased. Blanket MHRA waiver has been undertaken for all future research devices to account for CE wavering required only the laser safety process to be undertaken.

The OCT system pilot trial detailed in chapter 5 was extremely beneficial in the design process. Not only was it essential in deciding the metrics to be measured, analysed and quantified in the full

clinical trial, the pilot also allowed the effective quantification of the capabilities of the data analysis process. Discussion with the research partners was highly beneficial to further refine the specification. A first pilot investigation similar to this should be undertaking with all future large development projects. The pilot demonstrated that considerable automation to the analysis process was possible. However, as with all software systems there are competing factors in the design process. There is always a trade-off between; coding complexity, benefits gained by automation, and software development time. A compromise was reached where automation would be used where efficient, and human analysis where producing extremely robust fully automated systems was regarded as too time consuming or complex. The resultant clinical trial showed for the first time the true impact of a contact lens on the ocular surface and how this was influenced by contact lens base curve and edge design parameters. These findings will have direct application to refine future commercial designs which can again be evaluated on the instrumentation devised in this thesis.

8.2 Increasing the Functionality of a Commercial Instrument: The Dyna-WAM Open-Field Autorefractor

The second example of the potential of modern engineering techniques to enhance ophthalmic instrumentation focused on how the functionality of existing commercially available equipment could be increased. In this example a commercially available open-field autorefractor was converted from a basic pupil size and refraction device to one that allowed dynamic monitoring of ocular accommodation and pupil size allowing a project on the effect of ultra-violet light blocking contact lenses on ocular accommodation to be conducted.

The 3 iterations of Dyna-WAM presented in chapter 6, showed the linear progression of the design process with user feedback influencing the succeeding generation. The second genearation device featured over one order of mangnitude increase (moment time delay decreased from 1400ms to <30ms) of target presentation speeds. Hardware hacking tools and routines have been developed that will allow futures investigation into instrumentation to be undertaken with greater speed and efficiency.

The software developed to control and monitor the WAM-5500 was a unique and novel system in its own right. Interest has been generated from external companies about developing a software suite for further research with the WAM-5500. Future generations of the device are planned (explained in more detail in the future projects section). Miniaturised versions of both the Badal system and

targets are under development to expand Aston's wavefront sensing technology. The project successfully demonstrated the ability to reverse engineer and expand current instrumentation beyond its initial design criteria. This was demonstrated in the UV retrospective study in which the full study, not part of this thesis, demonstrated faster accommodative responses (faster rise and fall times) in eyes that had worn UV blocking contact lenses for the past five or more years compared to those who had worn non-UV blocking lenses. The enhanced utility of commercially available and CE marked instrumentation allowed the study to be conducted in traditional optometric high street practice without concerns about safety and unsightliness and the study is now being extended to at least 5 sites across the world which would not have been possible with off the self-instrument currently available. Therefore the modification of the WAM-5500 has given Aston a unique tool to undertake accommodative research and stay ahead of its competitors.

The Aston Badal Optometer detailed in chapter 7 was the largest production run of a single item undertaken to date by the engineering team at Aston University. A total of 43 units were produced with 41 delivered to the customer. A total of 5 people (led by the author) worked on the project continually completing it in less than 3 months. The project clearly indicates that the team at Aston University is capable of delivering custom instrumentation in bulk and with very short lead times, demonstrating our ability to liaise closely with industry. The most complex part of the project was the organisation of the more than 20 sub-contractors and suppliers. The project generated considerable income to allow other research activity's to be undertaking with greater efficacy and scope. One of the continuing benefits form the project is the development of advanced CAD engineering models of the WAM-5500 which have proved so effective in reducing physical waste and reworking, they will be rolled out across all devices. Internal testing had indicated at least 50% reduction in number of prototypes needed when this method is utilised.

8.3 Developing Smaller, More Portable Instrumentation: the TearMaster

The final example of modern engineering applied to ophthalmic instrumentation was in the form of recreating and expand the functionality of a no longer produced instrument (the Keeler Tearscope), but in a smaller, portable and lower cost device with objective evaluation capability. The project focused on the ability to assess the tear film and its dynamics *in-vivo* to allow a project on dry eye assessment repeatability to be conducted.

The device underwent two iterations with a trial undertaken with the second generation. The electroluminescence lighting was highly successful for generating interference and reflection patterns on the surface of the tear film. To our best knowledge, this is the first time that this technology has been used for illumination in any form of ophthalmic instrumentation. Although a difficult to implement technology, it can be utilised in future projects specifically for devices that required backlighting or diffuse illumination. The TearMaster clinical trial of 41 subjects tested 5 different types of tear break up assessment indicated that the TearMaster was a good match to the TearScope and validated the instrument accordingly.

The waveguide technology for dual wavelength illumination, worked well, but was not specifically tested *in-vivo* at this time. It will be integrated into future designed where applicable. Work to develop a computer model of this technology will be undertaken to optimise the design of future generations.

Utilisation of the Sanyo Xacti commercially available video camera proved to be difficult with optical, battery life and video storage problems and will be discontinued. A next generation device has been commissioned, but will not use a consumer imaging system. The next generation of device will focus on the development of software to automatically determine when the tear break up has occurred while simultaneously mapping its quality dynamically.

8.4 Experiential Learning

As well as the specific thesis examples developed and documented in this thesis, a number of key aspects of experiential learning can be reflected upon:

8.4.1 Budgeting, Costing and Specification

The cost of a research project is difficult to accurately determine beforehand, but is of uppermost importance when undertaking research and development (R&D) for external clients. Part of the scope of this thesis was to determine the correct approach to developing customised solutions, and a method to developed the costing criteria for both internal and external projects allowing accurate budgeting.

For effective costing it is believed the best metric to base the R&D cost is the required final recommended retail price (RRP). Even for items that are not specifically designed for retail this can be an effective approach. The need for budgeting is paramount in engineering development. The extremely broad nature of the engineering field gives rise to many different types of possible solutions, even for relatively complex systems. To develop a solution one must keep in mind the product specification and RRP when selecting components and fabrication techniques.

Experience with the Aston Badal System and OCT hardware development indicated that an initial budget varying from between 15 and 25 times the RRP should be sufficient for the development phase of the project. With the lower end specifically tailored towards the low cost products i.e. <1000 USD RRP. The material cost for each unit should be approximately 1/3rd of the RRP for the final production unit. With prototypes costs as high as 20 times the final RRP when utilising rapid prototyping and manufacturing techniques. With less expensive products, multiple prototypes should be built at each phase to enable parallel development to take place on the next generation device.

It is therefore recommended that at outset of a project a budget is decided on for the hardware fabrication phase of the project. Experience has indicated that without control of financing it is often difficult to determine the required level of complexity that should be integrated into a solution. A detailed specification of the products requirements is paramount not only for compliance, but also for managing the changing demands from the research partners.

It should be noted in the design of the OCT Support Unit that the research partners changed the requirements for alignment, necessitating a complete redesign of the unit costing over 1000 USD. Although this is to be expected in research work, with some leeway appropriate, it has to be quantified and controlled wherever possible to avoid excessive cost/time overruns. The name “Scope Creep” is given to this phenomenon where the addition of new previously not unknown (or budgeted) features are requested and is usually a consequence of poor communication or specification determination between parties. Projects should by carefully monitored to avoid excessive Scope Creep.

8.4.2 Testing and Clinical Trials

The validation of all instrumentation usually requires some form of trial against existing equipment and/or human participants. Deciding when the prototype system is ready for large scale testing is difficult to determine. There are quite naturally competing interests at play when deciding a device is ready for external trials. Engineers typical are more reserved about believing the headwear and software is ready for testing, and often need to be pushed to make the leap to larger scale testing. Managers naturally are more concerned with seeing results from the device, but are less involved in the design and verification phases. However ultimately the decision if a device is ready for testing has to be taken with reasoned, but not over cautious engineering thought. Experience gained over the previous 4 years developing instrumentation indicates that a device in the Block 2 or preferable Block 3 phase are the earliest that a device should be put forward for testing. Testing should be incremental with verification at each stage of testing at each inter block boundary.

8.4.3 Research Focused Design and Tools

As with all complex systems it can be difficult to keep track of a large project progress and point in the design process. It is quite possible in engineering to become side tracked with over-engineering particular aspects of a systems design. There is a constant requirement to ensure solutions under development are applicable for the required specifications. A design review process should be undertaken regularly, preferably in consultation with a more experienced engineer to ensure that the engineering process is on track. We propose using some form of information/project management specific software to keep track of this progress. Investigation into the feasibility of this concept are currently underway.

8.4.4 Rapid Prototyping and Rapid Manufacturing Technology in Ophthalmic Research

RP and RM have been used in all the projects presented in this thesis. The ability to fabricate a complex geometric shape out of structural plastics within 24 hours is essential for the rapid production of prototypes. When designing casings or covers, there are often no other fabrication techniques possible in house without considerable work producing mandrills and jigging fixtures. Testing has indicated that the use of RP components can reduce the work time required fabricate a solution by as much as 80%. Even given the extreme cost of materials of approximately £200 per kg in 2012. The savings in time far outweigh this expense. Experimentation with post processing of RP parts has shown surface finishes close to cast acrylic are also possible. The extensive use of RP and RM will afford Aston a comparative advantage in the ophthalmic instrumentation field.

8.4.5 Running Costs and Investing in Infrastructure

The current engineering team consist of 2 full time professional engineers responsible for design and analysis of instrumentation and a highly experienced master technician responsible for physical fabrication process. There are also up to 2 extra part time team members responsible for specific data analysis and design tasks.

As with all dynamic systems there is the requirements to replace worn out components and improve the working process as new technology and methods become available. Current the monthly replacement costs for worn totalling and replacement parts are between 150-200 GBP. This is sufficient to keep the system at a constant state of readiness. As of August 2012 we have never missed a significant deadline.

The total capital investment in the engineering infrastructure to support ophthalmic research at as Aston University of approximately 40,000 GBP and has successfully built a system that can rapidly design custom instrumentation with rapid turnaround times. A monthly trickle investment of £150 is required to ensure new access to new technology essential to keep engineering at the cutting edge. In total a yearly running cost excluding wages of approximately 4,000 GBP will keep the system in good condition and operating at high efficiency. The approach of having a team of full time dedicated research engineers and dedicated technicians within Optometry is quite unique, and it is believed to have now produced one of the most capable and responsive engineering teams at Aston University.

8.5 Study limitations and Future Aspirations

This thesis set out to demonstrate the potential of combining modern engineering expertise with ophthalmic applications to allow enhanced eye care through better imaging, detection and monitoring of ocular changes. This integration between clinicians and engineers has developed over the past 4 years to allow novel examples of cutting edge engineering with clinical application to be showcased, with examples from high to low end. Engineering design limitations are perhaps less obvious that those of a clinical trial, but the technology keeps advancing opening up new possibilities for enhancing clinical applications. There was not sufficient time to develop objective evaluation of the TearMaster dynamic imaging of the tear film due to the complexities of controlling for microsaccades and the complexity of the background behind the placido rings, but this will form part of an ongoing project.

Future aspirations focus around expanding the research into an enterprise based business model, with funding from industry and government sources for the creation of technology to better understand the physiology of the eye or the application of treatments as well as the adaptation of current and development of new instrumentation to enhance clinical eye-care worldwide.

8.6 The Expansion into an Enterprise Based Model

Much of the work undertaken at Aston University is increasingly becoming contract design and testing led by specific queries from industrial partners. The University environment is well suited for performing trials with human subjects, having all the required ethical standards, safeguards and insurances etc.. However, the physical fabrication of instrumentation can be difficult in an environment where procurement, contract negotiation, and staffing issues are led by a less business minded focus.

Specific issues tend to focus on the considerable difficulties with procurement and working with external partners. It has been noted that this has caused cost and time overruns with projects. We believe that "spinning off" and external incorporated component to the research group will bring benefits.

The increasing complexity of the new generation products has also highlighted the need for labour specialisation. As a device moves closer to mass production, the level of professional engineering increases, as tolerances and specifications become more stringent. As of 4th quarter 2012 an external company linked to research at Aston University have been founded with the aim of addressing some of these issues.

The research will still very much be based at Aston, but specific types of works and projects will be undertaken via the company. One of the major aims is to further Aston branding and penetration into instrument markets. It is believed that the company can aid in this function by been better able to propagate our activities externally.

The physical structure of the company is still yet to be decided but currently it's a loosely affiliated set of 8 professional engineers/computer scientists(Electrical/Mechanical and Software/Analytical) and product designs currently working on an Ad hoc consultancy basis. There are also optometrists and professional researchers but not directly involved in the technical design side.

We are currently working in partnership with a Birmingham based creative arts and media company to devolving specific branding and presentation styles. The aspiration had been to present a professional, modern and stylish persona. A contemporary website is also under development detailing historical projects, group members and our capabilities as a team. Overall the project has been successfully in developing customised instrumentation fruiting research in the ophthalmic industry.

Bibliography

Ameri, F. & Dutta, D., 2005. Product Lifecycle Management : Closing the Knowledge Loops. *Computer-Aided Design & Applications*, 2(5), pp.577–590.

Armstrong, R. a et al., 2011. Statistical guidelines for clinical studies of human vision. *Ophthalmic & physiological optics : the journal of the British College of Ophthalmic Opticians (Optometrists)*, 31(2), pp.123–36.

Atchison, D., Bradley, A. & Thibos, L., 1995. Useful variations of the Badal optometer. *Optometry & Vision*. Available at: http://journals.lww.com/optvissci/Abstract/1995/04000/Useful_Variations_of_the_Badal_Optometer.10.aspx [Accessed July 5, 2012].

Badal, J., 1876. Optomètre métrique international du Dr. Badal. Pour la measure simulanée de la refraction et de l'acuité visuelle meme chez le illetres. In *Annales d'Oculistique*. pp. 101–117.

Barbero, S., 2006. Refractive power of a multilayer rotationally symmetric model of the human cornea and tear film. *Journal of the Optical Society of America. A, Optics, image science, and vision*, 23(7), pp.1578–85. Available at: http://www.ncbi.nlm.nih.gov/pubmed/16783420.

Barrios Hernandez, C.R., 2006. Thinking parametric design: introducing parametric Gaudi. *Design Studies*, 27(3), pp.309–324.

Barry, J. & Backes, A., 1997. Limbus versus pupil center for ocular alignment measurement with corneal reflexes. *Investigative ophthalmology & visual science*, 38(12), pp.2597–2607. Available at: http://www.iovs.org/content/38/12/2597.short [Accessed December 30, 2012].

Beers, AP & Heijde, G. Van der, 1996. Age-related changes in the accommodation mechanism. *Optometry and vision science*, 73(4), pp.235–242.

Beers, APA & Heijde, G. Van Der, 1994. In vivo determination of the biomechanical properties of the component elements of the accommodation mechanism. *Vision research*, 34(21), pp.2897–2905.

Bentivoglio, A.R. et al., 1997. Analysis of blink rate patterns in normal subjects. *Movement disorders : official journal of the Movement Disorder Society*, 12(6), pp.1028–34.

Bibby, M. & Tomlinson, A., 1983. A model to explain the effect of soft lens design specifications on movement. *American journal of optometry and physiological optics*, (60), pp.287–91.

Bland, J.M. & Altman, D.G., 1986. Statistical methods for assessing agreement between two methods of clinical measurement. *Lancet*, 1(8476), pp.307–10.

Braun, R.J. & Fitt, A.D., 2003. Modelling drainage of the precorneal tear film after a blink. *Mathematical medicine and biology : a journal of the IMA*, 20(1), pp.1–28.

Brennan, N. et al., 1994. Soft lens movement: temporal characteristics. *Optometry and vision science*, 71, pp.359–63.

Bron, A., 2001. Diagnosis of dry eye. *Survey of ophthalmology*, 45 Suppl 2(March), pp.S221–6.

Bruce, A., 1994. Influence of corneal topography on centration and movement of low water content soft contact lenses. *International Contact Lens Clinic*, (21), pp.45–9.

Chinn, S., Swanson, E. & Fujimoto, J., 1997. Optical coherence tomography using a frequency-tunable optical source. *Optics Letters*, 22(5), pp.340–342.

Chong, C., Morosawa, A. & Sakai, T., 2008. High-Speed Wavelength-Swept Laser Source With High-Linearity Sweep for Optical Coherence Tomography. , 14(1), pp.235–242.

Chua, C.K., Leong, K.F. & Lim, C.S., 2003. *Rapid prototyping : principles and applications*, Singapore; New Jersey: World Scientific.

Colins, G., 1939. The electronic refractionometer. *The Australasian Journal of Optometry*, 22(2), pp.122–132.

Cosman, P.C. et al., 1994. Thoracic CT images: effect of lossy image compression on diagnostic accuracy. *Radiology*, 190(2), pp.517–524.

Craig, J. et al., 1995. Refractive index and osmolality of human tears. *Optometry & Vision Science*, 72(10), pp.718–724.

Cui L, W., J, W. & Shen, M, 2010. Dynamic Evaluation of Contact Lens Movement and Its Interaction with Blinking and Ocular Surface. *ARVO Poster*.

Davies, L. et al., 2003. Clinical evaluation of the Shin-Nippon NVision-K 5001/Grand Seiko WR-5100K autorefractor. *Optometry & Vision Science*, 80(4), pp.320–324.

Davis, J.R., 1993. *Aluminum and aluminum alloys* First., Metals Park, Ohio: ASM International.

DEWS, 2007. DEWS. The definition and classification of dry eye disease: report of the Definition and Classification Subcommittee of the International Dry Eye WorkShop (2007). *Ocular Surface*, 5(2), pp.75–92.

Driver, P. & Michael A, L., 1996. Meibomian gland dysfunction. *Survey of ophthalmology*, 40(5).

Erlich, P., 1886. Uber ide Methylenblau reaktion der lebenden Nervensubstang. *Deutsch Med. Wschr*, 12, pp.49–52.

Eyers, D. & Dotchev, K., 2010. Technology review for mass customisation using rapid manufacturing. *Assembly Automation*, 30(1), pp.39–46.

Fairchild, M.D., 1998. *Color appearance models*, Reading, Mass.: Addison-Wesley.

Fankhauser, F., Lörtscher, H. & Zypen, E., 1982. Clinical studies on high and low power laser radiation upon some structures of the anterior and posterior segments of the eye. *International ophthalmology*, 5(1), pp.15–32.

Feenstra, R. & Tseng, SCG, 1992. What is actually stained by rose bengal? *Archives of ophthalmology*, 110(7), p.984.

Fercher, A., Hitzenberger, C. & G, K., 1995. Measurement of intraocular distances by backscattering spectral interferometry. *Optics Communications*, 117(3), pp.43–48.

Fittock, A., 2010. Non-medical prescribing: by nurses, optometrists, pharmacists, physiotherapists, podiatrists and radiographers. Available at: http://www.npc.nhs.uk/non_medical/resources/NMP_QuickGuide.pdf.

Geer, D., 2005. Chip makers turn to multicore processors. *Computer*, (5), pp.11–13.

Gibson, I., Rosen, D.W. & Stucker, B., 2010. Additive manufacturing technologies rapid prototyping to direct digital manufacturing.

Golding, T., Bruce, A., et al., 1995. Soft lens movement: effect of blink rate on lens settling. *Acta ophthalmologica Scandinavica*, 73, pp.506–11.

Golding, T., Harris, M. & Smith, R., 1995. Soft lens movement: effects of humidity and hypertonic saline on lens settling. *Acta ophthalmologica Scandinavica*, 73, pp.139–44.

Goto, E. et al., 2003. Computer-Synthesis of an Interference Color Chart of Human Tear Lipid Layer, by a Colorimetric Approach. *Investigative Ophthalmology & Visual Science*, 44(11), pp.4693–4697.

Goto, E., 2004. Quantification of Tear Interference Image. *Cornea*, 23(8), pp.20–24.

Grantham, K., 2012. Dragon Becomes First Commercial Spacecraft to Attach to the Space Station. Available at: http://www.spacex.com/press.php?page=20120525 [Accessed August 14, 2012].

Grunwald, R., 2007. Thin film micro-optics new frontiers of spatio-temporal beam shaping. , p.287.

Guillon, J., 1998. NON-INVASIVE TEARSCOPE PLUS ROUTINE FOR CONTACT Principle of Tear Film Stability. *Contact Lens and Anterior Eye*, 21, pp.31–40.

Guillon, J., 1997. The Keeler Tearscope-Plus-an improved device for assessing the tear film. *Optician*.

Gupta, N., Wolffsohn, J.S.W. & Naroo, S. a, 2008. Optimizing measurement of subjective amplitude of accommodation with defocus curves. *Journal of cataract and refractive surgery*, 34(8), pp.1329–38.

Hall, L. et al., 2011. The Influence of Corneo-Scleral Topography on Soft Contact Lens Fit. *Invest Ophthalmol Vis Sci*, 52, pp.6801–6.

Harvey, W. & Franklin, A., 2005. *Routine eye examination*, Edinburgh; New York: Elsevier/Butterworth Heineman.

Heald, K. & Langham, M.E., 1956. Communication permeability of the cornea and the blood-aqueous barrier to oxygen. *British Journal of Ophthalmology*, 40(12), pp.705–720.

Hecht, E. & Zajac, A., 1974. *Optics*, Reading, Mass.: Addison-Wesley Pub. Co.

Heron, G., Charman, W.. & Schor, C., 2001. Dynamics of the accommodation response to abrupt changes in target vergence as a function of age. *Vision Research*, 41(4), pp.507–519.

Holly, F., 1986. Tear film formation and rupture: an update. *Dry Eye Insitute Inc*, pp.634–45.

Huang, D. et al., 1991. Optical coherence tomography. *Science*, 254(5035), pp.1178–1181.

Huber, R. & Adler, D., 2006. Buffered Fourier domain mode locking: unidirectional swept laser sources for optical coherence tomography imaging at 370,000 lines/s. *Optics letters*, 31(20), pp.2975–2977.

Hung, G.K., 2001. *Models of Oculmotor controle* First., World Scientific Publishing Company.

Ibrahim, M. & Bhandari, A., 2006. Making Sight Affordable (Part I) Aurolab Pioneers Production of. *Innovations: Technology, Governance, Globalization*, pp.25–41.

Jenkins, J. & Shimbo, M., 1984. The distribution of pressure behind a soft contact lens. *Journal of biomechanical engineering*, 106, pp.62–65.

Jos, J. et al., 2009. Measuring Lenny : the size of Debian 5 . 0. *Universidad Rey Juan Carlos*. Available at: http://gsyc.es/~frivas/paper.pdf.

Joseph, A.C. & Charles, C.P., 1951. The near infrared absorption spectrum of liquid water. *JOSA*, 41, p.302.

Kasthurirangan, S., Vilupuru, A.S. & Glasser, A., 2003. Amplitude dependent accommodative dynamics in humans. *Vision Research*, 43(27), pp.2945–2956.

Kaura, R. & Tiffany, J., 1986. The role of mucous glycoproteins in the tear film." The Preocular Tear Film in Health, Disease and Contact Lens. *Dry Eye Insitute Inc*, pp.728–732.

Kelly, S., Thornton, J. & Edwards, R., 2005. Smoking and cataract: review of causal association. *Journal of Cataract & Refractive Surgery*, 31(12), pp.2395–404.

King-Smith, P.E. et al., 2004. The thickness of the tear film. *Current eye research*, 29(4-5), pp.357–68.

Kok, J. et al., 1992. Fluorophotometric assessment of tear turnover under rigid contact lenses. *Cornea*, 11, pp.515–7.

Korb, D.R., 2002. *The tear film : structure, function, and clinical examination*, Oxford; Boston: Butterworth-Heinemann.

Kumar, A. & Buglass, E., 2009. Engierring UK 2009/10 Report. *Engeineering UK*, pp.22–30. Available at: http://www.engc.org.uk/ecukdocuments/internet/document library/Engineering UK 2009.pdf.

Lemp, M. a & Hamill, J.R., 1973. Factors affecting tear film breakup in normal eyes. *Archives of ophthalmology*, 89(2), pp.103–5.

Leon, N., 2009. The future of computer-aided innovation. *Computers in Industry*, 60(8), pp.539–550.

Li, W.D. et al., 2005. Collaborative computer-aided design—research and development status. *Computer-Aided Design*, 37(9), pp.931–940.

Lovie-kitchin, J.A.N.E. & Brown, B., 2000. Repeatability and Intercorrelations of Standard. *Optometry & Vision Science*, 77(8), pp.412–420.

Mailer, C., 1978. Automatic refraction and the private ophthalmologist: Dioptron II compared with subjective examination. *Canadian journal of ophthalmology. Journal*, 13(4), pp.252–257.

Mallen, E.A.H. et al., 2001. Clinical evaluation of the Shin-Nippon SRW- 5000 autorefractor in adults. *Ophthalmic and Physiological Optics*, 21(2), pp.101–107.

Martin, D. & Holden, B., 1986. Forces developed beneath hydrogel contact lenses due to squeeze pressure. *Physics in medicine and biology*, 30, pp.635–49.

Martin, D. & Holden, B., 1983. Variations in tear fluid osmolality, chord diameter and movement during wear of high water content hydrogel contact lenses. *Int Contact Lens Clin*, (10), pp.332–42.

Masters, M. & Mathy, M., 2002. Direct manufacturing of custom-made hearing instruments, an implementation of Digital Mechanical Processing. *SME Rapid Prototyping Conference and Exhibition, Cincinnati, OH*.

McBrien, N.A. & Millodot, M., 1985. Clinical evaluation of the Canon Autoref R-1. *American journal of optometry and physiological optics*, 62(11), pp.786–792.

McLin, L.N. & Schor, C.M., 1988. Voluntary effort as a stimulus to accommodation and vergence. *Investigative ophthalmology & visual science*, 29(11), pp.1739–46.

McNamara, N. et al., 1999. Tear mixing under a soft contact lens: effects of lens diameter. *American journal of ophthalmology*, 127, pp.659–65.

Mengher, L. et al., 1985. Effect of fluorescein instillation on the pre-corneal tear film stability. *Current Eye Research*, 4(1), pp.9–12.

Moldonado-Codina, C. & C Efron, N., 2004. Impact of manufacturing technology and material composition on the clinical performance of hydrogel lenses. *Optometry & Vision Science*, 81(6), p.44254.

Nichols, J.J. et al., 2002. Evaluation of tear film interference patterns and measures of tear break-up time. *Optometry and vision science : official publication of the American Academy of Optometry*, 79(6), pp.363–9.

Nichols, J.J., Mitchell, G.L. & King-Smith, P.E., 2005. Thinning rate of the precorneal and prelens tear films. *Investigative ophthalmology & visual science*, 46(7), pp.2353–61.

Nwosu, S.N., 1998. Ocular problems of young adults in rural Nigeria. *International ophthalmology*, 22(5), pp.259–63.

Nyquist, H., 1928. Certain topics in telegraph transmission theory. *American Institute of Electrical Engineers*, 90(2), pp.617–644.

Németh, J. et al., 2002. High-speed videotopographic measurement of tear film build-up time. *Investigative ophthalmology & visual science*, 43(6), pp.1783–90.

Oldenburg, A.L. et al., 2003. Fast-Fourier-domain delay line for in vivo optical coherence tomography with a polygonal scanner. *Applied optics*, 42(22), pp.4606–11.

Parkash, G. et al., 2012. Reliability and reproduucability of assessment of corneal epithelium thickness by fourier domain optical coherence tomography. *Invest Ophthalmol Vis Sci*, 53, pp.2580–5.

Patel, S, Bevan, R. & Farrell, J., 1988. Diurnal variation in precorneal tear film stability. *American journal of optometry and physiological optics*, 65(3), pp.151–154.

Patel, Sudi. & Blades, K.J., 2003. *The dry eye : a practical approach*, Edinburgh; New York: Butterworth-Heinemann.

Pearson, K. & Lee, A., 1903. On the laws of inheritance in man: I. Inheritance of physical characters. *Biometrika*, 2(4), pp.357–462.

Perrigin, D., Grosvenor, T. & Reis, A., 1984. Comparison of Dioptron Nova refractive data with conventional refractive data. *American journal of ophthalmology*, 61(7), pp.479–483.

Peterson, R.C., Wolffsohn, James S & Fowler, C.W., 2006. Optimization of anterior eye fluorescein viewing. *American journal of ophthalmology*, 142(4), pp.572–5.

Pflugfelder, S., Tseng, SC & Sanabria, O., 1998. Evaluation of subjective assessments and objective diagnostic tests for diagnosing tear-film disorders known to cause ocular irritation. *Cornea*, 17(1), pp.38–56.

Podoleanu, A. et al., 2004. Sequential optical coherence tomography and confocal imaging. *Frontiers in Optics*, 29(4), pp.364–366.

Potsaid, B. et al., 2008. Ultrahigh speed spectral/Fourier domain OCT ophthalmic imaging at 70,000 to 312,500 axial scans per second. *Optics*, 16(19), pp.15149–15169.

Prichard, N. & Fonn, D., 1995. Dehydration, lens movement and dryness ratings of hydrogel contact lenses. *Ophthalmic and Physiological Optics*, 15, pp.281–6.

Prydal, J.I. et al., 1992. Study of human precorneal tear film thickness and structure using laser interferometry. *Investigative ophthalmology & visual science*, 33(6), pp.2006–11.

Pugh, J. & Winn, B., 1988. Modification of the Canon Auto Ref R1 for use as a continuously recording infra-red optometer. *Ophthalmic and Physiological Optics*, 8(4), pp.460–464.

Purslow, C. & Wolffsohn, JS, 2005. Ocular surface temperature: a review. *Eye & contact lens*, 31(3), pp.117–123. Available at: http://journals.lww.com/claojournal/Abstract/2005/05000/Ocular_Surface_Temperature__A_Review.6.aspx [Accessed December 30, 2012].

Radhakrishnan, P., Subramanyan, S. & Raju, V., 2008. CAD/CAM/CIM.

Reinstein, D. et al., 2008. Epithelial thickness in the normal cornea: three-dimentional display with Artemis very high-frequency digital ultrasound. *J Refract Surg*, 24, pp.571–81.

Rieger, G., 1992. The importance of the precorneal tear film for the quality of optical imaging. *British Journal of Ophthalmology*, 76, pp.157–158.

Rosenfield, M. & Cohen, A., 1996. Repeatability of clinical measurements of the amplitude of accommodation. *Ophthalmic and Physiological Optics*, 30, pp.143–151.

Sangwine, S.J. & Horne, R.E.N., 1998. *The Colour image processing handbook*, London; New York: Chapman & Hall.

Santec, 2011. Coherence Tomography OCT solutions from santec. *Santec Sales litrature*, 1.5, pp.1–20.

Schwallie, J. & Bauman, R., 1998. Fitting characteristics of Dailies daily disposable hydrogel contact lenses. *CALO*, 24, pp.102–6.

Serway, R.A. & Jewett, J.W., 2004. *Physics for scientists and engineers.*, Belmont, CA: Thomson-Brooks/Cole.

Seyer, M.D., 1984. *RS-232 made easy : connecting computers, printers, terminals, and modems*, Englewood Cliffs, N.J.: Prentice Hall.

Shapiro, F.R., 2006. *The Yale book of quotations*, New Haven: Yale University Press.

Sharma, K.K., 2006. *Optics : principles and applications*, Amsterdam; Boston: Academic Press.

Shaw, A. et al., 2010. Eyelid pressure and contact with the ocular surface. *Investigative ophthalmology & visual science*, 51, pp.1911–7.

Shen, M, Cui, L & Riley, C, 2011. Characterization of soft contact lens edge fitting using ultra-high resolution and ultra-long scan depth optical coherence tomography. *Investigative ophthalmology & visual science*, 52, pp.4091–7.

Shen, M, Wang, J & Qu, J., 2008. Diurnal variation of ocular hysteresis, corneal thickness, and intraocular pressure. *Optom Vis Sci*, 85, pp.1185–1192.

Shen, M, Wang, M. & Wang, J, 2010. Entire contact lens imaged in vivo and in vitro with spectral domain optical coherence tomography. *Eye & contact lens*, 2(73), pp.73–76.

Shen, Meixiao et al., 2011. Characterization of soft contact lens edge fitting using ultra-high resolution and ultra-long scan depth optical coherence tomography. *Investigative ophthalmology & visual science*, 52(7), pp.4091–7.

Sheppard, A.L. & Davies, L.N., 2010. Clinical evaluation of the Grand Seiko Auto Ref/Keratometer WAM-5500. *Ophthalmic & physiological optics : the journal of the British College of Ophthalmic Opticians (Optometrists)*, 30(2), pp.143–51.

Shimazaki, J., Sakata, M. & Tsubota, K., 1995. Ocular surface changes and discomfort in patients with meibomian gland dysfunction. *Archives of ophthalmology*, 113(10), pp.1266–1270.

Snyder, C., 1989. Rotational position of toric soft contact lenses on the eye—clinical judgments. *International Contact Lens Clinic*, 16, pp.146–151.

Strang, N., Gray, L. & Winn, B., 1998. Clinical evaluation of patient tolerance to autorefractor prescriptions. *Clinical and Experimental Optometry*, 81(3), pp.112–118.

Swanson, E. a et al., 1993. In vivo retinal imaging by optical coherence tomography. *Optics letters*, 18(21), pp.1864–6. Available at: http://www.ncbi.nlm.nih.gov/pubmed/19829430.

Tearney, G.J. et al., 1997. In vivo endoscopic optical biopsy with optical coherence tomography. *Science (New York, N.Y.)*, 276(5321), pp.2037–9.

Tearney, G.J. et al., 1996. Rapid acquisition of in vivo biological images by use of optical coherence tomography. *Optics letters*, 21(17), pp.1408–10.

Tiffany, J., 1991. The viscosity of human tears. *International Ophthalmology*, 15, pp.371–376.

Tiffany, J.M., 1986. Refractive index of meibomian and other lipids. *Current Eye Research*, 5(11), pp.887–889.

Travis, J. & Kring, J., 2007. *LabVIEW for everyone : graphical programming made easy and fun.*, Upper Saddle River, NJ: Prentice Hall.

Truscott, R.J., 2009. Presbyopia. Emerging from a blur towards an understanding of the molecular basis for this most common eye condition. *Experimental eye research*, 88(2), pp.241–7.

Trusit, D., 2004. Automated refraction Design and applications. *Optometry Today*, June 4th, pp.28–32.

Tuchin, V., 2007. *Tissue optics : light scattering methods and instruments for medical diagnosis*, Bellingham, Wash.: SPIE/International Society for Optical Engineering.

Volker, W. et al., 2002. Real-time, high velocity-resolution color Doppler optical coherence tomography. *Optics Letters*, 27(1), pp.34–36.

Walker, J. et al., 2003. Evaluating steeper base curve lens movement. *Contact Lens Spectrum*, 18, pp.44–6.

Wang, J., 2003. Precorneal and Pre- and Postlens Tear Film Thickness Measured Indirectly with Optical Coherence Tomography. *Investigative Ophthalmology & Visual Science*, 44(6), pp.2524–2528.

Win-hall, D.M., Houser, J. & Glasser, A., 2010. Static and Dynamic Accommodation Measured Using the WAM-5500 Autorefractor. , 87(11), pp.873–882.

Wojtkowski, M & Bajraszewski, T., 2003. Real-time in vivo imaging by high-speed spectral optical coherence tomography. *Optics Letters*, 28(19), pp.1745–1747.

Wojtkowski, Maciej, 2010. High-speed optical coherence tomography: basics and applications. *Applied Optics*, 49(16), p.D30.

Wolffsohn, J S et al., 2004. Simultaneous continuous recording of accommodation and pupil size using the modified Shin-Nippon SRW-5000 autorefractor. *Ophthalmic & physiological optics : the journal of the British College of Ophthalmic Opticians (Optometrists)*, 24(2), pp.142–7.

Wolffsohn, J. S. et al., 2001. Continuous recording of accommodation and pupil size using the Shin-Nippon SRW-5000 autorefractor. *Ophthalmic and Physiological Optics*, 21(2), pp.108–113.

Wolffsohn, James S, 2008. *Ophthalmic imaging*, Edinburgh: Butterworth Heinemann Elsevier.

Wolffsohn, JS, Hunt, O. & Basra, A., 2009. Simplified recording of soft contact lens fit. *Contact Lens and Anterior Eye*, 32(1), pp.37–42.

Wolkoff, P. et al., 2005. Eye complaints in the office environment: precorneal tear film integrity influenced by eye blinking efficiency. *Occupational and environmental medicine*, 62(1), pp.4–12.

Wood, I.C., 1987. A review of autorefractors. *Eye (London, England)*, 1 (Pt 4)(4), pp.529–35.

Woods, W.D., 2008. *How Apollo flew to the Moon*, New York; Chichester, U.K.: Springer Verlag ; Published in association with Praxis Pub.

Yamada, T. & Ukai, K., 1997. Amount of defocus is not used as an error signal in the control system of accommodation dynamics. *Ophthalmic & physiological optics : the journal of the British College of Ophthalmic Opticians (Optometrists)*, 17(1), pp.55–60.

Yasuno, Y. et al., 2005. Three-dimensional and high-speed swept-source optical coherence tomography for in vivo investigation of human anterior eye segments. *Optics*, 13(26), pp.10652–10664.

Yokoi, N, Bron, A. & Tiffany, J., 2004. Relationship between tear volume and tear meniscus curvature. *Archives of ophthalmology*, 122, pp.1265–1269.

Yokoi, Norihiko et al., 2008. Rheology of tear film lipid layer spread in normal and aqueous tear-deficient dry eyes. *Investigative ophthalmology & visual science*, 49(12), pp.5319–24.

Young, G, 1996. Evaluation of soft contact lens fitting characteristics. *Optometry and vision science*, 73, pp.247–54.

Young, G, 1993. Influence of soft contact lens design on clinical performance. *Optometry & Vision Science*, (70), pp.394–403.

Young, G & Coleman, S., 2001. Poorly fitting soft lenses affect ocular integrity. *Eye & Contact Lens*, 27, pp.68–74.

Young, Graeme, 2004. Why one million contact lens wearers dropped out. *Contact lens & anterior eye : the journal of the British Contact Lens Association*, 27(2), pp.83–5.